

Multifunctional Carbon Dots-Based Nanocomposites for Sustainable Environmental Management and Solar-Driven Water Evaporation

Ph.D. Thesis

By

Nirmiti Mate



DEPARTMENT OF CHEMISTRY

INDIAN INSTITUTE OF TECHNOLOGY INDORE

JUNE 2025

Multifunctional Carbon Dots-Based Nanocomposites for Sustainable Environmental Management and Solar-Driven Water Evaporation

A THESIS

*Submitted in partial fulfillment of the
requirements for the award of the degree
of*
DOCTOR OF PHILOSOPHY

by
NIRMITI MATE



DEPARTMENT OF CHEMISTRY

INDIAN INSTITUTE OF TECHNOLOGY INDORE

JUNE 2025



INDIAN INSTITUTE OF TECHNOLOGY INDORE

I hereby certify that the work which is being presented in the thesis entitled **Multifunctional Carbon Dots-Based Nanocomposites for Sustainable Environmental Management and Solar-Driven Water Evaporation** in the partial fulfillment of the requirements for the award of the degree of **DOCTOR OF PHILOSOPHY** and submitted in the **DEPARTMENT OF CHEMISTRY, Indian Institute of Technology Indore**, is an authentic record of my own work carried out during the time period from **AUGUST 2020** to **JUNE 2025** under the supervision of **Dr. Shaikh M. Mobin**, Professor, Department of Chemistry, IIT Indore.

The matter presented in this thesis has not been submitted by me for the award of any other degree of this or any other institute.

Nirmite

Signature of the student with date
(NIRMITI MATE)

This is to certify that the above statement made by the candidate is correct to the best of my knowledge.

M. Shaikh

Signature of Thesis Supervisor with date
(PROF. SHAIKH M. MOBIN)

NIRMITI MATE has successfully given his/her Ph.D. Oral Examination held on *Dec. 9, 2025*

M. Shaikh

Signature of Thesis Supervisor with date
(PROF. SHAIKH M. MOBIN)

Acknowledgements

I take this opportunity to thank all those who have helped me carry out the work leading to this thesis and make my days memorable during my Ph.D. First and foremost, I express my sincere respect and deep gratitude to my supervisor, Prof. Shaikh M. Mobin, for his significant guidance, constant support, and encouragement throughout my research period. His dedication and unyielding attitude toward research and his students have been greatly responsible for completing my research work. His timely scholarly advice and meticulous scrutiny have assisted me greatly in accomplishing this thesis. His humble approach to research and problem-solving attitude has been an inspiration to me.

I sincerely thank my PSPC members, Prof. Rajneesh Misra and Dr. Umesh Kshirsagar, for their fruitful discussions, invaluable suggestions, and motivation during my PhD. I also express my immense gratitude to Prof. Suhas S. Joshi, Director, IIT Indore, for his continuous support in every panorama. Also, I would like to acknowledge IIT Indore for providing excellent facilities like the library, laboratory, and the Sophisticated Instrumentation Center (SIC) to carry out the work. I am also thankful to SAIF, IIT-Bombay, IIT-Delhi, IIT Jammu, IIT-Mandi, CSIR-NIIST, and MRC, MNIT-Jaipur, for providing characterization facilities.

I profusely thank Dr. Saju Pillai and Ms. Gopika Preethikumar for their collaborative work, cooperation, and scientific discussions during my projects. I extend my gratitude to all the faculty members of the chemistry department IIT Indore, for their timely help and guidance during different activities. I also thank all the staff members, Mr. Manish Kushwaha, Ms. Vinita Kothari, Mr. Rameshwar Dauhare, and Mr. Souvik, for their help and support during my PhD.

I would also like to thank the technical staff of SIC, IIT Indore, Mr. Ravinder Kumar, Mr. Kinny Pandey, Mr. Ghanshyam Bhavsar, Mr. Atul Singh, Mr. Ranjeet Raghuvanshi, and Ms. Kajal Chaudhari for their immense help during my experiments at SIC, IIT Indore. I would also

like to thank all library staff for their constant help whenever required. I am also grateful to the health center, transport, and housekeeping staff at IIT Indore for making things smoother during my Ph.D. tenure. I also thank UGC, India, for providing a research fellowship. I also thank SERB, BRNS, and NTTM, Delhi, for providing financial support for travel to present my thesis work in conferences.

I would like to extend my sincere thanks to all my current and past lab members for their warm support during these years. I would like to especially thank Dr. Nabeela and Dr. Neha, who guided and helped me in shaping my research goals like a sister in my initial years. I would like to thank my other group members Dr. Anoop Gupta, Dr. Vinay, Dr. Kaushik, Dr. Navpreet, Dr. Pranav, Dr. Viresh, Dr. Diptanshu, Mr. Ravinder, Mr. Nissar, Mr. Pawan, Mr. Praveen, Mr. Zahir, Dr. Imtiaz, Mr. Rakesh, Ms. Divya, Ms. Khushi, Ms. Priya, Ms. Afrin, Ms. Priya R., Ms. Saheli, Ms. Vinita, Mr. Kapil, Mr. Debasish Mr. Altaf, and Mr. Utkarsh for their suggestions during my work

I sincerely thank the editor and anonymous reviewers for their constructive comments and suggestions, which helped me improve the quality of my work and manuscripts. It would have been impossible for me to carry out my research successfully and write this thesis today without their critical assessment of my work and valuable suggestions to improve it. I am also grateful to the editors for accepting my research papers in their esteemed journals and giving my research findings a better reach.

This journey would not be so memorable without the smiles and gestures I have received and shared with my batchmates, seniors, and juniors. I would also like to thank my batchmates and friends, who have helped me overcome the obstacles and move forward during my PhD. I want to express my heartfelt gratitude to my dear friends, Navdeep Srivastava, Shivendu Mishra, Sandeep Das, Debanjan Bagchi, and Vidhi Agarwal, for making the PhD life much easier and enjoyable. I would also like to take this opportunity to thank Dr. Shivendra Singh for always motivating

and giving me mental support during this five-year journey. Without his support, this journey wouldn't be possible. He was always there in my hard times and motivated me to keep going.

Finally, I would like to express my sincere gratitude to my beloved parents, Mr. Narendra Mate and Mrs. Ketan Mate, and my uncle Mr. Kanhaiyalal Mate, for their unconditional love, unwavering support, and continuous encouragement during every phase of my life. Also, I want to thank my brother, Mr. Aakar Mate, for his encouragement during my ups and downs. Words can hardly describe my appreciation and feelings for them, but they have been my source of inspiration and motivation to course through life and excel in every aspect.

Nirmiti Mate

Dedicated to
My Beloved Parents
& Family

List of Publications

❖ Publications included in this Thesis:

- 1) **Mate N.**, Pranav, Kallayi N., Kaur N., Mobin S. M. (2022), Insight into the modulation of carbon-dot optical sensing attributes through a reduction pathway, *ACS Omega*, 7, 43759-43769. (DOI: 10.1021/acsomega.2c04766)
- 2) **Mate N.**, Khandelwal D., Kallayi N., Mobin S. M. (2023), Portable and non-invasive fluorescent thin films from photocatalytically active carbon dots for selective and trace-level detection of picric acid, *J. Mater. Chem. C*, 11, 16201-16213. (DOI: 10.1039/D3TC03625A)
- 3) **Mate N.**, Kallayi N., Preethikumar G., Pillai S., Mobin S. M. (2024), A lignin-derived carbon dot-upgraded bacterial cellulose membrane as an all-in-one interfacial evaporator for solar-driven water purification, *Mater. Horiz.*, 11, 5114-5122. (DOI: 10.1039/D4MH00591K)
- 4) **Mate N.**, Kallayi N., Mobin S. M. (2025), Carbon Dots Anchored Bacterial Cellulose Hybrid Platform as Fluorescent Sensor and Photocatalytic Remover of Pharmaceuticals, *J. Mater. Chem. C*, 13, 4691–4701. (DOI: 10.1039/D4TC04536J)
- 5) **Mate N.**, Prakash K., Kallayi N., Mobin S. M. (2025), Organic Network Comprising Sustainable Carbon Dots Upgraded Bacterial Cellulose Evaporator for Interfacial Solar-Driven Water Evaporation, *ACS Mater. Lett.*, 7, 2413-2421. (DOI: 10.1021/acsmaterialslett.5c00680)

❖ **Publications apart from this Thesis:**

- 6) Kaur N., Tiwari P., **Mate N.**, Sharma V., Mobin S. M. (2022), Photoactivatable carbon dots as a label-free fluorescent probe for picric acid detection and light-induced bacterial inactivation., *J. Photochem. Photobio. B.*, 229, 112412. (DOI: 10.1016/j.jphotobiol.2022.112412)
- 7) Parameswarreddy G., **Mate N.**, Arunachalam K., Sarathi R., Mobin S. M., Suematsu H. (2024), The Synergetic Effect of Nitrogen-Doped Carbon Dot and Short Carbon Fiber Reinforced Epoxy Composite on Electromagnetic Shielding in X-Band and Mechanical Properties, *IEEJ Trans. Fundam. Mater.*, 144, 87-94. (DOI: 10.1541/ieejfms.144.87)
- 8) Choudhary N., Kallayi N., **Mate N.**, Mobin S. M. (2024), Recent advances in CO₂ hydrogenation to methane using single-atom catalysts, *RSC Sustain.*, 2, 1179-1201 (DOI: 10.1039/D4SU00069B)
- 9) **Mate N.**, Satwani V., Pranav, Mobin S. M. (2024), Blazing Carbon Dots: Unfolding its Luminescence Mechanism to Photoinduced Biomedical Applications, *Chem. Asian J.*, 20, e202401098. (DOI: 10.1002/asia.202401098)
- 10) **Mate N.**, Asmat A., Agrahari S., Shaikh M. M. (2025), Unleashing the Multifunctionality of Carbon Dots for Solar-Driven Interfacial Evaporation: Recent Advances and Diverse Applications, *Chem. Asian J.*, 0, e70342. (DOI: 0.1002/asia.70342)

❖ **Conferences/Workshop/Oral/Poster presentation Attended**

1. Poster presentation at the 2025 Spring Meeting European Materials Research Society (E-MRS) held May 26-30, 2025, at

Strasbourg Convention Centre in Strasbourg, France.

2. Best Oral Presentation award during Research and Industry Conclave (RIC) 2025 at IIT Indore
3. Certificate of participation for poster presentation at International Conference on Fundamental and Advanced Research in Chemistry-2024 (FARC-2024), IIT Mandi
4. Poster presentation at “In-House Symposium CHEM-2024” Organized by the Department of Chemistry, Indian Institute of Technology Indore (IIT Indore)
5. Poster presentation in RSC Symposium on Materials Science Towards New Horizons-2023, Department of Chemistry, IIT Indore
6. Participated in the Indo-German conference on Sustainable Chemistry: 2023, IIT Indore
7. Poster presentation on 4th Commonwealth Chemistry Posters-2023, Commonwealth Chemistry Federation of Chemical Sciences Societies, Online Mode
8. Flash Talk presentation in 7th International Conference on Advanced Nanomaterials and Nanotechnology (ICANN2021), organized by Centre for Nanotechnology at Indian Institute of Technology Guwahati (IITG), India

List of Schemes

Chapter 2.

- Scheme 2.1. Schematic representation for the synthesis of BP-CD and rBP-CD 62

Chapter 3.

- Scheme 3.1. Schematic representation for the synthesis of TF-CDs from *c. thevetia* flowers by one-pot hydrothermal method. 102
- Scheme 3.2. Schematic illustration showing the preparation of TF-CD@PVDF film 109

Chapter 4

- Scheme 4.1 (a) Schematic illustration of the synthesized M-CDs, (b) photograph of the aqueous dispersion under UV ($\lambda_{\text{ex}} = 365 \text{ nm}$) and visible light illumination 138
- Scheme 4.2. Schematic suggested pathway for photocatalytic degradation of TET and their intermediates 163
- Scheme 4.3. Structure Schematic suggested pathway for the photocatalytic degradation of DOX and their intermediates 164

Chapter 5.

- Scheme 5.1. Illustration of the synthesis of N-LCDs 186
- Scheme 5.2. Factors Schematic illustration of (a) synthesis of BC@N-LCD by direct incorporation of N-LCD onto BC, (b) synthesis scheme of *c*-BC@N-LCD by *in situ* cross-linking of N-LCD and BC 192

Chapter 6.

- Scheme 6.1. Schematic of F-CDs synthesis through the 227
hydrothermal method
- Scheme 6.2. A schematic illustration shows the synthesis 229
of F-CD-POR
- Scheme 6.3. Schematic of the synthesis of F-CD-p@BC 232
hydrogel by incorporation of F-CD-POR onto
BC

List of Figures

Chapter 1.

Figure 1.1.	Representation of freshwater usage worldwide (data taken from the 2024 United Nations World Water Development Report)	3
Figure 1.2.	Schematic representation of the discovery timeline for key carbon-based nanomaterials	5
Figure 1.3.	Schematic illustration highlighting the distinct types of CDs	7
Figure 1.4.	Schematic representation of CDs synthesis utilizing top-down and bottom-up approaches	8
Figure 1.5.	CDs derived from various biomass, including (a) Orange peels, (b) banana peel, (c) <i>Rosa roxburghii</i> fruit, (d) chicken eggshell, (e) fish scalp, (f) elephant manure	9
Figure 1.6.	(a) Initial steps for the reaction of citric acid and phenylalanine to synthesize CDs, (b) synthesis route of CQDs by radical-assisted synthetic strategy using perylene precursors, (c) synthesis process of multicolor emissive CDs with ionic liquid as solvent and citric acid, pyrocatechol, and o-phenylenediamine as precursors	11
Figure 1.7.	Schematic illustrating carbon dots-based various nanocomposites	16
Figure 1.8.	Schematic illustration of BC culturing	18
Figure 1.9.	Illustration of CDs and CD-based nanocomposites for multifunctional applications	20
Figure 1.10.	Schematic Illustration of: (a) aggregation- induced FL enhancement mechanism of the SCD solution in the presence of mercury. (b)	22

	NCDs show turn-off strategy for detection of ascorbic acid and Fe^{3+} , (c) dual quenching mechanism for picric acid detection using NCD, and (d) TP-CQDs for CTC Detection	
Figure 1.11.	Schematic showing: (a) CDs generate reactive radical species for pollutant degradation, (b) BCQD@TiO ₂ for degradation of Favipiravir, (c) synthesis of PVP-CD hybrid hydrogel for adsorption and photodegradation of dye	25
Figure 1.12.	Schematic illustration of: (a) Efficient evaporation, salt resistance, and self-cleaning performance of C-LCDCA. (b) Fabrication of the CD-Wood evaporator and the setup of the solar steam generation device. (c) Synthesis of F-CDs, PA-CDs, and HA-CDs, and the formation mechanism of the HA-CD hierarchical assembly of the solar evaporator	27
Chapter 2.		
Figure 2.1.	(a) FTIR spectra of BP-CD and rBP-CD. XPS survey spectrum of (b) BP-CD (blue line) and rBP-CD (red line), deconvoluted C1s spectra of (c) BP-CDs and (d) rBP-CDs. BP-CDs (blue line) and rBP-CDs (red line): (e) raman spectra, (f) XRD spectra	64
Figure 2.2.	(a) TEM image of BP-CDs at low resolution, corresponding (b) histogram showing the size distribution of BP-CDs, (c) SAED pattern, and (d) HR-TEM image showing (002) planes with a d-spacing of 0.33 nm for BP-CD. (e) Low-resolution TEM image of rBP-CDs, corresponding (f) histogram showing the size distribution of rBP-CDs, (g) SAED pattern, and	65

	(h) HR-TEM image showing (002) lattices with a d-spacing of 0.34 nm for rBP-CD	
Figure 2.3.	Optical characterizations of BP-CD and rBP-CD. UV- vis absorption spectra of (a) BP-CD, and (b) rBP-CD with (insert: digital photographs of the corresponding CDs under visible light). FL emission spectra of (c) BP-CD and (d) rBP-CD with varying excitation wavelengths. FL lifetime plots of (e) BP-CD and rBP-CD	67
Figure 2.4.	Plots showing stability in fluorescent properties of BP-CDs and rBP-CDs under different conditions: (a) at various NaCl concentrations, (b) at different pH, and (c) under various temperatures	68
Figure 2.5.	Selective sensing response towards various metal ions and amino acids (concentration = 1.0×10^{-2} M): (a) BP-CDs (120 mg/mL), and (b) rBP-CD (132 mg/mL)	69
Figure 2.6.	(a) FL spectra of BP-CD after the addition of Co^{2+} in a concentration range of 50 μM to 1000 μM , (b) Co^{2+} concentration vs F/F_0 plot for BP-CD. (c) FL spectra of rBP-CD after the addition of Co^{2+} in a concentration range of 50 μM to 1000 μM , (d) relationship between Co^{2+} concentration and F/F_0 of rBP-CD, (e) rBP-CD FL spectra after reacting with Hg^{2+} of various concentrations in the 50 μM to 1000 μM range, (f) linear regression plot between Hg^{2+} concentration and F/F_0 of rBP-CD	70
Figure 2.7.	Competitive selectivity towards the sensing response of (a) BP-CD, (b) rBP-CD in the presence of various metal ions, and amino acids (concentration = 1.0×10^{-2} M)	70

- Figure 2.8.** (a) Absorption spectra of Co^{2+} overlapped with excitation and emission spectra of BP-CDs. (b) UV-vis spectra of Co^{2+} overlapped with excitation and emission spectra of rBP-CDs. (c) Hg^{2+} absorption spectra overlapped with excitation and emission spectra of rBP-CDs 76
- Figure 2.9.** Photographs showing changes in: (a) lifetime decay curves acquired for BP-CD in the presence and absence of Co^{2+} , (b) UV-vis spectra of BP-CDs in the presence and absence of Co^{2+} , (c) BP-CD colloid after adding Co^{2+} solution under visible and UV light, (d) scheme showing FL quenching of BP-CDs after addition of Co^{2+} 77
- Figure 2.10.** Lifetime decay curves were acquired for rBP-CD in the presence and absence of (a) Co^{2+} , and (d) Hg^{2+} . UV-vis absorbance spectra of rBP-CD in the presence and absence of (b) Co^{2+} , and (e) Hg^{2+} . Photographs showing changes in the appearance of (c) rBP-CD colloid after the addition of Co^{2+} , and (f) rBP-CD solution after adding Hg^{2+} under visible and UV light, (g) scheme showing FL quenching of rBP-CD after the addition of Co^{2+} and Hg^{2+} 78

Chapter 3

- Figure 3.1.** (a) TEM image, (b) Size distribution histogram, (c) HRTEM image with d-spacing of TF-CD, (d) XRD, and (e) FTIR of as-synthesized TF-CDs 103

Figure 3.2.	(a) XPS survey scan. Deconvoluted high-resolution XPS spectra of (b) P2p, (c) S2p, (d) C1s, (e) N1s, and (f) O1s of TF-CDs	104
Figure 3.3.	(a) UV-vis spectra (inset: TF-CDs solution in both visible and UV light), (b) FL emission spectra, and (c) TCSPC measurement recorded for TF-CDs. Stability plot of TF-CDs at under different: (d) temperatures, (e) pH and (f) NaCl concentrations	106
Figure 3.4.	(a) Selectivity of TF-CDs towards various NACs, (b) photographs of TF-CDs in the presence of various NACs captured under UV light, (c) FL spectra of TF-CDs after adding different concentrations of PA (0–200 mM), (d) relationship between PA concentration vs. F/F ₀ for TF-CDs, and (e) competitive selectivity towards sensing response of TF-CDs in the presence of nitro aromatic compounds ($c = 1.0 \times 10^{-2}$ M)	107
Figure 3.5.	(a) Lifetime data, (b) UV-vis absorption spectra of TF-CDs with the addition of PA (black line) and maximum fluorescence excitation of TF-CDs (blue line) showing spectral overlap, (c) UV-vis spectra of TF-CD for different concentrations of PA, and (d) schematic representation of quenching of TF-CD after the addition of PA	108
Figure 3.6.	(a) Effect on FL property of TF-CD@PVDF by varying the concentration of TF-CDs, (b) photographs of TF-CD@PVDF film under visible and UV light (365 nm). SEM images of (c) PVDF and (d) TF-CD@PVDF composite film	111

Figure 3.7.	(a) UV-vis spectra of PVDF film and TF-CD@PVDF composite film, (b) FL spectra of TF-CD@PVDF composite film under different excitation, (c) PXRD of PVDF and TF-CD@PVDF, (d) Sessile drop contact angle (θ) measurements of the (i) PVDF membrane, (ii) TFCD@PVDF	112
Figure 3.8.	The stability of TF-CD@PVDF film under different (a) pH, (b) NaCl concentrations, and (c) temperature.	113
Figure 3.9.	(a) Digital images of TF-CD@PVDF films after adding different concentrations of PA (under UV illumination of 365 nm), (b) linearity plot of F_0/F vs PA concentrations for TF-CD@PVDF composite film, (c) selectivity of TF-CD@PVDF film towards various NACs, and (d) recyclability study of composite film towards PA detection	114
Chapter 4.		
Figure 4.1.	(a) Absorption, (b) FL spectra, and (c) lifetime data. (d) TEM image (inset; histogram), and (e) HR-TEM showing lattice fringes. (f) XRD spectra. (g) FTIR spectrum of the synthesized M-CDs.	140
Figure 4.2.	(a) XPS survey spectrum. High-resolution XPS spectra of: (b) C1s, (c) O1s, (d) N1s of M-CDs.	141
Figure 4.3.	Stability plot of M-CDs in the presence of (a) NaOH (b) pH, and (c) temperature	141
Figure 4.4.	(a) Schematic illustration of the synthesis of M-CD@BC by incorporation of M-CDs onto BC. b) TEM image of M-CD@BC (red dotted arrows point to the attached M-CD on BC	142

fibers). SEM images of M-CD@BC (c) BC showing nanofibrous porous network structure (inset: histogram from a width of cellulose fibers), (d) (i) Nanofibrous porous network of BC incorporating M-CDs (inset: histogram from a width of cellulose fibers), and (ii) magnified image

Figure 4.5. Nitrogen adsorption and desorption analysis 143

conducted for control pristine BC and M-CD@BC aerogels: a) BET adsorption isotherms, and b) corresponding BJH pore volume plots for BC. c) BET adsorption isotherms, and d) corresponding BJH pore volume plots for M-CD@BC

Figure 4.6. (a) ATR-FTIR spectrum, and (b) comparative 145

XPS survey spectra of M-CD, BC, and M-CD@BC

Figure 4.7. (a) Absorbance spectra of BC (grey line) and 146

M-CD@BC (blue line), (b) band gap estimation of M-CD@BC. (c) FL spectra of BC (grey line) and M-CD@BC (blue line), and (d) digital photographs of M-CD@BC observed under visible and UV light ($\lambda_{\text{ex}} = 365$ nm)

Figure 4.8. (a) Fluorescence intensity of the M-CDs 147

recorded after incubation with the indicated different antibiotics for selective detection. M-CD emission spectra with different concentrations of (b) TET, and (c) DOX, ranging from 0-200 mM. The linearity plot of F/F_0 vs different concentrations of (d) TET and (e) DOX. (f) photographs of M-CDs in the presence of various antibiotics under UV light

Figure 4.9.	Competitive selectivity in the sensing response of M-CDs in the presence of various antibiotic compounds ($c = 1.0 \times 10^{-2}$ M)	149
Figure 4.10.	Lifetime decay curve with and without the presence of antibiotics: (a) TET, and (b) DOX. (c) UV-vis absorption spectra of TET and DOX showing spectral overlap with with fluorescence excitation of M-CDs. UV-vis spectra of M-CD for different concentrations of d) TET and e) DOX. (f) Illustration of fluorometric detection of TET and DOX based on M-CDs	150
Figure 4.11.	(a) Graph showing the relative FL intensity in the presence of different antibiotics, (b) fluorescent images of M-CD@BC after incubation with different antibiotics under UV irradiation ($\lambda_{ex}=365$ nm). Fluorescence response of M-CD@BC in the presence of (c) TET (0-200 mM), and corresponding Stern-Volmer plot depicting the linear relationship of (d) TET. (e) Fluorescence response of M-CD@BC in the presence of DOX (0-200 mM), and corresponding Stern-Volmer plot depicting the linear relationship of (f) DOX	153
Figure 4.12.	(a) Interfering studies for sensing response of M-CD@BC in the presence of various antibiotics ($c = 1.0 \times 10^{-2}$ M). Recyclability study for M-CD@BC (b) TET, and (c) DOX (200 mM)	154
Figure 4.13.	(a) Photocatalytic degradation studies of TET and DOX under various concentrations of M-CDs. (b) Degradation percentage of TET and	155

	DOX under sunlight without M-CDs, in the dark, and in sunlight with catalyst M-CDs	
Figure 4.14.	Degradation of (a) TET and (b) DOX under various conditions. Calculated rate constant of (c) TET and (d) DOX	156
Figure 4.15.	(a) Transient photocurrent density versus time plotted, and (b) EIS Nyquist plots of M-CDs under visible light in 0.5 M Na ₂ SO ₄ electrolyte. Effect of scavengers on degradation of (c) TET and (d) DOX. (e) Schematic illustration of charge transfer in M-CDs for TET and DOX degradation	158
Figure 4.16.	Removal of (a) TET, and (b) by M-CD@BC without sunlight illumination (experimental conditions: C ₀ = 20 mg L ⁻¹)	159
Figure 4.17.	(a, b) Photodegradation of TET under sunlight and their rate, respectively; (c, d) photodegradation of DOX under sunlight and their rate, respectively. Recyclability study of composite hydrogel M-CD@BC towards (e) TET and (f) DOX	161
Figure 4.18.	Mass spectra of (a) initial TET solution at 0 min, (b) degradation of TET in 120 min, and intermediate detected	162
Figure 4.19.	Mass spectra of (a) initial DOX solution at 0 min, (b) degradation of DOX in 120 min, and intermediate detected	164
Chapter 5.		
Figure 5.1.	Characterizations of N-LCD: (a) digital photographs of N-LCD dispersion captured under bright light (right) and UV light (left), (b) TEM images of N-LCD captured at different magnification levels, (c) histogram	188

	representing size distribution, (d) UV-visible absorption spectrum, (e) FL spectra taken under varied excitation wavelengths. (f) XRD pattern. (g) DRS spectrum of N-LCD in the NIR range	
Figure 5.2.	Chemical functional characterization of N-LCDs: (a) FTIR, (b) XPS survey scan. Details of XPS deconvoluted spectra of N-LCDs (c) C1s, (d) O1s, and (e) N1s	189
Figure 5.3.	Characterizations of BC: (a) digital photograph, (b) SEM image showing nanofibrous porous network structure, (c) histogram drawn for width of cellulose fibres, (d) ATR-FTIR spectrum, (e) XPS survey scan. HR deconvoluted peak for (f) C1s and (g) O1s	191
Figure 5.4.	Demonstration of leaching of N-L@CD from the hydrogel composites (a) before (BC@N-LCD), (b) after cross-linking with ECH (c-BC@N-LCD)	192
Figure 5.5.	(a) Digital photograph of the fabricated c-BC@N-LCD hydrogel. Morphological characterizations of c-BC@N-LCD by: (b) TEM (red dotted arrows point to the attached N-LCDs on BC fibres), and (c) SEM. Comparison study of c-BC@N-LCD, BC@N-LCD, and N-LCDs by (d) FTIR	193
Figure 5.6.	(a) XPS survey scan, and (b) HR scan of C1s	194
Figure 5.7.	Possible mechanisms of cross-linking by ECH: (i) and (ii) linking with the oxirane moiety by eliminating Cl^- of ECH by RO^- from N-LCDs and BC, respectively, and (iii) opening of the oxirane ring by $-\text{NH}_2$ of N-	195

	LCDs. (iv) Representative structure of <i>c</i> -BC@N-LCD formed after cross-linking	
Figure 5.8.	Nitrogen adsorption and desorption analysis conducted for <i>c</i> -BC@N-LCD and control pristine BC aerogels: (a) BET adsorption isotherms, and (b) corresponding BJH pore volume plots for <i>c</i> -BC@N-LCD. (c) BET adsorption isotherms, and (d) corresponding BJH pore volume plots for BC. The digital photographs of the samples analyzed are given as insets	195
Figure 5.9.	Wettability studies performed by contact angle measurements: (a) BC, (b) <i>c</i> -BC@N-LCD	196
Figure 5.10.	(a) DRS of N-LCD, BC, and <i>c</i> -BC@N-LCD acquired in full spectrum range, (b) corresponding % NIR reflectance. (c) The comparative temperature rise in water (blue), BC (grey), and <i>c</i> -BC@N-LCD (red) after illuminating the evaporator for approximately 2 min. (d) IR thermal image of BC and <i>c</i> -BC@N-LCD captured after illumination of 1 kW m ⁻² simulated solar light for 60 min (top view). (e) DSC curves showing a difference in evaporation of <i>c</i> -BC@N-LCD and pure water	198
Figure 5.11.	(a) Digital, and (b) IR thermal profile captured for demonstrating heat localization at the <i>c</i> -BC@N-LCD-water interface upon exposure to 1 kW m ⁻² solar light. (c) Schematic representation of a lab-made setup used for solar evaporation experiments (red arrow marks signify effective up-side bulk water transportation). Comparative studies of water mass loss for BC, water, and <i>c</i> -BC@N-LCD;	200

	(d) cumulative mass of water evaporated vs time plot, (e) rate performance plot, and (f) cyclic performance carried out for 10 cycles	
Figure 5.12.	(a) Evaporation rate of <i>c</i> -BC@N-LCDs under different loading. (b) Effect of irradiation intensity on photothermal evaporation performance	201
Figure 5.13.	Remediation of water by <i>c</i> -BC@N-LCD photothermal hydrogel membrane. Bar plots for: (a) evaporation rates calculated for various water sources, (b) the rate of evaporation in saline water. (c) Evaporation efficiency in saline water, (d) heavy metal ion removal from water bodies, (e) percentage degradation of various dyes from water bodies, (f) percentage degradation of pharmaceutical drugs present in water. Samples were irradiated for 60 min with 1 kW m ⁻² solar light	204
Figure 5.14.	Demonstration of fresh water production with the aid of <i>c</i> -BC@N-LCD performed outdoors. Digital photographs taken (a) initially (t=0 min) and (b) after steam is produced (t=10 min). The formation of water droplets conical roof ensures the formation and condensation of fresh water produced. (c) Formation, condensation (t=30 mins), and (d) collection of water droplets (t=120 mins). (e) Temperature, humidity, and intensity plots are drawn from the values recorded in real time	206
Chapter 6.		
Figure 6.1.	Characterization of F-CDs: (a) UV-vis absorption spectrum, (b) FL spectra taken	228

- under varied excitation wavelengths, (c) TEM Image with inset representing size distribution histogram, (d) XPS survey scan, (e) FTIR, and (f) XRD spectra
- Figure 6.2.** Representing the comparison between F-CD and F-CD-POR: (a) FTIR Spectra, (b) UV-vis spectra, (c) UV-vis spectra of F-CD-POR in comparison with fluorescence excitation spectra obtained by excitation at 500 nm, and (d) fluorescence spectra of F-CD-POR obtained in different solvents, excited at 420 nm 231
- Figure 6.3.** Characterization of fabricated F-CD-p@BC hydrogel: (a) Digital photograph, (b) TEM image at: (i) lower magnification, (ii) higher magnification (indicates the attached F-CD-POR on BC fibers), and (c) SEM image of (i) BC, (ii) F-CD-p@BC (indicates the incorporation of F-CD-POR on BC fibers). Comparison of (d) FTIR and (e) XPS spectra of F-CD-p@BC and BC 233
- Figure 6.4.** Details of XPS deconvoluted spectra of BC and F-CD-p@BC for (a) C1s, (b) O1s, and (c) N1s 234
- Figure 6.5.** Solar harvesting property of BC and F-CD-p@BC: (a) UV-vis-NIR diffuse reflection spectra of the aerogels, (b) corresponding %NIR reflectance, (c) Digital photograph of membrane utilized for photothermal conversion studies, (d) comparative temperature change curves of evaporation systems F-CD-p@BC (purple), BC (gray), and water (blue) totime under one solar irradiation 236

	(inset: respective thermal images), (e) Infrared thermal images of F-CD-p@BC surface captured at 0, 10, 20, 30, 40, 50, and 60 min intervals under 1 sun irradiation	
Figure 6.6.	Adsorption-desorption curves of nitrogen for (a) F-CD-p@BC, (b) BC, (c) comparative pore size distribution curve of F-CD-p@BC and BC	237
Figure 6.7.	Digital photographs of F-CD-p@BC and BC showing water contact angle measurements on each layer	237
Figure 6.8.	(a) Photographs of tissue paper placed on the top of F-CD-p@BC surface before and after wicking methyl orange solution, (b) deconvoluted Raman spectra with FW and IW peaks in F-CD-p@BC, and (c) pure water. (d) DSC measurement curves for pure water and water in F-CD-p@BC	238
Figure 6.9.	Illustrate heat localization at the F-CD-p@BC-water interface after exposure to 1 kW m ⁻² solar radiation, (a) a digital and (b) an infrared thermal profile. (c) Schematic representation of lab-made solar evaporation test setup (yellow arrows indicate efficient bulk water transportation in an upward direction)	240
Figure 6.10.	Water mass loss comparison between BC, bare water, and F-CD-p@BC: (a) the cumulative mass of evaporated water is plotted against time, (b) evaporation rate performance, (c) cyclic performance conducted across 10 cycles, (d) comparison of F-CD-p@BC with	241

	other photothermal materials reported in previous literature	
Figure 6.11.	Influence of radiation intensity on the rate of photothermal evaporation	242
Figure 6.12.	Illustrates the purification of water by utilizing the F-CD-p@BC photothermal membrane: (a) Depicting evaporation rates obtained for different water sources, (b, c) UV-vis spectra of MB and MO before and after purification, respectively, (d) removal of heavy metal ions from aquatic environments, (e) comparison showing pH of solution before and after purification	243
Figure 6.13.	Image showing salt ablation experiment on the surface of F-CD-p@BC in the dark, (b) Photographs showing no deposition of salt on the upper surface of F-CD-p@BC during solar desalination until 12 h, (c) recyclability and evaporation rate for saline water under 1 sun, (d) ions removal of simulated seawater after desalination	245
Figure 6.14.	(a) photographs of lab-made outdoor evaporation device containing the evaporator at 0 and 60 min (indicates the generation of steam), and (b) outdoor freshwater evaporation rate along with temperature, humidity, and intensity plots drawn from the values recorded in real-time	246

List of Tables

Chapter 2

Table 2.1.	Optical attributes of BP-CDs and rBP-CDs	67
Table 2.2.	State-of-the-art performance comparison of various FL-based Co^{2+}	71
Table 2.3.	State-of-the-art performance comparison of various FL-based Hg^{2+} sensors	72
Table 2.4.	Details of real-sample sensing and recovery of Co^{2+} from various natural samples using BP-CD as a probe. The experiments were performed by spiking Co^{2+} in tap water, milk, vegetable juice, and urine samples	73
Table 2.5.	Details of real-time sensing and recovery of Co^{2+} from various natural samples using rBP-CD as a probe	74
Table 2.6.	Details of real-time sensing and recovery of Hg^{2+} from various natural samples using rBP-CD as a prob	74
Table 2.7.	Comparison of carbon dots and their reduced form for various applications in previous literature reports	74

Chapter 3 75

Table 3.1.	The performance comparison for the PA sensing platform	114
Table 3.2.	Picric acid sensing in real water samples with TF-CDs and TF-CD@PVDF films (N=3)	115

Chapter 4

Table 4.1.	The comparative performance of the sensing platform of antibiotics	148
Table 4.2.	TET detection in real samples	151
Table 4.3.	DOX detection in real samples	151

Table 4.4.	Comparison of the photocatalytic degradation of antibiotics TET and DOX by various photocatalysts	156
-------------------	---	-----

Chapter 5

Table 5.1.	Represents the ER of the composite, BC, and water	200
Table 5.2.	Indicative of a different solar evaporator for comparing the composition and evaporation rate	202

Chapter 6

Table 6.1.	Represents the ER of Composite, BC, and Water	241
-------------------	---	-----

Acronyms

CD	Carbon dot
UV	Ultraviolet
PL	Photoluminescence
FL	Fluorescence
Vis	Visible
TCSPC	Time-correlated single-photon counting
ATR-FTIR	Attenuated total reflectance-Fourier transform infrared
PXRD	Powder X-ray diffraction
TEM	Transmission electron microscopy
HR-TEM	High-resolution transmission electron microscopy
SAED	Selected area diffraction
DRS	Diffused reflectance spectra
DSC	Differential Scanning Calorimeter
WAXS	Wide-angle X-ray scattering
XPS	X-ray photoelectron spectroscopy
QY	Quantum yield
NaOH	Sodium hydroxide
FE-SEM	Field emission-scanning electron microscopy
NaCl	Sodium chloride
LC-MS	Liquid chromatography mass spectrometry
MeOH	Methanol
TCSPC	Time-correlated single-photon counting
IRF	Instrument response function
XPS	X-ray photoelectron spectroscopy
EDTA	Ethylenediaminetetraacetic acid
DCM	Dichloromethane
DMF	Dimethylformamide
DDQ	2,3-Dichloro-5,6-dicyano-p-benzoquinone

TFA	Tetra-trifluoroacetic acid
NaBH ₄	Sodium borohydride
K ₂ Cr ₂ O ₇	Potassium dichromate
RhB	Rhodamine B
MB	Methylene blue
MO	Methyl orange
CR	Congo red
EDA	Ethylenediamine
NaF	Sodium fluoride
PBA	Phenyl boronic acid
TET	Tetracycline
DOX	Doxycycline
LOD	Limit of detection
ICP-AES	Inductively Coupled Plasma Atomic Emission Spectroscopy
BC	Bacterial cellulose
BET	Brunauer–Emmett–Teller
BJH	Barrett-Joyner-Halenda
ICP-MS	Inductively Coupled Plasma Mass Spectroscopy
LOD	Limit of detection
ROS	Reactive oxygen species
DI	Deionized water
PVDF	Polyvinylidene difluoride
NIR	Near infrared
Hg	Mercury
B	Boron
Co	Cobalt
As	Arsenic
Cd	Cadmium

Pb	Lead
Cr	Chromium
K	Potassium
Al	Aluminum
Ca	Calcium
Na	Sodium
Zn	Zinc
Sn	Tin
Zr	Zirconium
Ni	Nickel
PO ₄ ³⁻	Phosphate ion
P	Phosphor
Se	Selenium
I	Iodine
S	Sulfur
H ₂ SO ₄	Sulfuric acid
C	Carbon
O	Oxygen
Pt	Platinum
Ag	Silver
Cl	Chlorine
EIS	Electrochemical impedance spectra
F ₀	Initial fluorescence intensity
R ²	Linear correlation coefficient
Ref	References
PA	Picric acid
NAC	Nitroaromatic compounds
3-NA	3-nitroaniline
2,4-DNT	2,4-dinitrotoluene

4-IA	4-iodoaniline
2-NP	2-nitrophenol
4-NT	4-Nitrotoluene
t-BuOH	tert-butyl alcohol
NB	Nitrobenzene
Na ₂ SO ₄	Sodium sulphate
H ₃ PO ₄	Phosphoric acid
CoSO ₄ ·H ₂ O	Cobalt(II) sulphate monohydrate
FeCl ₂	Iron(II) chloride
AgNO ₃	Silver nitrate
CdCl ₂	Cadmium chloride
ECH	Epichlorohydrin
BZQ	p-benzoquinone
NMP	N-Methyl-2-pyrrolidone
FRET	Förster resonance energy transfer
VAN	Vancomycin hydrochloride
STR	Streptomycin hydrate
CIP	Ciprofloxacin hydrochloride hydrate
ERY	Erythromycin
NOR	Norfloxacin
AMP	Ampicillin sodium salt
IFE	Inner Filter Effect

Nomenclature

nm	Nanometer
cm	Centimeter
η	Refractive index
θ	Diffraction angle
d	Interplanar spacing
Hz	Hertz
AC	Alternating current
mV	Millivolt
kV	Kilovolt
h	Hour
kg	Kilogram
mg	Milligram
mL	Milliliter
pM	Picomolar
μ M	Micromolar
mM	Millimolar
M	Molar
rpm	Rotation per minute
min	Minute
μ g	Microgram
μ M	Micromolar
I	Intensity
ns	Nanosecond
τ	Excited-state lifetime
K	Kelvin
$^{\circ}$ C	Degree Celsius
A	Absorbance
eV	Electron Volt
nM	Nanomolar
C	Concentration
t	Time
T	Temperature

h	Planck's constant
ν	Frequency of radiation
k	Rate constant
ppm	Parts per million
ppb	Parts per billion
λ	Wavelength
s	Second
μm	Micrometer
λ_{max}	Absorption maxima
λ_{ex}	Excitation wavelength
λ_{em}	Emission wavelength
SD	Standard deviation
μL	Microliter
L	Liter
mg	Milligram
ng	Nanogram
g	Gram
\AA	Angstrom
Φ	Fluorescence Quantum yield
K_f	Fluorescence radiative rate
T_f	Fluorescence lifetime
σ	Error
K_{sv}	Quenching constant
%	Percentage
mA	Milliampere
R	Reflectance
S	Solar spectral irradiance
W	Watts
kW	Kilowatts
Q_s	Power of incident solar irradiation
Q_e	Power for water evaporation
η	Evaporation efficiency
h_{LV}	Enthalpy of vaporization of water

τ	Excited-state lifetime
m	Mass
R	Rate of evaporation
C_{opt}	Optical density
q_i	Solar radiation power
a.u.	Arbitrary unit
$^{\circ}$	Degree
π	Pi
q	Theta

Table of Contents

1. List of Schemes	ix
2. List of Figures	xi
3. List of Tables	xxvii
4. Acronyms	xxix
5. Nomenclature	xxxiii

Chapter 1: Introduction

1.1. General Background	2
1.2. Carbon Dots	5
1.2.1. Structural Classification of CDs	6
1.2.2. Synthesis of CDs	7
1.2.2.1 CDs Derived from Biomass	8
1.2.2.2. CDs Derived from Chemical Precursors	9
1.2.3. Approaches for Tuning the Fluorescence Efficiency of CDs	11
1.2.4. Carbon Dots Properties	13
1.2.4.1. Structural Properties	13
1.2.4.2. Optical Properties	14
1.3. Carbon Dot-Based Nanocomposites	15
1.3.1. Structural Supports for CD Nanocomposites	17
1.4. Multifunctional Applications	19
1.4.1. Fluorescent Detection of Pollutants	20
1.4.2. Photocatalytic Degradation	23
1.4.3. Interfacial Solar-Driven Water Evaporation	25
1.5. Scope of Present Work	28
1.6. References	29

Chapter 2: Insight into the Modulation of Carbon Dot Optical Sensing Attributes Through a Reduction Pathway

2.1.	Introduction	55
2.2.	Experimental Section	58
2.2.1.	Materials and Reagents	58
2.2.2.	Instrumentation	58
2.2.3.	Synthesis of BP-CDs and rBP-CDs	59
2.2.4.	QY, Radiative Rate Constant (K_f), and Limit of Detection (LOD) Evaluation	59
2.2.5.	Selectivity Studies, Detection of Co^{2+} and Hg^{2+} , and Interference Studies	60
2.2.6.	Detection of Analytes in Real Sample	61
2.3.	Results and Discussion	61
2.3.1.	Synthesis and Characterization of BP-CDs and rBP-CDs	61
2.3.2.	Study of the Fluorescence Stability	68
2.3.3.	Sensing Studies	68
2.3.4.	Real-Sample Analysis with BP-CDs and rBP-CDs	72
2.3.5.	Mechanism of Sensing by BP-CDs and rBP-CD for Co^{2+} and Hg^{2+}	75
2.4.	Conclusions	79
2.5.	References	80

Chapter 3: Portable and Non-Invasive Fluorescent Thin Films from Photocatalytically Active Carbon Dots for Selective and Trace-Level Detection of Picric Acid

3.1.	Introduction	95
-------------	--------------	----

3.2.	Experimental Section	97
3.2.1.	Materials and reagents	98
3.2.2.	Instrumentation	98
3.2.3.	Synthesis of TF-CDs	99
3.2.4.	Synthesis of PVDF Thin Films with TF-CDs	99
3.2.5.	Quantum Yield (QY) and LOD Measurement	100
3.2.6.	FL Sensing of PA using TF-CDs	100
3.2.7.	Sensing of PA with TF-CD@PVDF Composite Films	101
3.3.	Results and Discussion	101
3.3.1.	Preparations and Characterizations of TF-CD	101
3.3.2.	Study of Fluorescence Stability	105
3.3.3.	Fluorescent-based PA Detection with TF-CDs	106
3.3.4.	PA Sensing Mechanism	107
3.3.5.	Detection of PA on TF-CD@PVDF Strips	109
3.3.6.	Real Sample Analysis	115
3.4.	Conclusions	115
3.5.	References	117

Chapter 4: A Carbon Dots Anchored Bacterial Cellulose Hybrid Platform as a Fluorescent Sensor and Photocatalytic Remover of Pharmaceuticals

4.1.	Introduction	130
4.2.	Experimental Section	133
4.2.1.	Materials and Reagents	133
4.2.2.	Characterization Techniques	133
4.2.3.	QY	134
4.2.4.	Synthesis of M-CDs	134

4.2.5. Synthesis of M-CDs@BC	135
4.2.6. Detection of TET and DOX with M-CDs	135
4.2.7. Antibiotics Detection in Real Samples	136
4.2.8. M-CDs@BC Sensing TET and DOX	136
4.2.9. Photocatalytic Experiments	136
4.2.10. Electrochemical Photocurrent Measurement	138
4.3. Results and discussion	138
4.3.1. Preparation and Characterization of M-CDs	138
4.3.2. Fabrication of M-CD@BC	141
4.3.3. Selective Sensing of TET and DOX	146
4.3.4. Mechanism of FL Sensing	149
4.3.5. TET and DOX Detection in Real Samples	150
4.3.6. Detection of TET and DOX with M-CD@BC	
Hydrogel	151
4.3.7. Photocatalytic Degradation of TET and DOX	154
4.3.8. Photodegradation with M-CD@BC	158
4.3.9. Plausible Degradation Pathway for TET and DOX	161
4.4. Conclusions	164
4.5. References	166

Chapter 5: A Lignin-Derived Carbon Dot-Upgraded Bacterial Cellulose Membrane as an All-in-One Interfacial Evaporator for Solar-Driven Water Purification

5.1. Introduction	177
5.2. Experimental Section	180
5.2.1. Materials and Reagents	180
5.2.2. Synthesis of N-LCDs	181

5.2.3.	Preparation of Bacterial Cellulose (BC)	181
5.2.4.	In-situ Synthesis of BC@N-LCDs (Without Cross-Linking)	181
5.2.5.	Cross-Linking of BC@N-LCDs with ECH	182
5.2.6.	Characterization Technique	182
5.2.7.	Estimation of Photothermal Energy Conversion	184
5.2.8.	Real-Time Solar Evaporation Experiments	185
5.2.9.	Evaporation Rate at Different Water Sources, Desalination and Removal of Pollutants by <i>c</i> -BC@N-LCDs	185
5.3.	Results and discussion	186
5.3.1.	Preparations and Characterizations of N-LCDs	186
5.3.2.	Preparation Strategies of NIR-active Composite Membrane	189
5.3.3.	Characterization of <i>c</i> -BC@N-LCD Hydrogel Composite	192
5.3.4.	<i>c</i> -BC@N-LCD as a Photothermal Platform	196
5.3.5.	Solar Evaporation Performance Studies	198
5.3.6.	Practical All-Around Water Purification by <i>c</i> -BC@N-LCD	202
5.4.	Conclusions	207
5.5.	References	208

Chapter 6: Organic Network Comprising Sustainable Carbon Dot- Upgraded Bacterial Cellulose Evaporator for Interfacial Solar- Driven Water Evaporation

6.1.	Introduction	219
6.2.	Experimental Section	221
6.2.1.	Materials and Reagents	221
6.2.2.	Synthesis of F-CDs	222
6.2.3.	Preparation of BC	222
6.2.4.	Fabrication of F-CD-p@BC Photothermal Membrane	222

6.2.5. Characterization Technique	223
6.2.6. Solar Evaporation Experiments	224
6.2.7. Dark Evaporation Experiments	225
6.2.8. F-CD-p@BC for Water Purification Experiments	226
6.3. Results and Discussion	227
6.3.1. Characterization of F-CDs	227
6.3.2. Characterization of FCD-POR and F-CD-p@BC	228
6.3.3. Light Absorption and Photothermal Performance	234
6.3.4. Water Evaporation Performance of F-CD-p@BC	239
6.3.5. Practical all-around Water Purification	242
6.3.6. Real-time Application	245
6.4. Conclusions	246
6.5. References	248
Chapter 7: Conclusion and Future Scope	
7.1. Conclusions	258
7.2. Scope for Future Work	260
ANNEXURE 1	262-265

Table A1. Permission for reproducing the materials

ABSTRACT

The investigation outlined in the thesis entitled “Multifunctional Carbon Dots Based Nanocomposites for Sustainable Environmental Management” was launched in August 2020 at the Department of Chemistry, Indian Institute of Technology Indore. The aims of this thesis are to design and develop multifunctional carbon dots and nanocomposites for pollutant remediation and water purification through sensing, photocatalytic degradation, and interfacial solar-driven water evaporation. The main points of the thesis are as follows-

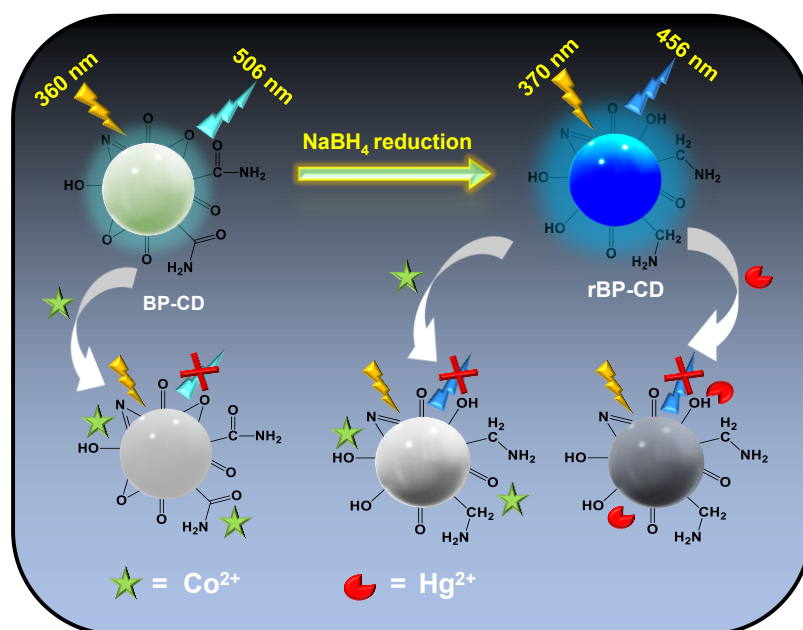
- 1) Modulation of green and chemical source-derived carbon dots through a post-synthetic reduction strategy for metal ion sensing.
- 2) Design a portable and non-invasive fluorescent thin film from *Cascabela thevetia*-derived carbon dots for picric acid detection.
- 3) To develop a hybrid platform from carbon dots anchored bacterial cellulose for the environmental remediation of pharmaceuticals.
- 4) To engineer a multifunctional photothermal membrane from carbon dots incorporated into bacterial cellulose for interfacial solar-driven water evaporation and purification.
- 5) To fabricate a photothermal membrane by integrating carbon dots-based organic network into bacterial cellulose for interfacial water evaporation.

This thesis includes seven chapters, and it starts with a general introduction to the topic and literature review (**Chapter 1**), followed by the synthesis of carbon dots from a sustainable source and their reduction to modulate the optoelectronic properties, and utilizes both carbon dots for the detection of metal ions (**Chapter 2**), synthesis of portable fluorescent thin film from Cascabela thevetia flower derived carbon dots for selective and trace-level detection of picric acid (**Chapter 3**), followed by fabrication of carbon dots anchored bacterial cellulose nanoplatform as a fluorescent sensor and photocatalytic remover of antibiotics (**Chapter 4**), interfacial solar driven water purification along with evaporation from NIR active carbon dots upgraded photothermal membrane (**Chapter 5**), and further synthesis of organic network comprising of carbon dots incorporated in bacterial cellulose for photothermal solar driven water evaporation (**Chapter 6**). Finally, the thesis concludes with a future perspective, especially focusing on further utilization of carbon-based membranes and developing new strategies for synthesizing photothermally active membranes at a larger scale (**Chapter 7**). The content of each chapter included in the thesis is discussed as follows:

Chapter 1 provides an overview of the challenges faced currently in water remediation applications. It begins by highlighting the urgent need for innovative approaches and the development of new materials that can overcome the limitations of existing technologies. After that, an introduction to the fundamentals of carbon dots is provided, which includes their structural classification, synthesis, tuning of optical properties, and physicochemical properties of carbon dots. This is followed by a brief discussion on the carbon dots-based nanocomposites and particularly those pertinent to applications in optical sensing, photocatalytic degradation, and solar-driven water evaporation, are critically discussed.

In **Chapter 2**, oxidized/reduced carbon dots (CDs) with tunable optical features have emerged as a new class of CDs having common “molecular origin” but different fluorescence (FL) behavior. Using “banana peel” as a sole carbon

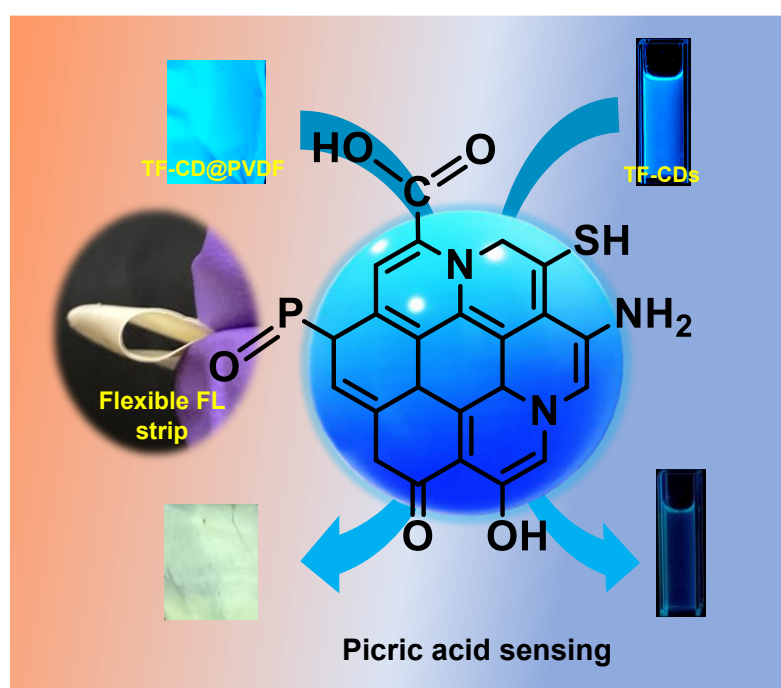
source, followed by doping with fluorine (F), boron (B), and nitrogen (N) over CDs, banana peel-derived carbon dots (BP-CDs) were synthesized using a well-known hydrothermal synthesis method. Moreover, as-synthesized BP-CDs were further reduced to “rBP-CDs” by NaBH_4 . At post-reduction, the FL performance (i.e., quantum yield) of rBP-CDs was found to be enhanced compared with the BP-CDs, along with variations in excitation and emission wavelengths. Interestingly, the optical sensing attributes of BP-CDs and rBP-CDs were varied; that is, BP-CDs selectively sense “ Co^{2+} with a limit of detection (LOD) value of 180 nM”, whereas rBP-CDs detected Co^{2+} (with an LOD value of 242 nM) as well as Hg^{2+} (with an LOD value of 190 nM). This work presents the very first report on the modulation of CDs’ sensing behavior after reduction. The modulation in the sensing behavior with the common carbon precursor and reduction paves a new possibility for exploring CDs for different commercial applications.



Scheme 1. Banana Peel-derived Carbon Dots (BP-CDs) and Their Reduced Form (r-BP-CDs) for Metal Ion Sensing.

In **Chapter 3**, N, S, and P-doped carbon dots (TF-CDs) have been synthesized from *C. thevetia* flowers through a simple one-pot method, which exhibit selectivity for the sensitive detection of picric acid (PA). Further integration of this fluorescent probe onto polyvinylidene fluoride (PVDF) enables the fabrication of a highly porous, thin, and flexible TF-CD@PVDF film strip *via* a

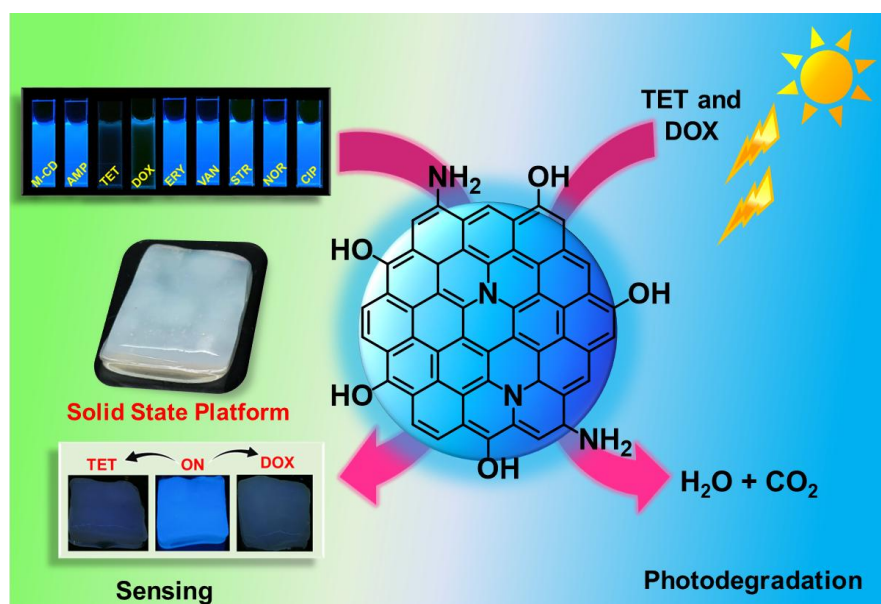
simple phase inversion method, enabling the selective and trace-level detection of a potent explosive, PA. The TF-CD@PVDF strip shows a limit of detection (LOD) of 244 nM for PA, whereas TF-CD itself in suspended form shows sensitivity as low as 104 nM. The findings reveal a static quenching mechanism for TF-CDs in the presence of PA. The real sample analysis was further performed by externally spiking real water samples, validating the real-world applicability of the as-prepared TF-CDs for sensing in polluted water. The present study paves the way for designing portable, flexible fluorescent platforms for extended applications.



Scheme 2. Portable and Non-invasive Fluorescent Thin Films for Sensitive Detection of Picric Acid.

In **Chapter 4**, a one-arrow two-bird approach was implemented to enable fluorometric trace level detection as well as photocatalytic remediation of antibiotic drugs tetracycline (TET) and doxycycline (DOX) using a melamine derived carbon dots (M-CD) and encapsulated bacterial cellulose (M-CDs@BC) luminescent hydrogel composite synthesized *via* a single-step one-pot hydrothermal method. The M-CDs showed a wide linear range and good sensitivity with lower limits of detection (LOD) of 133 nM and 138 nM for TET and DOX, respectively.

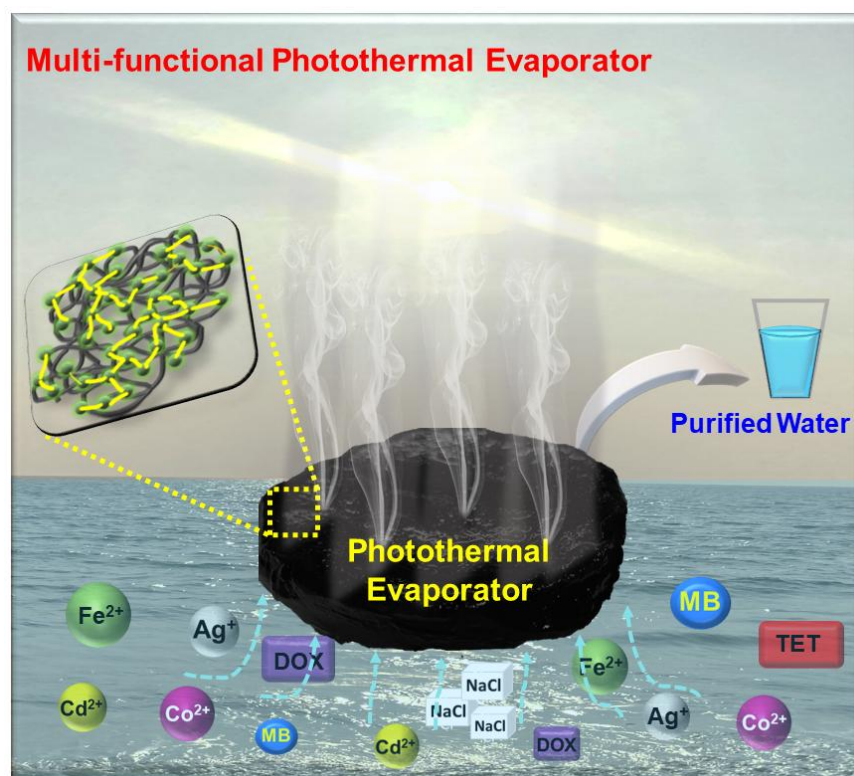
Encouraged by the remarkable fluorescence (FL) characteristics of M-CD@BC, the solid phase hydrogel platform was utilized to detect the concentration of TET and DOX in a sequential manner for the first time. The M-CDs@BC composite showed excellent sensing ability and selectivity towards TET and DOX, among other available antibiotics. Moreover, the photocatalytic activity of the M-CDs is found to be preserved in M-CDs@BC as well and played an effective role in the photodegradation of both TET and DOX (70.3% and 64.0%, respectively). Furthermore, the present M-CDs@BC hydrogels display high cycling performance for recurrent usage. Overall, our work paves the way for the generation of unique CDs composites for environmental remediation.



Scheme 3. Carbon Dots and Carbon Dots Embedded Fluorescent Hydrogel for the Sensitive Detection and Photocatalytic Degradation of Antibiotics.

In **Chapter 5**, a robust multi-purpose near-infrared (NIR)-active hydrogel composite (*c*-BC@N-LCD) from broad-spectrum active nitrogen-doped lignin-derived carbon dots (N-LCDs), which is covalently cross-linked with a bacterial cellulose (BC) matrix, has been synthesized. BC provides adequate porosity and hydrophilicity required for easy water transport while managing heat loss. A commendable evaporation rate (ER) of $2.2 \text{ kg m}^{-2} \text{ h}^{-1}$ under one sun (1 kW m^{-2})

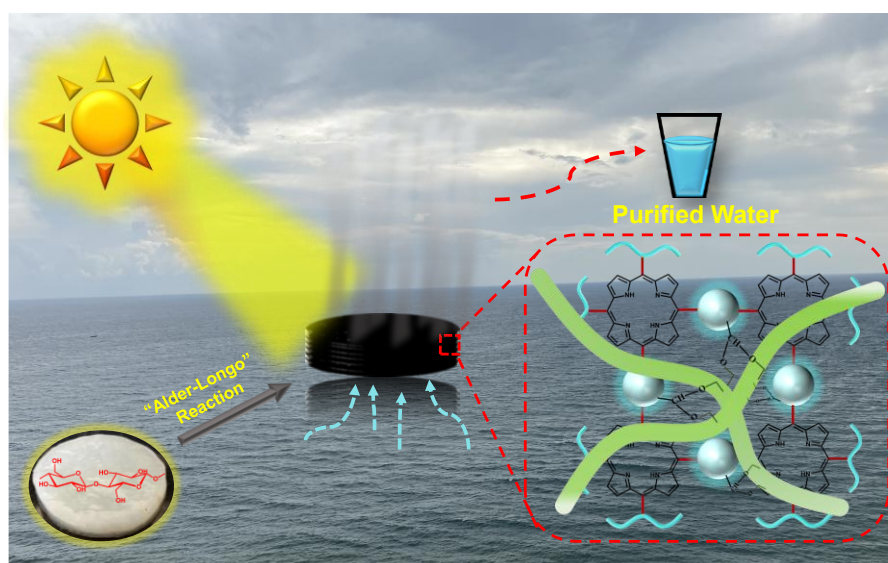
is achieved by *c*-BC@N-LCD. The developed hydrogel system is also found to be efficient for desalination ($\sim 2.1 \text{ kg m}^{-2} \text{ h}^{-1}$) and for remediating various pollutants (heavy metal ions, dyes, and pharmaceuticals) from feed water. The efficacy of the membrane remains unaltered by different grades of water, and hence can be adoptable for economically stressed communities living in water-polluted regions as well as those residing in coastal areas. This solar-driven interfacial evaporation has emerged as an efficient approach for wastewater treatment and seawater desalination.



Scheme 4. The Lignin-derived Carbon Dots (N-LCDs) Cross-linked with Bacterial Cellulose, i.e., *c*-BC@N-LCD, a Multifunctional Evaporator for Water Evaporation and Purification.

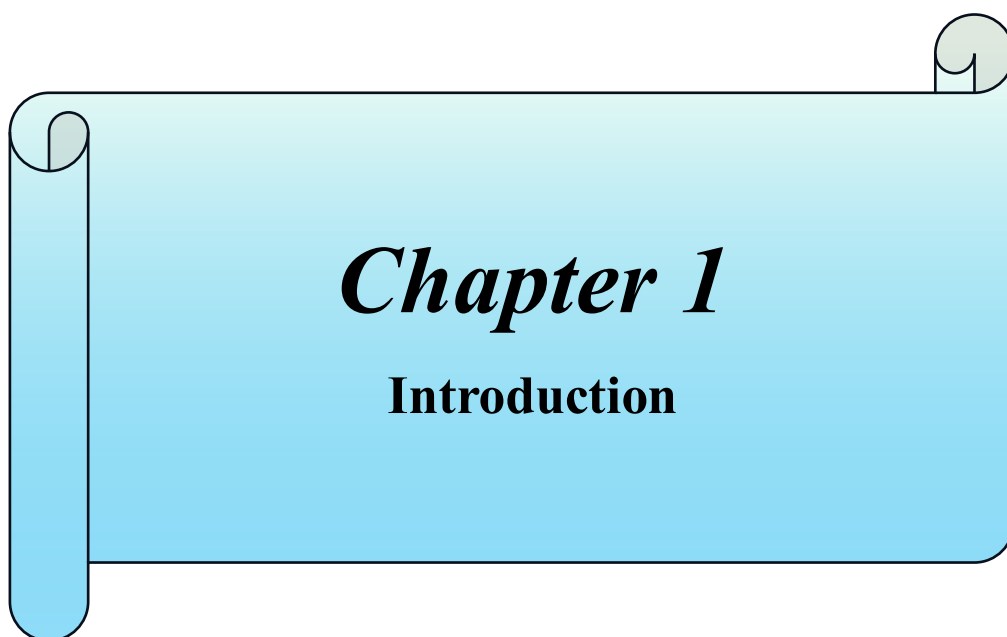
In **Chapter 6**, a high-performance photothermal membrane (F-CD-p@BC) was fabricated by integrating a carbon dots-based organic network (F-CD-POR) into bacterial cellulose (BC) using the Alder-Longo reaction. F-CD-p@BC exhibits superior solar water steam generation performance, longevity, and significant adaptability throughout numerous environments. The hydrophilic three-dimensional interlinked porous network of F-CD-p@BC is advantageous for fast

evaporation of water while reducing heat loss. Fabricated F-CD-p@BC membrane efficiently evaporates water at a $2.3 \text{ kg m}^{-2} \text{ h}^{-1}$ rate (1 sun) and also demonstrates high efficacy in desalination, removal of organic pollutants, and heavy metal ions from wastewater. Long-term stability confirms its durability across multiple cycles, while outdoor experiments validate its real-world applicability. Eco-friendly design of F-CD-p@BC provides an energy-efficient solution for water purification in resource-limited regions, opening new avenues for advanced photothermal applications.



Scheme 5. The Photothermal Membrane (F-CD-p@BC) Incorporates a Novel Carbon-Dot-Based Organic Network (F-CD-POR) into a Bacterial Cellulose Hydrogel Through a Novel Chemical Approach for Solar-Driven Water Evaporation.

Chapter 7 includes the conclusion and future perspective of this work.



Chapter 1

Introduction

1.1.General Background

With the rapid advancement of human society, surface water is increasingly polluted by complex substances from industrial effluents, including heavy metal ions [1], explosives [2], and pharmaceutical products [3], etc. Humans rely on water for a wide range of purposes, from drinking to domestic use and agricultural irrigation. It is essential for maintaining health, supporting sustainable development, and ensuring the survival of life. Water is essential for generating power, agricultural purposes, and industry, lacking any sustainable alternatives. Moreover, the maintenance and persistence of ecosystems are highly dependent on water, highlighting its fundamental ecological significance [4-6]. Approximately 70% of the Earth's crust is covered by water, predominantly present as groundwater, glaciers, rivers, lakes, and oceans. Nevertheless, 97% of the earth's water is saline, making it unsuitable for drinking or agricultural use. Of the remaining 3 % of Earth's water, approximately 2.3% is sequestered in glaciers and polar ice caps. Only about 0.7% is accessible for human use, with the majority found as groundwater (0.66%), and less than 0.03% present as freshwater in lakes and rivers [7, 8].

Consequently, water is regarded as a valuable and finite resource, necessitating its careful use to prevent unnecessary loss. The scarcity of water is further exacerbated by pollution, unregulated consumption, and inadequate management of water resources [9]. Global water demand is increasing annually by approximately 1%, driven primarily by population growth. The combined effects of globalization and industrialization have further intensified freshwater consumption, contributing to an emerging water crisis, as illustrated in **Figure 1.1**. As per the United Nations, over 2.2 billion people lack access to freshwater, and this number continues to rise with each passing day [10]. As a result of this critical situation, which led to an estimated 2.2 million deaths, primarily caused by consumption of contaminated drinking water and inadequate sanitation practices, leading to widespread disease outbreaks [11].

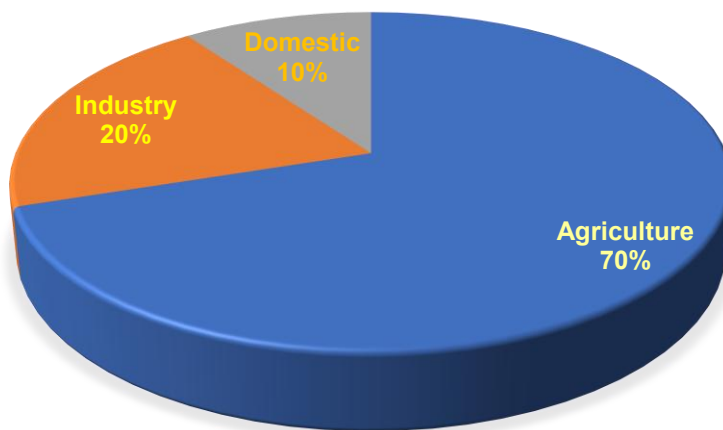


Figure 1.1. Representation of freshwater usage worldwide (data taken from the 2024 United Nations World Water Development Report). [12]

Addressing water scarcity and pollution requires the implementation of effective purification and water regeneration strategies. Emerging technologies are continually being investigated for the remediation and treatment of contaminated water [13-16]. Heavy metal ions [17], pharmaceuticals [18], explosive effluents [2], dye-polluted water [19], and industrial effluents [20] are just a few examples of many concerning contaminants. Various materials have been employed for wastewater treatment and solar water evaporation, and therefore, a wide variety of approaches have been exploited for this purpose. Recent research has emphasized the application of nanomaterials in advancing novel technologies for environmental remediation and sustainable solutions [21, 22].

Nanotechnology has garnered considerable attention in recent decades due to the unique physical properties of nanoscale materials and holds the prospect of significantly contributing to the development of cleaner, greener technologies that are advantageous over other techniques [23]. It is a field of science and engineering focused on designing and synthesizing materials at the atomic and molecular level [24]. At the nanoscale, traditional principles of chemistry and physics often no longer apply, as material properties like visual appearance, mechanical strength, electrical conductivity, and chemical sensitivity undergo significant changes between nano and macroscale dimensions

[25]. Owing to their high surface-to-volume ratio, nanomaterials exhibit significantly enhanced reactivity and functional efficiency compared to their bulk counterparts. Consequently, they are extensively employed across diverse domains, including scientific research, environmental remediation, industrial processes, and biomedical applications [26, 27]. The length of a nanometre can be understood through the example of five silicon atoms or 10 hydrogen atoms lined up, which is one nanometre. Materials are typically classified as nanomaterials when at least one of their dimensions falls within 1 to 100 nanometers. Naturally occurring nanomaterials have been present since the Earth's formation and have continued to evolve throughout its 4.5-billion-year geological history [28]. In contrast, incidental nanomaterials, which are generated as by-products of human activities, have seen a significant increase since the onset of the Industrial Revolution [29]. Engineered nanomaterials, purposefully synthesized to exhibit distinct and tunable physiochemical properties, are extensively utilized in diverse sectors, including biomedicine, electronics, energy systems, water purification, and environmental remediation. Nanomaterials are broadly defined as inorganic, organic, or hybrid materials that exhibit distinct electrical, physical, and/or chemical properties attributable to their ultrasmall dimensions, typically ranging from 1 nm to several tens of nanometres [29]. These materials demonstrate size-dependent property variations, primarily due to quantum confinement phenomena and their inherently large surface-to-volume ratios, which enhance their surface reactivity. The exciting physiochemical, photothermal, and optical properties of CDs, such as absorption, excellent photoluminescence, superior photostability, low photobleaching, biocompatible nature, and environment-friendliness, easy preparation, NIR-active nature, have made them highly important in multiple applications ranging from sensors, catalysis, optoelectronics, agriculture, environment, biomedical, and solar-driven interfacial evaporation field [30-33]. The sustainable environmental solution of CDs is extended to sensing, degradation, and solar water evaporation.

1.2. Carbon Dots

Over the past three decades, carbon-based nanomaterials have garnered immense attention since the initial discovery of fullerene produced through laser ablation of graphite [34]. The subsequent discoveries of fullerene [35], carbon nanotubes [36], graphene [37], and carbon dots [38] brought widespread attention to a diverse spectrum of 0-, 1-, 2-, and 3-dimensional carbon-based materials as shown in **Figure 1.2**, owing to their distinct properties, structures, and potential applications.

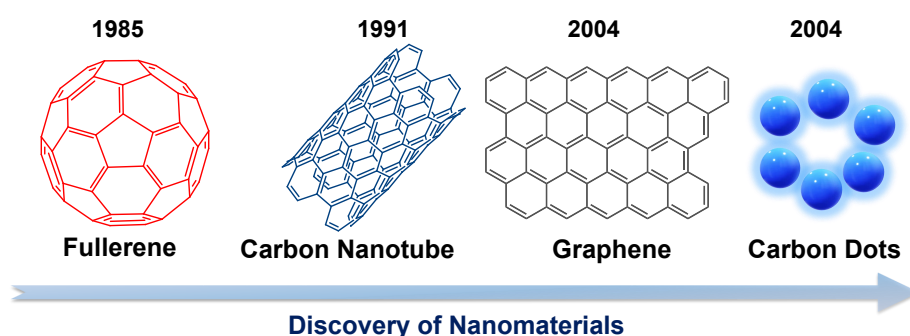


Figure 1.2. Schematic representation of the discovery timeline for key carbon-based nanomaterials.

Among the various carbon allotropes, carbon dots (CDs) exhibit excellent photoluminescence, high biocompatibility, aqueous dispersibility, biocompatibility, ultrasmall sizes (<10 nm), and tunable surface functionalities with diverse electron donor–acceptor characteristics [39, 40]. These fluorescent carbon nanoparticles were serendipitously found during the purification of single-walled carbon nanotubes by Xu et al. [38] for the first time in 2004.

In 2006, Sun et al. [41] synthesized fluorescent carbogenic nanoparticles (NPs) through laser ablation of a graphite powder and cement mixture and, for the first time, designated them as CDs, thereby initiating widespread research into their synthesis, purification, separation, characterization, and diverse applications [42–44]. PL, regarded as one of the most captivating characteristics of CDs, has been extensively investigated, with notable enhancements in their FL QY achieved over time. These properties have facilitated their

extensive use in diverse fields, including sensing [45], photocatalytic degradation [46], bioimaging [47], drug delivery [48], near-infrared (NIR) responsive systems [49], solar cells [50], light-emitting diodes [51], and photothermal therapy [52].

1.2.1. Structural Classification of CDs

Numerous hypothesized structures of CDs are often explored; nevertheless, a thorough investigation remains limited. CDs are frequently described as possessing a shell-core architecture, with the shell consisting of several surface functional groups [53]. Understanding the structure of CDs, encompassing their core and shell, is highly beneficial, as it helps us investigate the structure-property relationship between CDs and other related applications [54, 55]. Generally, CDs can be roughly classified into four discrete classes, i.e., carbonized polymer dots (CPDs), carbon nanodots (CNDs), carbon quantum dots (CQDs), and graphene quantum dots (GQDs) as indicated in **Figure 1.3**. The GQDs are graphene-based NPs with diameters under 100 nm, comprising a few layers of graphene in the core. The graphene layers in GQDs are responsible for rich π -electron density and high surface area. GQD consists of sp^2 hybridized carbon atoms with anisotropy. When the particle size of GQDs decreases below 10 nm, quantum confinement and edge effects result in distinguishing optoelectronic properties of GQDs. The optoelectronic characteristics of GQDs can be tuned by altering their morphologies and edges, resulting in variations in the band gaps of the valence and conduction bands [56, 57]. CQDs are a category of carbon-based quasi-spherical nanoparticles distinguished by either an amorphous configuration or a crystalline graphitic lattice. CQDs comprise more layers of graphite structure within their carbon core compared to GQDs. GQDs exhibit anisotropic characteristics with lateral dimensions greater than their height. So, the degree of spalling decides whether the resultant product is CQDs or GQDs. Moreover, CQDs involve mixed sp^2 and sp^3 hybridized carbon atoms, making them isotropic [58, 59]. CPDs are a new class of CDs that are synthesized

via cross-linking and aggregation of linear polymers, their monomers, or small organic molecules. Due to the utilization of polymers and some organic molecules during synthesis, the CPDs can possess numerous functional groups and polymer chains on their surface with a core similar to CQDs, leading to unique optoelectronic properties [60, 61]. CNDs exhibited excellent PL upon excitation. The presence of multiple surface functional groups on CNDs can alter their band gaps and impart distinctive features, such as selectivity towards metal ions in sensing applications and other catalytic applications, etc [62, 63]. Besides, the synthesis of CDs with various precursors can also tune the properties of CDs to have diverse applications, which will be further discussed in the subsequent section.

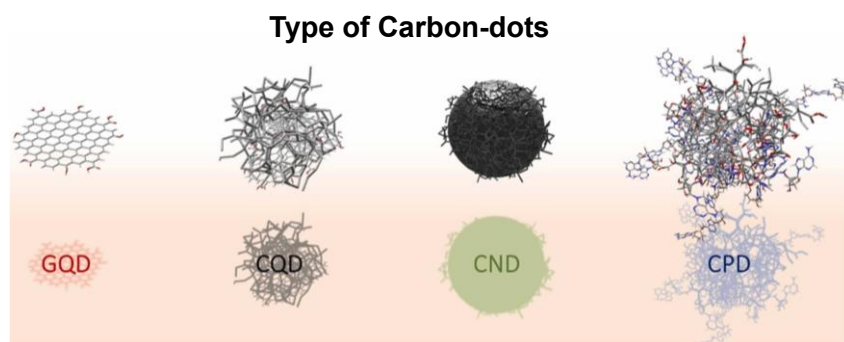


Figure 1.3. Schematic illustration highlighting the distinct types of carbon dots. [64]

1.2.2. Synthesis of CDs

The properties of CDs are closely linked to their structure, which is significantly dependent on the synthetic approach. In top-down methods, such as arc-discharge, laser ablation, oxidation, and electrochemical oxidation of bulk carbon materials, the resulting CDs often exhibit crystalline graphitic cores and abundant oxygen-containing functional groups due to harsh oxidative conditions [42, 65]. Conversely, bottom-up approaches like microwave-assisted method, hydrothermal/solvothermal synthesis, pyrolysis method, and ultrasonic method of organic precursors typically yield amorphous or partially crystalline carbon dots with tunable surface functionalities, size, and photoluminescence properties [66, 67]. The synthesis route

thus plays a crucial role in determining the size, morphology, surface chemistry, and optical behavior of CDs. A summarized representation of the synthetic approach is shown in **Figure 1.4**.

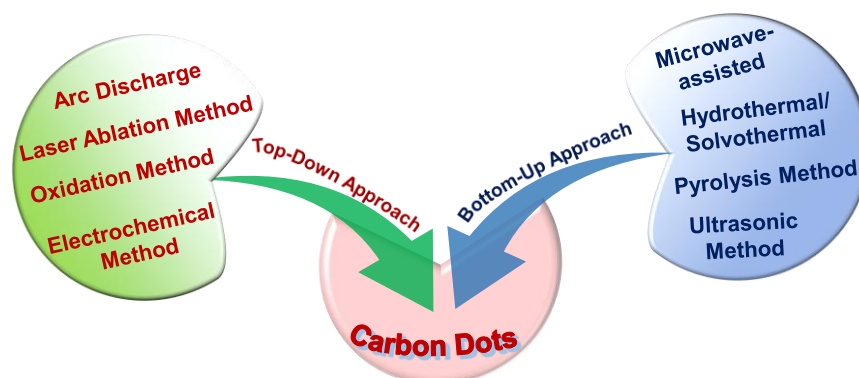


Figure 1.4. Schematic representation of CDs synthesis utilizing top-down and bottom-up approaches.

A variety of precursors were investigated for the synthesis of CDs. A significant number of chemical and green precursors are utilized for CDs synthesis. Notably, the nature of the precursor, dopant, reaction temperature, and synthesis route substantially influence the characteristics of CDs. Based on the precursor used for the synthesis of CDs, they have been categorized as CDs derived from chemical precursors and biomass-derived CDs.

1.2.2.1. CDs Derived from Biomass

Biomass as a renewable precursor is a crucial carbon source in the synthesis of CDs due to its abundance and cost-effectiveness [68]. Biomass-derived carbon sources, as renewable and environmentally benign alternatives to conventional precursors, offer distinct advantages for CDs synthesis, including cost-effectiveness, widespread availability, and environmental sustainability [69]. The synthesis of CDs from natural biomass enables the transformation of low-value biomass waste into high-value, nanomaterials with broad applicability. Biomass enriched with heteroatoms serves as an optimal precursor for CDs synthesis, as it facilitates in situ heteroatom doping, which enhances the properties of the resulting CDs [70]. In recent years, the

use of diverse biomass sources as renewable carbon precursors for the synthesis of CDs, including orange waste peel [71], banana peel [72], fish scalp [73], wild fruit [74], eggshells [75], elephant manure [76] has attracted significant attention (**Figure 1.5a-f**). The massive increase in the use of green sources for the synthesis of CDs has started a new era of CDs, and so far, a variety of green sources have been explored.

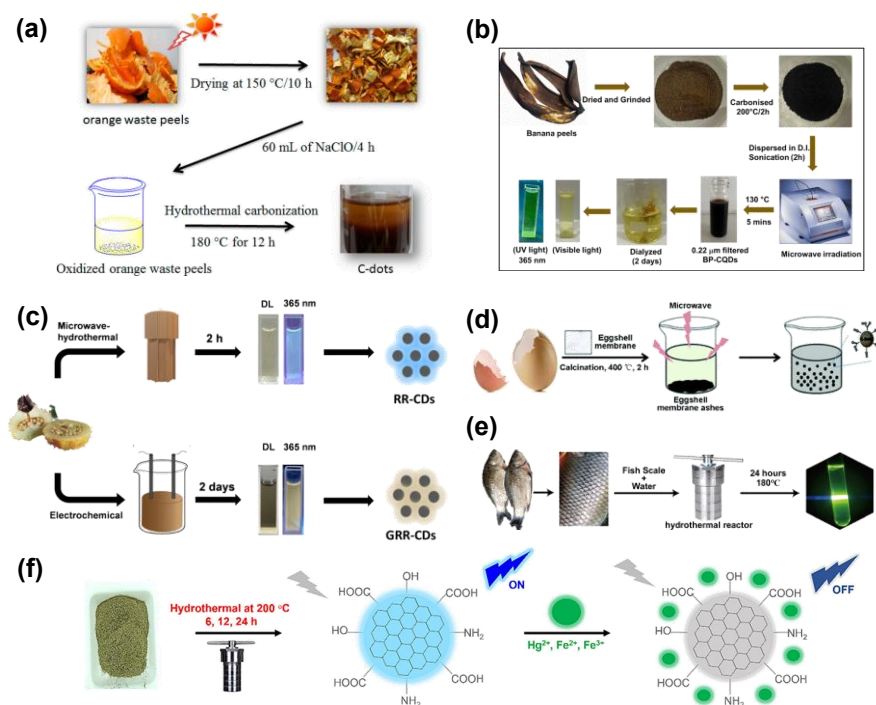


Figure 1.5. Carbon dots derived from various biomass, including (a) Orange peels [71], (b) banana peel [72], (c) *Rosa Roxburghii* fruit [73], (d) chicken eggshell [74], (e) fish scalp [75], (f) elephant manure [76].

1.2.2.2. CDs derived from Chemical Precursors

Numerous natural precursors have been employed in the synthesis of cost-effective, biocompatible chemical precursors of CDs, which are still under investigation to obtain an excellent QY. The benzene derivative is mostly explored as a carbon source, which includes phenolic, aromatic amines, polycyclic aromatic hydrocarbons, and various polymers. Various acid reagents such as citric acid [77], folic acid [78], tartaric acid [79], etc, and non-acidic reagents such as

chitosan [80], sugar [81], o-phenylenediamine [82], lignin [83], coal [84], etc, have been extensively employed for CD synthesis. Moreover, CDs with a high QY of 65 % are synthesized by Tufenkji and co-workers [85] utilizing citric acid and phenylalanine via a one-step hydrothermal method, as shown in **Figure 1.6a**. In this work, the role of stoichiometry on the chemical and structural composition of CDs and, in turn, its effect on QY was checked. In another study by Fan and co-workers [86] performed radical-assisted synthesis of hexagonally shaped CQDs from perylene precursor at a relatively low reaction temperature of 80 °C, achieving exceptionally high PL QY, i.e., near unity (96 %) (**Figure 1.6b**). Further, Gong and co-workers [87] developed a mild, one-step thermolysis method conducted at low temperature and pressure for rapid synthesis of CDs with ultrahigh PL QY as indicated in **Figure 1.6c**. In this method, citric acid, pyrocatechol, and o-phenylenediamine are utilized as a carbon source, and 1-butyl-3-methylimidazolium chloride as a solvent and surface passivating agent for CDs synthesis.

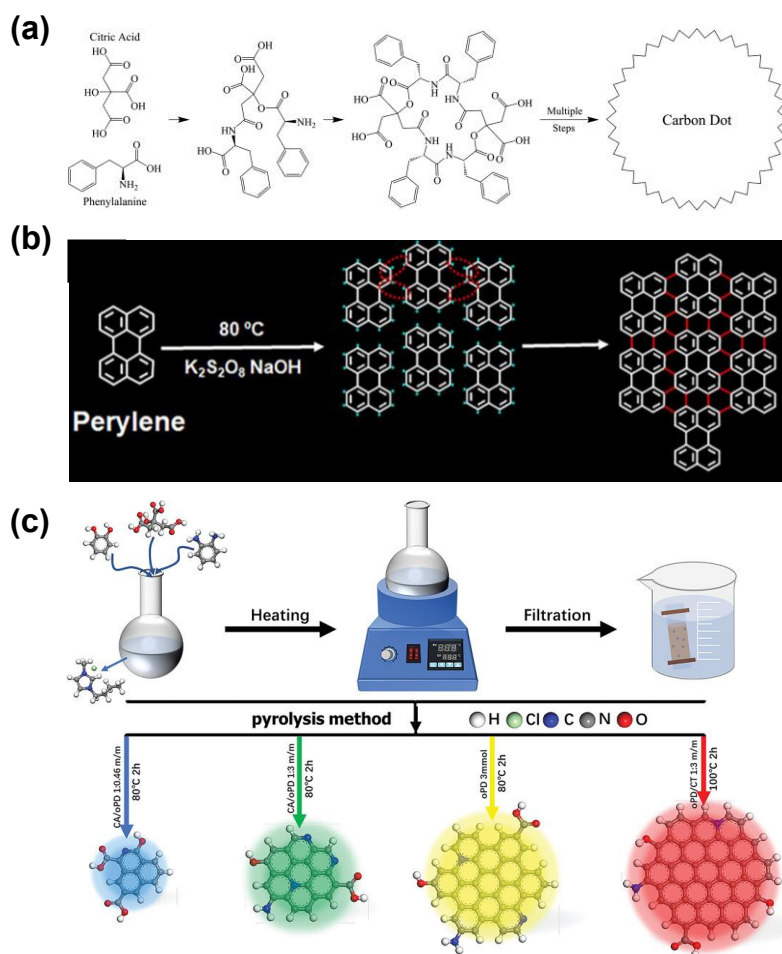


Figure 1.6. (a) Initial steps for the reaction of citric acid and phenylalanine to synthesize CDs, [85] (b) Synthesis route of CQDs by radical-assisted synthetic strategy using perylene precursors, [86] (c) Synthesis process of multicolor emissive CDs with ionic liquid as solvent and citric acid, pyrocatechol, and o-phenylenediamine as precursors. [87]

1.2.3. Approaches to Tuning the Fluorescence Efficiency of CDs

❖ **Passivation-** Passivation refers to coating and capping of the surface of carbon dots with polymers, surfactants, or small molecules to reduce non-radiative recombination sites. The surface modification or passivation plays a crucial role in altering the PL properties and band gaps of CDs. In some cases, CDs did not exhibit PL unless they underwent surface passivation [88]. In this study by Ren et al. [89] largely amorphous carbon nanoparticles were copolymerized with *N*-vinyl carbazole through microwave-

assisted radical reactions. The resulting copolymer is structurally analogous to a CD with each nanoparticle surface functionalized by multiple poly(*N*-vinyl carbazole) segments. Alas et al. [90] synthesized red emissive CDs from p-phenylenediamine by a single-step microwave-assisted solvothermal method. Further, the surface of CDs was modified with hyperbranched bis-MPA polyester hydroxyl polymers. The QY of CDs after passivation altered from 31.4 % to 79.8 %.

- ❖ **Doping-** The doping of CDs with various elements, such as phosphorus (P), sulfur (S), fluorine (F), nitrogen (N), and others, has been extensively employed to tailor their photophysical and optoelectronic characteristics [64, 91]. Notably, Wu et al. [92] reported a correlation between the nitrogen content of CDs and their photo-oxidative activity, highlighting the significance of doping, which influences the functional performance. The doping of CDs with highly electronegative atoms (such as N and S) typically induces a blue shift in PL emission. Moreover, Wu et al. synthesized nitrogen and sulfur doped carbon dots (N,S-CDs), resulting in improved PL QY from 11.2 % to 65.1 %. Through S element doping red-shifted the FL emission from 430 to 545 nm and suppressed non-radiative transitions. The N,S-CDs enabled dual-mode detection of Zr^{4+} and NO_2^- , and were also used for anti-counterfeiting applications. In contrast, doping with weak electron-donating elements, including P, B, and Se, tends to cause a red shift in PL emission relative to undoped CDs [93-95].
- ❖ **Reduction-** It is a new strategy based on the reduction reaction of synthesized CDs that was developed for improving their fluorescence performance. Shen et al. [96] developed a reduction pathway to tune FL QY and the emission wavelength of CDs. The original CDs, initially exhibiting a QY of 1.55 %, were reduced using $NaBH_4$ and $LiAlH_4$, resulting in QY enhancement to 7.25 % and 7.44 %, respectively. The variation in surface functional groups resulted in distinct fluorescence (FL) characteristics in unmodified, $NaBH_4$ -treated, and $LiAlH_4$ -treated CDs. Du et al. [97]

investigated the FL properties of coal-derived CDs and proposed strategies for their enhancement. In this work, they have utilized N-doping and a reduction with NaBH_4 to improve the optical properties of CDs. The reduced form of CDs indicated the blue-shifted FL and an increase in QY. Overall, reduction treatment offers a promising route for tailoring the PL properties of CDs by modifying their surface chemistry and electronic structure.

1.2.4. Carbon Dots Properties

The structural and optical properties of CDs are highly sensitive to the synthesis method and precursor composition. Hydrothermal and solvothermal methods offer tunability by adjusting reaction temperature, time, and precursor concentration. Doping with heteroatoms during or after synthesis not only modifies the bandgap of the CDs but also introduces new energy levels, affecting absorption and emission behavior.

1.2.4.1. Structural Characteristics

CDs are a class of carbon-based nanoparticles, typically exhibiting spherical or quasi-spherical morphologies with a diameter below 10 nm [98]. Their core structure can range from amorphous to crystalline carbon, depending upon the choice of precursors and synthesis methods.

The high-resolution transmission electron microscopy (HR-TEM) revealed the amorphous or crystalline structure of CDs, with an average size of around 10 nm. The lattice fringes with an interlayer spacing of a few nanometres correspond to the graphitic carbon domain [99]. These crystalline domains are more pronounced in CDs synthesized at elevated temperatures or under controlled atmospheres, while those synthesized at low temperatures through hydrothermal or microwave-assisted processes often exhibit amorphous internal structures [100, 101]. The crystallinity of CDs is further supported by X-ray diffraction (XRD) analysis, which typically shows a broad

diffraction peak around 20-25°, corresponding to the (002) plane of disordered graphitic carbon. The intensity and sharpness of this peak vary with the degree of graphitization, allowing to distinguish between the amorphous and crystalline nature of CDs [102]. Surface chemistry is another essential structural feature of CDs. Their surfaces are commonly decorated with abundant functional groups such as hydroxyl (-OH), carboxyl (-COOH), carbonyl (C=O), and amino (-NH₂), derived from both the precursor molecules and reaction conditions [103]. These surface moieties enhance water dispersibility, biocompatibility, and chemical reactivity, enabling facile post-synthetic modification for specific applications [104]. Analytical techniques, such as Fourier-transform infrared (FTIR) spectroscopy, X-ray photoelectron spectroscopy (XPS), and Raman spectroscopy, are also commonly employed to investigate the chemical structure of CDs [105]. The degree of crystallinity significantly influences the electronic and optical properties of CDs. Graphitic CDs with higher sp²-hybridized carbon content tend to exhibit better conductivity and well-defined optical transitions, while amorphous CDs are often more versatile for surface modification.

1.2.4.2. Optical Properties

The optical behaviour of CDs stands out as one of their most characteristic and thoroughly investigated aspects. CDs generally exhibit broad UV-visible absorption spectra, which arise from various electronic transitions associated with their carbonaceous structure and surface functionalities. The strong absorption band in the UV region, i.e., below 300 nm, is primarily attributed to π - π^* transitions of aromatic C=C bonds within the sp² hybridized carbon core. Additionally, n- π^* transitions originating from non-bonding electron pairs on oxygen-containing functional groups such as carbonyl or carboxyl moieties, at longer wavelengths (around 320-400 nm) [106]. In certain cases, CDs demonstrate absorption tailing to the visible or near infrared (NIR) region, attributed to surface defects or mid-gap

energy levels introduced during synthesis. NIR-emitting CDs are of particular interest due to their photothermal conversion efficiency, making them highly valuable for photothermal therapy and interfacial solar-driven water evaporation [52, 107]. A hallmark of CDs is their strong and tunable FL, which is often excitation-dependent and allows CDs to emit across a wide spectral range, which is particularly advantageous for applications in sensing and optoelectronics. Several mechanisms have been proposed to explain this unique FL behavior, including quantum confinement effects, surface defect states, and the presence of molecular fluorophores formed during synthesis [108, 109]. The carbon core structure, surface states, and molecular fluorophores determine not only the emission wavelength but also the FL QY, lifetime, and stability of CDs. QY for CDs varies significantly and can be greatly enhanced by surface passivation or heteroatom doping [110, 111]. The FL lifetime measurements, commonly obtained via time-correlated single-photon counting (TCSPC), show that CDs possess nanosecond-scale lifetimes, indicating their emission arises predominantly from allowed electronic transitions. CDs also exhibit excellent photostability, maintaining FL intensity under prolonged excitation without significant photobleaching. Furthermore, their emission remains stable under a wide range of pH, ionic strengths, and temperatures, enhancing their utility in diverse environmental and biological conditions [30, 112].

1.3. Carbon Dot-Based Nanocomposites

Carbon-based nanocomposites continue to emerge as the next generation of innovative materials. Many scientists have begun to notice the potential for utilizing these materials in novel applications such as sensing [113], removal of organic pollutants [114], and interfacial solar-driven water evaporation [115]. Moreover, among many carbon-based composite materials, carbon dot-based nanocomposites (CNCs) are fabricated by embedding CDs of diverse morphologies and sizes into a polymer matrix [116]. Nonetheless, the

incorporation of these nanoparticles is strongly influenced by their aspect ratio and degree of dispersion. The CDs impart mechanical strength, thermal stability, biocompatibility, UV resistance, and fluorescence to the polymer matrix. Notably, the polymeric network restricts the agglomeration of CDs, and CDs improve the optical and mechanical characteristics of as-synthesized composites owing to their small size and high surface area [11-119]. Some of the host matrices that have been utilized previously to immobilize CDs include graphene oxide [120], polyurethane [121], PVDF [122], metal-organic framework [123], cellulose [124], zeolites [125], chitosan [126], wood [83], etc, as shown in **Figure 1.7**.

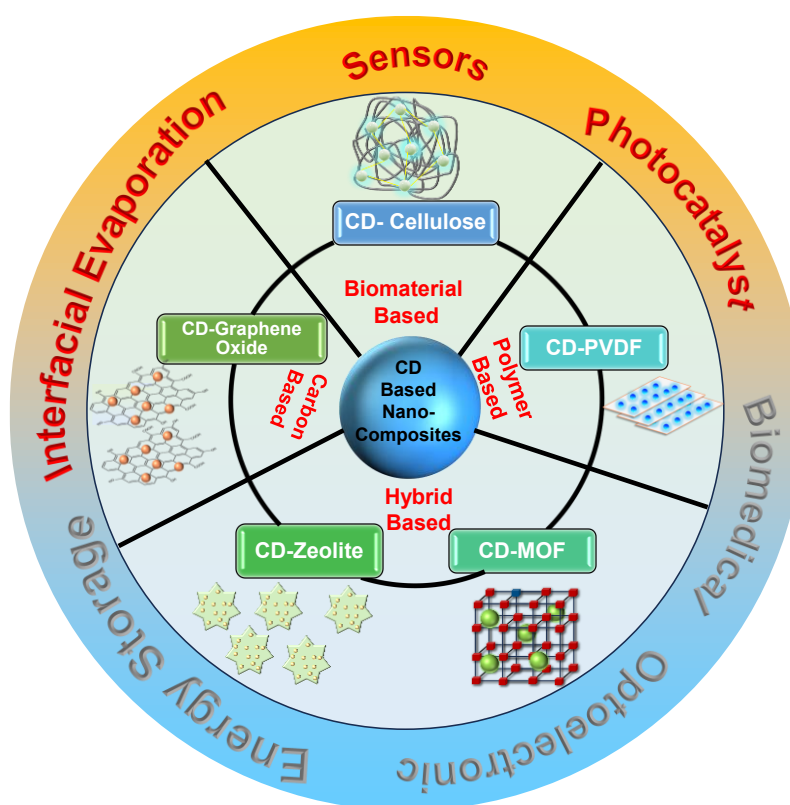


Figure 1.7. Schematic illustrating carbon dots-based various nanocomposites.

Notably, the one-step approach and the two-step approach are the two primary approaches utilized in the formulation of CD-based composites. In the one-step approach, both the CDs and the matrix form simultaneously within the reaction system, resulting in the in-situ

confinement of CDs within the host matrix. Towards this approach in 2017, Liu et al. [127] designed a facile method to integrate the CDs in zeolite matrices in situ in a dot-in-zeolites manner under solvothermal or hydrothermal conditions. In contrast, CDs are first synthesized via top-down or bottom-up methods and then subsequently incorporated into host matrices through a chemical or physical approach in the two-step approach. Alternatively, first, a host matrix is prepared, which is subsequently subjected to thermal treatment such as pyrolysis, combustion, or heating to generate CDs within it. Based on that Wang et al. [128] reported a CD@ZIF-8 composite which was prepared by solvothermal synthesis of ZIF-8 nanocrystals followed by calcination. Moreover, Tian et al. [129] synthesized N-doped CDs using isophorone diisocyanate (IPDI) as a carbon precursor under a microwave-assisted method. Next, dibutyltin dilaurate and polytetramethylene ether glycol were introduced into the N-doped CDs and IPDI mixture, which was then heated to 80 °C to form CDs@PU composites.

1.3.1. Structural Supports for CD Nanocomposites

➤ Bacterial Cellulose (BC)

In nature, pure cellulose is obtainable only as bacterial cellulose (BC), which is biosynthesized by specific bacterial species, primarily from the genera *Acetobacter*, *Sarcina ventriculi*, *Kombucha*, *Agrobacterium*, and others [130]. In their natural environment, they can produce a protective envelope composed of extracellular polysaccharides like cellulose, forming a thick, gel-like pellicle at the interface between the culture medium and air, as shown in the schematic of **Figure 1.8** [131]. In vivo cultivation of these bacteria under favorable environmental conditions, i.e., pH 4-6, temperature 28-30 °C, and a growth medium enriched with carbon, nitrogen, and various nutrients leads to the formation of cellulose nanofibers with 20-100 nm in diameter and several μm in length [132, 133]. These microfibrils offer

a versatile platform for embedding or stabilizing diverse nanomaterials. The nanosized fibrils of BC serve as a stable support for CDs, playing a crucial role in the development of versatile, portable membranes functioning as sensors or photothermally active membranes [134, 135]. In this context, nanoscale cellulose fibrils offer the necessary surface roughness to attain high sensitivity, making them suitable for applications in environmental monitoring [136], food safety [137], and biomedical diagnostics [138].

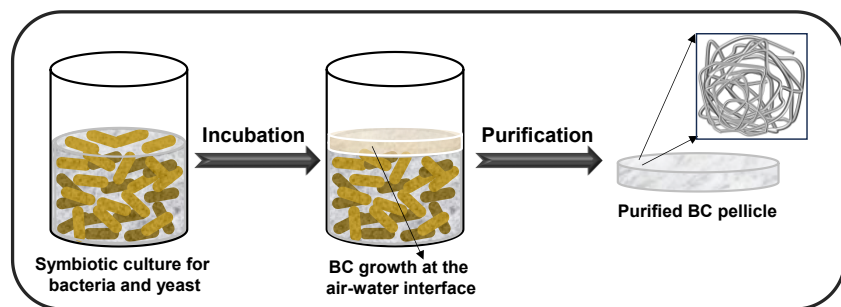


Figure 1.8. Schematic of BC culturing.

➤ Polyvinylidene Fluoride (PVDF)

PVDF is a versatile fluoropolymer characterized by abundant covalent C-F bonds, making it highly suitable for applications in sensors, piezoelectric devices, and polymer batteries due to its thermal stability, processability, high dielectric constant, and non-toxicity [139]. Owing to its excellent thermal stability, chemical resistance, mechanical robustness, flexibility, eco-friendliness, and affordability, PVDF emerges as a promising material for thin film fabrication [140]. The inherent hydrophobicity, combined with its strong adhesion properties, ensures a substantial mechanical strength, thereby preventing leaching of hydrophilic active FL agents from the film matrix [141]. Typically, PVDF membranes are synthesized through nonsolvent-induced phase separation by immersing the casting solution into a coagulation bath that promotes phase separation and film formation [142]. The film fabricated by PVDF possesses distinct properties like ease of processing, flexibility, and lightness. So, CNCs have garnered huge

attention in environmental remediation due to their exciting physicochemical properties like large surface area, tunable optical properties, biocompatible nature, mechanical stability, and exceptional durability [143, 144]. They are further explored for multifaceted applications, particularly in the domains of sensing, photocatalytic degradation, and photothermal applications.

1.4. Multifunctional Applications

Figure 1.9 illustrates the multifunctional applications of CDs and CDs-based nanocomposites and focuses mainly on three areas, i.e., sensing, photodegradation, and solar-driven water evaporation. These applications are enabled by key properties of CDs, including strong and tunable PL for sensitive and selective sensing, excellent photocatalytic activity driven by high surface area and efficient charge separation for effective photodegradation, and superior light absorption along with outstanding photothermal conversion efficiency for solar-driven interfacial evaporation. Additionally, their chemical stability, water solubility, biocompatibility, and ease of functionalization enhance their performance and integration into multifunctional nanocomposite systems. These combined attributes position CDs as promising materials for sustainable environmental solutions.

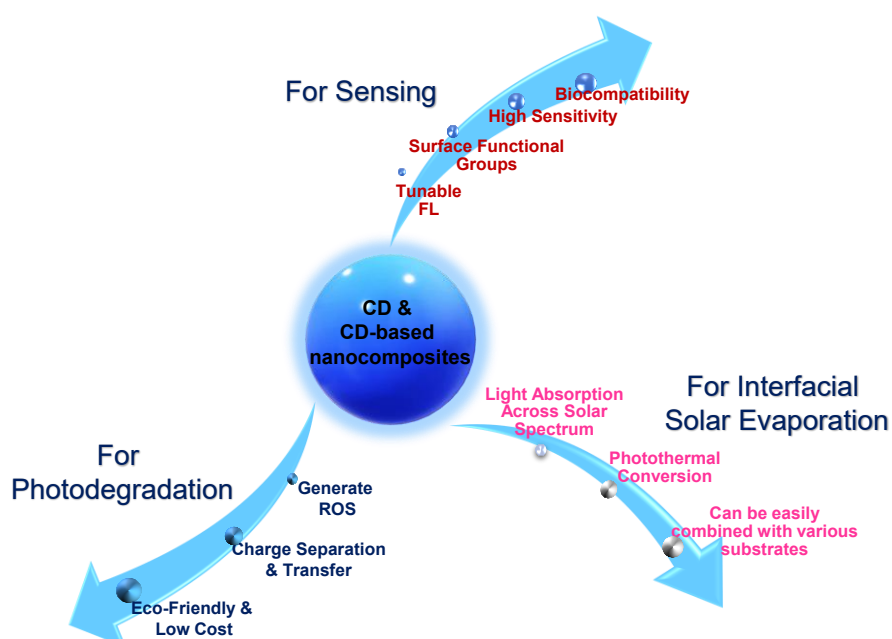


Figure 1.9. Illustration of CDs and CD-based nanocomposites for multifunctional applications.

1.4.1. Fluorescent Detection of Pollutants

The detection of toxic compounds, including metal ions, pharmaceuticals, pesticides, nitro compounds, and other environmental pollutants, is of critical importance due to their adverse effects even at trace concentrations on human health and ecosystems [26, 30]. Consequently, developing sensitive, selective, and rapid detection methods is essential for applications in food safety, environmental monitoring, and biomedical diagnostics. Recently, CDs have been considered a milestone in optical sensing due to their exceptional physical and chemical properties [42]. In this context, numerous CD-based sensors have been developed for the detection of a wide range of analytes [145-147]. CDs have attracted much attention as a sensor due to their multiple attributes, like stable PL, robust chemical inertness, excellent QY, water-solubility, resistance to photobleaching, a wide range of raw materials or precursors, excellent biocompatibility, low toxicity, tunable optical properties, cost-effectiveness, and on-site detection ability [148, 149]. These features enable CDs to selectively interact with various analytes such as metal ions,¹⁵⁰ biomolecules,¹⁵¹ antibiotics [145], pesticides [152], nitro compounds [2], which often results in a change in FL intensity, either FL turn off or turn on behaviour, wavelength shift, or quenching effects. The changes in optical behaviour of CDs could be due to electron transfer (ET), Forster resonance energy transfer (FRET), inner filter effect (IFE), aggregation-induced emission (AIE), aggregation-induced quenching (AIQ), static or dynamic quenching, charge transfer, bonding [26, 153], etc. Additionally, the low toxicity and excellent stability under light and extreme environmental conditions make them a suitable candidate for real-time application for environmental monitoring of toxic pollutants. To this end, Bavva et al. [154] synthesized sulfur-doped CDs (SCDs) hydrothermally using cellulose derived from waste

bamboo and sodium thiosulfate as precursors. The resulting SCDs demonstrated high selectivity and sensitivity towards Hg(II) ions, achieving a remarkably low detection limit as indicated in **Figure 1.10a**. The enhancement in FL observed upon interaction with mercury ions was attributed to complex formation between Hg(II) and functional groups on the SCDs, which effectively modulated the PL behaviour. In a related study, Cui et al. [155] designed a CD-based sensor using DL-malic acid and urea through a microwave-assisted approach. Furthermore, the obtained NCDs were utilized as the FL sensor to detect ascorbic acid and Fe³⁺ in solution, as shown in **Figure 1.10b** through static quenching and the inner filter mechanism. To effectively monitor nitro compounds, Mahto et al. [156] synthesized N-doped CDs (NCDs) using microwave-assisted pyrolysis of urea and malic acid (in a 3:1 molar ratio) and utilized them as fluorescent probes for the sensitive and selective detection of picric acid, as shown in **Figure 1.10c**. Furthermore, for analysing antibiotics, Dong et al. [157] synthesized two-photon CQDs (TP-CQD) using ethylenediamine and citric acid in phosphoric acid solution via the hydrothermal method. As shown in **Figure 1.10d**, the TP-CQD nanoprobe was applied as a chemosensor to detect chlortetracycline, which quenches the intrinsic FL of TP-CQD.

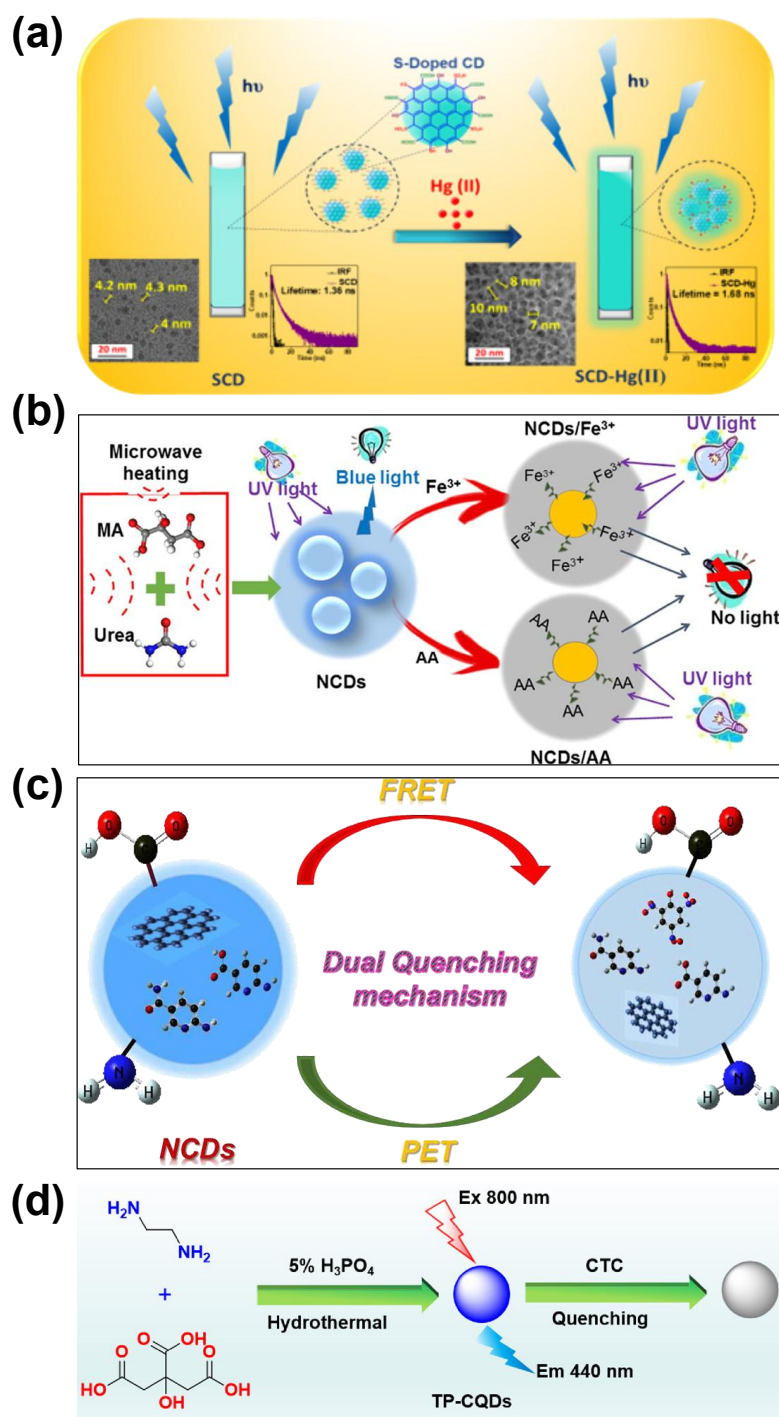


Figure 1.10. Schematic Illustration of: (a) aggregation-induced FL enhancement mechanism of the SCD solution in the presence of mercury. [154] (b) NCDs show a turn-off strategy for the detection of ascorbic acid and Fe^{3+} . [155] (c) Dual quenching mechanism for picric acid detection using NCD. [156] (d) TP-CQDs for CTC detection. [157]

Moreover, incorporating CDs into hydrogels or solid substrates significantly enhances their practical utility in sensing applications. Embedding CDs into solid support improves their photostability and protects against degradation. Additionally, immobilization facilitates the development of a portable, reusable sensing platform. Thakkar et al. [126] demonstrated this concept by developing a carbon dot-based hydrogel composite. In this study, they have synthesized CDs using lemon peels and incorporated them into a chitosan hydrogel for the detection of Fe(III) and glutathione. The hydrogel matrix not only provided mechanical support and ease of handling but also demonstrated the effectiveness of such integrated systems in practical sensing environments.

Photocatalytic Degradation

In addition to detecting environmental pollutants, their degradation is equally important to ensure complete removal from the environment to protect human health [158]. Numerous pollutants in the aquatic system are becoming public concerns, such as dyes [159], industrial effluents [160, 161], pharmaceuticals [162], and related byproducts. The presence of residues from these sediments has the potential to cause severe and chronic toxicity. Therefore, a major concern in environmental water quality monitoring and purification is the effective removal technique for organic contaminants from pharmaceutical waste to industrial wastewater [163]. In order to solve this problem, one of the most cutting-edge oxidation technologies is photocatalytic degradation using sustainable solar energy. This method offers numerous benefits, including affordability, straightforward photocatalyst synthesis, absence of external oxidizing agents, minimal toxicity, and efficient mineralization.

The photocatalytic degradation relies on photon absorption with energy slightly greater than the catalyst's band gap, generating photoinduced charge carriers that generate reactive oxygen species in the reaction medium [164, 165]. CDs [18] and CNCs [166] have received a lot of

attention in photocatalytic applications due to their optical, electronic, and surface properties. CDs can absorb light and generate electron-hole pairs, which participate in redox reactions that lead to the breakdown of organic pollutants into less harmful substances such as CO₂ and H₂O [158] (**Figure 1.11a**). In this context, Chen et al. [18] developed a cost-effective photocatalyst by modifying TiO₂ with blue algae-derived carbon quantum dots (B-CQDs). The resulting composite demonstrated the remarkable photocatalytic activity to degrade the antiviral drug favipiravir in 60 min, as indicated in **Figure 1.11b**. Furthermore, Nayak et al. [167] synthesized carbon quantum dots (CD) hydrothermally from lemon juice and cysteamine, which shows excellent photocatalytic performance in the degradation of anionic and cationic dyes (**Figure 1.11c**). Further advancing this concept, a novel polymeric hydrogel was fabricated using polyvinylpyrrolidone cross-linked with CD for the dual purpose of dye adsorption and photocatalytic degradation. Therefore, CDs and CD-based photocatalysts offer a sustainable and efficient approach for the degradation of various contaminants, including dyes, pharmaceuticals, etc.

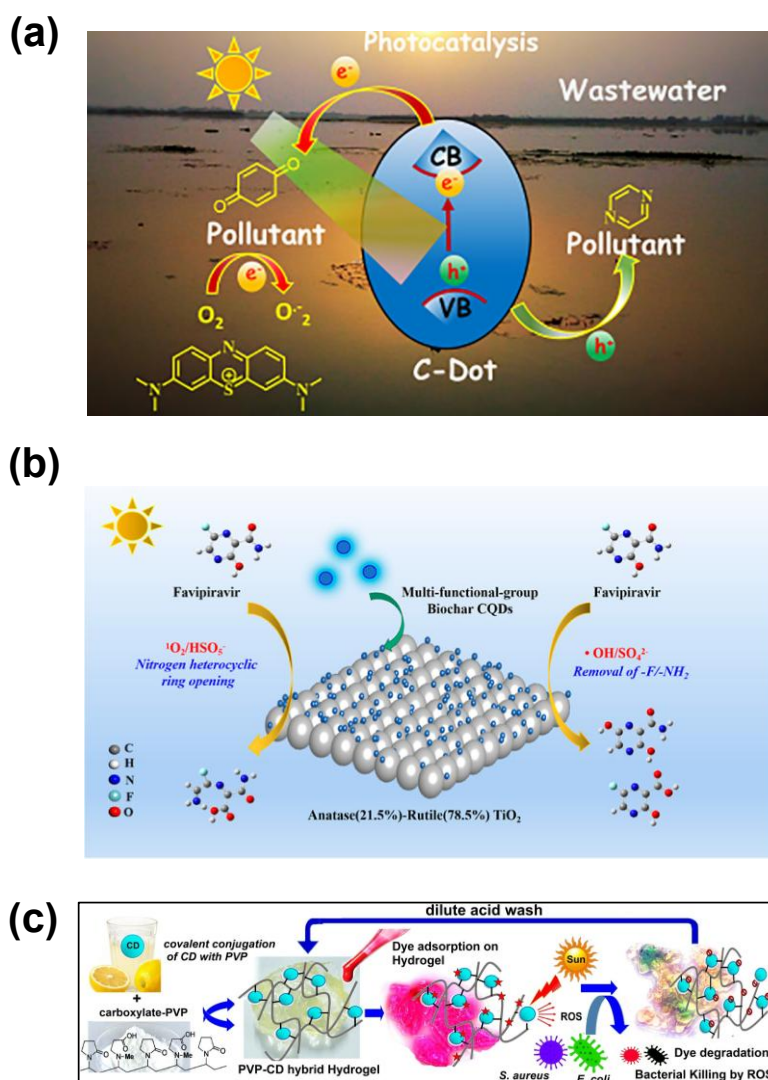


Figure 1.11. Schematic showing: (a) CDs generate reactive radical species for pollutant degradation, [158] (b) BCQD@TiO₂ for degradation of Favipiravir, [18] (c) synthesis of PVP-CD hybrid hydrogel for adsorption and photodegradation of dye. [167]

1.4.2. Interfacial Solar-Driven Water Evaporation

Solar evaporation is viewed as a promising solution to freshwater scarcity, leveraging sustainable and renewable energy, while minimizing ecological impact [168]. The solar-driven water evaporation utilizes the localized solar heating at the air-water interface to accelerate evaporation while minimizing energy loss to the bulk water [169]. Moreover, CDs have emerged as multifunctional nanomaterials with significant potential in environmental remediation

as well as solar-driven interfacial water evaporation [32]. The remarkable photothermal conversion and broad-spectrum light absorption of CDs make them an excellent candidate for the fabrication of photothermally active membranes [107]. The only hurdle in the case of CDs is their small size, rendering slow leaching, so better recyclability is achieved by embedding CDs into a polymer matrix (e.g., cellulose, hydrogels, or aerogels) [40, 170-173]. So, CDs have been incorporated into porous matrices to form a composite material that can be utilized for solar-driven water evaporation. As illustrated in **Figure 1.12a**, Li et al. [174] developed a high-performance solar evaporator using chitosan carbon aerogel modified with lignin-derived carbon quantum dots (C-LCDCA). The incorporation of LCQDs enhanced the light absorption and photothermal conversion efficiency of C-LCDCA. The C-LCDCA achieves a high evaporation rate of $1.71 \text{ kg m}^{-2} \text{ h}^{-1}$ and strong salt rejection ability. Similarly, Ji et al. [175] synthesized a wood-based solar evaporator (CD-wood) via a one-step in situ process, employing lignin inherently present in wood as the carbon source, as depicted in **Figure 1.12b**. The CD-wood evaporator demonstrated broadband absorption with high solar-steam conversion efficiency and offers a scalable, all-biomass-based material for efficient solar steam generation and water purification. Furthermore, Li et al. [176] recently introduced hierarchical assemblies of carbon dots (HA-CDs), synthesized through a stepwise assembly strategy, wherein monodispersed UV-absorbing CDs were combined into supra-CDs (PA-CDs), which were then cross-linked with Fe^{3+} ions to form 3D porous architectures as shown in **Figure 1.12c**. These HA-CDs exhibited full-spectrum solar absorption, superior water resistance, and an impressive 84 % solar-to-thermal energy conversion efficiency under simulated solar illumination. The HA-CDs-fabric exhibited efficient two-dimensional solar interfacial evaporation, along with electricity production and integrated water-electricity cogeneration, highlighting the multifunctionality of carbon dot-based photothermal materials. Together, carbon dots and CNCs represent the transformative role of carbon dots in designing next-generation solar

evaporators that are not only efficient and cost-effective but also sustainable and adaptable to a variety of water treatment challenges.

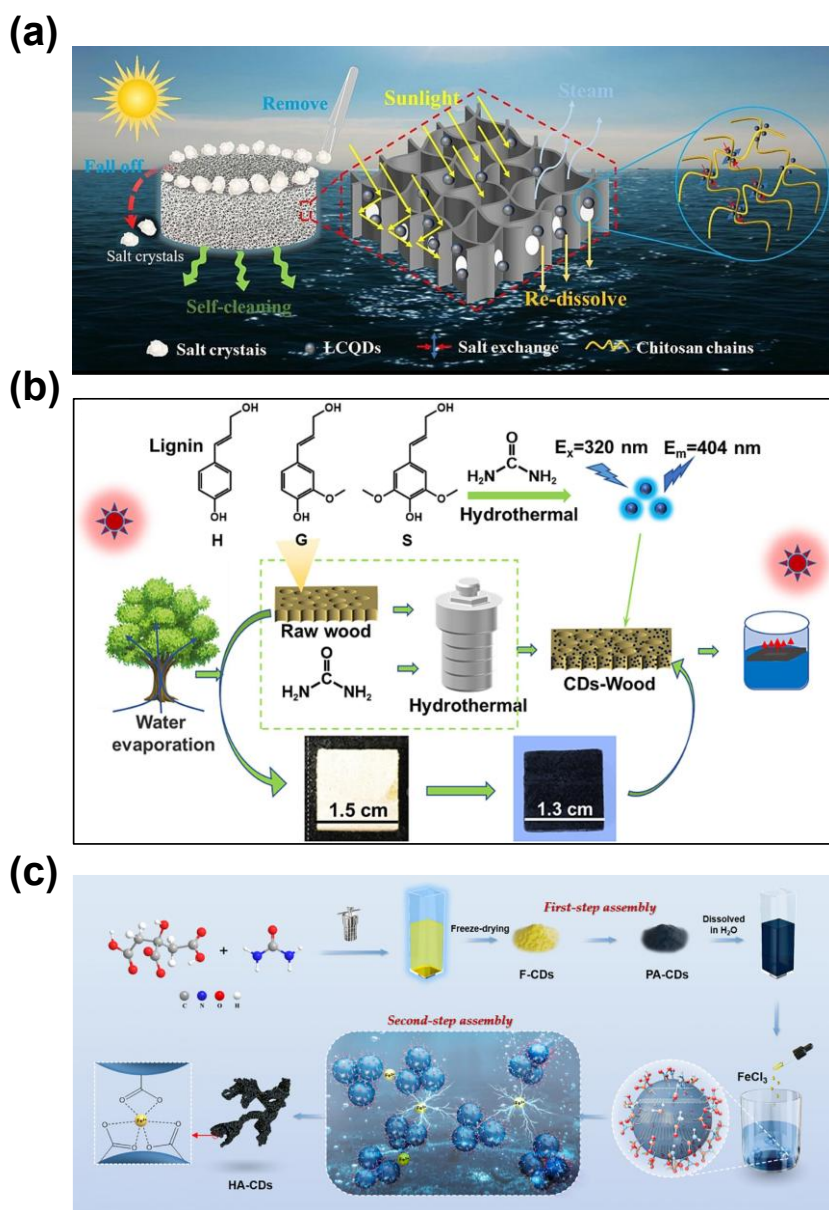


Figure 1.12. Schematic illustration of: (a) C-LCDCA material exhibiting high efficiency evaporation, salt tolerance, and self-cleaning ability. [174] (b) Fabrication of the CD-Wood evaporator and the setup of the solar steam generation device. [175] (c) Schematic representation of the synthesis pathways for F-CDs, PA-CDs, and HA-CDs, along with the hierarchical assembly mechanism of HA-CDs in the solar evaporator. [176]

1.5. Scope of the Present Work

The synthesis strategies, properties, and tuning of the photophysical characteristics of CDs and CD-based nanocomposites, along with their applications, are discussed in previous sections of the thesis, highlighting the importance of CDs in sustainable environmental management, including fluorescence sensing, photocatalytic degradation of various analytes. The present thesis work highlights the development of CDs using green and chemical precursors and incorporates them in solid matrices for the remediation of pollutants and solar-driven interfacial water evaporation. This work is motivated by the potential application of these CDs and CD-based nanocomposites in optical sensing, photocatalytic degradation, and solar-driven water evaporation for water purification.

The main highlights of the thesis work are mentioned below:

1. Modulation of photophysical characteristics of carbon dots through post-synthetic reduction strategy for metal ion sensing.
2. Develop a portable, non-invasive carbon dots-based fluorescent thin film for the detection of picric acid.
3. Design a carbon dot-bacterial cellulose hybrid platform for remediating pharmaceuticals.
4. Engineered a multifunctional photothermal membrane by incorporating carbon dots into bacterial cellulose for interfacial solar-driven water evaporation and purification.
5. Fabricate a photothermal membrane by integrating a carbon dot-based organic network into bacterial cellulose for interfacial water evaporation

1.6. References

1. Zhu P., Hou S.-L., Liu Z., Zhou Y., Alvarez P. J. J., Chen W., Zhang T. (2024), Multi-Emission Carbon Dots Combining Turn-On Sensing and Fluorescence Quenching Exhibit Ultrahigh Selectivity for Mercury in Real Water Samples, *Environ. Sci. Technol.*, 58, 9887–9895. (DOI: 10.1021/acs.est.4c02355)
2. Rani Y., Km M. P., Tripathi P. (2024), Curcumin-Derived (3-Aminopropyl) Trimethoxysilane-Functionalized Carbon Quantum Dots: A Fluorometric and Colorimetric Nanoprobe for Picric Acid Detection, Antioxidant Activity, and Liposome Encapsulation, *ACS Appl. Mater. Interfaces*, 16, 68936–68949. (DOI: 10.1021/acsami.4c15636)
3. Wang L., Liu L., Chen R., Jiao Y., Zhao K., Liu Y., Zhu G. (2024), Carbonized Polymer Dots-Based Molecular Imprinting: An Adsorbent with Enhanced Selectivity for Highly Efficient Recognition and Removal of Cefotiofur Sodium from Complex Samples, *J. Hazard. Mater.*, 473, 134637. (DOI: 10.1016/j.jhazmat.2024.134637)
4. Hu J., Yin R., Pan Y., Wang J., Ren H. (2025), Multimodal Learning-Assisted Identification of Effluent Water Quality and Toxicity in Wastewater Treatment Plants, *Environ. Sci. Technol.*, (DOI: 10.1021/acs.est.5c04143)
5. Ullah M., Innocenzi V., Ayedi K., Vegliò F., Ippolito N. M. (2024), Automotive Wastewater Treatment Processes and Technologies: A Review, *ACS EST Water*, 4, 3663–3680. (DOI:10.1021/acsestwater.4c00301)
6. Song Y., Fang S., Xu N., Zhu J. (2025), Solar-Driven Interfacial Evaporation Technologies for Food, Energy and Water, *Nat. Rev. Clean Technol.*, 1, 55–74. (DOI: 10.1038/s44359-024-00009-x)
7. Bezza F. A., Iwarere S. A., Brink H. G., Chirwa E. M. N. (2024), Design and Fabrication of Porous Three-dimensional Ag-Doped Reduced Graphene Oxide (3D Ag@rGO)

- Composite for Interfacial Solar Desalination, *Sci. Rep.*, *14*, 13793. (DOI: 10.1038/s41598-024-62987-z)
8. Meng F., Zhang Y., Zhang S., Ju B., Tang B. (2022), Rational Design of Biomass-Derived Composite Aerogels for Solar-Driven Seawater Desalination and Sewage Treatment, *Ind. Eng. Chem. Res.*, *61*, 9763–9773. (DOI: 10.1021/acs.iecr.2c01576)
 9. Kumar P., Abbas Z., Kumar P., Das D., Shaikh M. M. (2024), Highlights in Interface of Wastewater Treatment by Utilizing Metal Organic Frameworks: Purification and Adsorption Kinetics, *Langmuir*, *40*, 5040–5059. (DOI: 10.1021/acs.langmuir.3c03724)
 10. Camargos C. H. M., Yang L., Jackson J. C., Tanganini I. C., Francisco K. R., Ceccato-Antonini S. R., Rezende C. A., Faria A. F. (2025), Lignin and Nanolignin: Next-Generation Sustainable Materials for Water Treatment, *ACS Appl. Bio Mater.*, *8*, 2632–2673. (DOI: 10.1021/acsabm.4c01563)
 11. Prüss-Ustün A., Bartram J., Clasen T., Colford Jr J. M., Cumming O., Curtis V., Bonjour S., Dangour A. D., De France J., Fewtrell L., Freeman M. C., Gordon B., Hunter P. R., Johnston R. B., Mathers, C., Mäusezahl D., Medlicott K., Neira M., Stocks M., Wolf J., Cairncross, S. (2014), Burden of disease from inadequate water, sanitation and hygiene in low- and middle-income settings: a retrospective analysis of data from 145 countries, *Trop. Med. Intern. Health*, *19*, 894–905. (DOI: 10.1111/tmi.12329)
 12. UN World Water Development Report (2024). UN-Water. <https://www.unwater.org/publications/un-world-water-development-report-2024> (accessed 2025-06-17).
 13. Mohammadi S., Sandoval-Pauker C., Dorado Z. N., Senftle T. P., Pankow R., Sharifan H. (2025), Fluorescent Sodium Alginate Hydrogel–Carbon Dots Sensor for Detecting Perfluorooctanoic Acid in Potable Water, *Anal. Chem.*, *97*, 10075–10084. (DOI: 10.1021/acs.analchem.5c01991)

14. Dhiman N., Tripathi V. K., Dwivedi J., Gupta R. K., Tripathi K. M. (2024), Photoactive Graphene Aerogel from Biomass for the Visible-Light-Induced Degradation of Pharmaceutical Residues, *ACS Sustainable Resour. Manage.*, *1*, 1068–1075. (DOI: 10.1021/acssusresmgt.3c00088)
15. Uebele S., Goetz T., Ulbricht M., Schiestel T. (2022), Mixed-Matrix Membrane Adsorbers for the Simultaneous Removal of Different Pharmaceutical Micropollutants from Water, *ACS Appl. Polym. Mater.*, *4*, 1705–1716. (DOI: 10.1021/acsapm.1c01546)
16. Jiang C., Yan Z., Bai Y., Li R., Wu M., Yu W.-H., Chen H.-M., Hu P., Zhao K.-Q., Niu K., Liu Y., Ho S.-H., Wang W., Wei Y. (2025), Scalable, High-Efficiency Porous Monolithic Polymer Foam for Solar-Driven Interfacial Water Evaporation and Lithium Extraction, *npj Clean Water*, *8*, 47. (DOI: 10.1038/s41545-025-00474-2)
17. Nakahata M., Sumiya A., Ikemoto Y., Nakamura T., Dudin A., Schwieger J., Yamamoto A., Sakai S., Kaufmann S., Tanaka M. (2024), Hyperconfined Bio-Inspired Polymers in Integrative Flow-Through Systems for Highly Selective Removal of Heavy Metal Ions, *Nat. Commun.*, *15*, 5824. (DOI: 10.1038/s41467-024-49869-8)
18. Chen S., Zhang S.-Z., Jiang H. (2024), Modification of Crystal-Optimized TiO₂ with Biomass-Derived Carbon Quantum Dots for Highly Efficient Degradation of Favipiravir in Water, *ACS EST Water*, *4*, 531–542. (DOI: 10.1021/acsestwater.3c00595)
19. Gholami Derami H., Gupta P., Gupta R., Rath P., Morrissey J. J., Singamaneni S. (2020), Palladium Nanoparticle-Decorated Mesoporous Polydopamine/Bacterial Nanocellulose as a Catalytically Active Universal Dye Removal Ultrafiltration Membrane, *ACS Appl. Nano Mater.*, *3*, 5437–5448. (DOI: 10.1021/acsanm.0c00787)

20. Singh N., Goldsmith B. R. (2020), Role of Electrocatalysis in the Remediation of Water Pollutants, *ACS Catal.*, *10*, 3365–3371. (DOI: 10.1021/acscatal.9b04167)
21. M. P. A., Pardhiya S., Rajamani P. (2022), Carbon Dots: An Excellent Fluorescent Probe for Contaminant Sensing and Remediation, *Small*, *18*, 2105579. (DOI:10.1002/sml.202105579)
22. Ma Q., Yu Y., Sindoro M., Fane A. G., Wang R., Zhang H. (2017), Carbon-Based Functional Materials Derived from Waste for Water Remediation and Energy Storage, *Adv. Mater.*, *29*, 1605361. (DOI: 10.1002/adma.201605361)
23. Mauter M. S., Zucker I., Perreault F., Werber J. R., Kim J.-H., Elimelech M. (2018), The Role of Nanotechnology in Tackling Global Water Challenges, *Nat. Sustain.*, *1*, 166–175. (DOI: 10.1038/s41893-018-0046-8)
24. Pokrajac L., Abbas A., Chrzanowski W., Dias G. M., Eggleton B. J., Maguire S., Maine E., Malloy T., Nathwani J., Nazar L., Sips A., Sone J., van den Berg A., Weiss P. S., Mitra S. (2021), Nanotechnology for a Sustainable Future: Addressing Global Challenges with the International Network4Sustainable Nanotechnology, *ACS Nano*, *15*, 18608–18623. (DOI: 10.1021/acsnano.1c10919)
25. Ambika, Singh P. P. (2018), Nanotechnology: Greener Approach for Sustainable Environment, *Nanotechnol. Environ. Sci.*, *25*, 805–824. (DOI: 10.1002/9783527808854.ch25)
26. Yang Z., Xu T., Li H., She M., Chen J., Wang Z., Zhang S., Li J. (2023), Zero-Dimensional Carbon Nanomaterials for Fluorescent Sensing and Imaging, *Chem. Rev.*, *123*, 11047–11136. (DOI: 10.1021/acs.chemrev.3c00186)
27. Dhanapal A. R., Thiruvengadam M., Vairavanathan J., Venkidasamy B., Easwaran M., Ghorbanpour M. (2024), Nanotechnology Approaches for the Remediation of Agricultural Polluted Soils, *ACS Omega*, *9*, 13522–13533. (DOI: 10.1021/acsomega.3c09776)

28. F. Hochella M., G. Spencer M., L. Jones K. (2015), Nanotechnology: Nature's Gift or Scientists' Brainchild, *Environ. Sci.: Nano*, 2, 114–119. (DOI: 10.1039/C4EN00145A)
29. Hochella M. F., Mogk D. W., Ranville J., Allen I. C., Luther G. W., Marr L. C., McGrail B. P., Murayama M., Qafoku N. P., Rosso K. M., Sahai N., Schroeder P. A., Vikesland P., Westerhoff P., Yang Y. (2019), Natural, Incidental, and Engineered Nanomaterials and Their Impacts on the Earth System, *Sci.*, 363, eaau8299. (DOI: 10.1126/science.aau8299)
30. Dhenadhayalan N., Lin K.-C., Saleh T. A. (2020), Recent Advances in Functionalized Carbon Dots toward the Design of Efficient Materials for Sensing and Catalysis Applications, *Small*, 16, 1905767. (DOI: 10.1002/smll.201905767)
31. Sarkar A. N., Padhi S., Kumari S., Jagadevan S., Pal S. (2023), Facile Synthesis of Carbon Dot Deposited γ -FeOOH Nanosheet/Polypyrrole Composite: A Robust Photocatalyst for Degradation of Antibiotics under Sunlight Irradiation with Enhanced Antibacterial Activity, *Ind. Eng. Chem. Res.*, 62, 1227–1244. (DOI: 10.1021/acs.iecr.2c03172)
32. Singh S., Shauloff N., Jelinek R. (2019), Solar-Enabled Water Remediation via Recyclable Carbon Dot/Hydrogel Composites, *ACS Sustainable Chem. Eng.*, 7, 13186–13194. (DOI: 10.1021/acssuschemeng.9b02342)
33. Chen X., Yu M., Li P., Xu C., Zhang S., Wang Y., Xing X. (2023), Recent Progress on Chiral Carbon Dots: Synthetic Strategies and Biomedical Applications, *ACS Biomater. Sci. Eng.*, 9, 5548–5566. (DOI: 10.1021/acsbiomaterials.3c00918)
34. Schwarz H. (1993), The Mechanism of Fullerene Formation, *Angew. Chem. Int. Ed. Engl.*, 32, 1412–1415. (DOI: 10.1002/anie.199314121)
35. Kroto H. W., Heath J. R., O'Brien S. C., Curl R. F., Smalley R. E. (1985), C₆₀: Buckminsterfullerene, *Nat.*, 318, 162–163. (DOI: 10.1038/318162a0)

36. Iijima S. (1991), Helical Microtubules of Graphitic Carbon, *Nat.*, *354*, 56–58. (DOI: 10.1038/354056a0)
37. Novoselov K. S., Geim A. K., Morozov S. V., Jiang D., Zhang Y., Dubonos S. V., Grigorieva I. V., Firsov A. A. (2004), Electric Field Effect in Atomically Thin Carbon Films. *Sci.*, *306*, 666–669. (DOI: 10.1126/science.1102896)
38. Xu X., Ray R., Gu Y., Ploehn H. J., Gearheart L., Raker K., Scrivens W. A. (2004), Electrophoretic Analysis and Purification of Fluorescent Single-Walled Carbon Nanotube Fragments, *J. Am. Chem. Soc.*, *126*, 12736–12737. (DOI: 10.1021/ja040082h)
39. Bian Z., Wallum A., Mehmood A., Gomez E., Wang Z., Pandit S., Nie S., Link S., Levine B. G., Gruebele M. (2023), Properties of Carbon Dots versus Small Molecules from “Bottom-up” Synthesis, *ACS Nano*, *17*, 22788–22799. (DOI: 10.1021/acsnano.3c07486)
40. Indriyati, Ramadhani D. F. S., Permatasari F. A., Munir M. M., Nasir M., Iskandar F. (2024), Flexible Photothermal Membrane Based on PVA/Carbon Dot Hydrogel Films for High-Performance Interfacial Solar Evaporation, *ACS Appl. Polym. Mater.*, *6*, 6726–6736. (DOI: 10.1021/acsapm.4c00996)
41. Sun Y.-P., Zhou B., Lin Y., Wang W., Fernando K. A. S., Pathak P., Meziani M. J., Harruff B. A., Wang X., Wang H., Luo P. G., Yang H., Kose M. E., Chen B., Veca L. M., Xie S.-Y. (2006), Quantum-Sized Carbon Dots for Bright and Colorful Photoluminescence, *J. Am. Chem. Soc.*, *128*, 7756–7757. (DOI: 10.1021/ja062677d)
42. Lamba R., Yukta Y., Mondal J., Kumar R., Pani B., Singh B. (2024), Carbon Dots: Synthesis, Characterizations, and Recent Advancements in Biomedical, Optoelectronics, Sensing, and Catalysis Applications, *ACS Appl. Bio Mater.*, *7*, 2086–2127. (DOI: 10.1021/acsabm.4c00004)

43. Ullal N., Mehta R., Sunil D. (2024), Separation and Purification of Fluorescent Carbon Dots-an Unmet Challenge, *Anal.*, *149*, 1680–1700. (DOI: 10.1039/D3AN02134C)
44. Hu Y., Seivert O., Tang Y., Karahan H. E., Bianco A. (2024), Carbon Dot Synthesis and Purification: Trends, Challenges and Recommendations, *Angew. Chem. Int. Ed.*, *63*, e202412341. (DOI:10.1002/anie.202412341)
45. Jia L.-W., Zhang X. (2023), Versatile Red-Emissive Carbon Dots for Smart Textiles and Fluorescence Sensing, *ACS Appl. Nano Mater.*, *6*, 1379–1385. (DOI: 10.1021/acsanm.2c05012)
46. Saini D., Garg A. K., Dalal C., Anand S. R., Sonkar S. K., Sonker A. K., Westman G. (2022), Visible-Light-Promoted Photocatalytic Applications of Carbon Dots: A Review, *ACS Appl. Nano Mater.*, *5*, 3087–3109. (DOI: 10.1021/acsanm.1c04142)
47. Wang B., Cai H., Waterhouse G. I. N., Qu X., Yang B., Lu, S. (2022), Carbon Dots in Bioimaging, Biosensing and Therapeutics: A Comprehensive Review, *Small Sci.*, *2*, 2200012. (DOI: 10.1002/smssc.202200012)
48. Qi J., Zhang R., Liu X., Liu Y., Zhang Q., Cheng H., Li R., Wang L., Wu X., Li B. (2023), Carbon Dots as Advanced Drug-Delivery Nanoplatforams for Anti-inflammatory, Antibacterial, and Anticancer Applications: A Review, *ACS Appl. Nano Mater.*, *6*, 9071–9084. (DOI: 10.1021/acsanm.3c01207)
49. Chang Q., Guo Z., Shen Z., Li N., Xue C., Zhang H., Hao C., Yang J., Hu, S. (2021), Interaction Promotes the Formation and Photothermal Conversion of Carbon Dots/Polydopamine Composite for Solar-Driven Water Evaporation, *Adv. Mater. Interfaces*, *8*, 2100332. (DOI: 10.1002/admi.202100332)
50. Li X., Yan L., Ding C., Song H., Yang Y., Ma C.-Q. (2023), Carbon Dots in Perovskite Solar Cells: Properties, Applications, and Perspectives, *Energy Fuels*, *37*, 876–901. (DOI: 10.1021/acs.energyfuels.2c03362)

51. Ma G., Cai J., Wang X. (2025), Xylan-Derived Carbon Dots with Tunable Fluorescence for White Light Emitting Diodes, *ACS Sustainable Chem. Eng.*, *13*, 2720–2731. (DOI: 10.1021/acssuschemeng.4c07839)
52. Zhao S., Yan L., Cao M., Huang L., Yang K., Wu S., Lan M., Niu G., Zhang W. (2021), Near-Infrared Light-Triggered Lysosome-Targetable Carbon Dots for Photothermal Therapy of Cancer, *ACS Appl. Mater. Interfaces*, *13*, 53610–53617. (DOI: 10.1021/acsami.1c15926)
53. Morbiato L., Cardo L., Sturabotti E., Gobbo P., Filippini G., Prato M. (2025), Structure Matters: Tailored Graphitization of Carbon Dots Enhances Photocatalytic Performance, *ACS Nano*, *19*, 4887–4900. (DOI: 10.1021/acsnano.4c16538)
54. Zhou Y., Zhang W., Leblanc R. M. (2022), Structure-Property-Activity Relationships in Carbon Dots, *J. Phys. Chem. B*, *126*, 10777–10796. (DOI: 10.1021/acs.jpccb.2c06856)
55. Yu J., Yong X., Tang Z., Yang B., Lu S. (2021), Theoretical Understanding of Structure–Property Relationships in Luminescence of Carbon Dots, *J. Phys. Chem. Lett.*, *12*, 7671–7687. (DOI: 10.1021/acs.jpcclett.1c01856)
56. Yan Y., Gong J., Chen J., Zeng Z., Huang W., Pu K., Liu J., Chen P. (2019), Recent Advances on Graphene Quantum Dots: From Chemistry and Physics to Applications, *Adv. Mater.*, *31*, 1808283. (DOI: 10.1002/adma.201808283)
57. Ghosh S., Oleksiievets N., Enderlein J., Chizhik A. I. (2020), Emission States Variation of Single Graphene Quantum Dots, *J. Phys. Chem. Lett.*, *11*, 7356–7362. (DOI: 10.1021/acs.jpcclett.0c02008)
58. Rasal A. S., Yadav S., Yadav A., Kashale A. A., Manjunatha S. T., Altaee A., Chang J.-Y. (2021), Carbon Quantum Dots for Energy Applications: A Review, *ACS Appl. Nano Mater.*, *4*, 6515–6541. (DOI: 10.1021/acsanm.1c01372)

59. Sousa H. B. A., Prior J. A. V. (2024), The Role of Carbon Quantum Dots in Environmental Protection, *Adv. Mater. Techn.*, 9, 2301073. (DOI: 10.1002/admt.202301073)
60. Xia C., Zhu S., Feng T., Yang M., Yang B. (2019), Evolution and Synthesis of Carbon Dots: From Carbon Dots to Carbonized Polymer Dots, *Adv. Sci.*, 6, 1901316. (DOI: 10.1002/advs.201901316)
61. Yang K., Lv C., Sun H., Lin X., Liu C., Zheng Y., Hou D., Gao H., Yang F. (2025), Fe-Doped 4-Aminophenylacetylene-Derived Red Emissive Polymer Carbon Dots: Synthesis and Anti-Counterfeiting Applications, *ACS Appl. Mater. Interfaces*, 17, 1942–1952. (DOI: 10.1021/acsami.4c17053)
62. Song S.-Y., Liu K.-K., Wei J.-Y., Lou Q., Shang Y., Shan C.-X. (2019), Deep-Ultraviolet Emissive Carbon Nanodots, *Nano Lett.*, 19, 5553–5561. (DOI: 10.1021/acs.nanolett.9b02093)
63. Ravishankar K., Shelly K. M., Narayanan A., Dhamodharan R. (2019), Rapid, Solvent-Free Synthesis of Amorphous, Photoluminescent, Carbon Nanodots from Imidazole and Maleic Anhydride Solids, *ACS Sustainable Chem. Eng.*, 7, 13206–13216. (DOI: 10.1021/acssuschemeng.9b02446)
64. Mate N., Satwani V., Pranav, Shaikh M. M. (2025), Blazing Carbon Dots: Unfolding Its Luminescence Mechanism to Photoinduced Biomedical Applications, *Chem. Asian J.*, 20, e202401098. (DOI: 10.1002/asia.202401098)
65. Alafeef M., Srivastava I., Aditya T., Pan D. (2024), Carbon Dots: From Synthesis to Unraveling the Fluorescence Mechanism, *Small*, 20, 2303937. (DOI: 10.1002/sml.202303937)
66. Đorđević L., Arcudi F., Cacioppo M., Prato M. (2022), A Multifunctional Chemical Toolbox to Engineer Carbon Dots for Biomedical and Energy Applications, *Nat. Nanotechnol.*, 17, 112–130. (DOI: 10.1038/s41565-021-01051-7)

67. Li M., Chen T., Gooding J. J., Liu J. (2019), Review of Carbon and Graphene Quantum Dots for Sensing, *ACS Sens.*, *4*, 1732–1748. (DOI: 10.1021/acssensors.9b00514)
68. Wareing T. C., Gentile P., Phan A. N. (2021), Biomass-Based Carbon Dots: Current Development and Future Perspectives, *ACS Nano*, *15*, 15471–15501. (DOI: 10.1021/acsnano.1c03886)
69. Zhu L., Shen D., Wu C., Gu S. (2020), State-of-the-Art on the Preparation, Modification, and Application of Biomass-Derived Carbon Quantum Dots, *Ind. Eng. Chem. Res.* **2020**, *59* (51), 22017–22039. (DOI: 10.1021/acs.iecr.0c04760)
70. Zhong B., Liu C., Xiong D., Cai J., Li J., Li D., Cao Z., Song B., Deng W., Peng H., Hou H., Zou G., Ji X. (2024), Biomass-Derived Hard Carbon for Sodium-Ion Batteries: Basic Research and Industrial Application, *ACS Nano*, *18*, 16468–16488. (DOI: 10.1021/acsnano.4c03484)
71. Prasannan A., Imae T. (2013), One-Pot Synthesis of Fluorescent Carbon Dots from Orange Waste Peels, *Ind. Eng. Chem. Res.*, *52*, 15673–15678. (DOI: 10.1021/ie402421s)
72. Kundu A., Brar J., Mishra A., Maity B., Basu S. (2025), A Portable Microcontroller-Enabled Spectroscopy Sensor Module for the Fluorometric Detection of Cr(VI) and Ascorbic Acid, Utilizing Banana Peel-Derived Carbon Quantum Dots as Versatile Nanoprobes, *Mater. Adv.*, *6*, 743–755. (DOI: 10.1039/D4MA00925H)
73. Xu Q., Han J., Wang D., Zhuang J., Hu C., Dong H., Li W., Lei B., Liu Y. (2025), Unlocking Photosynthetic Potential: Harnessing Rosa Roxburghii Derived Carbon Dots as Nanofertilizers for Enhanced Plant Growth, *ACS Appl. Bio Mater.*, *8*, 774–783. (DOI: 10.1021/acsaabm.4c01609)
74. Zhang H., Wu S., Xing Z., Wang H.-B. (2021), Turning Waste into Treasure: Chicken Eggshell Membrane Derived Fluorescent Carbon Nanodots for the Rapid and Sensitive

- Detection of Hg^{2+} and Glutathione, *Anal.*, *146*, 7250–7256. (DOI: 10.1039/D1AN01582F)
75. Kang X., Jiang K., Ge S., Wei K., Zhou Y., Xu B. B., Wang K., Zhang X. (2025), Frontier in Advanced Luminescent Biomass Nanocomposites for Surface Anticounterfeiting, *ACS Nano*, *19*, 11547–11575. (DOI: 10.1021/acsnano.4c17883)
 76. Seesuea C., Sansenya S., Thangsunan P., Wechakorn K. (2024), Green Synthesis of Elephant Manure-Derived Carbon Dots and Multifunctional Applications: Metal Sensing, Antioxidant, and Rice Plant Promotion, *Sustainable Mater. Technol.*, *39*, e00786. (DOI: 10.1016/j.susmat.2023.e00786)
 77. Kasprzyk W., Świergosz T., P. Romańczyk P., Feldmann J., K. Stolarczyk J. (2022), The Role of Molecular Fluorophores in the Photoluminescence of Carbon Dots Derived from Citric Acid: Current State-of-the-Art and Future Perspectives, *Nanoscale*, *14*, 14368–14384. (DOI: 10.1039/D2NR03176K)
 78. Li S., Zhang H., Bao Y., Zhang H., Wang J., Liu M., Yan R., Wang Z., Wu X., Jin Y. (2024), Immunoantitumor Activity and Oxygenation Effect Based on Iron–Copper-Doped Folic Acid Carbon Dots, *ACS Appl. Mater. Interfaces*, *16*, 16653–16668. (DOI: 10.1021/acsami.3c18331)]
 79. Wang H., Lu F., Ma C., Ma Y., Zhang M., Wang B., Zhang Y., Liu Y., Huang H., Kang Z. (2021), Carbon Dots with Positive Surface Charge from Tartaric Acid and m -Aminophenol for Selective Killing of Gram-Positive Bacteria, *J. Mater. Chem. B*, *9*, 125–130. (DOI: 10.1039/D0TB02332A)
 80. Wu Q., Wang L., Yan Y., Li S., Yu S., Wang J., Huang L. (2022), Chitosan-Derived Carbon Dots with Room-Temperature Phosphorescence and Energy Storage Enhancement Properties, *ACS Sustainable Chem. Eng.*, *10*, 3027–3036. (DOI: 10.1021/acssuschemeng.1c08299)
 81. Mukherjee B., Pant N., Dolai J., Joshi P., Roy D., Maity A., Jana N. R. (2024), Sugar-Derived Carbon Dots with Variable Fluorescence Blinking Property as a Super-Resolution Imaging

- Probe, *J. Phys. Chem. C*, *128*, 19260–19269. (DOI: 10.1021/acs.jpcc.4c05736)
82. Han Q., Xu W., Deng J., Zhang X., Li J., Peng Z. (2023), Multicolor Carbon Dots for Warm White Light-Emitting Diodes with a High Color Rendering Index of 93.2, *ACS Appl. Nano Mater.*, *6*, 16373–16382. (DOI: 10.1021/acsanm.3c02520)
83. Liu Y., Yang H., Ma C., Luo S., Xu M., Wu Z., Li W., Liu S. (2020), Luminescent Transparent Wood Based on Lignin-Derived Carbon Dots as a Building Material for Dual-Channel, Real-Time, and Visual Detection of Formaldehyde Gas, *ACS Appl. Mater. Interfaces*, *12*, 36628–36638. (DOI: 10.1021/acsami.0c10240)
84. Zheng Y., Ye S., Chang Q., Xue C., Li N., Wang Y., Liu B., Yang J., Hu S. (2024), Tailoring the Optical Properties of Coal Pitch-Derived Carbon Dots by Graphitization Controlling, *Energy Fuels*, *38*, 14475–14482. (DOI: 10.1021/acs.energyfuels.4c02129)
85. Chahal S., Yousefi N., Tufenkji N. (2020), Green Synthesis of High Quantum Yield Carbon Dots from Phenylalanine and Citric Acid: Role of Stoichiometry and Nitrogen Doping, *ACS Sustainable Chem. Eng.*, *8*, 5566–5575. (DOI: 10.1021/acssuschemeng.9b07463)
86. Yuan T., Yuan F., Sui L., Zhang Y., Li Y., Li X., Tan Z., Fan L. (2023), Carbon Quantum Dots with Near-Unity Quantum Yield Bandgap Emission for Electroluminescent Light-Emitting Diodes, *Angew. Chem.*, *135*, e202218568. (DOI: 10.1002/ange.202218568)
87. Cao M., Zhao X., Gong X. (2022), Ionic Liquid-Assisted Fast Synthesis of Carbon Dots with Strong Fluorescence and Their Tunable Multicolor Emission, *Small*, *18*, 2106683. (DOI: 10.1002/sml.202106683)

88. Hu C., Li M., Qiu J., Sun Y.-P. (2019), Design and Fabrication of Carbon Dots for Energy Conversion and Storage, *Chem. Soc. Rev.*, *48*, 2315–2337. (DOI: 10.1039/C8CS00750K)
89. Ren X., Cao L., Liang W., Wang P., Bunker C. E., Yang L., Teisl L. R., Sun Y.-P. (2022), Photoexcited State Properties of Poly(9-Vinylcarbazole)-Functionalized Carbon Dots in Solution versus in Nanocomposite Films: Implications for Solid-State Optoelectronic Devices, *ACS Appl. Nano Mater.*, *5*, 2820–2827. (DOI: 10.1021/acsanm.1c04560)
90. Alaş M. Ö., Genç R. (2021), Solvatochromic Surface-Passivated Carbon Dots for Fluorometric Moisture Sensing in Organic Solvents, *ACS Appl. Nano Mater.*, *4*, 7974–7987. (DOI: 10.1021/acsanm.1c01282)
91. Miao S., Liang K., Zhu J., Yang B., Zhao D., Kong B. (2020), Hetero-Atom-Doped Carbon Dots: Doping Strategies, Properties and Applications, *Nano Today*, *33*, 100879. (DOI: 10.1016/j.nantod.2020.100879)
92. Zhang J., Lu X., Tang D., Wu S., Hou X., Liu J., Wu P. (2018), Phosphorescent Carbon Dots for Highly Efficient Oxygen Photosensitization and as Photo-Oxidative Nanozymes, *ACS Appl. Mater. Interfaces*, *10*, 40808–40814. (DOI: 10.1021/acsami.8b15318)
93. Su R., Shi J., Pu Y., Wang J.-X., Wang D., Chen J.-F. (2020), Synthesis of Ultrasmall and Monodisperse Selenium-Doped Carbon Dots from Amino Acids for Free Radical Scavenging, *Ind. Eng. Chem. Res.*, *59*, 16876–16883. (DOI: 10.1021/acs.iecr.0c03402)
94. Lin W., Wei Y., Feng M., Li C., Zhang B., Kang J., Liu W., Guan S. (2025), Visible-Light Excited Multicolor Room Temperature Phosphorescence of Boron and Nitrogen Co-Doped Carbon Dots, *ACS Appl. Opt. Mater.*, *3*, 712–719. (DOI: 10.1021/acsaom.4c00516)
95. Bhati A., Anand S. R., Saini D., Gunture, Sonkar S. K. (2019), Sunlight-Induced Photoreduction of Cr(VI) to Cr(III) in

- Wastewater by Nitrogen-Phosphorus-Doped Carbon Dots, *npj Clean Water*, 2, 12. (DOI: 10.1038/s41545-019-0036-z)
96. Shen D., Long Y., Wang J., Yu Y., Pi J., Yang L., Zheng H. (2019), Tuning the Fluorescence Performance of Carbon Dots with a Reduction Pathway, *Nanoscale*, 11, 5998–6003. (DOI: 10.1039/C8NR09587F)
 97. Du M., Wang C., Liu X., Ding X., Xiang C. (2024), Morphological Insights into Uncompetitive Fluorescence of Coal-Based Carbon Dots and Strategies for Improvement, *Carbon*, 228, 119396. (DOI: 10.1016/j.carbon.2024.119396)
 98. Wang J., Fu Y., Gu Z., Pan H., Zhou P., Gan Q., Yuan Y., Liu C. (2024), Multifunctional Carbon Dots for Biomedical Applications: Diagnosis, Therapy, and Theranostic, *Small*, 20, 2303773. (DOI: 10.1002/smll.202303773)
 99. Xian, Y., Li K. (2022), Hydrothermal Synthesis of High-Yield Red Fluorescent Carbon Dots with Ultra-Narrow Emission by Controlled O/N Elements, *Adv. Mater.*, 34, 2201031. (DOI: 10.1002/adma.202201031)
 100. Zhu L., Shen D., Liu Q., Luo K. H., Li C. (2022), Mild Acidolysis-Assisted Hydrothermal Carbonization of Lignin for Simultaneous Preparation of Green and Blue Fluorescent Carbon Quantum Dots, *ACS Sustainable Chem. Eng.*, 10, 9888–9898. (DOI: 10.1021/acssuschemeng.2c02223)
 101. De R., Jo K. W., Lee B. H., Some S., Kim K.-T. (2023), Microwave-Assisted Rapid Synthesis of Nitrogen-Enriched Amphibious Carbon Quantum Dots for Sensitive Detection of ROS and Multiple Other Applications, *J. Mater. Chem. B*, 11, 6024–6043. (DOI: 10.1039/D3TB00614J)
 102. Srivastava I., Moitra P., Fayyaz M., Pandit S., Kampert T. L., Fathi P., Alanagh H. R., Dighe K., Alafeef M., Vuong K., Jabeen M., Nie S., Irudayaraj J., Pan, D. (2021), Rational Design of Surface-State Controlled Multicolor Cross-Linked Carbon Dots with Distinct Photoluminescence and Cellular

- Uptake Properties, *ACS Appl. Mater. Interfaces*, *13*, 59747–59760. (DOI: 10.1021/acsami.1c19995)
103. Ge G., Li L., Wang D., Chen M., Zeng Z., Xiong W., Wu X., Guo C. (2021), Carbon Dots: Synthesis, Properties and Biomedical Applications, *J. Mater. Chem. B*, *9*, 6553–6575. (DOI: 10.1039/D1TB01077H)
 104. Liu H., Zhong X., Pan Q., Zhang Y., Deng W., Zou G., Hou H., Ji X. (2024), A Review of Carbon Dots in Synthesis Strategy, *Coord. Chem. Rev.*, *498*, 215468. (DOI: 10.1016/j.ccr.2023.215468)
 105. Li J., Gong X. (2022), The Emerging Development of Multicolor Carbon Dots, *Small*, *18*, 2205099. (DOI: 10.1002/smll.202205099)
 106. Javed N., O’Carroll D. M. (2021), Carbon Dots and Stability of Their Optical Properties, *Part. Part. Syst. Charact.*, *38*, 2000271. (DOI: 10.1002/ppsc.202000271)
 107. Rahmawati I., Indriyati, Permatasari F. A., Irham M. A., Nugraha M. I., Anthopoulos T. D., Iskandar F. (2023), Modulating Photothermal Properties of Carbon Dots through Nitrogen Incorporation Enables Efficient Solar Water Evaporation, *ACS Appl. Nano Mater.*, *6*, 2517–2526. (DOI: 10.1021/acsanm.2c04893)
 108. Soni N., Singh S., Sharma S., Batra G., Kaushik K., Rao C., Verma N. C., Mondal B., Yadav A., Nandi C. K. (2021), Absorption and Emission of Light in Red Emissive Carbon Nanodots, *Chem. Sci.*, *12*, 3615–3626. (DOI: 10.1039/D0SC05879C)
 109. Li Liu M., Bin Chen B., Mei Li C., Zhi Huang C. (2019), Carbon Dots: Synthesis, Formation Mechanism, Fluorescence Origin and Sensing Applications, *Green Chem.*, *21*, 449–471. (DOI: 10.1039/C8GC02736F)
 110. Im M. J., Kim J. I., Hyeon S.-K., Moon B. J., Bae S. (2023), From Pristine to Heteroatom-Doped Graphene

- Quantum Dots: An Essential Review and Prospects for Future Research, *Small*, *19*, 2304497. (DOI: 10.1002/smll.202304497)
111. Innocenzi P., Stagi L. (2023), Carbon Dots as Oxidant-Antioxidant Nanomaterials, Understanding the Structure-Properties Relationship. A Critical Review, *Nano Today*, *50*, 101837. (DOI: 10.1016/j.nantod.2023.101837)
 112. Kato Y. S., Shimazaki Y., Chuma S., Shiraya K., Nakane Y., Sugi T., Okabe K., Harada Y., Sotoma S. (2025), Fluorescent Thermometers Based on Carbon Quantum Dots with Various Detection Modes for Intracellular Temperature Measurement, *Nano Lett.*, *25*, 5688–5696. (DOI: 10.1021/acs.nanolett.4c06642)
 113. Shin M., Lim J., Park Y., Lee J.-Y., Yoon J., Choi J.-W. (2024), Carbon-Based Nanocomposites for Biomedical Applications, *RSC Adv.*, *14*, 7142–7156. (DOI: 10.1039/D3RA08946K)
 114. Zou W., Gao B., Ok Y. S., Dong, L. (2019), Integrated Adsorption and Photocatalytic Degradation of Volatile Organic Compounds (VOCs) Using Carbon-Based Nanocomposites: A Critical Review, *Chemosphere*, *218*, 845–859. (DOI: 10.1016/j.chemosphere.2018.11.175)
 115. Khoei J. K., Bafqi M. S. S., Saeidiharzand S., Mohammadilooy M., Hezarkhani M., Okan B. S., Koşar A., Sadaghiani A. K. (2023), Upcycled Graphene Integrated Fiber-Based Photothermal Hybrid Nanocomposites for Solar-Driven Interfacial Water Evaporation, *Desalination*, *562*, 116707. (DOI: 10.1016/j.desal.2023.116707)
 116. Kar D. K., V P., Si S., Panigrahi H., Mishra S. (2024), Carbon Dots and Their Polymeric Nanocomposites: Insight into Their Synthesis, Photoluminescence Mechanisms, and Recent Trends in Sensing Applications, *ACS Omega*, *9*, 11050–11080. (DOI: 10.1021/acsomega.3c07612)
 117. Wang Y., Lv T., Yin K., Feng N., Sun X., Zhou J., Li H. (2023), Carbon Dot-Based Hydrogels: Preparations, Properties,

- and Applications, *Small*, *19*, 2207048. (DOI: 10.1002/sml.202207048)
118. Ma S., Ma H., Yang K., Tan Z., Zhao B., Deng J. (2023), Intense Circularly Polarized Fluorescence and Room-Temperature Phosphorescence in Carbon Dots/Chiral Helical Polymer Composite Films, *ACS Nano*, *17*, 6912–6921. (DOI: 10.1021/acsnano.3c00713)
 119. Koç Ö. K., Üzer A., Apak R. (2023), Heteroatom-Doped Carbon Quantum Dots and Polymer Composite as Dual-Mode Nanoprobe for Fluorometric and Colorimetric Determination of Picric Acid, *ACS Appl. Mater. Interfaces*, *15*, 42066–42079. (DOI: 10.1021/acsami.3c07938)
 120. Anand A., Unnikrishnan B., Wei S.-C., Perry Chou C., Zhang L.-Z., Huang C.-C. (2019), Graphene Oxide and Carbon Dots as Broad-Spectrum Antimicrobial Agents-a Minireview, *Nanoscale Horiz.*, *4*, 117–137. (DOI: 10.1039/C8NH00174J)
 121. Ma Y., Pan L., Jiang K., Wang Q., Zhu Z., Tian Y. (2023), Hydrophobic Carbon Dots Modified Porous Thermoplastic Polyurethane for Effective and Durable Oil/Water Separation, *Chem. Eng. J. Adv.*, *16*, 100557. (DOI: 10.1016/j.cej.2023.100557)
 122. Singh V. P., Singh A. K., Ordu M. (2025), Nanointerface Insights in PVDF Films with Low Loading of Nitrogen-Doped Carbon Dots for High Energy Density Storage and Harvesting, *ACS Appl. Electron. Mater.*, *7*, 1080–1094. (DOI: 10.1021/acsaelm.4c01882)
 123. Olorunyomi J. F., White J. F., Gengenbach T. R., Caruso R. A., Doherty C. M. (2022), Fabrication of a Reusable Carbon Dot/Gold Nanoparticle/Metal–Organic Framework Film for Fluorescence Detection of Lead Ions in Water, *ACS Appl. Mater. Interfaces*, *14*, 35755–35768. (DOI: 10.1021/acsami.2c09122)
 124. Sui B., Zhang Y., Huang L., Chen Y., Li D., Li Y., Yang B. (2020), Fluorescent Nanofibrillar Hydrogels of Carbon Dots

- and Cellulose Nanocrystals and Their Biocompatibility, *ACS Sustainable Chem. Eng.*, **8**, 18492–18499. (DOI: 10.1021/acssuschemeng.0c06198)
125. Yang X., Li J., Lu S. (2024), Effects of Amino Compounds and Zeolite Matrix on the Afterglow Performance of Carbon Dots@Zeolite Composites, *Adv. Funct. Mater.*, **34**, 2410233. (DOI: 10.1002/adfm.202410233)
 126. Thakkar H., Bhandary P., Thakore S. (2023), Biogenic Carbon Dot-Embedded Chitosan Hydrogels as a Two-Stage Fluorescence OFF-ON Probe for Sequential and Ratiometric Detection of Fe(III) and Glutathione, *ACS Appl. Nano Mater.*, **6**, 16253–16266. (DOI: 10.1021/acsanm.3c02345)
 127. Liu J., Wang N., Yu Y., Yan Y., Zhang H., Li J., Yu J. (2017), Carbon Dots in Zeolites: A New Class of Thermally Activated Delayed Fluorescence Materials with Ultralong Lifetimes, *Sci. Adv.*, **3**, e1603171. (DOI: 10.1126/sciadv.1603171)
 128. Wang Y., Wang B., Shi H., Zhang C., Tao C., Li J. (2018), Carbon Nanodots in ZIF-8: Synthesis, Tunable Luminescence and Temperature Sensing, *Inorg. Chem. Front.*, **5**, 2739–2745. (DOI: 10.1039/C8QI00637G)
 129. Tian Z., Li D., Ushakova E. V., Maslov V. G., Zhou D., Jing P., Shen D., Qu S., Rogach A. L. (2018), Multilevel Data Encryption Using Thermal-Treatment Controlled Room Temperature Phosphorescence of Carbon Dot/Polyvinylalcohol Composites, *Adv. Sci.*, **5**, 1800795. (DOI: 10.1002/advs.201800795)
 130. Wang J., Tavakoli J., Tang Y. (2019), Bacterial Cellulose Production, Properties and Applications with Different Culture Methods-A Review, *Carbohydr. Polym.*, **219**, 63–76. (DOI: 10.1016/j.carbpol.2019.05.008)
 131. Pepicelli M., Binelli M. R., Studart A. R., Rühls P. A., Fischer P. (2021), Self-Grown Bacterial Cellulose Capsules

- Made through Emulsion Templating, *ACS Biomater. Sci. Eng.*, **7**, 3221–3228. (DOI: 10.1021/acsbiomaterials.1c00399)
132. Liu F., McMaster M., Mekala S., Singer K., Gross R. A. (2018), Grown Ultrathin Bacterial Cellulose Mats for Optical Applications, *Biomacromolecules*, **19**, 4576–4584. (DOI: 10.1021/acs.biomac.8b01269)
 133. Thomas B., Raj M. C., B A. K., H R. M., Joy J., Moores A., Drisko G. L., Sanchez C. (2018), Nanocellulose, a Versatile Green Platform: From Biosources to Materials and Their Applications, *Chem. Rev.*, **118**, 11575–11625. (DOI: 10.1021/acs.chemrev.7b00627)
 134. Jiang Q., Ghim D., Cao S., Tadepalli S., Liu K.-K., Kwon H., Luan J., Min Y., Jun Y.-S., Singamaneni S. (2019), Photothermally Active Reduced Graphene Oxide/Bacterial Nanocellulose Composites as Biofouling-Resistant Ultrafiltration Membranes, *Environ. Sci. Technol.*, **53**, 412–421. (DOI: 10.1021/acs.est.8b02772)
 135. Wang M., Li R., Feng X., Dang C., Dai F., Yin X., He M., Liu D., Qi H. (2020), Cellulose Nanofiber-Reinforced Ionic Conductors for Multifunctional Sensors and Devices, *ACS Appl. Mater. Interfaces*, **12**, 27545–27554. (DOI: 10.1021/acsami.0c04907)
 136. Purwidyantri A., Karina M., Hsu C.-H., Srikandace Y., Prabowo B. A., Lai C.-S. (2020), Facile Bacterial Cellulose Nanofibrillation for the Development of a Plasmonic Paper Sensor. *ACS Biomater. Sci. Eng.*, **6**, 3122–3131. (DOI: 10.1021/acsbiomaterials.9b01890)
 137. Li Q., Gao R., Wang L., Xu M., Yuan Y., Ma L., Wan Z., Yang X. (2020), Nanocomposites of Bacterial Cellulose Nanofibrils and Zein Nanoparticles for Food Packaging, *ACS Appl. Nano Mater.*, **3**, 2899–2910. (DOI: 10.1021/acsanm.0c00159)
 138. Liu W., Du H., Zhang M., Liu K., Liu H., Xie H., Zhang X., Si C. (2020), Bacterial Cellulose-Based Composite

- Scaffolds for Biomedical Applications: A Review, *ACS Sustainable Chem. Eng.*, **8**, 7536–7562. (DOI: 10.1021/acssuschemeng.0c00125)
139. Khurana V., Kisannagar R. R., Domala S. S., Gupta D. (2020), In Situ Polarized Ultrathin PVDF Film-Based Flexible Piezoelectric Nanogenerators, *ACS Appl. Electron. Mater.*, **2**, 3409–3417. (DOI: 10.1021/acsaelm.0c00667)
 140. Singh G., Sharma M., Vaish R. (2021), Flexible Ag@LiNbO₃/PVDF Composite Film for Piezocatalytic Dye/Pharmaceutical Degradation and Bacterial Disinfection, *ACS Appl. Mater. Interfaces*, **13**, 22914–22925. (DOI: 10.1021/acsami.1c01314)
 141. Zhang D., Jiang W., Zhao Y., Dong Y., Feng X., Chen L. (2019), Carbon Dots Rooted PVDF Membrane for Fluorescence Detection of Heavy Metal Ions, *Appl. Surf. Sci.*, **494**, 635–643. (DOI: 10.1016/j.apsusc.2019.07.141)
 142. Wang J., Lin Q., Wang D., Yu H., He W., Jiang W., Liu C., Zhu E., Li H. (2022), Synthesis of PVDF Membrane Loaded with Wrinkled Au NPs for Sensitive Detection of R6G, *Talanta*, **249**, 123676. (DOI: 10.1016/j.talanta.2022.123676)
 143. Roopaa T. S., Narasimha Murthy H. N., Praveen Kumar V. V., Krishna M. (2018), Development and Characterization of PVDF Thin Films for Pressure Sensors, *Mater. Today: Proc.*, **5**, 21082–21090. (DOI: 10.1016/j.matpr.2018.06.503)
 144. Guan J., Song M., Chen L., Shu Y., Jin D., Fan G., Xu Q., Hu X.-Y. (2021), Carbon Quantum Dots Passivated CsPbBr₃ Film with Improved Water Stability and Photocurrent: Preparation, Characterization and Application, *Carbon*, **175**, 93–100. (DOI: 10.1016/j.carbon.2020.12.091)
 145. Hu J., Wu S. (2025), L-Tetramethylammonium-Derived Blue Fluorescent Carbon Dots for Tetracycline Sensing and Memristor Technology, *ACS Appl. Nano Mater.*, **8**, 11166–11172. (DOI: 10.1021/acsanm.5c01911)

146. Wang W., Wu J., Xing Y., Wang Z. (2022), Solvent-Dependent Red Emissive Carbon Dots and Their Applications in Sensing and Solid-State Luminescence, *Sens. Actuators, B*, 360, 131645. (DOI: 10.1016/j.snb.2022.131645)
147. Liu M., Zhang H., Wang C., Su K., Hu K., Liu E., Sun B., Li X., Sun G., Lu L. (2025), Dual Ratiometric Fluorescence Sensors Based on Chiral Carbon Dots for the Sensitive and Specific Detection of Arginine, *Anal. Chem.*, 97, 1941–1948. (DOI: 10.1021/acs.analchem.4c06405)
148. Anwar S., Ding H., Xu M., Hu X., Li Z., Wang J., Liu L., Jiang L., Wang D., Dong C., Yan M., Wang Q., Bi H. (2019), Recent Advances in Synthesis, Optical Properties, and Biomedical Applications of Carbon Dots, *ACS Appl. Bio Mater.*, 2, 2317–2338. (DOI: 10.1021/acsabm.9b00112)
149. Fernando K. A. S., Sahu S., Liu Y., Lewis W. K., Gulianti E. A., Jafariyan A., Wang P., Bunker C. E., Sun Y.-P. (2015), Carbon Quantum Dots and Applications in Photocatalytic Energy Conversion, *ACS Appl. Mater. Interfaces*, 7, 8363–8376. (DOI: 10.1021/acsami.5b00448)
150. Li X., Fu Y., Zhao S., Xiao J., Lan M., Wang B., Zhang K., Song X., Zeng L. (2022), Metal Ions-Doped Carbon Dots: Synthesis, Properties, and Applications, *Chem. Eng. J.*, 430, 133101. (DOI: 10.1016/j.cej.2021.133101)
151. Lu W., Guo Y., Zhang J., Yue Y., Fan L., Li F., Dong C., Shuang S. (2022). A High Catalytic Activity Nanozyme Based on Cobalt-Doped Carbon Dots for Biosensor and Anticancer Cell Effect, *ACS Appl. Mater. Interfaces*, 14, 57206–57214. (DOI: 10.1021/acsami.2c19495)
152. Li H., Su D., Gao H., Yan X., Kong D., Jin R., Liu X., Wang C., Lu G. (2020), Design of Red Emissive Carbon Dots: Robust Performance for Analytical Applications in Pesticide Monitoring, *Anal. Chem.*, 92, 3198–3205. (DOI: 10.1021/acs.analchem.9b04917)

153. Tian J., An M., Zhao X., Wang Y., Hasan M. (2023), Advances in Fluorescent Sensing Carbon Dots: An Account of Food Analysis, *ACS Omega*, 8, 9031–9039. (DOI: 10.1021/acsomega.2c07986)
154. Bavya V., Rajan T. P. D., Suresh K. I. (2025), Design of Fluorescence Enhancing Sensor for Mercury Detection via Bamboo Cellulose-Derived Carbon Dots, *Langmuir*, 41, 1333–1343. (DOI: 10.1021/acs.langmuir.4c03942)
155. Cui J., Zhu X., Liu Y., Liang L., Peng Y., Wu S., Zhao Y. (2022), N-Doped Carbon Dots as Fluorescent “Turn-Off” Nanosensors for Ascorbic Acid and Fe³⁺ Detection, *ACS Appl. Nano Mater.*, 5, 7268–7277. (DOI: 10.1021/acsanm.2c01170)
156. Mahto M. Kr., Samanta D., Shaw M., Shaik M. A. S., Basu R., Mondal I., Bhattacharya A., Pathak A. (2023), Blue-Emissive Nitrogen-Doped Carbon Dots for Picric Acid Detection: Molecular Fluorescence Quenching Mechanism, *ACS Appl. Nano Mater.*, 6, 8059–8070. (DOI: 10.1021/acsanm.3c01523)
157. Dong H., Zheng L., Wang M., Zhao L., Xu K., Zhou Y., Zhang Y., Xu M. (2023), Two-Photon Carbon Quantum Dots for Detection of Chlortetracycline in Foods, *ACS Appl. Nano Mater.*, 6, 19168–19175. (DOI: 10.1021/acsanm.3c03635)
158. Bhunia S., Ghorai N., Burai S., Purkayastha P., Ghosh H. N., Mondal S. (2021), Unraveling the Carrier Dynamics and Photocatalytic Pathway in Carbon Dots and Pollutants of Wastewater System, *J. Phys. Chem. C*, 125, 27252–27259. (DOI: 10.1021/acs.jpcc.1c06135)
159. Shi J., Li J., Li X., Zhang Y., Hu J., Ning Y., Zhou C.-H., Xia Z., Liu C. (2025), Coordination of Mg(II) Enhancing Photoinduced Oxidase-Like Activity of Carbon Dots for Efficient Degradation of Organic Dyes, *Chem. Mater.*, 37, 2290–2301. (DOI: 10.1021/acs.chemmater.5c00037)
160. Li Q., Yang D., Yin Q., Li W., Yang Y. (2022), Graphitic Carbon Nitride Nanosheets Decorated with Cu-Doped Carbon

- Dots for the Detection and Degradation of Phenolic Pollutants, *ACS Appl. Nano Mater.*, **5**, 1925–1934. (DOI: 10.1021/acsanm.1c03551)
161. Dar A. A., Usman M., Zhang W., Zhu Q., Pan B., Sial A., Wang C. (2022), Synergistic Degradation of 2,4,4'-Trihydroxybenzophenone Using Carbon Quantum Dots, Ferrate, and Visible Light Irradiation: Insights into Electron Generation/Consumption Mechanism, *ACS EST Eng.*, **2**, 1942–1952. (DOI: 10.1021/acsestengg.2c00118)
 162. Habibi-Yangjeh A., Pournemati K., Ahmadi Z., Khataee A. (2024), Decoration of Carbon Dots on Oxygen-Vacancy-Enriched S-Scheme TiO₂ Quantum Dots/TiO₂ Oxygen Vacancies Photocatalysts: Impressive Quantum-Dot-Sized Photocatalysts for Remediation of Antibiotics, Bacteria, and Dyes, *Langmuir*, **40**, 8503–8519. (DOI: 10.1021/acs.langmuir.4c00060)
 163. Akbar K., Moretti E., Vomiero A. (2021), Carbon Dots for Photocatalytic Degradation of Aqueous Pollutants: Recent Advancements, *Adv. Opt. Mater.*, **9**, 2100532. (DOI: 10.1002/adom.202100532)
 164. Mukherjee I., Cilamkoti V., Dutta R. K. (2021), Sunlight-Driven Photocatalytic Degradation of Ciprofloxacin by Carbon Dots Embedded in ZnO Nanostructures, *ACS Appl. Nano Mater.*, **4**, 7686–7697. (DOI: 10.1021/acsanm.1c00883)
 165. Wang C., Yang L., Chu K., Xu J., Wang D., Zhao W. (2024), Fluorescent Carbon Dots Synthesized by Waste Wind Turbine Blade for Photocatalytic Degradation, *Luminescence*, **39**, e4608. (DOI: 10.1002/bio.4608)
 166. Li J., Wang Y., Yue Y. (2023), A Transparent, High-Strength, and Recyclable Core–Shell Structured Wood Hydrogel Integrated with Carbon Dots for Photodegradation of Rhodamine B, *ACS Appl. Nano Mater.*, **6**, 2894–2907. (DOI: 10.1021/acsanm.2c05271)

167. Nayak S., Prasad S. R., Mandal D., Das P. (2020), Carbon Dot Cross-Linked Polyvinylpyrrolidone Hybrid Hydrogel for Simultaneous Dye Adsorption, Photodegradation and Bacterial Elimination from Waste Water, *J. Hazard. Mater.*, 392, 122287. (DOI: 10.1016/j.jhazmat.2020.122287)
168. Tao P., Ni G., Song C., Shang W., Wu J., Zhu J., Chen G., Deng T. (2018), Solar-Driven Interfacial Evaporation, *Nat Energy*, 3, 1031–1041. (DOI: 10.1038/s41560-018-0260-7)
169. Chen Z., Wang J., Zhou H., Xie Z., Shao L., Chen A., Wang S.-B., Jiang N. (2023), Janus Nano-Micro Structure-Enabled Coupling of Photothermal Conversion, Heat Localization and Water Supply for High-Efficiency Solar-Driven Interfacial Evaporation, *Adv. Funct. Mater.*, 33, 2303656. (DOI: 10.1002/adfm.202303656)
170. Xu X., Chang Q., Xue C., Li N., Wang H., Yang J., Hu S. (2022), A Carbonized Carbon Dot-Modified Starch Aerogel for Efficient Solar-Powered Water Evaporation, *J. Mater. Chem. A*, 10, 11712–11720. (DOI: 10.1039/D2TA02302D)
171. Wang L., Wang Y., Wang H., Xu G., Döring A., Daoud W. A., Xu J., Rogach A. L., Xi Y., Zi Y. (2020), Carbon Dot-Based Composite Films for Simultaneously Harvesting Raindrop Energy and Boosting Solar Energy Conversion Efficiency in Hybrid Cells, *ACS Nano*, 14, 10359–10369. (DOI: 10.1021/acsnano.0c03986)
172. Hou Q., Xue C., Li N., Wang H., Chang Q., Liu H., Yang J., Hu S. (2019), Self-Assembly Carbon Dots for Powerful Solar Water Evaporation, *Carbon*, 149, 556–563. (DOI: 10.1016/j.carbon.2019.04.083)
173. Gan W., Wang Y., Xiao S., Gao R., Shang Y., Xie Y., Liu J., Li J. (2021), Magnetically Driven 3D Cellulose Film for Improved Energy Efficiency in Solar Evaporation, *ACS Appl. Mater. Interfaces*, 13, 7756–7765. (DOI: 10.1021/acsaami.0c21384)

174. Li Z., Li D., Wei S., Jin X., Zhang Z., Liu L., Ge Y., Li Z. (2024), Chitosan-Derived Carbon Aerogel Modified with Lignin Carbon Quantum Dots for Efficient Solar Evaporation, *Chem. Eng. J.*, 486, 150157. (DOI: 10.1016/j.cej.2024.150157)
175. Ji C., Wang T., Wang Y., Yang H. (2024), Highly Efficient Solar Water Evaporation by Wood through One-Step in-Situ Synthesis of Carbon Dots, *Chem. Eng. J.*, 479, 147680. (DOI: 10.1016/j.cej.2023.147680)
176. Li L., Li D., Qu Y., Zhang R., Qi S., Liu M., Bi H., Jia T., Qu S., Zheng W. (2025), Hierarchical Assembly of Carbon Dots with Full-Solar-Spectrum Absorption for Solar Energy Applications, *Adv. Sci.*, 12, 2417457. (DOI: 10.1002/advs.202417457)



Chapter 2

**Insight into the Modulation of Carbon
Dot Optical Sensing Attributes Through
a Reduction Pathway**

2.1. Introduction

Among the various classes of carbon nanomaterials, carbon dots (CDs) have emerged as one of the most exciting nanomaterials owing to their small size, easy functionalization, and amazing fluorescence (FL) behavior. Carbon-based quantum dots have been established as one of the promising and divulged candidates in fluorescent sensing applications, enabling the replacement of many toxic quantum dots (QDs) and dyes, thanks to their highly tunable luminescent properties, water miscibility, and photostability [1-4]. Since the discovery of QDs, a plethora of luminous quantum dots of semiconductors and carbon families have been showcased in various sensing applications. So far, surface manipulation of CDs by passivation/functionalization and doping is the two prominent approaches to attain desirable surface features required for the anticipated application [5, 6]. It is well documented that doping may introduce additional impurity states for dissipating energy in the form of heat or photons [7, 8]. In this respect, heteroatom doping or co-doping may be adopted to attribute vivid photophysical features to the CDs as desired. For instance, nitrogen (N) doping, i.e., the introduction of an n-type impurity, can enrich the electron density in the skeletal structure [9]. Moreover, boron (B) may serve the role of a p-type impurity. Co-doping of both these atoms, therefore, can fine-tune the optoelectronic features of carbon dots (CDs) such as delaying radiative decay time [10]. Fluorine (F) embellishment, on the other hand, may be an attractive strategy to increase photostability and biocompatibility [11].

On the other hand, introducing functionalities such as epoxide, carboxyl, or amides may in fact act as trapping sites for electrons, preventing them from direct recombination with holes [12, 13]. Many groups have reported reduction as a useful strategy to modify the photoelectron transition channel by introducing electron-rich surface groups [9, 12]. For example, Dongjun et al. [14] reported the reduced form of CD showing an increase in the quantum yield (QY) of CDs upon reduction. Furthermore, the FL performance of reduced CDs was

better than that of the original CDs, demonstrating the applicability of reduced CDs for bioimaging and as a biomarker. Similarly, Pranav et al. [15] reported reduced CDs co-doped with N, B, and F as an effective strategy to achieve enhanced photophysical properties for bioimaging applications. Apparently, reducing CDs without affecting the size of the CD is an effective approach to augment the electron density at the CD surface. Though the earlier work has shed some light on the photophysical properties of reduced CDs but its applicability in the field of environmental sensing is yet to be explored properly.

The above-mentioned approaches to regulating the FL emission features of CDs have direct implications for tracing waterborne pollutants within a heavy metal family. It is well documented that many of the heavy metals, such as Hg^{2+} , As^{3+} , Cd^{2+} , Pb^{2+} , Co^{2+} , and $\text{Cr}^{3+}/\text{Cr}^{6+}$, etc., serve as grounds for fatal health conditions upon long-term exposure above a threshold level [16-20]. For instance, though cobalt (Co) ion is known to be an essential micronutrient, the presence of Co in blood above the permissible level can make it a carcinogen, and cause respiratory, circulatory, neurological, and allergic diseases [21]. The prime sources of Co (II) are industries, sewage, and mining [22], which can directly enter into the aquatic life and ultimately into the human body. While only the high concentration of Co is harmful to the ecosystem, the release of even trace amounts of other heavy metals like Hg (II) into the water bodies can be fatal. Its release into the ecosystem may happen *via* either anthropogenic activities, *viz.*, industrial indiscriminate dumping of industrial effluents, coal production, metal extraction, etc., or natural events like volcanic eruption and erosion of mineral deposits [22]. Mercury (Hg) contamination arises due to its high affinity with diverse biomolecules within the human body. The persistent Hg in nature makes its tracking crucial to avoid a long-term threat [24].

Hitherto, numerous techniques have been utilized to detect/analyze Co^{2+} and/or Hg^{2+} [25]. Out of them, highly sensitive and selective techniques such as inductively coupled plasma-mass spectrometry

(ICP-MS) [26], atomic absorption spectroscopy (AAS), etc., require complex preparation steps, experienced personnel, and installation of sophisticated instrumentation, making them less reliable for rapid and on-site detection of heavy metal pollutants. To find out more feasible substitutes for these sophisticated techniques, enormous research has been devoted to alternative tools such as colorimetric detection [27], resonance scattering assay [28], surface-enhanced Raman scattering (SERS) [29], electrochemical methods [30], etc. Nevertheless, an FL sensor renders much more flexibility in terms of simple instrumentation/operation, fast response, multiple analysis, high sensitivity, and good selectivity with ample scopes to attune CDs as required. Furthermore, a wide range of cheaper sources with green synthesis routes, such as the hydrothermal method, have also been explored to date to make them more reliable in practical applications [31, 32].

Though many attempts have already been made to detect a range of contaminants, including heavy metals, by differently functionalized green CDs, very few works have particularized a detailed investigation of the physicochemical attributes of CDs responsible for their heavy metal sensing behavior. Herein, a deliberate attempt has been made to understand how the reduction could affect the surface functionalities for tuning useful photophysical attributes to be used for the speciation of heavy metal (Co^{2+} and Hg^{2+}) and its dual-sensing at trace level. The CDs required for this study are prepared from banana peel extract, waste biomass heavily dumped after the consumption of edible fruits in household garbage, and the marketplace. Cellulose, hemicellulose, lignin, and pectin, which are the main components of banana peel, could thus be effectively used as a major carbon source for synthesizing CDs with varied surface functionalities [33]. Further, the viability of the said CD systems is tested for real samples. To the best of our knowledge, this work presents the very first report on the modulation of CDs' sensing behavior after reduction.

2.2. Experimental Section

2.2.1. Materials and Reagents

The purchasing of bananas (ripe bananas) was done in a local market. Ethylenediamine (EDA) and Sodium fluoride (NaF) were procured from SRL chemicals. Phenyl boronic acid (PBA) and sodium borohydride (NaBH_4) were procured from Spectrochem. The various metal salts of Co^{2+} , Pb^{2+} , K^+ , Al^{3+} , Ca^{2+} , Cr^{3+} , Na^+ , Zn^{2+} , Sn^{2+} , Hg^{2+} , Zr^{4+} , Ni^{2+} , PO_4^{3-} , Se^{4+} , I^- , S^{2-} , and vitamin B6 (VitB6) and amino acids like L-tyrosine (L-tyr), histidine (His), and nicotinamide (Nico) were procured from SRL, Sigma-Aldrich, and Merck. All the chemicals were utilized without any further purification. All the experiments were performed using deionized water (DI) obtained from a Sartorius Milli-Q system (Germany).

2.2.2. Instrumentation

A Rigaku RINT Smart Lab2500V X-ray diffractometer with $\text{CuK}\alpha$ radiation (1.5406 \AA) was used for performing X-ray diffraction (XRD). Raman spectra were recorded using a Horiba Jobin Yvon micro-Raman spectrometer with a 633 nm excitation laser with minimum power to avoid any laser-induced heating. Transmission electron micrographs (TEM), high-resolution TEM (HR-TEM) images, and SAED (selected area electron diffraction) of BP-CDs and rBP-CDs were captured in an FEI Tecnai 30 G2S-TWIN transmission electron microscope at an accelerating voltage of 300 kV. The SAED pattern was acquired to determine the crystallinity of carbon dots. To know more about the atomic compositions and changes in chemical functionalities of CD samples, survey spectra, and high-resolution spectra were recorded on a Thermo Scientific NEXA Surface analyzer X-ray photoelectron spectrometer (XPS). A model 3000 Hyperion microscope with a Vertex 80 Fourier transform infrared (FTIR) system was used for recording ($4000\text{--}400 \text{ cm}^{-1}$). The UV-visible spectroscopic studies were conducted on a Varian UV-Vis spectrophotometer (Carry 100 Bio). The FL spectra of BP-CDs and rBP-CDs were obtained by using a

Fluoromax-4 spectrofluorometer (HORIBA Jobin Yvon, model FM100) with an excitation and emission slit width of 2 nm. FL lifetime studies were performed using time-correlated single-photon counting (TCSPC) on a HORIBA Jobin Yvon system of model Fluorocube-01-NL.

2.2.3. Synthesis of BP-CDs and rBP-CDs

BP-CDs were synthesized using a simple one-step hydrothermal method. The banana peels were cleaned with tap water and soaked in 500 mL of distilled water for 2 h. The obtained peels were then chopped and ground using a domestic mixer. The obtained thick extract was then diluted with 15 mL of distilled water. To this solution, 5 mL of EDA, NaF (0.8M in 5 mL), and PBA (0.4 M in 5 mL) were added. The obtained mixture was then sonicated for 15 min to get a homogeneous solution. This solution was poured into a Teflon-lined autoclave and reacted hydrothermally at 180°C for 12h. The autoclave was cooled down to room temperature, and the obtained solution was centrifuged at 5000 rpm to remove any solid remains. The rBP-CDs were prepared from BP-CDs by adopting an earlier reported study [14]. Briefly, 0.35 g of NaBH₄ was added to BP-CDs and stirred for 6 h at room temperature to obtain the rBP-CDs. Any unwanted NaBH₄ was removed by heating the solution at 80°C.

2.2.4. QY, Radiative Rate Constant (K_r), and Limit of Detection (LOD) Evaluation

The FL QY (Φ) of BP-CDs and rBP-CDs were calculated by the procedure stated in the manual Guide to Recording FL QY by HORIBA Jobin Yvon IBH Ltd., and also the published procedure [34]. The BP-CDs and rBP-CDs FL QY were calculated by equation 2.1, keeping quinine sulfate (with 0.54 QY) dissolved in 0.1 M H₂SO₄ as a standard.

$$\Phi = \Phi_{st} \times \frac{S_s}{S_{st}} \times \frac{A_s}{A_{st}} \times \frac{n_s^2}{n_{st}^2} \quad (2.1)$$

Here, Φ and Φ_{st} stand for sample and standard QY. S_s and S_{st} are the sample and standard slopes from the plot of the FL integrated intensity versus the absorbance, respectively. A_s and A_{st} are the absorbance of the standard and the sample at (excitation wavelength) λ_{ex} , respectively. n_s and n_{st} are the solvent refractive index of the sample and standard, respectively.

The FL radiative rate constant of the CDs was also computed with the help of the following equation 2.2:

$$K_f = \Phi_f/T_f \quad (2.2)$$

Whereas k_f is the FL radiative rate constant, Φ_f is the QY of CDs, and T_f is the FL lifetime of CDs.

The LOD was calculated by equation 2.3.

$$LOD = 3.3 \times (\sigma/S) \quad (2.3)$$

Where S is the slope of the calibration plot and σ is the error.

2.2.5. Selectivity Studies, Detection of Co^{2+} and Hg^{2+} , and Interference Studies

The selectivity of BP-CDs toward various analytes such as metal ions, amino acids, and VitB6 (10 mM) was determined by adding various metal ions, amino acids, and VitB6 in 2 mL of the BP-CD solution bearing a concentration of 120 mg/mL, which was kept for 5 min in static conditions for equilibration, and same conditions were followed throughout the experiment, and then the FL spectra at λ_{ex} 370 nm were recorded. Then, for the sensitivity study, different concentrations of Co^{2+} solutions were added, and the FL spectra at λ_{ex} 370 nm were recorded by setting the maximum obtained intensity as a control (I_0). Next, the interference study was performed. For that purpose, the other metal ions, amino acids, and Vit B6 were mixed with BP-CDs. Then, in the same system, the Co^{2+} solution was added. Then, the FL spectra were recorded. The concentration of the Co^{2+} solution was kept at 10 mM. The selectivity study of rBP-CD toward different metal ions,

amino acids, and a Vit B6 solution of 10 mM was performed. The FL spectra for rBP-CDs were taken at λ_{ex} 360 nm, and emission spectra were recorded. Further, for the sensitivity study, different concentrations of Hg^{2+} ions and Co^{2+} ions solutions were added to a 2 mL rBP-CDs solution of a 132 mg/mL concentration, followed by FL measurements. The interference study was performed with rBP-CDs containing various metal ions, amino acids, and Vit B6. In this solution, the Hg^{2+} was mixed and, at λ_{ex} 360 nm, the emission spectrum was recorded. The 10 mM Hg^{2+} solution was used for all interference studies. The selectivity and sensitivity experiments were performed three times, and the error bar was calculated. All the experiments were performed under identical conditions unless otherwise mentioned.

2.2.6. Detection of Analytes in Real Samples

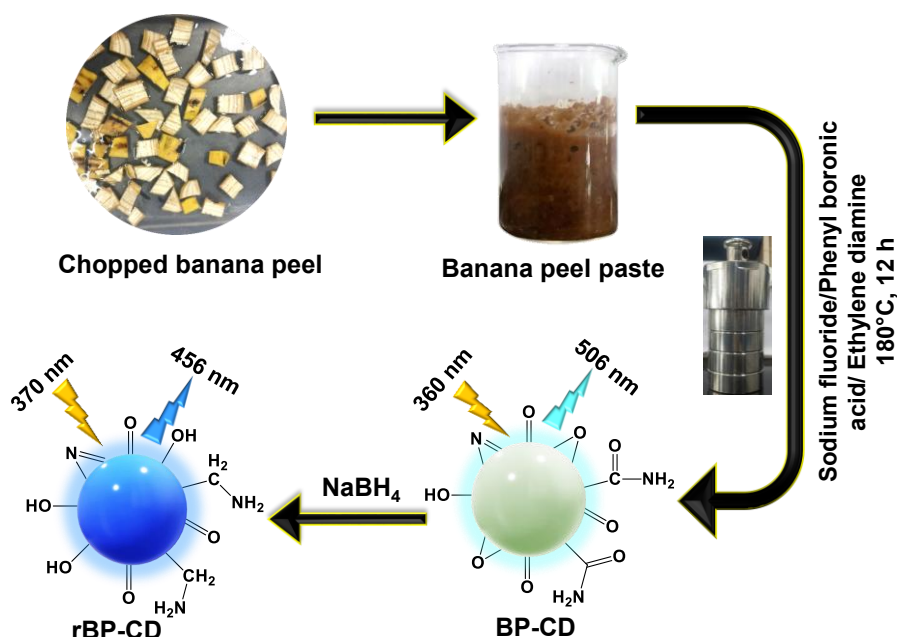
All the samples (the tap water (corporation water, Simrol area, Madhya Pradesh), milk (Amul, India), vegetable juice (spinach, local market, Simrol, Madhya Pradesh), and urine (female, human)) were utilized after pre-treatment. These samples were spiked with different concentrations of metal ions, and sensing in the same conditions was performed by following the procedure stated in the previous section, and recovery was calculated. All the samples were utilized after pre-treatment. The sensors' (BP-CD and rBP-CD) efficiency was studied by spiking the real samples with 20, 40, and 60 μM metal ion concentrations. The BP-CDs were added to prepared real samples spiked with Co^{2+} and rBP-CDs to samples spiked with Co^{2+} and Hg^{2+} . The FL spectra at λ_{ex} of 370 and 360 nm for BP-CD and rBP-CD, respectively, were recorded, and recoveries were calculated.

2.3. Results and Discussion

2.3.1. Synthesis and Characterization of BP-CDs and rBP-CDs

The B, N, and F-doped CDs were hydrothermally synthesized using banana peel as a green precursor and PBA, EDA, and NaF as doping agents for B, N, and F, respectively. The prepared banana peel-derived

carbon dots (BP-CDs) were further reduced at room temperature by using NaBH_4 and termed as rBP-CDs, shown in **Scheme 2.1**, to tune their photophysical properties.



Scheme 2.1. Schematic representation for the synthesis of BP-CD and rBP-CD.

The optical properties of CDs were further altered through tri-elemental doping with B, N, and F. It is reported that the introduction of new trapped states within an energy level could be achieved by N-doping, enabling a high yield of radiative recombination while suppressing non-radiative recombination, which contributes to an improved QY and PL (photoluminescence) [35, 36]. B on the other hand, is integrated into CDs by covalent bonding, modifying the electronic structure and providing more active sites, resulting in CDs with good optical and electrical properties [37]. F, being a highly electronegative element, will strongly attract the adjacent electron. This tends to increase the separation between negative and positive charges, thereby altering the electronic structure and excitation and emission characteristics of CDs [38, 39]. Therefore, heteroatom doping improves the photophysical and electronic properties [40-41]. A detailed study of the variation in photophysical, surface, and morphological properties between BP-CDs and rBP-CDs was done using

spectroscopic and microscopic techniques. Furthermore, the applicability of both CDs was explored towards heavy metal sensing.

For further assessing the surface functionalities upon reduction of original CDs, FTIR spectra were acquired for BP-CDs (**Figure 2.1a**, black spectrum) and rBP-CDs (**Figure 2.1a**, red spectrum). Since the stretching vibration absorption of C=C and C=O is analogous, a small peak at 1636 cm^{-1} in BP-CDs is assigned for C=C/C=O stretching vibrations. However, this peak disappeared in rBP-CD, signifying its effective reduction. The peak at 1048 cm^{-1} corresponds to C-O-C (epoxide ring), present in BP-CDs, and was evidently diminished in rBP-CDs [42]. Apparently, stretching vibrations of O-H at 3440 cm^{-1} and C-H at 2930 cm^{-1} were found largely enhanced in the reduced form. A similar trend was observed in N-H bending vibrations, probably from an amide group, positioned at 1577 cm^{-1} [43, 44]. Both imply the emergence of a large number of surface O-H/N-H functionalities upon reduction [14, 42]. To further support the reduction of BP-CDs, XPS analysis of both BP-CDs and rBP-CDs was performed (**Figure 2.1b**). The major peaks that appeared in the survey spectra from both samples were assigned to specific elemental orbitals according to their binding energies, such as 192.8 eV (B1s), 285.6 eV (C1s), 399.2 eV (N1s), 532.0 eV (O1s), and 688.2 eV (F1s) [45, 46]. It confirmed the doping B, N, and F in the initial BP-CDs sample to an extent of 0.1 %, 1.4 %, and 0.5 %, respectively, calculated from their respective peak areas. It is estimated that the percentage of doping remains roughly the same in rBP-CDs even after reduction. The C1s high-resolution spectra of BP-CD and rBP-CDs (**Figure 2.1c-d**, respectively, supporting information) could be resolved into 3 peaks centering at 284.5 eV (C=C), 285.9 eV (C-O/C-N/C-O-C), and 288.4 eV (C=O). A significant diminishing of peak area at 288.4 hints at the prominent hydrogenation of 'C=O' functionalities upon reduction [7, 47, 48]. Further, the raman spectra of the BP-CD and rBP-CD were acquired (**Figure 2.1e**) to confirm their physicochemical structures. It is evident that both the raman spectra display two broad peaks at approximately 1373 and 1588 cm^{-1} , which

are attributed to the “disorder” D-band (sp^3) and “crystalline” G-band (sp^2), respectively. The I_D/I_G value calculated from integrated intensities of deconvoluted I_D and I_G bands [49, 50] for BP-CD was 0.9, and that of rBP-CD was 1.2. These values signify the introduction of more defects with a partially disordered crystal structure arising from the sp^2 carbon core upon the reduction of BP-CDs. Also, the observed broadness in the region of 1540-1690 cm^{-1} could be attributed to the attachment of other functional groups to the sp^2 carbon atom of BP-CD and rBP-CD [51, 52]. The results obtained from XRD patterns of both CDs have broad peaks at 23.5° and 23.2° for BP-CD and rBP-CD, respectively, as shown in **Figure 2.1f**. The broadness of these peaks might be attributed to the amorphous carbon phase of CDs [53].

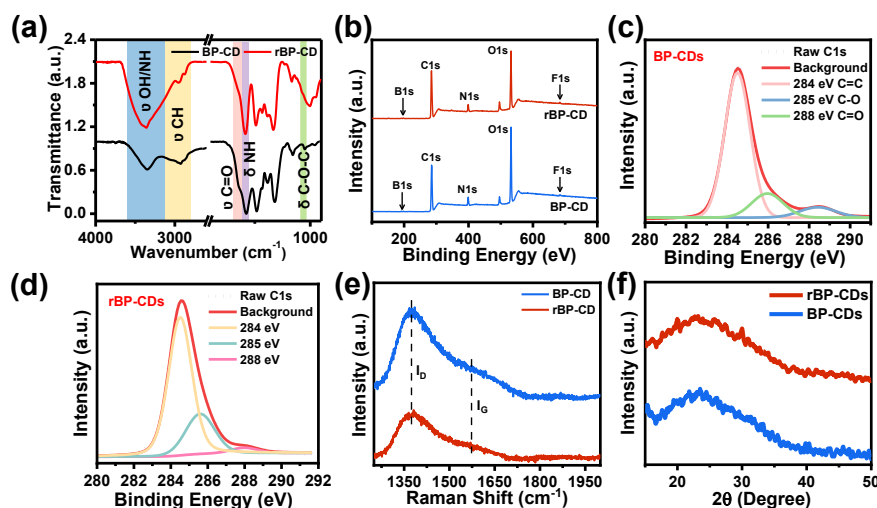


Figure 2.1. (a) FTIR spectra of BP-CD and rBP-CD. XPS survey spectrum of (b) BP-CD (blue line) and rBP-CD (red line), deconvoluted C1s spectra of (c) BP-CDs and (d) rBP-CDs. BP-CDs (blue line) and rBP-CDs (red line): (e) raman spectra, (f) XRD spectra.

Furthermore, the morphology and shapes of CDs were obtained by HR-TEM imaging. The low-resolution TEM image of BP-CDs given in **Figure 2.2a** and its histogram (**Figure 2.2b**) describe the narrow size distribution of spherical BP-CDs with a particle size of 1.8-3.4 nm. The corresponding SAED pattern shows diffused rings as shown in **Figure 2.2c**, suggesting the amorphous nature of CDs. The HR-TEM image of BP-CDs in **Figure 2.2d** reveals the lattice fringes (002) plane with a d-

spacing of 0.33 nm. Similarly, the TEM image of rBP-CDs shown in **Figure 2.2e** indicates the presence of evenly dispersed spherical CDs. The size distribution histogram of rBP-CDs shows a particle size in the range of 2.0-3.8 nm (**Figure 2.2f**). The diffused rings observed in the SAED pattern (**Figure 2.2g**) support the amorphous nature of rBP-CDs. The prominent lattice fringes seen in **Figure 2.2h** correspond to the (002) plane with a d-spacing of 0.34 nm. TEM results indicated no variation in morphology and size after the reduction of BP-CDs to rBP-CDs. This again supports that the change in optical behavior after reduction occurs solely because of the changes in surface functionalities [54].

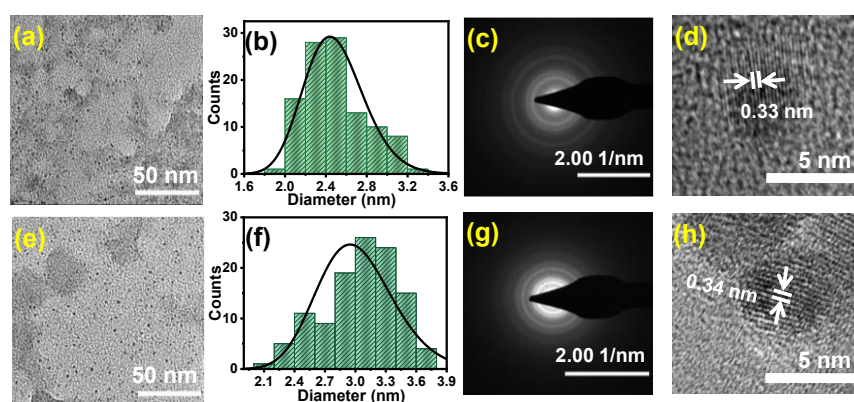


Figure 2.2. (a) TEM image of BP-CDs at low resolution, corresponding (b) histogram showing the size distribution of BP-CDs, (c) SAED pattern, and (d) HR-TEM image showing (002) planes with a d-spacing of 0.33 nm for BP-CD. (e) Low-resolution TEM image of rBP-CDs, corresponding (f) histogram showing the size distribution of rBP-CDs, (g) SAED pattern, and (h) HR-TEM image showing (002) lattices with a d-spacing of 0.34 nm for rBP-CD.

To start with the optical behavior, the absorbance and emission of BP-CDs and rBP-CDs were studied using UV-vis and FL spectrometers (**Figure 2.3**). The BP-CDs showed two absorbance peaks, as shown in **Figure 2.3a**. The main peak obtained at 288 nm can be attributed to the π - π^* transition of sp^2 carbon (C=C), which red-shifted to 290 nm upon reduction, as shown in **Figure 2.3b**. Whereas, a shoulder peak obtained at 370 nm, assigned to the n - π^* transition of C=O, disappears after reduction due to a decrease in the concentration of carbonyl and epoxide [43, 55-

57]. The FL spectra of BP-CDs at various λ_{ex} from 290–390 nm are shown in **Figure 2.3c**. The BP-CDs exhibited excitation-dependent emission behavior with FL intensity increasing initially and then decreasing. Also, the emission peak was red-shifted from λ_{ex} 310–350 nm and came back to a blue shift from 370–390 nm. The BP-CDs showed a maximum emission peak at 506 nm against an λ_{ex} of 370 nm. The FL of CDs is thought to be primarily controlled by surface states [58]. Similarly, the FL spectra of rBP-CDs were recorded at various λ_{ex} (280–400 nm range; **Figure 2.3d**). The rBP-CDs also show excitation-dependent emission behavior, where they show an increase in FL in the beginning, followed by a subsequent reduction. This could be attributed to variable emissive states of CDs as reported earlier [45, 59]. The blue shift of 10 nm in λ_{ex} of BP-CDs was observed after the reduction, with emission at 456 nm when excited at 360 nm. Interestingly, a blue shift in FL maxima along with an increase in FL intensity upon reduction of BP-CDs to rBP-CDs has been observed due to the reduction of carbonyl and epoxide [55]. Obviously, surface states are regarded as the primary determinant of CD FL. Moreover, about a 30 % increase in QY for BP-CDs was also observed upon reduction to rBP-CDs from 10.39 % to 13.28 %, calculated via **Equation 2.1**, respectively. After the reduction with NaBH_4 , more defects were created when the carbonyl and epoxide groups were reduced to hydroxyl groups. The appearance of these defects infers the influx of π electron density, due to which radiative recombination rates increase, which ultimately increases QY and also leads to an enhancement in FL [60, 61]. The FL lifetime of BP-CDs and rBP-CDs was calculated through the TCSPC technique as shown in **Figure 2.3e**. The BP-CDs and rBP-CDs were excited with a 334 nm diode laser, and the emissions were monitored at 506 nm and 456 nm, respectively. The PL decay curves fit well with two exponential decay functions. The change in PL lifetime was observed from 3.48 ns to 3.81 ns for BP-CDs to rBP-CDs. The average lifetimes of BP-CDs and rBP-CDs were approximately the same.

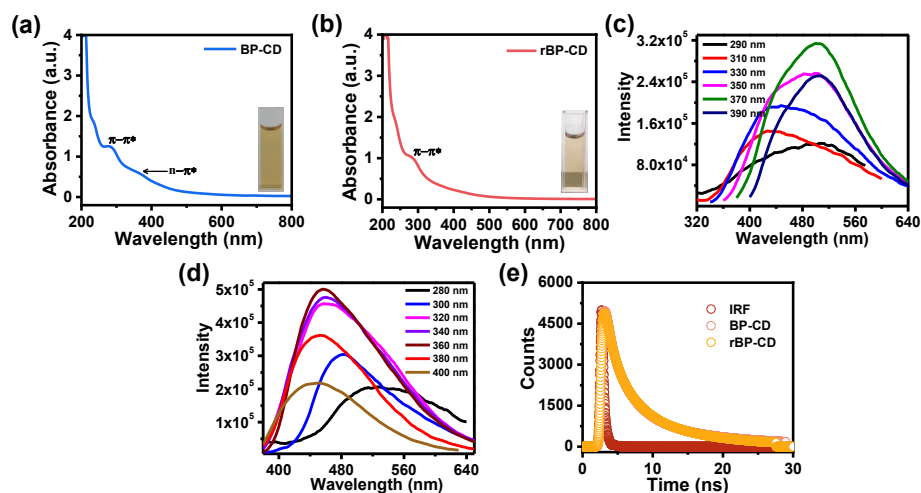


Figure 2.3. Optical characterizations of BP-CD and rBP-CD. UV-vis absorption spectra of (a) BP-CD, and (b) rBP-CD with (insert: digital photographs of the corresponding CDs under visible light). FL emission spectra of (c) BP-CD and (d) rBP-CD with varying excitation wavelengths. FL lifetime plots of (e) BP-CD and rBP-CD.

Further, **Equation 2.2** has been utilized to compute the k_f of CDs. The k_f for BP-CDs and rBP-CDs were found to be 2.9×10^7 and $3.4 \times 10^7 \text{ s}^{-1}$, respectively. As the value of k_f increases, the number of radiative transition centers increases while the number of non-radiative transition centers reduces in rBP-CDs as compared to BP-CDs, which is in accordance with the advanced unified defect model (AUDM) theory's prediction [62, 63]. Notably, the increase in the FL and QY of rBP-CDs indicates that the FL intensity, emission wavelength (λ_{em}), and QY can be favorably tuned simply by the reduction of as-synthesized CDs [64, 65]. The consolidated optical properties of BP-CDs and rBP-CDs have been shown in **Table 2.1** for comparing the changes that occurred in the optical properties of CDs before and after reduction.

Table 2.1. Optical attributes of BP-CDs and rBP-CDs.

Sample	λ_{ex} (nm)	λ_{em} (nm)	Φ (%)	τ_{ave} (ns)
BP-CDs	370	506	10.39	3.48
rBP-CDs	360	456	13.28	3.81

2.3.2. Study of the Fluorescence Stability

Since the fluorescent nature of these CDs has proven applications in the areas of optical sensing, validating the stability of their FL properties under different harsh conditions is crucial. Accordingly, the FL stability of BP-CDs and rBP-CDs was checked under different conditions, and the results are summarized in **Figure 2.4a-c**. The obtained results showed that both BP-CDs and rBP-CDs FL spectra were stable, suggesting their usefulness in sensing applications. Since the main aim of the present work was to check the FL sensing nature of synthesized carbon dots (BP-CDs) and their reduced counterpart (rBP-CDs), the following subsections discuss the sensing attributes of BP-CDs in detail and followed by rBP-CDs. After having excellent photophysical properties of both BP-CDs and rBP-CDs, we were prompted to explore their sensing behavior.

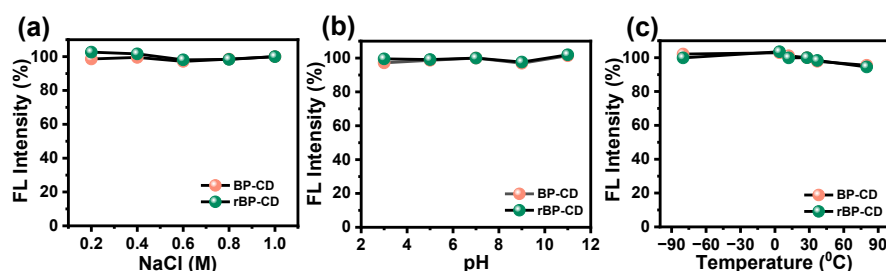


Figure 2.4. Plots showing stability in fluorescent properties of BP-CDs and rBP-CDs under different conditions: (a) at various NaCl concentrations, (b) at different pH, and (c) under various temperatures.

2.3.3. Sensing Studies

The selectivity of BP-CDs and rBP-CDs towards various metal ions such as Co^{2+} , Pb^{2+} , K^+ , Al^{3+} , Ca^{2+} , Cr^{3+} , Na^+ , Zn^{2+} , Sn^{2+} , Hg^{2+} , Zr^{4+} , Ni^{2+} , PO_4^{3-} , Se^{4+} , I^- , S^{2-} , and Vit B6, L-tyr, His and Nico were also checked. As represented in **Figure 2.5a**, Co^{2+} showed the strongest quenching effect on the FL intensity of BP-CDs out of all the metal ions, amino acids, and Vit B6. Whereas, in the case of rBP-CDs, both Hg^{2+} and Co^{2+} showed profound quenching in FL intensity (**Figure 2.5b**). The error bar on

both the bar graphs indicates the uncertainty in the measurement, which is very low as shown in **Figure 2.5a-b**.

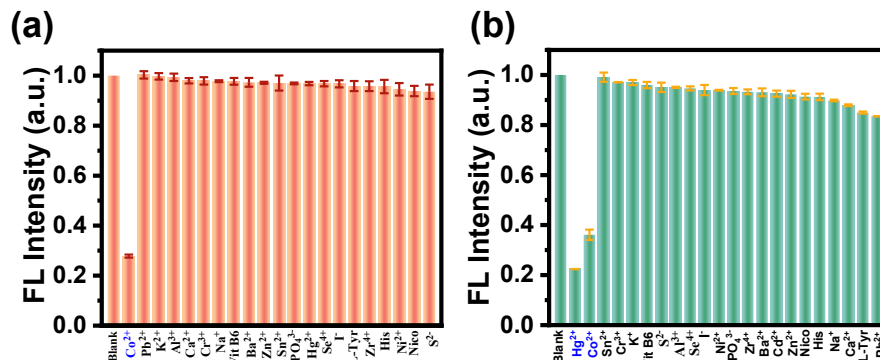


Figure 2.5. Selective sensing response towards various metal ions and amino acids (concentration = 1.0×10^{-2} M): (a) BP-CDs (120 mg/mL), and (b) rBP-CD (132 mg/mL).

As the next step, the fluorescent sensing behavior of different metal ions was explored with the BP-CDs. It showed a sensing response towards Co^{2+} . The sensitivity was monitored through quenching of the FL intensity of BP-CDs for Co^{2+} ions. After the addition of 10 mM of Co^{2+} with a concentration range of 50-1000 μM in an aqueous solution of BP-CDs, a visible decrease in FL intensity was noticed, as shown in **Figure 2.6a**. For the linearity study, F/F_0 was plotted against the concentration of Co^{2+} (50-1000 μM) (**Figure 2.6b**). A good linear correlation is obtained for the 50-250 μM concentration range with a linear correlation coefficient, $R^2 = 0.9986$, with error bars that indicate the precision in measurements. The LODs for all the samples were calculated by using **Equation 2.3**. The LOD for BP-CDs with Co^{2+} ions was calculated as 180 nM. Furthermore, the reduced form of CDs (rBP-CDs) was used to investigate their FL sensing behavior towards several metal ions; among these, rBP-CDs were found to be specific towards sensing of Co^{2+} and Hg^{2+} at different concentrations. The sensitivity was monitored through quenching of the FL intensity of rBP-CDs towards Co^{2+} and Hg^{2+} . The Co^{2+} and Hg^{2+} solutions in the range of 50-1000 μM were added to the rBP-CDs separately and showed a turn-off behavior and decrease in FL intensity of rBP-CDs as shown in **Figure 2.6c and e**, respectively. The superior correlations obtained for Co^{2+} (**Figure 2.6d**, R^2 value of 0.9942 within the 50-250 μM

range) and Hg^{2+} (**Figure 2.6f**, R^2 value of 0.9876 within the 50-200 μM range) with rBP-CDs, with uncertainty in measurements indicated by error bars. The LOD for both Co^{2+} and Hg^{2+} ions was found to be 242 nM and 190 nM, respectively, with rBP-CDs.

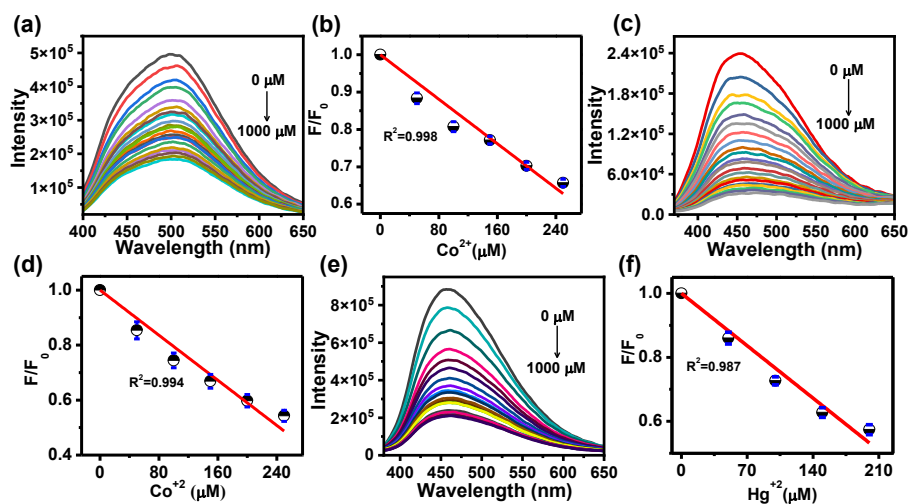


Figure 2.6. (a) FL spectra of BP-CD after the addition of Co^{2+} in a concentration range of 50 μM to 1000 μM , (b) Co^{2+} concentration vs F/F_0 plot for BP-CD. (c) FL spectra of rBP-CD after the addition of Co^{2+} in a concentration range of 50 μM to 1000 μM , (d) relationship between Co^{2+} concentration and F/F_0 of rBP-CD, (e) rBP-CD FL spectra after reacting with Hg^{2+} of various concentrations in the 50 μM to 1000 μM range, (f) linear regression plot between Hg^{2+} concentration and F/F_0 of rBP-CD.

Furthermore, the competitive selectivity of BP-CDs and rBP-CDs was checked by combining them with other anions, cations, amino acids, and Vit B6. Despite the presence of various foreign components, BP-CDs showed upright sensing behavior for Co^{2+} , and rBP-CDs showed a good sensing response towards Co^{2+} and Hg^{2+} (**Figure 2.7a-b**).

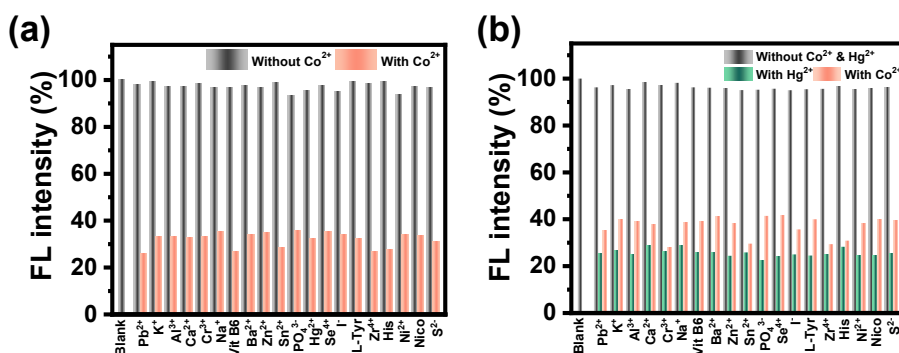


Figure 2.7. Competitive selectivity towards the sensing response of (a) BP-CD, (b) rBP-CD in the presence of various metal ions, and amino acids (concentration = 1.0×10^{-2} M).

The performance of the present CD system was found to be superior in comparison to the other earlier reported FL-based Co^{2+} and Hg^{2+} sensors. Moreover, the simple and environment-friendly synthesis of the current CDs makes them superior as compared to other sensors. (Table 2.2-2.3). Our samples show good detection capability in a broad linear range as well as a better LOD. Their applicability to real sample analysis makes them valuable for practical applications. Therefore, the current work presents a facile preparation route for a multifaceted heavy metal ion sensor with impressive sensitivity.

Table 2.2. State-of-the-art performance comparison of various FL-based Co^{2+} .

Sr. No.	Sensing Element	Linear Range (μM)	LOD (nM)	Real Sample	Ref.
1.	Carbon dots (Carbopol)	0-40	450	Lake water and Tap water	66
2.	Carbon dots (citric acid)	1-90	400	Injection sample	67
3.	Carbon quantum dots (Pyridoxal)	0-60	53	River water	68
4.	Carbon dots (α -cellulose)	1870	16840	No	69
5.	Carbon dots (acrylic acid)	1-60	250	Tap water	70
6.	Carbon dots (Kelp)	1-200	390	River water	71
7.	Polymer dots (Polyvinyl alcohol)	3.4-50	1000	Pond and river water	72
8.	Carbon dots (citric acid)	0-40	1250	Drinking water and Tap water	73
9.	Carbon dots (flax straw)	0-500	380	Tap and River water	20
10.	Mn^{2+} :ZnS QDs/ZIF-8	2-100	270	human serum albumin	74
11.	Salicylal-derived Schiff base L	800-2000	780	Lake and Tap water	75
12.	PEI-MA	0-200	270	-	76
13.	DBA Chemosensor	-	682	Ground, canal, distilled , tap water	77
14.	Carbon dots (Banana peel)	50-250	180	Tap water and Milk	Present Work
15.	Reduced Carbon dots (banana peel)	50-250	242	Tap water and Milk	Present Work

Table 2.3. State-of-the-art performance comparison of various FL-based Hg^{2+} sensors.

Sr. No.	Sensing Element	Linear Range (μM)	LOD (nM)	Real Sample	Ref.
1	Graphene quantum dots (Graphene)	0.79-9.0	99.99	No	78
2	Carbon dots	0-40	2000	Lake water and tap water	79
3	Carbon dots (Adipic acid)	4-18	2470	-	80
4	Carbon dots (Citric acid)	0-80	201	Lake water and urine of cattle	81
5.	Carbon dots (Folic acid)	0-41.86	118	Tap water	82
6.	Graphene quantum dots (Ammonium hydroxide)	2.5-800	2500	Lake water and waste water	83
7.	Carbon dots (China grass carp scales)	0.014-30	14	Lake water and cosmetic samples	84
8.	Carbon dots (Citric acid)	0.2-2.6	160	Biological and environmental system	85
9.	Carbon dots (Citric acid)	5-50	1780	Waste water and river water	86
10.	Carbon dots (Citric acid)	2-14	440	Breast milk	87
11.	Carbon dots (Guava plant leaf)	60-380	82000	No	88
12.	Carbazole benzothiazole sensor	0-1.2	141	-	89
13.	TFPPy-CHYD COF	0.05-4.0	17	-	90
14.	Lanthanide MOF	0-240	220	River water	91
15.	Tetra-phenylethane-based FL sensor	0-1.2	183.4	-	92
16.	Reduced Carbon dots (banana peel)	50-200	190	Tap water and Milk	Present Work

2.3.4. Real-Sample Analysis with BP-CDs and rBP-CDs

Furthermore, regular tap water, milk, vegetable juice, and urine samples were utilized as solvents to assess the reliability of the developed CDs as analytical tools for real-time examination. The above-mentioned samples were tested with the as-prepared BP-CD fluorescent probe, and it was found that the metal ions were initially absent in any of them. All the samples were spiked with 20, 40, and 60 μM concentrations of Co^{2+} metal ions, and the recovery tests with BP-CDs were performed. The recovery here means the amount of metal ion simulated to the amount of metal ion detected by the FL probe. The results are tabulated in **Table 2.4**. With tap water, the recovery of Co^{2+} ions was in the range of 92-99 %. The recovery of milk was found to be in the range of 97-103 %. The recovery rate was 102-103 % for Co^{2+} ions in vegetable juice. With a urine sample, the recovery of Co^{2+} ions was in the range of 103-104 %. The high recovery rate, as

well as the sensor's precision and reliability, demonstrated the sensor's utility in real-world applications.

Table 2.4. Details of real-sample sensing and recovery of Co^{2+} from various natural samples using BP-CD as a probe. The experiments were performed by spiking Co^{2+} in tap water, milk, vegetable juice, and urine samples.

Sample	Claimed Concentration (μM)	Obtained Concentration (μM)	Recovery (%)	SD (n=3)
Tap water	20	20.00	98.34	0.19
	40	39.79	97.72	0.63
	60	58.38	92.74	0.08
Milk	20	20.00	103.15	1.2
	40	39.79	101.35	0.55
	60	59.19	97.10	0.82
Vegetable juice	20	20.00	103.5	1.04
	40	39.70	103.4	1.2
	60	59.59	102.3	1.04
Urine	20	20.00	104	0.62
	40	39.39	104.1	0.88
	60	59.79	103.8	0.83

In addition, to check the reliability of as-developed rBP-CDs as an analytical tool for real-time analysis, a similar fluorescent analysis was performed as discussed in the case of the non-reduced form. For this, normal tap water, milk, vegetable juice, and urine samples were used as solvents. Metal ions were not present initially in any of the solutions, as ensured by analyzing using an as-prepared fluorescent probe. All of the samples were spiked with different concentrations of metal ions (i.e., Co^{2+} and Hg^{2+}), and recovery assays with rBP-CDs were performed (**Table 2.5-2.6**). The recovery of the Co^{2+} ion was 96-97 %, and that of the Hg^{2+} ion was 97-104 % with tap water. The recovery of Co^{2+} and Hg^{2+} ions in milk was found to be in the range of 93-94 % and 98-103 %, respectively. The recovery rate for Co^{2+} ion in vegetable juice was found to be 101-103 %, and for Hg^{2+} it is 99-102 %. The recovery of the Co^{2+} ion from a urine sample was 101-102 %, and that of the Hg^{2+} ion was 101-102 %. Thus, the sensor's utility in

real-world applications was established by its high recovery rate, as well as its precision and reliability.

Table 2.5. Details of real-time sensing and recovery of Co^{2+} from various natural samples using rBP-CD as a probe.

Sample	Claimed Concentration (μM)	Obtained Concentration (μM)	Recovery (%)	SD (n=3)
Tap water	20	20.00	96.15	1.2
	40	38.58	96.89	0.24
	60	59.19	97.35	0.67
Milk	20	20.00	94.80	1.4
	40	39.39	93.53	0.70
	60	59.59	93.65	0.62
Vegetable juice	20	20.00	103.8	0.36
	40	39.79	101.2	1.2
	60	59.59	101.1	1.2
Urine	20	20.00	102.6	0.6
	40	39.79	102.0	1.0
	60	59.19	101.1	1.0

Table 2.6. Details of real-time sensing and recovery of Hg^{2+} from various natural samples using rBP-CD as a probe.

Sample	Claimed Concentration (μM)	Obtained Concentration (μM)	Recovery (%)	SD (n=3)
Tap water	20	20.00	104.1	0.27
	40	39.79	97.94	0.67
	60	58.38	99.83	0.54
Milk	20	20.00	100	1.2
	40	39.79	98.60	1.2
	60	59.19	103.4	0.78
Vegetable juice	20	20.00	101.5	1.04
	40	39.79	99.3	0.66
	60	59.19	99.3	1.1
Urine	20	20.00	102.9	0.56
	40	39.79	102.0	0.56
	60	58.38	101.8	0.57

For comparison, a summary of reduced CDs explored so far for multifarious applications such as tuning of FL property, catalysis, synthesis of nanoparticles, utilization as a drug carrier, and bioimaging agent have been listed in **Table 2.7** which indicates that the reduced

form of CD has been utilized for metal ion sensing for the very first time.

Table 2.7. Comparison of carbon dots and their reduced form for various applications in previous literature reports.

Sr. No.	Sensor	Tuned FL	Catalysis	Synthesizing nanoparticles	Drug Carrier	Bioimaging	Sensing	Reference
1.	CNBF, rCNBF	✓	X	X	X	X	X	15
2.	CDs, rCDs	✓	X	X	X	X	X	62
3.	CDS, rCD1s, rCD2s	✓	X	X	X	X	X	14
4.	GQDs, rGQDs	✓	X	X	X	X	X	54
5.	CD, rCD	✓	X	X	X	X	X	93
6.	GQDs, rGQDs	✓	X	X	X	X	X	64
7.	rCD-AuNCs, rCDs-AgNPs	X	X	✓	X	X	X	48
8.	GQD, rGQD	✓	X	X	X	✓	X	42
9.	r-FCD	X	X	X	✓	✓	X	94
10.	Thermally reduced t-CDs	X	X	X	X	X	✓	55
11.	r-CD	X	X	X	X	X	✓	95
12.	BP-CDs & rBP-CDs	X	X	X	X	X	✓	Present Work

2.3.5. Mechanism of Sensing by BP-CDs and rBP-CD for Co^{2+} and Hg^{2+}

The FL sensing mechanism usually includes static quenching, dynamic quenching, inner filter effect (IFE), and photoinduced electron transfer (PET). The plausible quenching mechanism in the case of BP-CDs and rBP-CDs towards metal ions has been revealed by UV-vis studies and the FL lifetime curve. As the result shown in **Figure 2.8a-c**, the absorption spectrum of Co^{2+} and Hg^{2+} did not overlap with the excitation spectrum of BP-CDs and rBP-CDs, respectively. So, Co^{2+} and Hg^{2+} ions were not able to shield the excitation light for BP-CDs and rBP-CDs, respectively, and also did not absorb the emission light of both CDs. Therefore, the inner filter effect quenching mechanism was not possible in both cases.

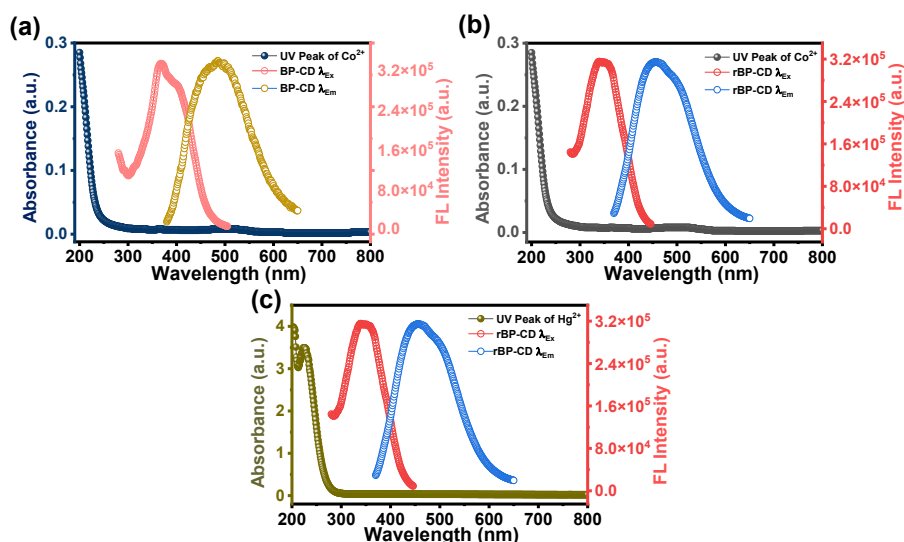


Figure 2.8. (a) Absorption spectra of Co^{2+} overlapped with excitation and emission spectra of BP-CDs. (b) UV-vis spectra of Co^{2+} overlapped with excitation and emission spectra of rBP-CDs. (c) Hg^{2+} absorption spectra overlapped with the excitation and emission spectra of rBP-CDs.

Moreover, the dynamic and PET mechanisms are easily distinguished from the static quenching mechanism by TCSPC curves because the FL lifetime of the fluorophore remains constant in the case of static quenching, but it gets altered in the case of dynamic quenching. So, the FL lifetime decay curves for BP-CDs in the presence and absence of Co^{2+} were recorded to point out the quenching phenomenon and presented in **Figure 2.9a**. The decay curves with and without Co^{2+} remain unaltered in both cases, which elucidates the static quenching with ground state complex formation as the plausible mechanism for Co^{2+} ions sensing by BP-CDs. Further, the corresponding absorbance spectra were acquired to further confirm the sensing mechanism. As shown in **Figure 2.9b**, after the addition of Co^{2+} in BP-CDs, the peak of absorption at 288 nm was shifted to 358 nm, confirming that Co^{2+} changes the electronic structure of BP-CDs by forming a non-fluorescent stable complex between the surface functional groups, such as carbonyl/pyridinyl N of BP-CDs and Co^{2+} . The gradual color change in BP-CDs colloid before and after the addition of Co^{2+} under visible and UV (365 nm) light has been captured and presented in

digital photographs shown in **Figure 2.9c**, which also indicates the quenching of BP-CDs by Co^{2+} . The obtained results confirmed that static quenching is the sole mechanism for Co^{2+} induced FL quenching. **Figure 2.9d** illustrates the schematic of cobalt ion sensing with BP-CDs.

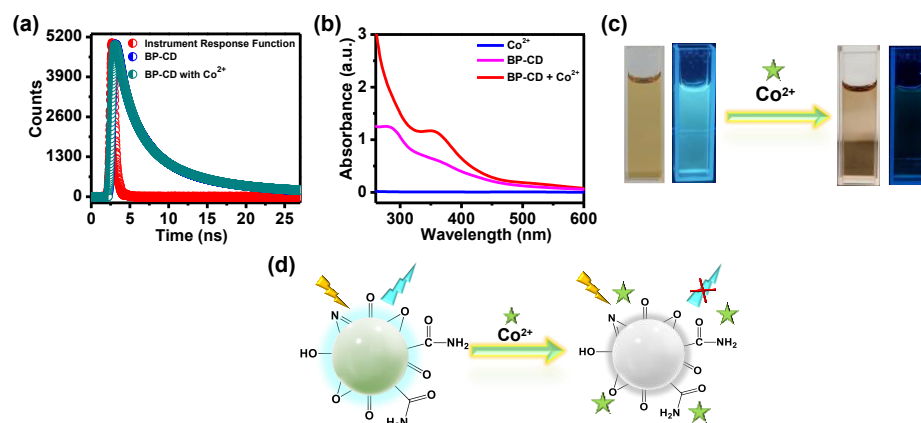


Figure 2.9. Photographs showing changes in: (a) lifetime decay curves acquired for BP-CD in the presence and absence of Co^{2+} , (b) UV-vis spectra of BP-CDs in the presence and absence of Co^{2+} , (c) BP-CD colloid after adding Co^{2+} solution under visible and UV light, (d) scheme showing FL quenching of BP-CDs after addition of Co^{2+} .

The PL lifetime decay curves of rBP-CDs in the presence and absence of Co^{2+} remain almost unchanged, with little to no change in their PL lifetime, evidencing static quenching with ground state complex formation as the feasible mechanism for Co^{2+} ions sensing (**Figure 2.10a**). The UV absorption spectra were obtained to further confirm the static mechanism. The absorbance peak at 290 nm in rBP-CDs was red-shifted to 358 nm upon the addition of Co^{2+} , as shown in **Figure 2.10b**, suggesting the formation of a complex between the surface functional groups, such as carbonyl/pyridinyl N groups of rBP-CDs and Co^{2+} . Besides, the color change in rBP-CDs solution before and after the addition of Co^{2+} under visible and UV (365 nm) light was captured and exhibited in digital images shown in **Figure 2.10c**, indicating the quenching of FL [70, 96-98]. Likewise, with an emphasis on further exploring the mechanism for Hg^{2+} ion sensing by

the rBP-CDs probe, similar studies were carried out. The similar lifetime decay curves of rBP-CDs in the presence and absence of Hg^{2+} , with almost no change in their PL lifetime, further confirm rBP-CDs undergoing ground-state complex formation with static quenching as a possible mechanism (**Figure 2.10d**). Furthermore, the red shift in the absorbance peak of rBP-CDs from 290 nm to 313 nm (**Figure 2.10e**) suggested the formation of a ground-state complex between the amine and hydroxyl surface functional groups of rBP-CDs and Hg^{2+} . The moderate change in color of rBP-CDs is depicted in **Figure 2.10f** in the presence and absence of Hg^{2+} under UV light (365 nm) and visible light, indicating the quenching in FL [99]. Our above findings clearly show that rBP-CDs undergo static quenching with both Co^{2+} and Hg^{2+} , which is further illustrated through the schematic representation in **Figure 2.10g**.

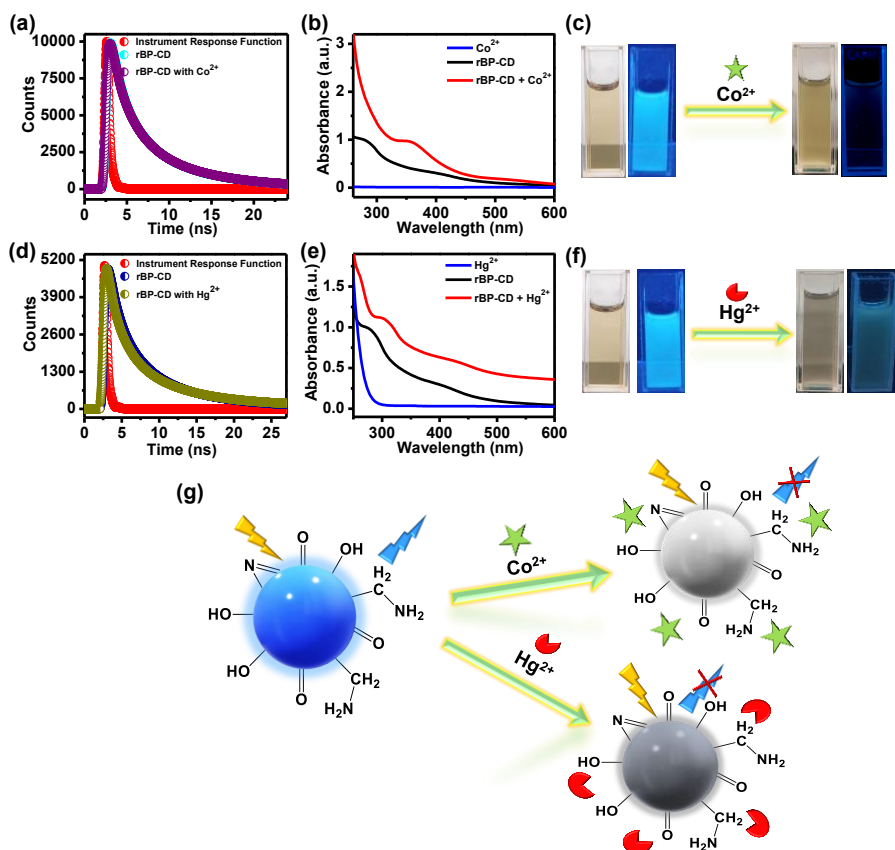


Figure 2.10. Lifetime decay curves were acquired for rBP-CD in the presence and absence of (a) Co^{2+} , and (d) Hg^{2+} . UV-vis absorbance spectra of rBP-CD in the presence and absence of (b) Co^{2+} , and (e)

Hg²⁺. Photographs showing changes in the appearance of (c) rBP-CD colloid after the addition of Co²⁺, and (f) rBP-CD solution after adding Hg²⁺ under visible and UV light, (g) scheme showing FL quenching of rBP-CD after the addition of Co²⁺ and Hg²⁺.

2.4. Conclusions

In conclusion, B, N, and F-doped carbon dots (BP-CDs) were synthesized by using banana peel as an economically viable carbon precursor. A simple reduction with NaBH₄ resulted in reduced BP-CDs (rBP-CD) with an enhanced QY, which tuned their optical properties. Interestingly, rBP-CDs also revealed a similar composition but with different optical features. A visible change in sensing behavior was observed between the original BP-CDs and their reduced form (rBP-CDs). Surprisingly, rBP-CDs showed dual-sensing behavior toward both Co²⁺ (LOD value of 242 nM) and Hg²⁺ (LOD Value of 190 nM), whereas BP-CDs sensed only Co²⁺ (with LOD value of 180 nM). Despite the variation in surface and optical features, both CDs showed consistent QY and excellent stability under diverse harsh conditions such as a range of temperatures, salinities, and pHs. Furthermore, the present CD probes showed excellent detection ability of Hg²⁺ and Co²⁺ in various real samples such as milk, tap water, vegetable juice, and urine. Our results clearly highlight the importance of the above probes in the fabrication of a new and efficient sensor for real sample analysis. To the best of our knowledge, this is the first report in which a comparative study has been attempted toward the sensing application of both as-synthesized carbon dots and their reduced form as fluorescent probes. Our present study paves a new pathway for designing multiple sensors based on a single carbon dot synthesized, through tailoring surface states by the reduction method.

Note: This is copyrighted material with permission of the American Chemical Society.

2.5. References

1. Xu X., Ray R., Gu Y., Ploehn H. J., Gearheart L., Raker K., Scrivens W. A. (2004), Electrophoretic Analysis and Purification of Fluorescent Single-Walled Carbon Nanotube Fragments, *J. Am. Chem. Soc.*, *126*, 12736–12737. (DOI: 10.1021/ja040082h)
2. Han Y., Tang B., Wang L., Bao H., Lu Y., Guan C., Zhang L., Le M., Liu Z., Wu M. (2020), Machine-Learning-Driven Synthesis of Carbon Dots with Enhanced Quantum Yields, *ACS Nano*, *14*, 14761–14768. (DOI: 10.1021/acsnano.0c01899)
3. Wang L., Li M., Li Y., Wu B., Chen H., Wang R., Xu T., Guo H., Li W., Joyner J., Shen X., Le M., Vajtai R., Ajayan P. M., Ren W., Wu M. (2021), Designing a Sustainable Fluorescent Targeting Probe for Super Selective Nucleus Imaging, *Carbon*, *180*, 48–55. (DOI: 10.1016/j.carbon.2021.04.099)
4. Wang L., Li W., Yin L., Liu Y., Guo H., Lai J., Han Y., Li G., Li M., Zhang J., iop. R., Ajayan P. M., Wu M. (2020), Full-Color Fluorescent Carbon Quantum Dots, *Sci. Adv.*, *6*, eabb6772. (DOI: 10.1126/sciadv.abb6772)
5. Miao X., Qu D., Yang D., Nie B., Zhao Y., Fan H., Sun Z. (2018), Synthesis of Carbon Dots with Multiple Color Emission by Controlled Graphitization and Surface Functionalization, *Adv. Mater.*, *30*, 1704740. (DOI: 10.1002/adma.201704740)
6. Guo H., Liu Z., Shen X., Wang L. (2022), One-Pot Synthesis of Orange Emissive Carbon Quantum Dots for All-Type High Color Rendering Index White Light-Emitting Diodes, *ACS Sustainable Chem. Eng.*, *10*, 8289–8296. (DOI: 10.1021/acssuschemeng.2c00715)
7. Li L., Dong T. (2018), Photoluminescence Tuning in Carbon Dots: Surface Passivation or/and Functionalization, Heteroatom Doping, *J. Mater. Chem. C*, *6*, 7944–7970. (DOI: 10.1039/C7TC05878K)
8. Liao J., Cheng Z., Zhou L. (2016), Nitrogen-Doping Enhanced Fluorescent Carbon Dots: Green Synthesis and Their Applications for Bioimaging and Label-Free Detection of Au³⁺ Ions, *ACS*

- Sustainable Chem. Eng.*, **4**, 3053–3061. (DOI: 10.1021/acssuschemeng.6b00018)
9. Xu Y., Wu M., Feng X.-Z., Yin X.-B., He X.-W., Zhang Y.-K. (2013), Reduced Carbon Dots versus Oxidized Carbon Dots: Photo- and Electrochemiluminescence Investigations for Selected Applications, *Chem. Eur. J.*, **19**, 6282–6288. (DOI: 10.1002/chem.201204372)
 10. Miao S., Liang K., Zhu J., Yang B., Zhao D., Kong B. (2020), Hetero-Atom-Doped Carbon Dots: Doping Strategies, Properties and Applications, *Nano Today*, **33**, 100879. (DOI: 10.1016/j.nantod.2020.100879)
 11. Liu L., Anwar S., Ding H., Xu M., Yin Q., Xiao Y., Yang X., Yan M., Bi H. (2019), Electrochemical Sensor Based on F, N-Doped Carbon Dots Decorated Laccase for Detection of Catechol, *J. Electroanal. Chem.*, **840**, 84–92. (DOI: 10.1016/j.jelechem.2019.03.071)
 12. Long L., Wu Q., Chao Q., Dong Y., Wu L., Zhang Q., Zhou Y., Wang D. (2020), Surface-State-Mediated Interfacial Charge Dynamics between Carbon Dots and ZnO toward Highly Promoting Photocatalytic Activity, *J. Chem. Phys.*, **153**, 044708. (DOI: 10.1063/5.0011474)
 13. Shi R., Ye H.-F., Liang F., Wang Z., Li K., Weng Y., Lin Z., Fu W.-F., Che C.-M., Chen Y. (2018), Interstitial P-Doped CdS with Long-Lived Photogenerated Electrons for Photocatalytic Water Splitting without Sacrificial Agents, *Adv. Mater.*, **30**, 1705941. (DOI: 10.1002/adma.201705941)
 14. Shen D., Long Y., Wang J., Yu Y., Pi J., Yang L., Zheng H. (2019), Tuning the Fluorescence Performance of Carbon Dots with a Reduction Pathway, *Nanoscale*, **11**, 5998–6003. (DOI: 10.1039/C8NR09587F)
 15. Tiwari P., Kaur N., Sharma V., Mobin S. M. (2020), A Spectroscopic Investigation of Carbon Dots and Its Reduced State towards Fluorescence Performance, *J. Photochem. Photobiol. A: Chem.*, **403**, 112847. (DOI: 10.1016/j.jphotochem.2020.112847)

16. Yan F., Zou Y., Wang M., Mu X., Yang N., Chen L. (2014), Highly Photoluminescent Carbon Dots-Based Fluorescent Chemosensors for Sensitive and Selective Detection of Mercury Ions and Application of Imaging in Living Cells, *Sens. Actuators, B*, *192*, 488–495. (DOI: 10.1016/j.snb.2013.11.041)
17. Radhakrishnan K., Panneerselvam P. (2018), Green Synthesis of Surface-Passivated Carbon Dots from the Prickly Pear Cactus as a Fluorescent Probe for the Dual Detection of Arsenic (III) and Hypochlorite Ions from Drinking Water, *RSC Adv.*, *8*, 30455–30467. (DOI: 10.1039/C8RA05861J)
18. Pandey S. C., Kumar A., Sahu S. K. (2020), Single Step Green Synthesis of Carbon Dots from *Murraya Koenigii* Leaves; A Unique Turn-off Fluorescent Contrivance for Selective Sensing of Cd(II) Ion, *J. Photochem. Photobiol. A: Chem.*, *400*, 112620. (DOI: 10.1016/j.jphotochem.2020.112620)
19. Gupta A., Verma N. C., Khan S., Tiwari S., Chaudhary A., Nandi C. K. (2016), Paper Strip Based and Live Cell Ultrasensitive Lead Sensor Using Carbon Dots Synthesized from Biological Media, *Sens. Actuators, B*, *232*, 107–114. (DOI: 10.1016/j.snb.2016.03.110)
20. Hu G., Ge L., Li Y., Mukhtar M., Shen B., Yang D., Li J. (2020), Carbon Dots Derived from Flax Straw for Highly Sensitive and Selective Detections of Cobalt, Chromium, and Ascorbic Acid, *J. Colloid Interface Sci.*, *579*, 96–108. (DOI: 10.1016/j.jcis.2020.06.034)
21. Tian M., Liu Y., Wang Y., Zhang Y. (2019), Facile Synthesis of Yellow Fluorescent Carbon Dots for Highly Sensitive Sensing of Cobalt Ions and Biological Imaging, *Anal. Methods*, *11*, 4077–4083. (DOI: 10.1039/C9AY01244C)
22. Sun L., Liu Y., Wang Y., Xu J., Xiong Z., Zhao X., Xia Y. (2021), Nitrogen and Sulfur Co-Doped Carbon Dots as Selective and Visual Sensors for Monitoring Cobalt Ions, *Opt. Mater.*, *112*, 110787. (DOI: 10.1016/j.optmat.2020.110787)
23. Streets D. G., Horowitz H. M., Jacob D. J., Lu Z., Levin L., ter Schure A. F. H., Sunderland E. M. (2017), Total Mercury Released

- to the Environment by Human Activities, *Environ. Sci. Technol.*, **51**, 5969–5977. (DOI: 10.1021/acs.est.7b00451)
24. Tchounwou P. B., Ayensu W. K., Ninashvili N., Sutton D. (2003), Review: Environmental Exposure to Mercury and Its Toxic Pathologic Implications for Public Health, *Environ. Toxicol.*, **18**, 149–175. (DOI: 10.1002/tox.10116)
 25. Tian M., Zhang J., Liu Y., Wang Y., Zhang Y. (2021), One-Pot Synthesis of Nitrogen-Doped Carbon Dots for Highly Sensitive Determination of Cobalt Ions and Biological Imaging, *Spectrochim. Acta, Part A*, **252**, 119541. (DOI: 10.1016/j.saa.2021.119541)
 26. Li L., Yu C., Bai J., Wang Q., Luo Z. (2012), Heavy Metal Characterization of Circulating Fluidized Bed Derived Biomass Ash, *J. Hazard. Mater.*, **233–234**, 41–47. (DOI: 10.1016/j.jhazmat.2012.06.053)
 27. Wang W., Zhao Y., Jin Y. (2013), Gold-Nanorod-Based Colorimetric and Fluorescent Approach for Sensitive and Specific Assay of Disease-Related Gene and Mutation, *ACS Appl. Mater. Interfaces*, **5**, 11741–11746. (DOI: 10.1021/am4034119)
 28. Wu Y., Zhan S., Xu L., Shi W., Xi T., Zhan X., Zhou P. (2011), A Simple and Label-Free Sensor for Mercury(II) Detection in Aqueous Solution by Malachite Green Based on a Resonance Scattering Spectral Assay, *Chem. Commun.*, **47**, 6027–6029. (DOI: 10.1039/C1CC10563A)
 29. Ding X., Kong L., Wang J., Fang F., Li D., Liu J. (2013), Highly Sensitive SERS Detection of Hg²⁺ Ions in Aqueous Media Using Gold Nanoparticles/Graphene Heterojunctions, *ACS Appl. Mater. Interfaces*, **5**, 7072–7078. (DOI: 10.1021/am401373e)
 30. Muralikrishna S., Sureshkumar K., Varley T. S., Nagaraju D. H., Ramakrishnappa, T. (2014), In Situ Reduction and Functionalization of Graphene Oxide with L-Cysteine for Simultaneous Electrochemical Determination of Cadmium(II), Lead(II), Copper(II), and Mercury(II) Ions, *Anal. Methods*, **6**, 8698–8705. (DOI: 10.1039/C4AY01945H)

31. Das S., Kaushik R., Goswami P. (2022), Multifaceted Interaction Studies between Carbon Dots and Proteins of Clinical Importance for Optical Sensing Signals, *ACS Appl. Bio Mater.*, 5, 889–896. (DOI: 10.1021/acsabm.1c01278)
32. Wareing T. C., Gentile P., Phan A. N. (2021), Biomass-Based Carbon Dots: Current Development and Future Perspectives, *ACS Nano*, 15, 15471–15501. (DOI: 10.1021/acsnano.1c03886)
33. Hashem A. H., Saied E., Hasanin M. S. (2020), Green and Ecofriendly Bio-Removal of Methylene Blue Dye from Aqueous Solution Using Biologically Activated Banana Peel Waste, *Sustain. Chem. Pharm.*, 18, 100333. (DOI: 10.1016/j.scp.2020.100333)
34. Kaur N., Tiwari P., Mate N., Sharma V., Mobin S. M. (2022), Photoactivatable Carbon Dots as a Label-Free Fluorescent Probe for Picric Acid Detection and Light-Induced Bacterial Inactivation, *J. Photochem. Photobiol. B*, 229, 112412. (DOI: 10.1016/j.jphotobiol.2022.112412)
35. Guo L., Ge J., Liu W., Niu G., Jia Q., Wang H., Wang, P. (2016), Tunable Multicolor Carbon Dots Prepared from Well-Defined Polythiophene Derivatives and Their Emission Mechanism, *Nanoscale*, 8, 729–734. (DOI: 10.1039/C5NR07153D)
36. Huan Yuan Y., Xi Liu Z., Sheng Li R., Yan Zou H., Lin M., Liu H., Zhi Huang C. (2016), Synthesis of Nitrogen-Doping Carbon Dots with Different Photoluminescence Properties by Controlling the Surface States, *Nanoscale*, 8, 6770–6776. (DOI: 10.1039/C6NR00402D)
37. Bourlinos A. B., Trivizas G., Karakassides M. A., Baikousi M., Kouloumpis A., Gournis D., Bakandritsos A., Hola K., Kozak O., Zboril R., Papagiannouli I., Aloukos P., Couris S. (2015), Green and Simple Route toward Boron Doped Carbon Dots with Significantly Enhanced Non-Linear Optical Properties, *Carbon*, 83, 173–179. (DOI: 10.1016/j.carbon.2014.11.032)
38. Zuo G., Xie A., Li J., Su T., Pan X., Dong W. (2017), Large Emission Red-Shift of Carbon Dots by Fluorine Doping and Their Applications for Red Cell Imaging and Sensitive Intracellular Ag⁺

- Detection, *J. Phys. Chem. C*, *121*, 26558–26565. (DOI: 10.1021/acs.jpcc.7b10179)
39. Yang W., Zhang H., Lai J., Peng X., Hu Y., Gu W., Ye L. (2018), Carbon Dots with Red-Shifted Photoluminescence by Fluorine Doping for Optical Bio-Imaging, *Carbon*, *128*, 78-85. (DOI: 10.1016/j.carbon.2017.11.069)
 40. Xu Q., Kuang T., Liu Y., Cai L., Peng X., Sreeprasad T. S., Zhao P., Yu Z., Li N. (2016), Heteroatom-Doped Carbon Dots: Synthesis, Characterization, Properties, Photoluminescence Mechanism and Biological Applications, *J. Mater. Chem. B*, *4*, 7204–7219. (DOI: 10.1039/C6TB02131J)
 41. Yang G., Wu C., Luo X., Liu X., Gao Y., Wu P., Cai C., Saavedra S. S. (2018), Exploring the Emissive States of Heteroatom-Doped Graphene Quantum Dots, *J. Phys. Chem. C*, *122*, 6483–6492. (DOI: 10.1021/acs.jpcc.8b01385)
 42. Zhu S., Zhang J., Tang S., Qiao C., Wang L., Wang H., Liu X., Li B., Li Y., Yu W., Wang X., Sun H., Yang B. (2012), Surface Chemistry Routes to Modulate the Photoluminescence of Graphene Quantum Dots: From Fluorescence Mechanism to Up-Conversion Bioimaging Applications, *Adv. Funct. Mater.*, *22*, 4732–4740. (DOI: 10.1002/adfm.201201499)
 43. Hu Y., Geng X., Zhang L., Huang Z., Ge J., Li Z. (2017), Nitrogen-Doped Carbon Dots Mediated Fluorescent on-off Assay for Rapid and Highly Sensitive Pyrophosphate and Alkaline Phosphatase Detection, *Sci Rep.*, *7*, 5849. (DOI: 10.1038/s41598-017-06356-z)
 44. Song D., Guo H., Huang K., Zhang H., Chen J., Wang L., Lian C., Wang Y. (2022), Carboxylated Carbon Quantum Dot-Induced Binary Metal–Organic Framework Nanosheet Synthesis to Boost the Electrocatalytic Performance, *Mater. Today*, *54*, 42–51. (DOI: 10.1016/j.mattod.2022.02.011)
 45. Jiang L., Ding H., Lu S., Geng T., Xiao G., Zou B., Bi H. (2020), Photoactivated Fluorescence Enhancement in F, N-Doped Carbon Dots with Piezochromic Behavior, *Angew. Chem.*, *132*, 10072–10077. (DOI: 10.1002/ange.201913800)

46. Xiao N., Liu S. G., Mo S., Li N., Ju Y. J., Ling Y., Li N. B., Luo H. Q. (2018), Highly Selective Detection of P-Nitrophenol Using Fluorescence Assay Based on Boron, Nitrogen Co-Doped Carbon Dots, *Talanta*, *184*, 184–192. (DOI: 10.1016/j.talanta.2018.02.114)
47. Gong X., Zhang Q., Gao Y., Shuang S., Choi M. M. F., Dong C. (2016), Phosphorus and Nitrogen Dual-Doped Hollow Carbon Dot as a Nanocarrier for Doxorubicin Delivery and Biological Imaging, *ACS Appl. Mater. Interfaces*, *8*, 11288–11297. (DOI: 10.1021/acsami.6b01577)
48. Zhuo Y., Zhong D., Miao H., Yang X. (2015), Reduced Carbon Dots Employed for Synthesizing Metal Nanoclusters and Nanoparticles, *RSC Adv.*, *5*, 32669–32674. (DOI: 10.1039/C5RA02598B)
49. Dervishi E., Ji Z., Htoon H., Sykora M., Doorn, S. K. (2019), Raman Spectroscopy of Bottom-up Synthesized Graphene Quantum Dots: Size and Structure Dependence, *Nanoscale*, *11*, 16571–16581. (DOI: 10.1039/C9NR05345J)
50. Vinci J. C., Ferrer I. M., Guterry N. W., Colón V. M., Destino J. F., Bright F. V., Colón L. A. (2015), Spectroscopic Characteristics of Carbon Dots (C-Dots) Derived from Carbon Fibers and Conversion to Sulfur-Bridged C-Dots Nanosheets, *Appl Spectrosc.*, *69*, 1082–1090. (DOI: doi.org/10.1366/14-07749)
51. Stan C. S., Albu C., Coroaba A., Popa M., Sutiman D. (2015), One Step Synthesis of Fluorescent Carbon Dots through Pyrolysis of N-Hydroxy Succinimide, *J. Mater. Chem. C.*, *3*, 789–795. (DOI: 10.1039/C4TC02382J)
52. Gong X., Lu W., Paau M. C., Hu Q., Wu X., Shuang S., Dong C., Choi M. M. F. (2015), Facile Synthesis of Nitrogen-Doped Carbon Dots for Fe³⁺ Sensing and Cellular Imaging, *Anal. Chim. Acta*, *861*, 74–84. (DOI: 10.1016/j.aca.2014.12.045)
53. Mehta V. N., Jha S., Basu H., Singhal R. K., Kailasa S. K. (2015), One-Step Hydrothermal Approach to Fabricate Carbon Dots from Apple Juice for Imaging of Mycobacterium and Fungal Cells, *Sens. Actuators, B*, *213*, 434–443. (DOI: 10.1016/j.snb.2015.02.104)

54. Feng Y., Zhao J., Yan X., Tang F., Xue Q. (2014), Enhancement in the Fluorescence of Graphene Quantum Dots by Hydrazine Hydrate Reduction, *Carbon*, 66, 334–339. (DOI: 10.1016/j.carbon.2013.09.008)
55. Wang J., Wei J., Su S., Qiu J. (2015), Novel Fluorescence Resonance Energy Transfer Optical Sensors for Vitamin B 12 Detection Using Thermally Reduced Carbon Dots, *New J. Chem.*, 39, 501–507. <https://doi.org/10.1039/C4NJ00538D>.
56. Eda G., Lin Y.-Y., Mattevi C., Yamaguchi H., Chen H.-A., Chen I.-S., Chen C.-W., Chhowalla M. (2010), Blue Photoluminescence from Chemically Derived Graphene Oxide, *Adv. Mater.*, 22, 505–509. (DOI: 10.1002/adma.200901996)
57. Soni N., Singh S., Sharma S., Batra G., Kaushik K., Rao C., Verma N. C., Mondal B., Yadav A., Nandi C. K. (2021), Absorption and Emission of Light in Red Emissive Carbon Nanodots, *Chem. Sci.*, 12, 3615–3626. (DOI: 10.1039/D0SC05879C)
58. Liu M., Xu Y., Niu F., Justin Gooding J., Liu J. (2016), Carbon Quantum Dots Directly Generated from Electrochemical Oxidation of Graphite Electrodes in Alkaline Alcohols and the Applications for Specific Ferric Ion Detection and Cell Imaging, *Anal.*, 141, 2657–2664. (DOI: 10.1039/C5AN02231B)
59. Lian Wu Z., Zhang P., Xuan Gao M., Fang Liu C., Wang W., Leng F., Zhi Huang C. (2013), One-Pot Hydrothermal Synthesis of Highly Luminescent Nitrogen -Doped Amphoteric Carbon Dots for Bioimaging from Bombyx Mori Silk-Natural Proteins, *J. Mater. Chem. B.*, 1, 2868–2873. (DOI: 10.1039/C3TB20418A)
60. Dong P., Jiang B.-P., Liang W.-Q., Huang Y., Shi Z., Shen X.-C. (2017), Synthesis of White-Light-Emitting Graphene Quantum Dots via a One-Step Reduction and Their Interfacial Characteristics-Dependent Luminescence Properties, *Inorg. Chem. Front.*, 4, 712–718. (DOI: 10.1039/C6QI00587J)
61. Tian R., Hu S., Wu L., Chang Q., Yang J., Liu J. (2014), Tailoring Surface Groups of Carbon Quantum Dots to Improve

- Photoluminescence Behaviors, *Appl. Surf. Sci.*, *301*, 156–160. (DOI: 10.1016/j.apsusc.2014.02.028)
62. Zheng H., Wang Q., Long Y., Zhang H., Huang X., Zhu R. (2011), Enhancing the Luminescence of Carbon Dots with a Reduction Pathway, *Chem. Commun.*, *47*, 10650–10652. (DOI: 10.1039/C1CC14741B)
 63. Shen R., Song K., Liu H., Li Y., Liu H. (2012), Dramatic Fluorescence Enhancement of Bare Carbon Dots through Facile Reduction Chemistry, *Chem. Phys. Chem.*, *13*, 3549–3555. (DOI: 10.1002/cphc.201200018)
 64. Zhang W., Liu Y., Meng X., Ding T., Xu Y., Xu H., Ren Y., Liu B., Huang J., Yang J., Fang X. (2015), Graphenol Defects Induced Blue Emission Enhancement in Chemically Reduced Graphene Quantum Dots, *Phys. Chem. Chem. Phys.*, *17*, 22361–22366. (DOI: 10.1039/C5CP03434E)
 65. Wang X., Long Y., Wang Q., Zhang H., Huang X., Zhu R., Teng P., Liang L., Zheng H. (2013), Reduced State Carbon Dots as Both Reductant and Stabilizer for the Synthesis of Gold Nanoparticles, *Carbon*, *64*, 499–506. (DOI: 10.1016/j.carbon.2013.07.104)
 66. Kong D., Yan F., Han Z., Xu J., Guo X., Chen L. (2016), Cobalt(II) Ions Detection Using Carbon Dots as a Sensitive and Selective Fluorescent Probe, *RSC Adv.*, *6*, 67481–67487. (DOI: 10.1039/C6RA12986B)
 67. Liu X., Wei S., Diao Q., Ma P., Xu L., Xu S., Sun Y., Song D., Wang X. (2017), Hydrothermal Synthesis of N-Doped Carbon Dots for Selective Fluorescent Sensing and Cellular Imaging of Cobalt(II), *Microchim. Acta*, *184*, 3825–3831. (DOI: 10.1007/s00604-017-2367-0)
 68. Liao S., Zhu F., Zhao X., Yang H., Chen X. (2018), A Reusable P, N-Doped Carbon Quantum Dot Fluorescent Sensor for Cobalt Ion, *Sens. Actuators, B*, *260*, 156–164. (DOI: 10.1016/j.snb.2017.12.206)
 69. Ng Y. H., Chin S. F., Pang S. C., Ng S. M. (2018), Utilising the Interface Interaction on Tris (Hydroxymethyl) Aminomethane-Capped Carbon Dots to Enhance the Sensitivity and Selectivity

- towards the Detection of Co(II) Ions, *Sens. Actuators, B*, 273, 83–92. (DOI: 10.1016/j.snb.2018.05.178)
70. Jing N., Tian M., Wang Y., Zhang Y. (2019), Nitrogen-Doped Carbon Dots Synthesized from Acrylic Acid and Ethylenediamine for Simple and Selective Determination of Cobalt Ions in Aqueous Media, *J. Luminescence*, 206, 169–175. (DOI: 10.1016/j.jlumin.2018.10.059)
71. Zhao C., Li X., Cheng C., Yang Y. (2019), Green and Microwave-Assisted Synthesis of Carbon Dots and Application for Visual Detection of Cobalt(II) Ions and pH Sensing, *Microchem. J.*, 147, 183–190. (DOI: 10.1016/j.microc.2019.03.029)
72. Zhao L., Li H., Liu H., Liu M., Huang N., He Z., Li Y., Chen Y., Ding L. (2019), Microwave-Assisted Facile Synthesis of Polymer Dots as a Fluorescent Probe for Detection of Cobalt(II) and Manganese(II), *Anal Bioanal Chem.*, 411, 2373–2381. (DOI: 10.1007/s00216-019-01678-5)
73. Boonta W., Talodthaisong C., Sattayaporn S., Chaicham C., Chaicham A., Sahasithiwat S., Kangkaew L., Kulchat S. (2020), The Synthesis of Nitrogen and Sulfur Co-Doped Graphene Quantum Dots for Fluorescence Detection of Cobalt(II) Ions in Water, *Mater. Chem. Front.*, 4, 507–516. (DOI: 10.1039/C9QM00587K)
74. Fu X., Li H., Lv R., Hong D., Yang B., Gu W., Liu X. (2018), Synthesis of Mn²⁺ Doped ZnS Quantum Dots/ZIF-8 Composite and Its Applications as a Fluorescent Probe for Sensing Co²⁺ and Dichromate, *J. Solid State Chem.*, 264, 35–41. (DOI: 10.1016/j.jssc.2018.04.021)
75. Zhang J., Liu Y., Fei Q., Shan H., Chen F., Liu Q., Chai G., Feng G., Huan Y. (2017), A Salicylal-Derived Schiff Base as Co(II) Selective Fluorescent Probe, *Sens. Actuators, B*, 239, 203–210. (DOI: 10.1016/j.snb.2016.07.178)
76. Yang J., Chen W., Ma Y., Bright G., Jie X., Zhao H., Zhou H., Jin X. (2022), Tailored Polyethyleneimine-Based Fluorescent Nanoparticles for Functionalized Applications in Detection and

- Adsorption of Cobalt(II), *Dyes Pigm.*, *202*, 110271. (DOI: 10.1016/j.dyepig.2022.110271)
77. Bhalla P., Goel A., Tomer N., Malhotra R. (2022), Multi Responsive Chemosensor for the Determination of Metal Ions (Co^{2+} , Cu^{2+} , and Zn^{2+} Ions), *Inorg. Chem. Commun.*, *136*, 109181. (DOI: 10.1016/j.inoche.2021.109181)
 78. Wang B., Zhuo S., Chen L., Zhang Y. (2014), Fluorescent Graphene Quantum Dot Nanoprobes for the Sensitive and Selective Detection of Mercury Ions, *Spectrochim. Acta, Part A*, *131*, 384–387. (DOI: 10.1016/j.saa.2014.04.129)
 79. Li L., Yu B., You T. (2015), Nitrogen and Sulfur Co-Doped Carbon Dots for Highly Selective and Sensitive Detection of Hg (II) Ions, *Biosens. Bioelectron.*, *74*, 263–269. (DOI: 10.1016/j.bios.2015.06.050)
 80. Yan F., Kong D., Luo Y., Ye Q., He J., Guo X., Chen L. (2016), Carbon Dots Serve as an Effective Probe for the Quantitative Determination and for Intracellular Imaging of Mercury(II), *Microchim. Acta*, *183*, 1611–1618. (DOI: 10.1007/s00604-016-1788-5)
 81. He J., Zhang H., Zou J., Liu Y., Zhuang J., Xiao Y., Lei B. (2016), Carbon Dots-Based Fluorescent Probe for “off-on” Sensing of Hg(II) and I^- , *Biosens. Bioelectron.*, *79*, 531–535. (DOI: 10.1016/j.bios.2015.12.084)
 82. Meng A., Xu Q., Zhao K., Li Z., Liang J., Li Q. (2018), A Highly Selective and Sensitive “on-off-on” Fluorescent Probe for Detecting Hg(II) Based on Au/N-Doped Carbon Quantum Dots, *Sens. Actuators, B*, *255*, 657–665. (DOI: 10.1016/j.snb.2017.08.028)
 83. Liu Y., Tang X., Deng M., Cao Y., Li Y., Zheng H., Li F., Yan F., Lan T., Shi L., Gao L., Huang L., Zhu T., Lin H., Bai Y., Qu D., Huang X., Qiu F. (2019), Nitrogen Doped Graphene Quantum Dots as a Fluorescent Probe for Mercury(II) Ions, *Microchim. Acta*, *186*, 140. (DOI: 10.1007/s00604-019-3249-4)
 84. Liu G., Jia H., Li N., Li X., Yu Z., Wang J., Song Y. (2019), High-Fluorescent Carbon Dots (CDs) Originated from China Grass Carp

- Scales (CGCS) for Effective Detection of Hg(II) Ions, *Microchem. J.*, *145*, 718–728. (DOI: 10.1016/j.microc.2018.11.044)
85. Yang P., Su J., Guo R., Yao F., Yuan C. (2019), B, N-Co-Doped Graphene Quantum Dots as Fluorescence Sensor for Detection of Hg^{2+} and F^- Ions, *Anal. Methods*, *11*, 1879–1883. (DOI: 10.1039/C9AY00249A)
 86. Pajewska-Szmyt M., Buszewski B., Gadzała-Kopciuch R. (2020), Sulphur and Nitrogen Doped Carbon Dots Synthesis by Microwave Assisted Method as Quantitative Analytical Nano-Tool for Mercury Ion Sensing, *Mater. Chem. Phys.*, *242*, 122484. (DOI: 10.1016/j.matchemphys.2019.122484)
 87. Pajewska-Szmyt M., Buszewski B., Gadzała-Kopciuch R. (2020), Carbon Dots as Rapid Assays for Detection of Mercury(II) Ions Based on Turn-off Mode and Breast Milk, *Spectrochim. Acta, Part A*, *236*, 118320. (DOI: 10.1016/j.saa.2020.118320)
 88. Khose R. V., Chakraborty G., Bondarde M. P., Wadekar P. H., Ray A. K., Some, S. (2021), Red-Fluorescent Graphene Quantum Dots from Guava Leaf as a Turn-off Probe for Sensing Aqueous Hg(II), *New J. Chem.*, *45*, 4617–4625. (DOI: 10.1039/D0NJ06259F)
 89. Christopher Leslee D. B., Karuppannan S., Kothottil M. M. (2021), Carbazole-Hydrazinobenzothiazole a Selective Turn-on Fluorescent Sensor for Hg^{2+} ions- Its Protein Binding and Electrochemical Application Studies, *J. Photochem. Photobiol., A*, *415*, 113303. (DOI: 10.1016/j.jphotochem.2021.113303)
 90. Cui W.-R., Jiang W., Zhang C.-R., Liang R.-P., Liu J., Qiu J.-D. (2020), Regenerable Carbohydrazide-Linked Fluorescent Covalent Organic Frameworks for Ultrasensitive Detection and Removal of Mercury, *ACS Sustainable Chem. Eng.*, *8*, 445–451. (DOI: 10.1021/acssuschemeng.9b05725)
 91. Wang H., Wang X., Liang M., Chen G., Kong R.-M., Xia L., Qu F. (2020), A Boric Acid-Functionalized Lanthanide Metal–Organic Framework as a Fluorescence “Turn-on” Probe for Selective Monitoring of Hg^{2+} and CH_3Hg^+ , *Anal. Chem.*, *92*, 3366–3372. (DOI: 10.1021/acs.analchem.9b05410)

92. Jagadhane K. S., Bhosale S. R., Gunjal D. B., Nille O. S., Kolekar G. B., Kolekar S. S., Dongale T. D., Anbhule P. V. (2022), Tetraphenylethene-Based Fluorescent Chemosensor with Mechanochromic and Aggregation-Induced Emission (AIE) Properties for the Selective and Sensitive Detection of Hg^{2+} and Ag^+ Ions in Aqueous Media: Application to Environmental Analysis, *ACS Omega*, 7, 34888–34900. (DOI: 10.1021/acsomega.2c03437)
93. Teng P., Xie J., Long Y., Huang X., Zhu R., Wang X., Liang L., Huang Y., Zheng H. (2014), Chemiluminescence Behavior of the Carbon Dots and the Reduced State Carbon Dots, *J. Luminescence*, 146, 464–469. (DOI: 10.1016/j.jlumin.2013.09.036)
94. Rai S., Singh B. K., Bhartiya P., Singh A., Kumar H., Dutta P. K., Mehrotra G. K. (2017), Lignin Derived Reduced Fluorescence Carbon Dots with Theranostic Approaches: Nano-Drug-Carrier and Bioimaging, *J. Luminescence*, 190, 492–503. (DOI: 10.1016/j.jlumin.2017.06.008)
95. Long Y., Wang X., Shen D., Zheng H. (2016), Detection of Glucose Based on the Peroxidase-like Activity of Reduced State Carbon Dots, *Talanta*, 159, 122–126. (DOI: 10.1016/j.talanta.2016.06.012)
96. Zhao X., Wang L., Liu Q., Chen M., Chen X. (2021), Facile Synthesis of B, N-Doped CQDs as Versatile Fluorescence Probes for Sensitive Detection of Cobalt Ions in Environmental Water and Biological Samples, *Microchem. J.*, 163, 105888. (DOI: 10.1016/j.microc.2020.105888)
97. Zu F., Yan F., Bai Z., Xu J., Wang Y., Huang Y., Zhou X. (2017), The Quenching of the Fluorescence of Carbon Dots: A Review on Mechanisms and Applications, *Microchim. Acta*, 184, 1899–1914. (DOI: 10.1007/s00604-017-2318-9)
98. Huang S., Wang L., Huang C., Xie J., Su W., Sheng J., Xiao Q. (2015), A Carbon Dots Based Fluorescent Probe for Selective and Sensitive Detection of Hemoglobin, *Sens. Actuators, B*, 221, 1215–1222. (DOI: 10.1016/j.snb.2015.07.099)

99. Tang M., Ren G., Zhu B., Yu L., Liu X., Chai F., Wu H., Wang C. (2019), Facile Synthesis of Orange Emissive Carbon Dots and Their Application for Mercury Ion Detection and Fast Fingerprint Development, *Anal. Methods*, *11*, 2072–2081. (DOI: 10.1039/C9AY00178F)



Chapter 3

**Portable and Non-Invasive Fluorescent
Thin Films from Photocatalytically
Active Carbon Dots for Selective and
Trace-Level Detection of Picric Acid**

3.1. Introduction

Making detection and remediation of environmental pollutants smart and versatile has strong implications in the modern era. In the past decade, carbon dots (CDs) have proven to be efficient fluorescent (FL) sensors due to their exceptional and stable luminescent properties with minimal photobleaching and excellent biocompatibility [1-3]. The abundance of various precursor molecules and simple synthetic routes with ease of surface modification make CDs quite versatile and highly useful in myriad applications, such as sensing [4], bio-imaging [5], drug delivery [6], energy storage [7], photodynamic therapy [8], photocatalysis [9], etc. Recent studies show that the CD structure could be better controlled by the wise selection of carbon precursor. Unlike top-down approaches, a logical manipulation of the CD structure is possible in a bottom-up approach [10]. It has been established that structural features of precursor fragments are retained to various extents in the partial carbonization step of CD formation as per the specific synthetic parameters employed [11]. Though the mechanism behind the structural formation is yet to be fully understood, a large number of oxygen-nitrogen containing groups or polymerizable functionalities like -OH, -NH₂, -COOH, -C=O, -C=C-, etc., in the precursor units facilitate the polymerization-carbonization process under hydrothermal conditions [12]. From this point of view, several biomass-based precursors, viz., lignocellulose [13], pectin [14], vitamins [15], amino acids [16], tannins [17], alkaloids [18], etc., that are rich in polyols, amines, heteroaromatics, and/or carbonyl groups, have been exploited as the major carbon source, a green approach, as well as cost cost-effective way to achieve desirable end optoelectronic attributes such as luminescence to the intended CD [19, 20].

The photophysical properties of CDs not only make them a good candidate for the detection of a wide range of pollutants but also enable the removal of several wastewater contaminants through photocatalytic degradation pathways [21, 22]. The exponential increase of harmful contaminants such as explosives and organic dyes in water bodies

requires stern actions for their trace-level detection, quantification, and/or removal for a clean and sustainable ecosystem. Picric acid (PA), a key member of the nitroaromatic compounds (NAC) family, is extensively utilized in the production of matches, glass, rocket fuel, dyes, and pharmaceuticals [23]. It is known for its high explosive power with low safety value and high detonation velocity, and is considered a significant groundwater contaminant being a potent irritant and allergen [24]. PA is discharged into the water ecosystem either directly or indirectly, leading to several diseases like liver dysfunction, cyanosis, anemia, and other chronic disorders, as well as skin and eye irritation in exposed mammals, including humans [25]. Therefore, effective monitoring and trace-level detection of PA is important for social and environmental safety [26]. Till now, many fluorescent systems have been employed for detecting NAC. The most successful demonstrations of the FL detection of PA were focused mainly on graphene quantum dots (QDs) [27], semiconductor QDs [28], perovskite QDs [29], fluorescent polymers [30], metal-organic frameworks [31, 32], chemosensors [33, 34], supramolecular assembly [35], etc. Very few reports are available with CD as FL probe for detecting PA, that too in the solution phase [36, 37]. Also, plentiful reports available for detecting a wide range of other pollutants (e.g., metal ions, pharmaceuticals, and dyes) were mostly carried out in aqueous medium [37, 38]. This made the process simple but limits the recyclability/reusability of CDs as a practical sensor since CDs tend to agglomerate in aqueous medium upon the addition of foreign analytes due to electrostatic interactions among them [39].

Parallel efforts have been invested to fabricate flexible CD composites to confront the above-mentioned issues [40-42]. An effective way is to integrate sensor material with a stable polymer matrix without compromising the FL properties of the luminescent probe. This helps to make the sensor portable and reusable, bestowing fast and sensitive on-site detection of pollutants [43-45]. Many polymeric platforms have been reported to form a film-based fluorescent platform for

detecting potential pollutants by incorporating various PL sensing probes. However, most of the FL polymeric sensor strips or films reported so far [46-48] lack the combined merits of a simple fabrication procedure, a high limit of detection (LOD) with good selectivity, portability, less toxicity, less photo bleachability, and multicycle detection ability. Cross-linking with starch [49], physical incorporation with PVA [50], TLC plate [51], or SiO₂-based nano mesh scaffold technology [52], etc, are some strategies for integrating FL active sensing probe with a film platform. In this respect, polyvinylidene fluoride (PVDF) can be considered a potential candidate for thin film formation due to its high thermal stability and chemical resistance, mechanical strength, flexibility, environmentally friendly nature, and low cost [53, 54]. Its inherent hydrophobicity and excellent binding property ensure high mechanical robustness in an aqueous system, preventing the gradual leaching of hydrophilic FL active components from the composite film.

Herein, we have utilized fluorescent CDs derived from the *Cascabela thevetia* (*C. thevetia*) flower (as a green multicomponent carbon source that adds desired functionalities to the final CD structure) and N, S, and P doping agents for the fabrication of luminescent, photocatalytically active N, S, P-doped CDs (TF-CD). A highly porous, thin, flexible, and reusable TF-CD@PVDF strip is then fabricated by a simple phase-inversion method, enabling easy and selective sensing of PA without compromising much sensitivity (with a LOD of 244 nM). Furthermore, the photocatalytic efficacy of TF-CDs towards environmental remediation using the photocatalytic degradation of methyl orange (MO) was also explored. TF-CDs showed fast degradation kinetics for MO under sunlight with a removal efficiency of 96.8% within ~60 min. Real sample analysis was also carried out for both sensing and degradation to validate the versatility of the as-prepared TF-CDs in real-world applications.

3.2. Experimental Section

3.2.1. Materials and Reagents

The flowers of *C. thevetia* were plucked from the Simrol area (Indian Institute of Technology Indore campus, Madhya Pradesh, India); methyl orange (MO), L-cysteine, 3-nitroaniline (3-NA), 4-iodoaniline (4-IA), and the sodium salt of ethylenediaminetetraacetic acid (Na₂-EDTA) were purchased from Sigma Aldrich. Phosphoric acid (H₃PO₄) and 2,4-dinitrotoluene (2,4-DNT) were procured from Himedia. Polyvinylidene fluoride (PVDF), aniline, 2-nitrophenol (2-NP), and tert-butyl alcohol (t-BuOH) were provided by Thermo Fisher Scientific, Finar, S D Fine Chem Limited, and SRL chemicals, respectively. 4-Nitrotoluene (4-NT) and p-benzoquinone (BZQ) were purchased from Lobachem. N-methyl-2-pyrrolidone (NMP) was purchased from Rankem Chemicals. PA and nitrobenzene (NB) were purchased from Merck. The studies were carried out using deionized water (DI) acquired from the Sartorius Milli-Q system (Germany), without further treatment.

3.2.2. Instrumentation

The UV-vis spectroscopic studies were recorded using a Shimadzu UV-1900 spectrophotometer. All fluorescence (FL) data were taken on a Fluoromax-4 spectrofluorometer (HORIBA Jobin Yvon, model FM100) with an excitation and emission slit width of 2 nm in a quartz cell (1×1 cm). All decay studies were performed using time-correlated single-photon counting (TCSPC) on a HORIBA Jobin Yvon system of model Fluorocube01-NL. For obtaining FTIR spectra (4000-400 cm⁻¹), an attenuated total reflectance-Fourier transform infrared spectroscopy (ATR-FTIR) Bruker Alpha II system was used. The powder X-ray diffraction (PXRD) pattern was obtained from a Rigaku Smart Lab X-ray diffractometer with a Cu K α radiation source (1.5406 Å). Transmission electron micrographs (TEM), high-resolution TEM (HR-TEM) images for morphological characterization, and SAED (selected area electron diffraction) patterns of samples were obtained to know about the morphology and crystallinity of CDs using an FEI Tecnai 30

G2S-TWIN transmission electron microscope at an accelerating voltage of 300 kV. To know more about the atomic compositions and changes in chemical functionalities of CD samples, survey spectra and HR spectra were recorded using an X-ray photoelectron spectrophotometer (XPS) using PHI 5000 Versa Probe II (ULVAC-PHI Inc., USA) equipped with a micro-focused (200 μ m, 15 kV), monochromatic Al K α X-ray source ($h\nu = 1486.6$ eV). Morphological data of the films were recorded using a Supra55 Zeiss field emission scanning electron microscope (FE-SEM). The wettability of samples was checked using a contact angle goniometer (KYOWA, DMe-201) by placing sessile-dropping water (2.0 mL) droplets on the film.

3.2.3. Synthesis of TF-CDs

The fluorescent CDs were synthesized from *C. thevetia* flowers as a green precursor by a one-step hydrothermal method. First, flowers were washed thoroughly and chopped into small pieces, dried, and a domestic mixer was used for grinding. The obtained powder was used further for the synthesis of CDs. Briefly, 0.2 g of flower powder, 0.1 g of L-cysteine, and 2 mL of H₃PO₄ were mixed with 20 mL of DI water on a stirrer for 30 min to prepare a homogenous solution. Then, the above solution was poured into a 50 mL Teflon-lined autoclave, and the reaction mixture was treated hydrothermally at 180 °C for 12 h. The as-obtained brown solution was centrifuged (10000 rpm; 15 min) to remove any solid product. Further purification was performed by dialyzing the obtained product against DI water. The final product obtained was stored in a refrigerator until further use and referred to as TF-CDs.

3.2.4. Synthesis of PVDF Thin Films with TF-CDs

PVDF films were prepared as described earlier [55]. Briefly, 15 wt% PVDF was dissolved in NMP through vigorous stirring at 80-90 °C. To this solution, 0.5 mL of TF-CDs (674 mg/mL) was added and mixed well. Then, the solution was poured on a glass slide, and a thin film was cast on a glass slide with uniform thickness. Furthermore, the

glass slides were immersed in a coagulation bath containing DI water to accomplish the phase inversion procedure. Finally, the porous TF-CDs@PVDF film was obtained and dried at room temperature. After forming the film, it was allowed to dry overnight. For a control experiment, the casting solution without TF-CDs was prepared by a similar procedure.

3.2.5. Quantum Yield (QY) and LOD Measurement

The QY of TF-CDs was determined by using quinine sulfate as the reference standard solution. It was calculated using the following equation 3.1:

$$\Phi = \Phi_{QS} \times \frac{S_S}{S_{QS}} \times \frac{A_S}{A_{QS}} \times \frac{n_S^2}{n_{QS}^2} \quad (3.1)$$

Here, Φ and Φ_{QS} is the QY of the TF-CDs and quinine sulfate, respectively. A_S and A_{QS} represent the absorbance, S_S and S_{QS} are the integrated intensity, and n_S and n_{QS} represent the refractive indices of TF-CDs and quinine sulfate, respectively.

The LOD was calculated using the following expression;

$$LOD = 3.3 \times (\sigma/S) \quad (3.2)$$

Here, S is the slope of the calibration plot, and σ is the error.

3.2.6. FL Sensing of PA using TF-CDs

To evaluate the sensitivity and selectivity of the synthesized TF-CDs, different nitro compounds, viz., PA, 2,4-DNT, 4-NT, NB, 4-IA, 2-NP, and 3-NA, were tested. The selectivity was determined by adding each NAC (200 mM concentration each) to 2 mL of TF-CD (674 mg/mL) solutions. The solutions were kept under static conditions for equilibration, and their FL intensities at an excitation wavelength (λ_{ex}) of 340 nm were subsequently recorded. Among the various NACs under test, the sensor exhibited high specificity towards PA. Therefore, further studies were carried out with PA. To study the sensitivity of TF-CDs, different concentrations of PA (0-200 mM) were added, and the

FL spectra were examined when excited at a wavelength of 340 nm. After that, the interference study was carried out in which different NACs were mixed with TF-CD, as well as the PA and FL of the mixtures were recorded at λ_{ex} 340 nm. The following Stern–Volmer equation was used to determine the quenching constant (K_{sv}):

$$\frac{I_0}{I} = 1 + K_{\text{SV}}[C] \quad (3.3)$$

where I_0 and I are the CD's emission intensities before and following the addition of analytes, respectively, and $[C]$ is the analyte concentration.

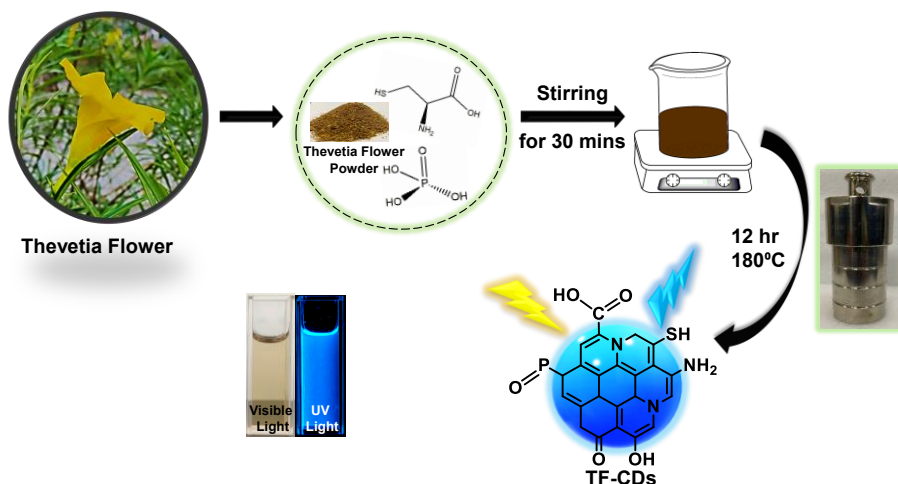
3.2.7. Sensing of PA with TF-CD@PVDF Composite Films

The sensitivity of TF-CD@PVDF composite films was checked by dropping different concentrations of PA (ranging from 0-100 mM) onto 2×2 cm films and incubating the films for 5 min. The films were then dried and subjected to FL studies at 330 nm λ_{ex} .

3.3. Results and Discussion

3.3.1. Preparations and Characterizations of TF-CD

The TF-CDs were prepared from *C. thevetia* flowers via simple one-pot, single-step hydrothermal synthesis as shown in **Scheme 3.1**. *C. thevetia* extracts have proven to contain alkaloids, steroids, volatile oils, flavonoids, and tannins, as constituents which are responsible for major functionalities observed on TF-CDs, etc [56]. To enhance the optical and electronic properties of the CDs, doping with N, S, and P was accomplished utilizing L-cysteine and H_3PO_4 as doping agents [57, 58]. It is well known that the heteroatom doping in CDs not only improves their fluorescence efficiency but can also add new functionality and active sites on the surface of CDs [28].



Scheme 3.1. Schematic representation for the synthesis of TF-CDs from *C. thevetia* flowers by one-pot hydrothermal method.

The successful synthesis of TF-CDs was confirmed using various morphological and spectroscopic techniques. To that end, we first performed HR-TEM to analyze the morphology of CDs. **Figure 3.1a** shows the TEM image of TF-CDs, proving the presence of spherical dots with a mean diameter of 2.7 nm revealed from the histogram drawn (**Figure 3.1b**). The magnified HR-TEM image (**Figure 3.1c**) clearly shows the distinct lattice fringes of CDs with a 0.25 nm d-spacing that is related to the (100) graphite plane [59, 60].

The XRD analysis was used to investigate the crystalline properties of CDs. The diffraction pattern of TF-CDs (**Figure 3.1d**) features a characteristic broad diffraction peak of CD at an angle of 22.41° , assigned to the (002) plane. The broadness of the diffraction peak indicates an amorphous nature of TF-CDs [8]. The surface functional groups were confirmed using ATR-FTIR spectroscopy. According to **Figure 3.1e**, stretching vibration of the O-H/N-H results in the broad band at 3291 cm^{-1} . The peaks at 2942 and 2872 cm^{-1} are assigned to C-H stretching from sp^3 carbon. The peak reflected at 2140 cm^{-1} is attributed to the S-H bond. The peak centered at 1631 cm^{-1} is due to the stretches of C=O/C=C groups. Peaks at 1561 cm^{-1} (N-H bending) and 1380 cm^{-1} (C-N stretching) indicated the amide functional groups in the TF-CD structure. The distinct peaks C-O, P-O, P=O, and C-S groups were

observed at 1146 cm^{-1} , 1041 cm^{-1} , 669 cm^{-1} , and 581 cm^{-1} , respectively [61-63].

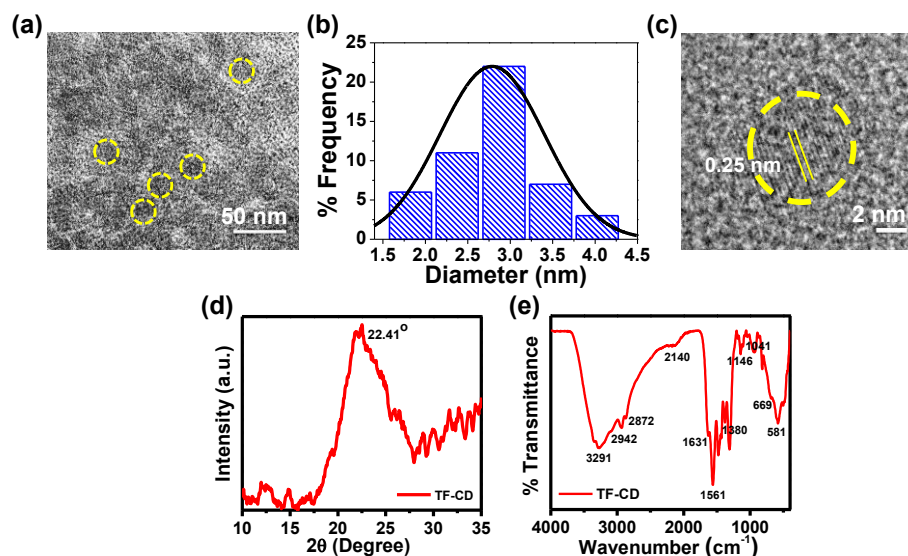


Figure 3.1. (a) TEM image, (b) Size distribution histogram, (c) HR-TEM image with d-spacing of TF-CD, (d) XRD, and (e) FTIR of as-synthesized TF-CDs.

Moreover, the chemical composition and functionalities of CDs could be better elucidated with XPS analysis. The XPS survey spectrum of TF-CD, as shown in **Figure 3.2a**, confirms the doping of P (135 eV, 2.3%), S (164 eV, <.1%), and N (399 eV, 0.5%) elements in the TF-CDs. The HR XPS peak for P2p (**Figure 3.2b**) deconvoluted into several binding energies at 133.0 and 134.2 eV indicates the presence of P-C and P-O groups, respectively. Similarly, the S2p spectra were deconvoluted into two peaks, centered at 164.7 and 167.1 eV binding energies as shown in **Figure 3.2c**, attributed to C-S and S-H, respectively, which corroborate the incorporation of sulfur on TF-CDs. The deconvoluted high-resolution C1s spectrum exhibits four peaks at the binding energy values of 284.1, 284.9, 285.7, and 287.1 eV, corresponding to C-S, C=C, C-N/C-P, and C=O, respectively (**Figure 3.2d**). **Figure 3.2e** shows the N1s spectrum with two peaks at 399.1 eV from pyridinic-N and 400.6 eV arising from pyrrolic-N. **Figure 3.2f** shows the HR scans of the O1s spectrum resolved to two peaks centering at 532.5 and 533.9 eV assigned to C-O and C=O/P=O [64, 65].

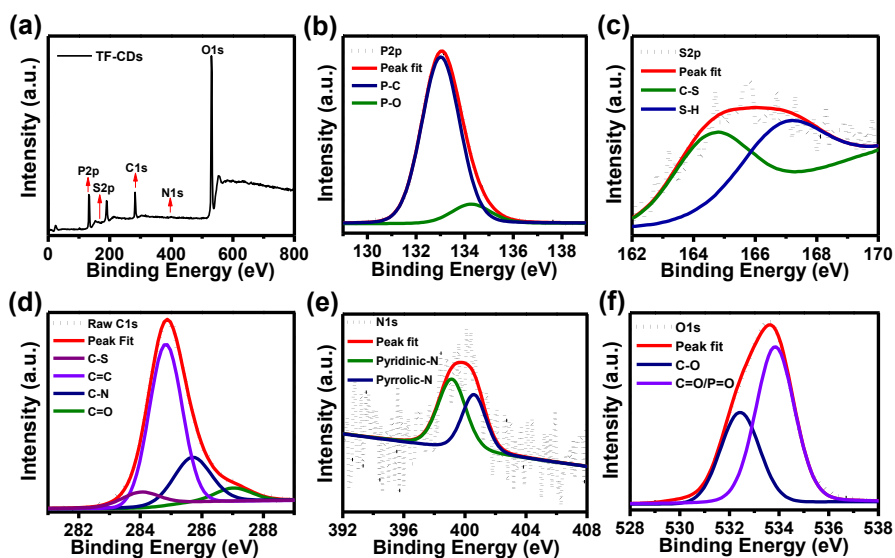


Figure 3.2. (a) XPS survey scan. Deconvoluted high-resolution XPS spectra of (b) P2p, (c) S2p, (d) C1s, (e) N1s, and (f) O1s of TF-CDs.

The XPS and FTIR studies confirm how N, S, and P were being doped in TF-CDs as functionalities such as -NH_2 , -COOH , -SH , P-O , P=O , and -OH . Apart from the H_3PO_4 and cysteine as P and S and N doping agents, we speculate that the major C-O, phenolic/hydroxyl functionalities observed on TF-CD were derived mainly from the constituents of *C. thevetia* biomass (alkaloids, steroids, volatile oils, flavonoids, and tannins) [66] acting as a major C source for CD formation.

The optical behavior of the as-synthesized TF-CDs catalyst was studied by UV-vis spectroscopy. As shown in **Figure 3.3a** UV-vis absorption spectrum exhibits absorption peaks at 260 nm, typically ascribed to the $\pi\text{-}\pi^*$ transition belonging to the carbon core ($\text{C}=\text{C}$ bonds), along with its peaks positioned at 344 and 400 nm, assigned to $\text{n-}\pi^*$ from the surface states [67]. The band gap energy of a photocatalyst is an important optical parameter to predict the formation and transfer of photoinduced electrons and holes [68]. The digital photographs in the inset of **Figure 3.3a** show that the aqueous solution of TF-CDs was light yellow under visible light and showed a bright blue FL when irradiated with 365 nm UV light. FL studies performed in **Figure 3.3b** show the excitation dependency of TF-CD. A progressive increase in FL intensity was observed as the λ_{ex} was

increased from 280 nm to 400 nm, reaching a maximum emission at 406 nm (with $\lambda_{\text{ex}} = 340$ nm). The excitation-dependent behavior indicates the different distribution of emission trap sites and different sizes of CDs. The major hypotheses existing for the luminescence mechanism of CDs are related to the molecular state, carbon core state, surface state, and size-dependent emission [11]. In the case of TF-CD, we adopted a hydrothermal synthesis and confirmed the retention of most of the active electron-rich functionalities of precursor molecules (from FTIR and XPS analysis) along with a graphitized core (evidenced by TEM and XRD analysis). This is in accordance with the report saying that the hydrothermal condition induces a partial condensation-polymerization-carbonization mechanism to form CDs retaining some sp^3 features of precursor molecules [11]. Thus, being a QD, the plausible FL centers observed for as-prepared TF-CD could be attributed to carbon core, surface-state, and size-dependent emission. Besides, the FL lifetime, an inherent property of CDs that is related to the FL site and its environment, was also recorded. The decay curve, as shown in **Figure 3.3c**, indicates the average FL lifetime of TF-CD, calculated to be 0.76 ns, which was fitted biexponentially. Additionally, **Equation 3.1** was utilized to measure FL QY of TF-CDs, which was found to be 16.5 %, with quinine sulfate at 330 nm wavelength with bright blue FL. This result demonstrates the potential of as-prepared TF-CDs for sensing and photocatalytic applications.

3.3.2. Study of Fluorescence Stability

The FL stability of TF-CDs was examined under different conditions, like temperature, pH, and NaCl. Stability is a very important parameter of CDs when used for sensing and degradation applications. Moreover, the FL of TF-CDs was observed to be stable up to 99 % at various temperature ranges (from a lower temperature of -25 °C to a temperature as high as 100 °C) (**Figure 3.3d**). The FL emission of TF-CD was relatively stable (with a retention of up to 94 % FL) in the pH range of 3-11 (**Figure 3.3e**). Similarly, TF-CDs exhibited considerable stability under a very high saline concentration (1 M NaCl) up to 90 %,

as shown in **Figure 3.3f**. Thus, TF-CDs could be an exciting applicant for environmental remediation.

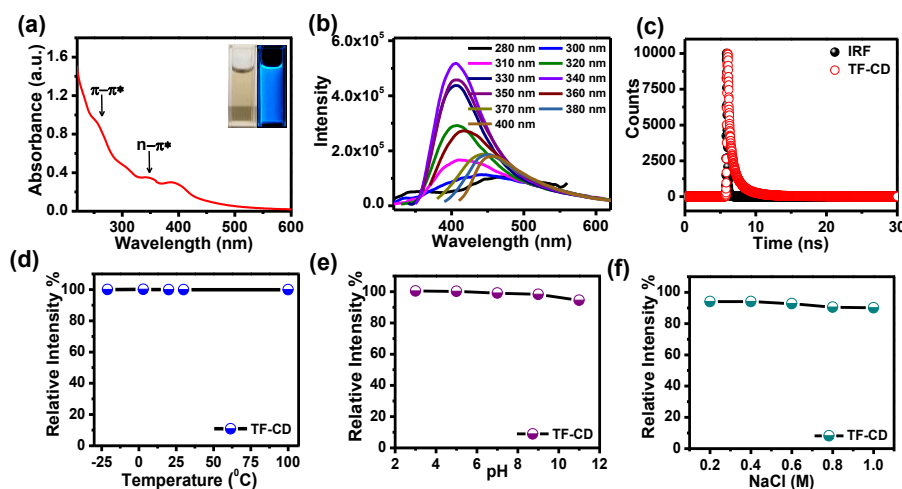


Figure 3.3. (a) UV-vis spectra (inset: TF-CDs solution in both visible and UV light), (b) FL emission spectra, and (c) TCSPC measurement recorded for TF-CDs. Stability plot of TF-CDs under different: (d) temperatures, (e) pH, and (f) NaCl concentrations.

3.3.3. Fluorescent-based PA Detection with TF-CDs

Aqueous dispersions of TF-CDs were mixed with a series of NACs to investigate the selectivity. TF-CD solutions were separately treated with 200 μM of PA, 3-NT, 2,4-DNT, aniline, 4-IA, NB, 2-NP, 4-NT, and 3-NA, and their FL emissions were recorded at 406 nm as shown in **Figure 3.4a**. Complete FL quenching of the blue TF-CDs solution was observed in the presence of PA. The remaining NACs caused negligible quenching in FL. The photograph given in **Figure 3.4b** portrays visible selective quenching of CDs' bright blue FL with PA compared with other NACs. The FL titration of the TF-CDs was further carried out to calculate the LOD and quenching constant by incubating with different concentrations of PA (0-200 μM). **Figure 3.4c** displays a consistent decrease in the FL of CDs upon treatment with different doses of PA, showing a 96 % quenching response at a maximum concentration of 200 μM . **Figure 3.4d** is the intensity variation vs PA concentrations plot, revealing a linear relationship (with an excellent correlation coefficient R^2 of 0.9976), and a LOD of

104 nM determined by **Equation 3.2**. The value of the quenching constant was found to be $2.8 \times 10^{-2} \text{ M}^{-1}$ calculated by **Equation 3.3**. The results obtained suggest that the interaction of TF-CDs with PA is quite strong. The higher the value of K_{sv} better the quenching efficiency of TF-CD towards PA detection [69]. Next, we performed the interference study to ascertain the effectiveness of TF-CDs in the detection of PA in the presence of other NACs. **Figure 3.4e** shows the anti-interference ability of TF-CDs towards PA, where there was no hindrance in the detection of PA even with the other competitive ions. This validates the high selectivity of TF-CDs' FL response among NACs.

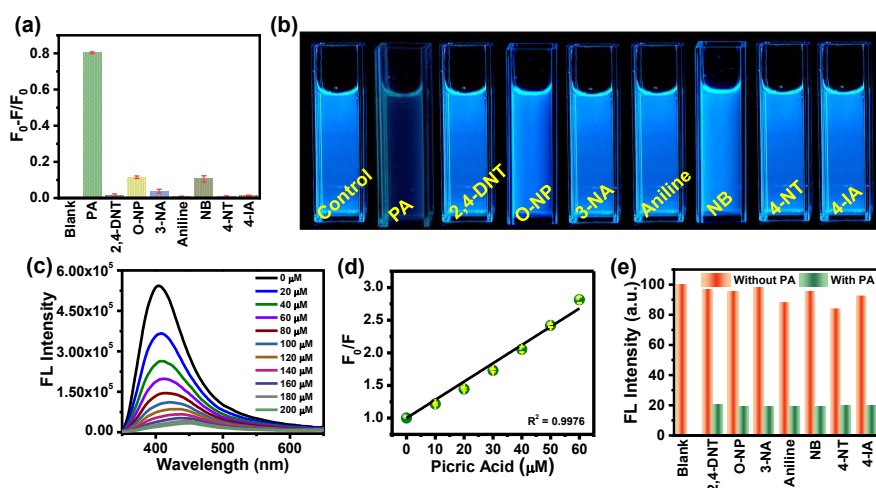


Figure 3.4. (a) Selectivity of TF-CDs towards various NACs, (b) photographs of TF-CDs in the presence of various NACs captured under UV light, (c) FL spectra of TF-CDs after adding different concentrations of PA (0-200 μM), (d) relationship between PA concentration vs. F/F_0 for TF-CDs, and (e) competitive selectivity towards sensing response of TF-CDs in the presence of nitro aromatic compounds ($c = 1.0 \times 10^{-2} \text{ M}$).

3.3.4. PA Sensing Mechanism

The FL quenching mechanism of PA with TF-CDs was elucidated with the help of UV-vis spectroscopy and FL lifetime measurements (**Figure 3.5a-d**). The FL quenching mainly occurs either due to Förster resonance energy transfer (FRET) [70] or the inner filter effect (IFE)

[71]. Interestingly, no change in the FL lifetime of TF-CDs (0.76 ns) was observed in the absence and presence of PA (**Figure 3.5a**), i.e., 100 μM and 200 μM of PA were added in TF-CDs, and the lifetime was obtained to be 0.77 and 0.74 ns, respectively, which shows a lack of possibility of any excited state quenching process like FRET. Furthermore, to check the possibility of IFE, we utilized UV-vis spectroscopy to study the changes in the UV-vis spectra of TF-CDs in the presence of different concentrations of PA (**Figure 3.5b**). Notably, the absorption intensity of TF-CDs increased upon increasing the concentration of PA with no changes in the absorption maxima (λ_{max}) of TF-CDs. The increase in the absorption intensity can be attributed to the spectral overlap between the absorption spectra of PA and excitation spectra of TF-CDs (**Figure 3.5c**). The lack of any FRET and the presence of good spectral overlap between the absorption of PA and the excitation of TF-CDs indicate a secondary mechanism of FL quenching, i.e., IFE mechanism for the detection of PA [72]. **Figure 3.5d** shows the schematic illustration of the FL quenching of TF-CDs in the presence of PA. The above results clearly show that the synthesized TF-CDs have excellent sensitivity and selectivity towards the detection of PA and can be utilized to quantify the concentration of PA in contaminated water.

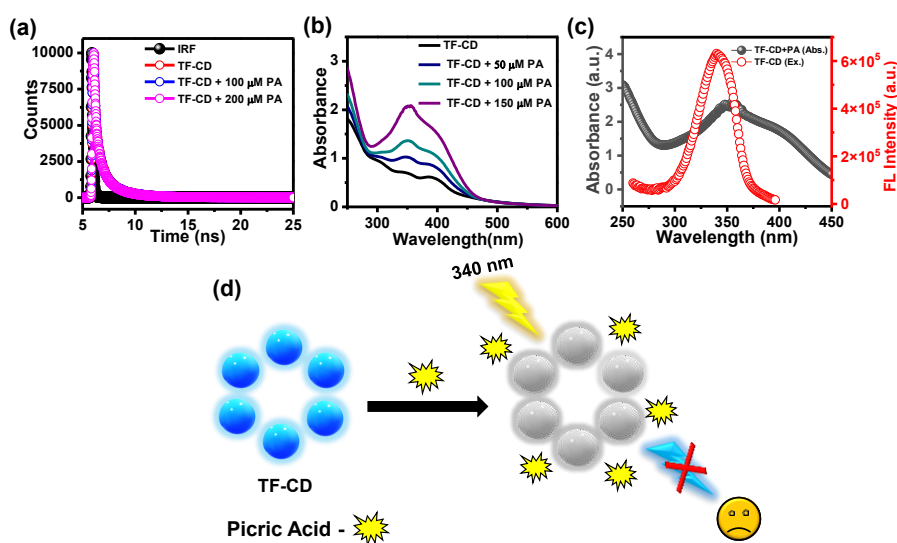
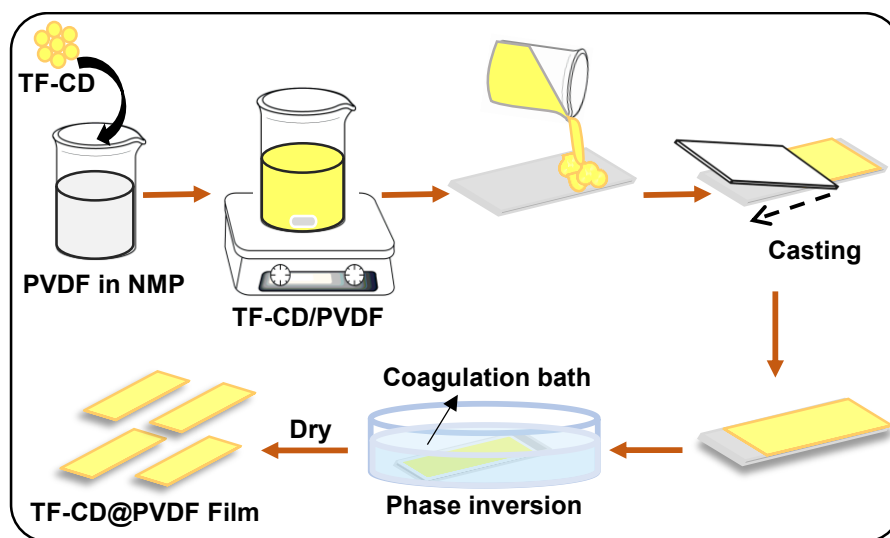


Figure 3.5. (a) Lifetime data, (b) UV-vis absorption spectra of TF-CDs with the addition of PA (black line) and maximum fluorescence

excitation of TF-CDs (blue line) showing spectral overlap, (c) UV-vis spectra of TF-CD for different concentrations of PA, and (d) schematic representation of quenching of TF-CD after the addition of PA.

3.3.5. Detection of PA on TF-CD@PVDF Strips

Encouraged by the remarkable sensing attributes of TF-CDs, we further established their sensing potential as a portable device in practical applications for the on-site detection of PA using PVDF-based thin film strips. Highly porous TF-CDs incorporated PVDF (TF-CD@PVDF) thin films were fabricated by adopting a phase inversion method as depicted in **Scheme 3.2**. A uniform distribution of hydrophilic TF-CDs in hydrophobic PVDF film was indeed challenging during the film formation. Therefore, the selection of the solvent was made thoughtfully. The chosen NMP as a solvent for PVDF was not only an excellent dispersant for TF-CDs but also known to improve processability for film formation. During the phase inversion process, NMP was replaced by fast diffusion of water from the coagulation bath, forming porous PVDF film embedded with TF-CD. In addition, when PVDF formed a slurry in TF-CD dispersed NMP medium, we speculated a possible interaction of fluorine atoms of PVDF with the amine hydrogen or hydroxyl hydrogen present on the TF-CD surface. Hence, a uniform dispersion of as-prepared CD with PVDF in moderate concentration is justifiable.



Scheme 3.2. Schematic illustration showing the preparation of TF-CD@PVDF film.

We observed a reduction in FL intensity upon higher loading of TF-CD, possibly due to the increased aggregation-induced quenching at higher CD concentrations. **Figure 3.6a** shows the effect of different concentrations of TF-CDs on PVDF film on FL emission intensity. The fabrication method of these hybrid films is simple and can be used for scale-up production. Furthermore, the present method is highly cost-effective as the coagulation bath utilized for immersion can be reused several times [73]. The incorporation of CDs in these films provides good optoelectronic characteristics that can be utilized for a broad range of applications. Moreover, **Figure 3.6b** demonstrates the retention of bright blue FL of TF-CDs in free-standing film form (photographs captured under visible and UV light) with flexibility. The surface morphology of a control PVDF film and TF-CD@PVDF composite film thus prepared was analyzed using FESEM (**Figure 3.6c-d**). It is observed that a highly perforated thin film structure was formed with a control film (**Figure 3.6c**). The porous features were created on TF-CD@PVDF due to phase separation. Notably, this porous structure will be retained in the composite film even after the incorporation of TF-CDs into PVDF (**Figure 3.6d**). The inset of **Figure 3.6d** represents the low-magnification SEM image of TF-CD@PVDF.

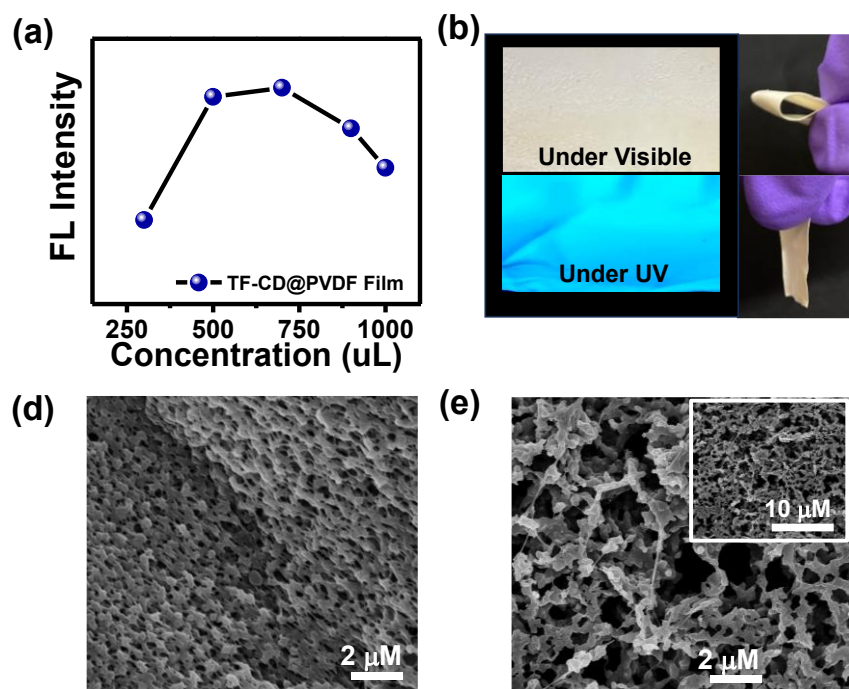


Figure 3.6. (a) Effect on FL property of TF-CD@PVDF by varying the concentration of TF-CDs, (b) photographs of TF-CD@PVDF film under visible and UV light (365 nm). SEM images of (c) PVDF and (d) TF-CD@PVDF composite film.

Moreover, **Figure 3.7a** shows the UV-vis absorption spectra of PVDF and TF-CD@PVDF composite. Notably, bare PVDF film does not feature any evident absorption peaks, while two apparent peaks centered at 260 and 344 nm, characteristic of CDs, emerged upon the incorporation of TF-CDs into the PVDF film. Furthermore, the FL spectra of TF-CD@PVDF (**Figure 3.7b**) exhibit a maximum emission wavelength at 398 nm upon excitation at 330 nm, which further indicates a blue shift in the FL maximum of the composite film with respect to TF-CDs. **Figure 3.7c** shows the PXRD pattern of PVDF, as well as TF-CD@PVDF, with peaks centered at 18.4° (020), 20.0° (110), and 26.5° (110), which can be ascribed to the crystalline nature of PVDF α phase [74]. Moreover, the peak intensity at 20.0° was increased, and peaks at 18.5° and 26.5° were merged in the case of TF-CD@PVDF [75]. The contact angles of PVDF and TF-CD@PVDF films were checked with a contact angle goniometer by sessile drop experiment. The contact angle of a bare PVDF membrane was found to

be $96.9 \pm 1^\circ$, which was reduced to $77.1 \pm 1^\circ$ after adding TF-CDs in PVDF. The difference in contact angle of PVDF (**Figure 3.7di**) and that of TF-CD@PVDF (**Figure 3.7dii**) proves that the hydrophobic nature of PVDF was reduced after the incorporation of hydrophilic CDs into PVDF film. This is beneficial for the applicability of TF-CD@PVDF for sensing waterborne pollutants [76].

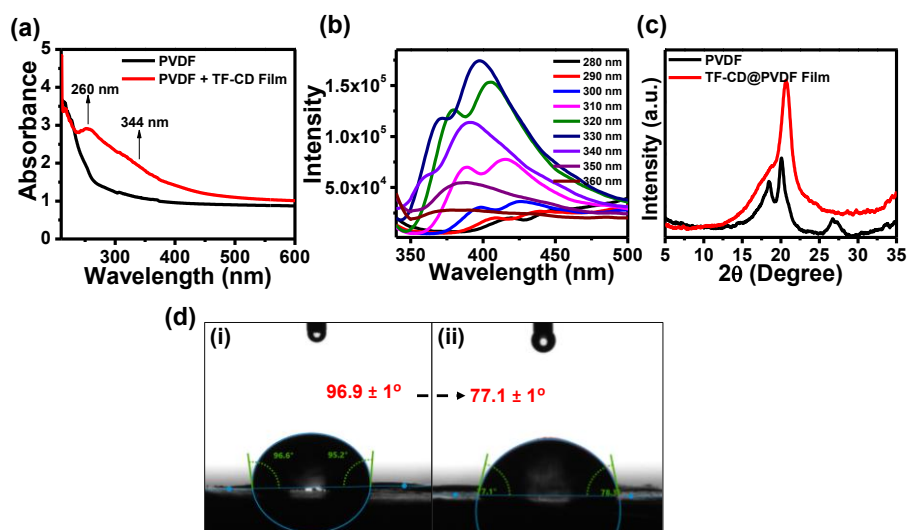


Figure 3.7. (a) UV-vis spectra of PVDF film and TF-CD@PVDF composite film, (b) FL spectra of TF-CD@PVDF composite film under different excitation, (c) PXRD of PVDF and TF-CD@PVDF, (d) Sessile drop contact angle (θ) measurements of the (i) PVDF membrane, (ii) TFCD@PVDF.

Further, the stability of TF-CDs@PVDF film was determined at various pH levels, by varying the concentration of NaCl, and at various temperatures. The TF-CDs@PVDF stability is depicted in **Figure 3.8a-c**. The film is relatively stable in the pH range of 3-11 as indicated in **Figure 3.8a**. Under an adverse NaCl concentration, as shown in **Figure 3.8b**, the film is stable and retains the FL up to 79 %. Similarly, FL was stable at different temperatures up to 96 % when kept at - 21 °C, 3 °C, 20 °C, 37 °C, and 100 °C as indicated in **Figure 3.8c**.

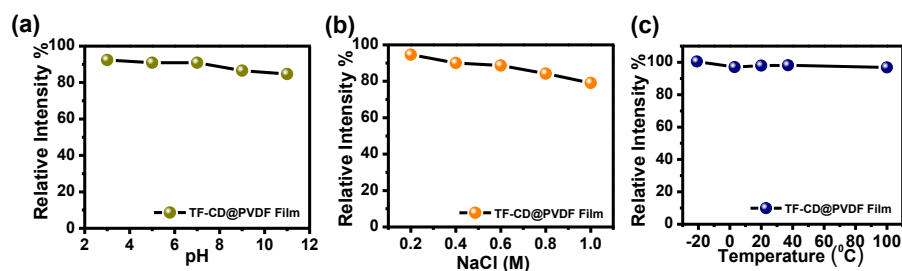


Figure 3.8. The stability of TF-CD@PVDF film under different (a) pH, (b) NaCl concentrations, and (c) temperature.

The porous structure of the fabricated TF-CD@PVDF film can further provide an efficient diffusion pathway for the fast detection of PA. The pale-yellow color strips exhibit bright blue-colored FL upon 365 nm UV illumination. The changes in the blue FL behavior were visible under UV light after adding different concentrations of PA solutions on strips (photographs are given in **Figure 3.9a**), and the changes in the FL intensity were further examined with an FL spectrophotometer. The FL of the thin film is successively turned off by increasing PA concentration (from 0-100 μ M). Furthermore, the FL intensity ratio F/F_0 is linearly correlated ($R^2 = 0.9904$) in the range of 0-100 μ M PA concentrations (**Figure 3.9b**). The detection limit was calculated to be 244 nM, which is superior to any other solid FL sensing platform reported for PA sensing (**Table 3.1**). Further, we performed the selectivity of TF-CD@PVDF in the presence of other NAC compounds. The selectivity was determined by immersing the films in each NAC (100 μ M concentration each) for 5 min in static conditions for equilibration, and further, their FL intensities were recorded at λ_{ex} of 330 nm. Among the various NACs under test, the TF-CD@PVDF film showed high specificity towards PA, as indicated in **Figure 3.9c**. **Figure 3.9d** is the recyclability plot of the as-prepared FL sensor strip, presenting stability and reusability (at least for 5 cycles). After each cycle, the film was washed with DI water, dried, and further reused for PA detection. Therefore, the as-developed flexible and portable sensing strip renders multiple reuses of the sensor, inhibiting the elution of FL active CD into the environment.

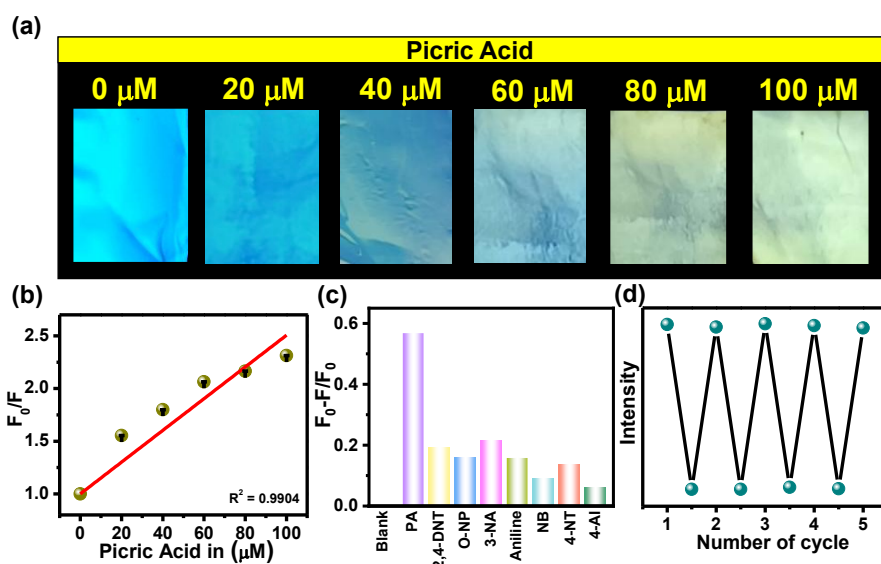


Figure 3.9. (a) Digital images of TF-CD@PVDF films after adding different concentrations of PA (under UV illumination of 365 nm), (b) linearity plot of F_0/F vs PA concentrations for TF-CD@PVDF composite film, (c) selectivity of TF-CD@PVDF film towards various NACs, and (d) recyclability study of composite film towards PA detection.

Table 3.1. The performance comparison for the PA sensing platform.

Sr. No.	Sensing Element	Linear range (μM)	LOD (nm)	Portable platform	Real Sample	Recyclability of Sensor	Reference
1.	AIE luminogen-functionalized MM	0 to 50	1700	-	-	Yes	77
2.	N-GQDs	1 to 60	300	-	Lake water	-	78
3.	N-CNPs	0–20	250	-	-	-	79
4.	Cdot-Ppy film	-	148.4	Film	Ground water and soil	-	80
5.	N doped GQDs	0 – 4	420	-	-	-	81
6.	Polymeric Thin Films	10 - 90	56000	Film	-	Yes	82
7.	MOFs	0 - 1000	5000	-	-	-	83
8.	(Na -Ala/Chit -cl - polyAAm	-	-	Yes	-	Yes	84
9.	Ce-Doped ZnO	0 - 12	278	-	-	-	85
10.	TF-CD@PVDF	0 - 100	244	Yes	Tap, ground and river water	Yes	Present Work

3.3.6. Real Sample Analysis

The developed system was further utilized for the determination of PA in water samples from various sources, such as river water (Narmada River, Madhya Pradesh), tap water (Simrol, Madhya Pradesh), and groundwater (Simrol, Madhya Pradesh). The collected water samples were filtered through a 0.22 μm membrane. As expected, initially there were no traces of PA were found in the above-mentioned water samples when checked by FL TF-CDs. Next, the above water samples were spiked with different concentrations of PA (20, 40, and 60 μM), and recovery tests were performed. The recovery of 73-100 % with a standard deviation of less than 2 was obtained for TF-CDs (**Table 3.2**). The same experiment was performed for TF-CD@PVDF film. A recovery of 91-104 % with a standard deviation of below 2 was obtained as shown in **Table 3.2**. The excellent recovery rate with good precision and reliability demonstrates the vast applicability of TF-CD and TF-CD@PVDF composite film to be used as a sensor in real sample analysis.

Table 3.2. PA sensing in real water samples with TF-CDs and TF-CD@PVDF films (N=3).

Sample	Claimed Concentration (μM)	TF-CD			TF-CD@PVDF		
		Obtained Concentration (μM)	Recovery (%)	SD (n=3)	Obtained Concentration (μM)	Recovery (%)	SD (n=3)
Tap water	20	20	97.86	0.86	20	91.25	1.38
	40	39.39	100.05	0.30	39.89	104.85	0.52
	60	59.71	99.75	0.46	59.80	99.75	0.28
River water	20	19.83	97.33	1.52	19.97	96.15	2.8
	40	39.93	99.95	1.49	39.80	100.67	1.03
	60	59.94	93.78	0.01	59.94	99.06	1.89
Ground water	20	19.88	88.47	0.14	20	91.24	1.36
	40	39.75	82.45	1.42	39.93	95.64	0.45
	60	59.89	73.27	0.61	59.71	100.07	1.01

3.4. Conclusions

In the current work, we have synthesized N, S, and P co-doped CDs from *C. thevetia* flower by a simple one-pot hydrothermal method. Further, the aqueous solution of TF-CDs shows a significant and

selective FL quenching towards PA among the other nitro compounds under examination. We developed TF-CDs loaded with highly porous PVDF film strips, portable for on-site detection of PA. The TF-CDs@PVDF film shows a blue color FL, which gets quenched upon the addition of PA. The TSCPC and UV-vis measurements revealed a static quenching mechanism for PA detection. Moreover, the sensor can also be used for further real sample analysis, highlighting its practicality. The synthesized material is utilized for easy, fast, and selective detection of PA both in aqueous and film form.

Note: This is copyrighted material with permission from the Royal Society of Chemistry.

3.5. References

1. Yu C., Li X., Qiao X., Zhang Z., Zhang D., Liu H., Hao X.-L., Wang Z., You H., Zhou L. (2023), High-Yield, Stable, and Ultrasensitive Carbon Dots for pH Sensing and Fe²⁺ Detection Are Synthesized at Room Temperature, *J. Phys. Chem. C*, *127*, 3176–3183. (DOI: 10.1021/acs.jpcc.2c06449)
2. Mate N., Pranav, Nabeela K., Kaur N., Mobin S. M. (2022), Insight into the Modulation of Carbon-Dot Optical Sensing Attributes through a Reduction Pathway, *ACS Omega*, *7*, 43759–43769. (DOI: 10.1021/acsomega.2c04766)
3. Wu Y., Qin D., Luo Z., Meng S., Mo G., Jiang X., Deng B. (2022), High Quantum Yield Boron and Nitrogen Codoped Carbon Quantum Dots with Red/Purple Emissions for Ratiometric Fluorescent IO₄[−] Sensing and Cell Imaging, *ACS Sustainable Chem. Eng.*, *10*, 5195–5202. (DOI: 10.1021/acssuschemeng.1c08676)
4. Barhum H., Alon T., Attrash M., Machnev A., Shishkin I., Ginzburg P. (2021), Multicolor Phenylenediamine Carbon Dots for Metal-Ion Detection with Picomolar Sensitivity, *ACS Appl. Nano Mater.*, *4*, 9919–9931. (DOI: 10.1021/acsanm.1c02496)
5. Marković Z. M., Labudová M., Danko M., Matijašević D., Mičušík M., Nádaždy V., Kováčová M., Kleinová A., Špitalský Z., Pavlović V., Milivojević D. D., Medić M., Todorović Marković B. M. (2020), Highly Efficient Antioxidant F- and Cl-Doped Carbon Quantum Dots for Bioimaging, *ACS Sustainable Chem. Eng.*, *8*, 16327–16338. (DOI: 10.1021/acssuschemeng.0c06260)
6. John, T. S., Yadav P. K., Kumar D., Singh S. K., Hasan S. H. (2020), Highly Fluorescent Carbon Dots from Wheat Bran as a Novel Drug Delivery System for Bacterial Inhibition, *Luminescence*, *35*, 913–923. (DOI: 10.1002/bio.3801)
7. Wu Q., Wang L., Yan Y., Li S., Yu S., Wang J., Huang L. (2022), Chitosan-Derived Carbon Dots with Room-Temperature Phosphorescence and Energy Storage Enhancement Properties,

- ACS Sustainable Chem. Eng.*, **10**, 3027–3036. (DOI: 10.1021/acssuschemeng.1c08299)
8. Yue L., Li H., Sun Q., Zhang J., Luo X., Wu F., Zhu, X. (2020), Red-Emissive Ruthenium-Containing Carbon Dots for Bioimaging and Photodynamic Cancer Therapy, *ACS Appl. Nano Mater.*, **3**, 869–876. (DOI: 10.1021/acsanm.9b02394)
 9. Li N., Liu Z., Liu M., Xue C., Chang Q., Wang H., Li Y., Song Z., Hu S. (2019), Facile Synthesis of Carbon Dots@2D MoS₂ Heterostructure with Enhanced Photocatalytic Properties, *Inorg. Chem.*, **58**, 5746–5752. (DOI: 10.1021/acs.inorgchem.9b00111)
 10. Ragazzon G., Cadranet A., Ushakova E. V., Wang Y., Guldi D. M., Rogach A. L., Kotov N. A., Prato M. (2021), Optical Processes in Carbon Nanocolloids, *Chem*, **7**, 606–628. (DOI: 10.1016/j.chempr.2020.11.012)
 11. Zeng Q., Feng T., Tao S., Zhu S., Yang B. (2021), Precursor-Dependent Structural Diversity in Luminescent Carbonized Polymer Dots (CPDs): The Nomenclature, *Light Sci Appl.*, **10**, 142. (DOI: 10.1038/s41377-021-00579-6)
 12. Yuan F., Yuan T., Sui L., Wang Z., Xi Z., Li Y., Li X., Fan L., Tan Z., Chen A., Jin M., Yang S. (2018), Engineering Triangular Carbon Quantum Dots with Unprecedented Narrow Bandwidth Emission for Multicolored LEDs, *Nat Commun.*, **9**, 2249. (DOI: 10.1038/s41467-018-04635-5)
 13. Rodríguez-Padrón D., Algarra M., Tarelho L. A. C., Frade J., Franco A., de Miguel G., Jiménez J., Rodríguez-Castellón E., Luque R. (2018), Catalyzed Microwave-Assisted Preparation of Carbon Quantum Dots from Lignocellulosic Residues, *ACS Sustainable Chem. Eng.*, **6**, 7200–7205. (DOI: 10.1021/acssuschemeng.7b03848)
 14. Ankireddy S. R., Vo V. G., An S. S. A., Kim J. (2020), Solvent-Free Synthesis of Fluorescent Carbon Dots: An Ecofriendly Approach for the Bioimaging and Screening of Anticancer Activity via Caspase-Induced Apoptosis, *ACS Appl. Bio Mater.*, **3**, 4873–4882. (DOI: 10.1021/acsabm.0c00377)

15. Lu W., Guo Y., Zhang J., Yue Y., Fan L., Li F., Dong C., Shuang S. (2022), A High Catalytic Activity Nanozyme Based on Cobalt-Doped Carbon Dots for Biosensor and Anticancer Cell Effect, *ACS Appl. Mater. Interfaces*, *14*, 57206–57214. (DOI: 10.1021/acsami.2c19495)
16. Ran Y., Wang S., Yin Q., Wen A., Peng X., Long Y., Chen S. (2020), Green Synthesis of Fluorescent Carbon Dots Using Chloroplast Dispersions as Precursors and Application for Fe³⁺ Ion Sensing, *Luminescence*, *35*, 870–876. (DOI: 10.1002/bio.3794)
17. Li Y., Liu C., Chen M., Zheng Y., Tian H., Shi R., He X., Lin X. (2022), Preparing Colour-Tunable Tannic Acid-Based Carbon Dots by Changing the pH Value of the Reaction System, *Nanomaterials*, *12*, 3062. (DOI: 10.3390/nano12173062)
18. Sangubotla R., Won S., Kim J. (2023), Boronic Acid-Modified Fluorescent Sensor Using Coffee Biowaste-Based Carbon Dots for the Detection of Dopamine, *J. Photochem. Photobiol., A*, *438*, 114542. (DOI: 10.1016/j.jphotochem.2023.114542)
19. Bhati A., Anand S. R., Gunture, Garg A. K., Khare P., Sonkar S. K. (2018), Sunlight-Induced Photocatalytic Degradation of Pollutant Dye by Highly Fluorescent Red-Emitting Mg-N-Embedded Carbon Dots, *ACS Sustainable Chem. Eng.*, *6*, 9246–9256. (DOI: 10.1021/acssuschemeng.8b01559)
20. Milenković I., Borišev M., Zhou Y. Spasić S. Z., Leblanc R. M., Radotić K. (2021), Photosynthesis Enhancement in Maize via Nontoxic Orange Carbon Dots, *J. Agric. Food Chem.*, *69*, 5446–5451. (DOI: 10.1021/acs.jafc.1c01094)
21. Tyagi A., Tripathi K. M., Singh N., Choudhary S., Gupta R. K. (2016), Green Synthesis of Carbon Quantum Dots from Lemon Peel Waste: Applications in Sensing and Photocatalysis, *RSC Adv.*, *6*, 72423–72432. (DOI: 10.1039/C6RA10488F)
22. Tai J. Y., Leong K. H., Saravanan P., Tan S. T., Chong W. C., Sim L. C. (2021), Facile Green Synthesis of Fingernails Derived Carbon Quantum Dots for Cu²⁺ Sensing and Photodegradation of

- 2,4-Dichlorophenol, *J. Environ. Chem. Eng.*, **9**, 104622. (DOI: 10.1016/j.jece.2020.104622)
23. Senapati S., Nanda K. K. (2018), MgO Nanocubes as Self-Calibrating Optical Probes for Efficient Ratiometric Detection of Picric Acid in the Solid State, *ACS Sustainable Chem. Eng.*, **6**, 13719–13729. (DOI: 10.1021/acssuschemeng.8b01330)
 24. Chowdhury A., Mukherjee P. S. (2015), Electron-Rich Triphenylamine-Based Sensors for Picric Acid Detection, *J. Org. Chem.*, **80**, 4064–4075. (DOI: 10.1021/acs.joc.5b00348)
 25. Purba P. C., Venkateswaralu M., Bhattacharyya S., Mukherjee P. S. (2022), Silver(I)–Carbene Bond-Directed Rigidification-Induced Emissive Metallacage for Picric Acid Detection, *Inorg. Chem.*, **61**, 713–722. (DOI: 10.1021/acs.inorgchem.1c03527)
 26. Nailwal Y., Devi M., Pal S. K. (2022), Luminescent Conjugated Microporous Polymers for Selective Sensing and Ultrafast Detection of Picric Acid, *ACS Appl. Polym. Mater.*, **4**, 2648–2655. (DOI: 10.1021/acsapm.1c01905)
 27. Fan Y., Tao T., Wang H., Liu Z., Huang W., Cao H. (2021), A Schiff Base-Functionalized Graphene Quantum Dot Nanocomposite for Preferable Picric Acid Sensing, *Dyes Pigm.*, **191**, 109355. (DOI: 10.1016/j.dyepig.2021.109355)
 28. Sharma V., Mehata M. S. (2021), Rapid Optical Sensor for Recognition of Explosive 2,4,6-TNP Traces in Water through Fluorescent ZnSe Quantum Dots, *Spectrochim. Acta, Part A*, **260**, 119937. (DOI: 10.1016/j.saa.2021.119937)
 29. Chen X., Sun C., Liu Y., Yu L., Zhang K., Asiri A. M., Marwani H. M., Tan H., Ai Y., Wang X., Wang S. (2020), All-Inorganic Perovskite Quantum Dots CsPbX₃ (Br/I) for Highly Sensitive and Selective Detection of Explosive Picric Acid, *Chem. Eng. J.*, **379**, 122360. (DOI: 10.1016/j.cej.2019.122360)
 30. Zhao Y., Xu L., Kong F., Yu L. (2021), Design and Preparation of Poly(Tannic Acid) Nanoparticles with Intrinsic Fluorescence: A Sensitive Detector of Picric Acid, *Chem. Eng. J.*, **416**, 129090. (DOI: 10.1016/j.cej.2021.129090)

31. Chongdar, S., Mondal U., Chakraborty T., Banerjee P., Bhaumik A. (2023), A Ni-MOF as Fluorescent/Electrochemical Dual Probe for Ultrasensitive Detection of Picric Acid from Aqueous Media, *ACS Appl. Mater. Interfaces*, *15*, 14575–14586. (DOI: 10.1021/acsami.3c00604)
32. Yu H., Liu Q., Fan M., Sun J., Su Z.-M., Li X., Wang X. (2022), Novel Eu-MOF-Based Mixed Matrix Membranes and 1D Eu-MOF-Based Ratiometric Fluorescent Sensor for the Detection of Metronidazole and PA in Water, *Dyes Pigm.*, *197*, 109812. (DOI: 10.1016/j.dyepig.2021.109812)
33. Acharyya K., Mukherjee P. S. (2014), A Fluorescent Organic Cage for Picric Acid Detection, *Chem. Commun.*, *50*, 15788–15791. (DOI: 10.1039/C4CC06225F)
34. Xiong J.-F., Li J.-X., Mo G.-Z., Huo J.-P., Liu J.-Y., Chen X.-Y., Wang Z.-Y. (2014), Benzimidazole Derivatives: Selective Fluorescent Chemosensors for the Picogram Detection of Picric Acid, *J. Org. Chem.*, *79*, 11619–11630. (DOI: 10.1021/jo502281b)
35. Hu J.-H., Zhang W., Ren C.-X., Xiong Y., Zhang J.-Y., He J., Huang Y., Tao Z., Xiao X. (2023), A Novel Portable Smart Phone Sensing Platform Based on a Supramolecular Fluorescence Probe for Quick Visual Quantitative Detection of Picric Acid, *Anal. Chim. Acta*, *1254*, 341095. (DOI: 10.1016/j.aca.2023.341095)
36. Saravanan A., Maruthapandi M., Das P., Ganguly S., Margel S., Luong J. H. T., Gedanken A. (2020), Applications of N-Doped Carbon Dots as Antimicrobial Agents, Antibiotic Carriers, and Selective Fluorescent Probes for Nitro Explosives, *ACS Appl. Bio Mater.*, *3*, 8023–8031. (DOI: 10.1021/acsabm.0c01104)
37. Pagidi S., Sadhanala H. K., Sharma K., Gedanken A. (2022), One-Pot Synthesis of Deep Blue Hydrophobic Carbon Dots with Room Temperature Phosphorescence, White Light Emission, and Explosive Sensor, *Adv. Electron. Mater.*, *8*, 2100969. (DOI: 10.1002/aelm.202100969)
38. Das P., Maruthapandi M., Saravanan A., Natan M., Jacobi G., Banin E., Gedanken A. (2020), Carbon Dots for Heavy-Metal

- Sensing, pH-Sensitive Cargo Delivery, and Antibacterial Applications, *ACS Appl. Nano Mater.*, **3**, 11777–11790. (DOI: 10.1021/acsanm.0c02305)
39. López-Beltrán A., Iriarte-Mesa C., Murru C., Chao-Mujica F. J., Corcho-Valdés A. L., Morales-Álvarez L., Desdín-García L. F., Deschamps J., Antuch M. (2023), Design of Fluorescent Carbon Dots (CDs) for the Selective Detection of Metal-Containing Ions, *Chem. – Eur. J.*, **29**, e202300188. (DOI: 10.1002/chem.202300188)
 40. M. Facure M. H., Schneider R., A. Mercante L., S. Correa D. (2020), A Review on Graphene Quantum Dots and Their Nanocomposites: From Laboratory Synthesis towards Agricultural and Environmental Applications, *Environ. Sci.: Nano*, **7**, 3710–3734. (DOI: 10.1039/D0EN00787K)
 41. Teodoro K. B. R., Facure M. H. M., Schneider R., Alvarenga A. D., Andre R. S., Correa D. S. (2023), Self-Standing Thin Films of Cellulose Nanocrystals and Graphene Quantum Dots for Detection of Trace Iron(III), *ACS Appl. Nano Mater.*, **6**, 11561–11571. (DOI: 10.1021/acsanm.3c01584)
 42. Ng Hau Kwan M., Leo C. P., Arosa Senanayake S. M. N., Lim G. K., Tan M. K. (2020), Carbon-Dot Dispersal in PVA Thin Film for Food Colorant Sensing, *J. Environ. Chem. Eng.*, **8**, 103187. (DOI: 10.1016/j.jece.2019.103187)
 43. Ren X., Cao L., Liang W., Wang P., Bunker C. E., Yang L., Teisl L. R., Sun Y.-P. (2022), Photoexcited State Properties of Poly(9-Vinylcarbazole)-Functionalized Carbon Dots in Solution versus in Nanocomposite Films: Implications for Solid-State Optoelectronic Devices, *ACS Appl. Nano Mater.*, **5**, 2820–2827. (DOI: 10.1021/acsanm.1c04560)
 44. Das P., Ganguly S., Ahmed S. R., Sherazee M., Margel S., Gedanken A., Srinivasan S., Rajabzadeh A. R. (2022), Carbon Dot Biopolymer-Based Flexible Functional Films for Antioxidant and Food Monitoring Applications, *ACS Appl. Polym. Mater.*, **4**, 9323–9340. (DOI: 10.1021/acsapm.2c01579)

45. Feng Z., Adolfsson K. H., Xu Y., Fang H., Hakkarainen M., Wu M. (2021), Carbon Dot/Polymer Nanocomposites: From Green Synthesis to Energy, Environmental and Biomedical Applications, *Sustainable Mater. Technol.*, *29*, e00304. (DOI: 10.1016/j.susmat.2021.e00304)
46. Zhang Y., Gao L., Ma S., Hu T. (2022), Cd (II) Coordination Polymer as a Strip Based Fluorescence Sensor for Sensing Fe³⁺ Ions in Aqueous System, *Spectrochim. Acta, Part A*, *267*, 120525. (DOI: 10.1016/j.saa.2021.120525)
47. Jin Y.-J., Si B.-M., Kim E., Lee J., Kim H., Kwak G., Sakaguchi T., Lee J., Song I. Y., Lee C.-L., Kim J. H., Heo K., Lee W.-E. (2023), Reusable, Ultrasensitive, Patterned Conjugated Polyelectrolyte–Surfactant Complex Film with a Wide Detection Range for Copper Ion Detection, *ACS Appl. Mater. Interfaces*, *15*, 12339–12349. (DOI: 10.1021/acsami.2c21388)
48. Kanjo M., Gon M., Tanaka K. (2023), Stimuli-Responsive π -Conjugated Polymers Showing Solid-State Emission Based on Boron-Fused Azomethine Complexes with NNO-Tridentate Ligands, *ACS Appl. Mater. Interfaces*, *15*, 31927–31934. (DOI: 10.1021/acsami.3c06277)
49. Kanzariya D. B., Goswami R., Muthukumar D., Pillai R. S., Pal T. K. (2022), Highly Luminescent MOF and Its In Situ Fabricated Sustainable Corn Starch Gel Composite as a Fluoro-Switchable Reversible Sensor Triggered by Antibiotics and Oxo-Anions, *ACS Appl. Mater. Interfaces*, *14*, 48658–48674. (DOI: 10.1021/acsami.2c13571)
50. Goswami K. J., Sultana N., Sen Sarma N. (2023), Dual Phase Selective Inner Filter Effect-Based Luminescent Sensing for the Detection of Para-Nitrophenol and Picric Acid, *Sens. Actuators, B*, *374*, 132778. (DOI: 10.1016/j.snb.2022.132778)
51. Mitra R., Saha A. (2017), Reduced Graphene Oxide Based “Turn-On” Fluorescence Sensor for Highly Reproducible and Sensitive Detection of Small Organic Pollutants, *ACS Sustainable Chem. Eng.*, *5*, 604–615. (DOI: 10.1021/acssuschemeng.6b01971)

52. Liu Q., Liu M., Li D., Li K., Xu H., Lu J., Shao X., Liu T. (2022), Highly Improved Performance of a Film-Based Fluorescent Sensor via a Nanomesh Scaffold Strategy, *Sens. Diagn.*, *1*, 130–133. (DOI: 10.1039/D1SD00016K)
53. Dong L., Xiong Z., Liu X., Sheng D., Zhou Y., Yang Y. (2019), Synthesis of Carbon Quantum Dots to Fabricate Ultraviolet-Shielding Poly(Vinylidene Fluoride) Films, *J. Appl. Polym. Sci.*, *136*, 47555. (DOI: 10.1002/app.47555)
54. Ram R., Khastgir D., Rahaman M. (2018), Physical Properties of Polyvinylidene Fluoride/Multi-Walled Carbon Nanotube Nanocomposites with Special Reference to Electromagnetic Interference Shielding Effectiveness, *Adv. Polym. Technol.*, *37*, 3287–3296. (DOI: 10.1002/adv.22113)
55. Zhang D., Jiang W., Zhao Y., Dong Y., Feng X., Chen L. (2019), Carbon Dots Rooted PVDF Membrane for Fluorescence Detection of Heavy Metal Ions, *Appl. Surf. Sci.*, *494*, 635–643. (DOI: 10.1016/j.apsusc.2019.07.141)
56. Tufail S., Ali Z., Hanif S., Sajjad A., Zia M. (2022), Synthesis and Morphological & Biological Characterization of Campsis Radicans and Cascabela Thevetia Petals Derived Silver Nanoparticles, *Biochem. Syst. Ecol.*, *105*, 104526. (DOI: 10.1016/j.bse.2022.104526)
57. Karami S., Shamsipur M., Taherpour A. A., Jamshidi M., Barati A. (2020), In Situ Chromophore Doping: A New Mechanism for the Long-Wavelength Emission of Carbon Dots, *J. Phys. Chem. C*, *124*, 10638–10646. (DOI: 10.1021/acs.jpcc.0c00833)
58. Das D., Dutta R. k. (2021), N-Doped Carbon Dots Synthesized from Ethylene Glycol and β -Alanine for Detection of Cr(VI) and 4-Nitrophenol via Photoluminescence Quenching, *ACS Appl. Nano Mater.*, *4*, 3444–3454. (DOI: 10.1021/acsanm.0c03329)
59. Xu Q., Kuang T., Liu Y., Cai L., Peng X., Sreeprasad T. S., Zhao P., Yu Z., Li N. (2016), Heteroatom-Doped Carbon Dots: Synthesis, Characterization, Properties, Photoluminescence Mechanism and

- Biological Applications, *J. Mater. Chem. B*, *4*, 7204–7219. (DOI: 10.1039/C6TB02131J)
60. Li L., Li Y., Ye Y., Guo R., Wang A., Zou G., Hou H., Ji X. (2021), Kilogram-Scale Synthesis and Functionalization of Carbon Dots for Superior Electrochemical Potassium Storage, *ACS Nano*, *15*, 6872–6885. (DOI: 10.1021/acsnano.0c10624)
 61. Lu C., Zhu Q., Zhang X., Ji H., Zhou Y., Wang H., Liu Q., Nie J., Han W., Li X. (2019), Decoration of Pd Nanoparticles with N and S Doped Carbon Quantum Dots as a Robust Catalyst for the Chemoselective Hydrogenation Reaction, *ACS Sustainable Chem. Eng.*, *7*, 8542–8553. (DOI: 10.1021/acssuschemeng.9b00322)
 62. Hahn, M.; Kim, J. M.; Hong, H.; Lee, C.; Kim, D.; Han, M. Y.; Kim, H. S.; Piao, Y. Sterically Stabilized Carbon Dots as Solid-State Phosphors for White-Light-Emitting Diodes. *ACS Appl. Nano Mater.* **2022**, *5* (8), 11896–11905. (DOI: 10.1021/acsanm.2c02908)
 63. Wang W., Chen J., Wang D., Shen Y., Yang L., Zhang T., Ge J. (2021), Facile Synthesis of Biomass Waste-Derived Fluorescent N, S, P Co-Doped Carbon Dots for Detection of Fe³⁺ Ions in Solutions and Living Cells, *Anal. Methods*, *13* (6), 789–795. (DOI: 10.1039/D0AY02186E)
 64. Bishwal L., Kar S., Bhattacharyya S. (2023), Role of Noncovalent Interactions in N, P-Functionalized Luminescent Carbon Dots for Ultrasensitive Detection of Moisture in D₂O: Boosting Visible-NIR Light Sensitivity, *ACS Appl. Mater. Interfaces*, *15*, 15907–15916. (DOI: 10.1021/acсами.3c01620)
 65. Saini D., Aggarwal R., Sonker A. K., Sonkar S. K. (2021), Photodegradation of Azo Dyes in Sunlight Promoted by Nitrogen–Sulfur–Phosphorus Codoped Carbon Dots, *ACS Appl. Nano Mater.*, *4*, 9303–9312. (DOI: 10.1021/acsanm.1c01810)
 66. Meena B. R., Meena S., Chittora D., Sharma K. (2021), Antifungal Efficacy of Thevetia Peruviana Leaf Extract against Alternaria Solani and Characterization of Novel Inhibitory Compounds by Gas Chromatography-Mass Spectrometry Analysis, *Biochem. Biophys. Rep.* *25*, 100914. (DOI: 10.1016/j.bbrep.2021.100914)

67. Soni N., Singh S., Sharma S., Batra G., Kaushik K., Rao C., Verma N. C., Mondal B., Yadav A., Nandi C. K. (2021), Absorption and Emission of Light in Red Emissive Carbon Nanodots, *Chem. Sci.*, *12*, 3615–3626. (DOI: 10.1039/D0SC05879C)
68. Gao Y., Li S., Li Y., Yao L., Zhang H. (2017), Accelerated Photocatalytic Degradation of Organic Pollutant over Metal-Organic Framework MIL-53(Fe) under Visible LED Light Mediated by Persulfate, *Appl. Catal., B*, *202*, 165–174. (DOI: 10.1016/j.apcatb.2016.09.005)
69. Wang Y.-Q., Fang Z., Min H., Xu X.-Y., Li Y. (2022), Sensitive Determination of Ofloxacin by Molecularly Imprinted Polymers Containing Ionic Liquid Functionalized Carbon Quantum Dots and Europium Ion, *ACS Appl. Nano Mater.*, *5*, 8467–8474. (DOI: 10.1021/acsanm.2c01583)
70. Stepanova M., Gromova Y., Dubavik A., Maslov V., Orlova A., Zakharov V. (2022), Carbon Dot Films with Efficient Interdot Förster Resonance Energy Transfer for Optical Coding by Ultraviolet Photooxidation, *J. Phys. Chem. C*, *126*, 10441–10448. (DOI: 10.1021/acs.jpcc.2c01736)
71. Dalal C., Garg A. K., Mathur M., Sonkar S. K. (2022), Fluorescent Polymer Carbon Dots for the Sensitive–Selective Sensing of Fe³⁺ Metal Ions and Cellular Imaging, *ACS Appl. Nano Mater.*, *5*, 12699–12710. (DOI: 10.1021/acsanm.2c02544)
72. Mahto M. Kr., Samanta D., Shaw M., Shaik M. A. S., Basu R., Mondal I., Bhattacharya A., Pathak A. (2023), Blue-Emissive Nitrogen-Doped Carbon Dots for Picric Acid Detection: Molecular Fluorescence Quenching Mechanism, *ACS Appl. Nano Mater.*, *6*, 8059–8070. (DOI: 10.1021/acsanm.3c01523)
73. Yuan X.-T., Xu C.-X., Geng H.-Z., Ji Q., Wang L., He B., Jiang Y., Kong J., Li J. (2020), Multifunctional PVDF/CNT/GO Mixed Matrix Membranes for Ultrafiltration and Fouling Detection. *J. Hazard. Mater.*, *384*, 120978. (DOI: 10.1016/j.jhazmat.2019.120978)

74. Jayakumar O. D., Mandal B. P., Majeed J., Lawes G., Naik R., Tyagi A. K. (2013), Inorganic–Organic Multiferroic Hybrid Films of Fe₃O₄ and PVDF with Significant Magneto-Dielectric Coupling, *J. Mater. Chem. C*, *1*, 3710–3715. (DOI: 10.1039/C3TC30216D)
75. Huang P., Xu S., Zhong W., Fu H., Luo Y., Xiao Z., Zhang M. (2021), Carbon Quantum Dots Inducing Formation of β Phase in PVDF-HFP to Improve the Piezoelectric Performance, *Sens. Actuators, A*, *330*, 112880. (DOI: 10.1016/j.sna.2021.112880)
76. Singh S., Shauloff N., Sharma C. P., Shimoni R., Arnusch C. J., Jelinek R. (2021), Carbon Dot-Polymer Nanoporous Membrane for Recyclable Sunlight-Sterilized Facemasks, *J. Colloid Interface Sci.*, *592*, 342–348. (DOI: 10.1016/j.jcis.2021.02.049)
77. Li D., Liu J., Kwok R. T. K., Liang Z., Tang B. Z., Yu J. (2012), Supersensitive Detection of Explosives by Recyclable AIE Luminogen-Functionalized Mesoporous Materials, *Chem. Commun.*, *48*, 7167–7169. (DOI: 10.1039/C2CC31890C)
78. Lin L., Rong M., Lu S., Song X., Zhong Y., Yan J., Wang Y., Chen X. (2015), A Facile Synthesis of Highly Luminescent Nitrogen-Doped Graphene Quantum Dots for the Detection of 2,4,6-Trinitrophenol in Aqueous Solution, *Nanoscale*, *7*, 1872–1878. (DOI: 10.1039/C4NR06365A)
79. Sun X., He J., Meng Y., Zhang L., Zhang S., Ma X., Dey S., Zhao J., Lei Y. (2016), Microwave-Assisted Ultrafast and Facile Synthesis of Fluorescent Carbon Nanoparticles from a Single Precursor: Preparation, Characterization and Their Application for the Highly Selective Detection of Explosive Picric Acid, *J. Mater. Chem. A*, *4*, 4161–4171. (DOI: 10.1039/C5TA10027E)
80. Pal A., Sk M. P., Chattopadhyay A. (2016), Conducting Carbon Dot–Polypyrrole Nanocomposite for Sensitive Detection of Picric Acid, *ACS Appl. Mater. Interfaces*, *8*, 5758–5762. (DOI: 10.1021/acsami.5b11572)
81. Kaur M., Mehta S. K., Kansal S. K. (2017), Nitrogen Doped Graphene Quantum Dots: Efficient Fluorescent Chemosensor for

- the Selective and Sensitive Detection of 2,4,6-Trinitrophenol, *Sens. Actuators, B*, *245*, 938–945. (DOI: 10.1016/j.snb.2017.02.026)
82. Gupta M., Lee H. (2018), Recyclable Polymeric Thin Films for the Selective Detection and Separation of Picric Acid, *ACS Appl. Mater. Interfaces*, *10*, 41717–41723. (DOI: 10.1021/acsami.8b15369)
83. Liu W., Chen C., Wu Z., Pan Y., Ye C., Mu Z., Luo X., Chen W., Liu W. (2020), Construction of Multifunctional Luminescent Lanthanide MOFs by Hydrogen Bond Functionalization for Picric Acid Detection and Fluorescent Dyes Encapsulation, *ACS Sustainable Chem. Eng.*, *8*, 13497–13506. (DOI: 10.1021/acssuschemeng.0c04713)
84. Priya, Sharma A. K., Kaith B. S., Vipula, Chandel K., Singh A., Isha. (2020), Chemically Modified Chitosan-sodium Alginate as Chemo-Sensor Adsorbent for the Detection of Picric Acid and Removal of Biebrich Scarlet, *Int. J. Biol. Macromol.*, *147*, 582–594. (DOI: 10.1016/j.ijbiomac.2020.01.090)
85. Kumar M., Chauhan M. S., Akhtar M. S., Umar A. (2021), Effect of Cerium Ions in Ce-Doped ZnO Nanostructures on Their Photocatalytic and Picric Acid Chemical Sensing, *Ceram. Int.*, *47*, 3089–3098. (DOI: 10.1016/j.ceramint.2020.09.145)



Chapter 4

**A Carbon Dots Anchored Bacterial
Cellulose Hybrid Platform as a
Fluorescent Sensor and Photocatalytic
Remover of Pharmaceuticals**

4.1. Introduction

Throughout the 20th century, antibiotics have been significant drugs in the global medical market, which have been used to treat bacterial diseases and other microorganisms. Unfortunately, the widespread use of these antibiotic drugs, particularly those that combat bacterial resistance or operate as antibacterial agents, has detrimental effects on human health as well as soil and water sources [1, 2]. Therefore, a wide range of analytical techniques have been developed to examine the presence of antibiotics in the environment, humans, and pharmaceutical formulations [3]. Many important antibiotics, including benzylpenicillin, macrolides, tetracyclines, streptomycetes, chloramphenicol, and doxycycline (DOX), are typically found in or derived from living organisms [4]. Among them, tetracycline (TET) and DOX are the most widely used groups of antibiotics for the prevention and treatment of microbial infections due to their availability, affordability, and broad-spectrum antibacterial effect [5, 6]. However, overdosing or prolonged low-dose exposure to TET and DOX can lead to residues in environmental matrices that can cause allergic reactions, bacterial resistance, liver damage, and direct toxicity [7]. Moreover, they can also harm human health through long-term enrichment in the food chain. Therefore, there is an urgent need to design quick and sensitive approaches for the detection and removal of antibiotics in environmental waters [8].

Furthermore, the extensively utilized conventional detection and separation methods mainly include liquid chromatography integrated mass spectrometry, high-performance liquid chromatography, capillary electrophoresis, and so on. However, although these methods show high specificity and sensitivity, they also have various drawbacks, such as long-time consumption, the need for a precise instrument, complicated sample preparation, as well as they are costly [9]. Recently, the development of a new type of sensor that involves the use of immunological [10], fluorescence (FL) [5], and electrochemical techniques [11], which have gained immense interest. Among them,

FL sensors are considered desirable candidates for TET and DOX detection owing to their remarkable characteristics of simplicity, rapidity, and operability [7, 12]. Also, the timely upgradation of sensing technologies is needed in this era, as the volume and severity of water and soil pollution are reaching new heights. Previously, a wide range of sensors involving nanomaterials and synthetic organic and inorganic compounds have been developed to achieve superior detection of pollutants [13-15]. Recently, carbon-based nanomaterials [16-18], perovskites [19, 20], hybrid coacervates [21], plasmonic nanomaterials [22], etc., have gained a lot of interest in the field of environmental remediation due to their unique optoelectronic and photophysical properties. Among them, Carbon dots (CDs) have been extensively employed in sensing applications, especially for the detection of numerous analytes such as metal ions [23], antibiotics [24], biomolecules [25], explosive nitro compounds [26], etc. CDs are predominantly utilized as fluorescent probes in FL-based sensors due to their prominent water solubility, photostability, low toxicity, superior biocompatibility, and tunable FL properties. The small size (2-10 nm) of CDs with high quantum yield (QY) and tunable surface functionalization makes them promising candidates for FL sensing applications [27, 28]. Notably, the catalytic property of CDs has also been further explored toward the removal of pollutants from the ecosystem, as it is equally important to the analytical detection of the contaminants. CDs act as photocatalysts to degrade various pollutants via the generation of electrons and holes [29-31]. Altogether, the excellent optical and catalytic properties of CDs make them attractive, multifaceted nanomaterials for the simultaneous degradation and detection of pollutants, which is anticipated to effectively address the important challenge of sensing and catalyzing the degradation of pollutants.

Furthermore, enhanced efficiency, reusability issues, and material loss were achieved for CD-based composites. By taking advantage of surface functional groups present on CDs that can be easily incorporated into polymers, membranes, or papers [32-34]. In this

aspect, Bacterial cellulose (BC), a prevalent biomass material, is widely recognized as an exceptionally attractive three-dimensional (3D) polymer composed of a large number of intertwined fibers that can be utilized [35]. BC, which is free from lignin and hemicellulose, is synthesized by bacteria instead of plants and possesses a nanofibrous structure [36]. It is an excellent substrate to host CDs with attractive properties such as phenomenal aqueous solubility, high mechanical strength, low cost, biodegradability, biocompatibility, flexibility, porous matrix, and chemical stability [37], which makes BC much superior to many synthetic polymeric materials in device fabrication. The incorporation of CDs into BC hydrogel therefore yields a robust FL active hydrogel system with greater flexibility, surface area, porosity, etc.

Previously, many groups have focused on CD-based hydrogel composites for sensing as well as photocatalysis applications. For example, Huang et al. prepared a hydrogel by incorporating optically active CDs into a polyacrylamide hydrogel network for recognizing dual metal ions [33]. Similarly, Ehtesabi et al. reported the detection of TET by CDs encapsulated in sodium alginate hydrogel [9]. Also, Das et al. synthesized a MoS₂ nanoflower decorated on graphene aerogel for photocatalytic degradation of TET. However, it is worth mentioning that most of these recent reports demonstrate different hydrogel systems for sensing and degradation applications. The scope of simultaneous usage of a single system for sensing as well as pollutant elimination is yet under investigation. To fill this gap, we have synthesized a single entity and explored its FL and catalytic properties for sensing and degradation of antibiotics TET and DOX. Furthermore, this work was designed to synthesize CDs from melamine and sodium citrate precursors via a single-step hydrothermal method to produce the photocatalytically active, luminescent M-CDs. The obtained M-CDs were subsequently incorporated into a fibrous three-dimensional BC to fabricate fluorescent sensor M-CD@BC, which is used for FL detection as well as photocatalytic degradation of

TET and DOX under sunlight illumination. M-CD@BC showed FL quenching upon the addition of TET and DOX with high sensitivity. The sustained stability of M-CDs@BC FL further justified the reusability of the composite system.

4.2. Experimental Section

4.2.1. Materials and Reagents

The sodium salt of ethylenediaminetetraacetic acid ($\text{Na}_2\text{-EDTA}$), melamine, and erythromycin (ERY) were obtained from Sigma-Aldrich. Sodium citrate was procured from Spectrochem, TET hydrochloride, DOX hyclate, norfloxacin (NOR), ampicillin sodium salt (AMP), vancomycin hydrochloride (VAN), ciprofloxacin hydrochloride hydrate (CIP), streptomycin hydrate (STR), sodium sulphate (Na_2SO_4), and tert-butyl (t-BuOH) were obtained from SRL, and NaOH was obtained from TCI. Benzoquinone (BZQ) was purchased from Lobachem. Deionized (DI) water was procured from the instrument central facility of IIT Indore.

4.2.2. Characterization Techniques

The prepared samples were thoroughly characterized to functionally elucidate the structure, morphology, particle shape, size, surface area, and energy absorption sites. The structure was determined and highlighted by X-ray diffraction (XRD) analyses with Cu $K\alpha$ radiation (model D/max2200PC, Rigaku Co., made in Japan). The morphology and microstructure of samples were characterized by scanning electron microscopy (SEM) (Verios 460, FEI, USA) and transmission electron microscopy (TEM) (Tecnai G2 F20, FEI, USA). The particle shape and size were determined from TEM images, and surface electronic states were evaluated by using X-ray photoelectron microscopy (XPS) using PHI 5000 Versa Probe II (ULVAC-PHI Inc., USA) equipped with a micro-focused (200 mm, 15 kV) monochromatic Al $K\alpha$ X-ray source ($h\nu = 1486.6$ eV). Photoluminescence (PL) spectra were determined using a Fluoromax-4 spectrofluorometer (HORIBA Jobin Yvon, model FM100) with an excitation and emission slit width of 2 nm in a quartz

cell (1×1 cm). The Fourier transform infrared (FTIR) spectra were collected in the 4000-400 cm⁻¹ range using an attenuated total reflectance-Fourier transform infrared spectroscope (ATR-FTIR) (Bruker Alpha II system). The absorption spectra in the photocatalytic degradation process were obtained by a Shimadzu 2100 UV-vis spectrometer. The specific surface areas of the aerogels were measured by the Brunauer-Emmett-Teller (BET) method using Autosorb-1C (AX1C-MP-LP) at 298 K. The pore size distribution was obtained by the Barrett-Joyner-Halenda (BJH) method. Electrospray Ionization Quadrupole time-of-flight Liquid Chromatography-Mass Spectrometer (LC-MS) designed by a Bruker MicrOTOF-Q II Daltonik, utilized for exact mass and true isotopic measurements. Liquid Chromatography-Mass Spectrometry (LC-MS) Brunker micrOTOF-Q II Daltonik.

4.2.3. Quantum Yield (QY)

The QY of M-CDs was determined by using quinine sulfate as the reference standard solution. It was calculated using the following equation:

$$\Phi = \Phi_{QS} \times \frac{S_S}{S_{QS}} \times \frac{A_S}{A_{QS}} \times \frac{n_S^2}{n_{QS}^2} \quad (4.1)$$

Whereas, Φ and Φ_{QS} are the QYs of the M-CDs and quinine sulfate, respectively. A_S and A_{QS} represent the absorbance, S_S and S_{QS} represent integrated intensity, and n_S and n_{QS} represent the refractive indices of M-CDs and quinine sulfate, respectively.

4.2.4. Synthesis of M-CDs

In a typical synthesis, melamine and sodium citrate were used as precursors. Briefly, 0.08 M melamine was dissolved in 20 mL of DI water, consisting of 0.014 M sodium citrate, under ultrasonication for 30 min. The resulting mixture was added into a Teflon-lined sealed stainless-steel autoclave and treated at 200 °C for 12 h; then the autoclave was cooled down to room temperature. The obtained product

was centrifuged at 10000 rpm and then dialyzed for 12 h against DI water. The obtained yellow dispersion was named M-CDs.

4.2.5. Synthesis of M-CDs@BC

A BC pellicle ($3 \times 3 \times 0.5 \text{ cm}^3$) was pre-soaked in M-CD precursor solution (reaction mixture prepared as for M-CDs) and added to a Teflon-lined stainless-steel autoclave. The same procedure was followed as above to obtain M-CDs anchored on BC hydrogel (M-CDs@BC).

4.2.6. Detection of TET and DOX with M-CDs

For analyzing the selectivity of synthesized M-CDs towards pharmaceuticals, different antibiotics, viz. TET, DOX, NOR, AMP, VAN, CIP, ERY, and STR were checked. The interactions between M-CDs and various analytes were analyzed using FL studies, where the concentration of M-CDs was set as 11.2 mg/mL, mixed with 200 μM of different antibiotics. The solution was kept in a static condition to maintain the equilibrium for 1 min. Each of the samples was studied at least three times. The FL spectra of the resulting solutions were recorded under the same experimental conditions.

Further, sensitivity studies were carried out with TET and DOX. A series of TET and DOX, and M-CDs (11.2 mg/mL) with different concentrations of TET and DOX (0-200 μM) were prepared, and their FL signals were recorded. Afterward, to explore the selectivity of M-CDs for TET and DOX detection while coexisting with other antibiotics such as NOR, AMP, VAN, CIP, AMO, and STR were also checked by FL spectroscopy.

The limit of detection (LOD) was calculated by the following equation:

$$\text{LOD} = 3.3 \times \sigma / S \quad (4.2)$$

Where σ is the error, and S is the slope of the calibration plot.

The Stern-Volmer equation was used to determine the quenching constant (K_{sv}):

$$\frac{I_0}{I} = 1 + K_{SV}[C] \quad (4.3)$$

where I_0 and I are the CDs' emission intensities before and following the addition of analytes, respectively, and $[C]$ is the analyte concentration. All the experiments were triplicated under similar conditions. The stability tests of M-CDs under different conditions, such as ionic strength, pH, and temperature, are performed with the aid of FL spectroscopy.

4.2.7. Antibiotics Detection in Real Samples

The reliability of this analytical sensor for real-time applications was checked using milk (procured from a local milk shop), tap water (from the laboratory), groundwater (Simrol, Indore), and seawater (Arabian Sea, Mumbai). The milk samples for detecting TET and DOX were prepared using the previously reported literature [38]. Briefly, the raw milk was diluted 2.5 times, then the pH of the milk was lowered to 4.5 by adding 10 % trifluoroacetic acid. Then sonicate the above solution at room temperature for 15 min. This solution was centrifuged for 15 min at 12000 rpm to get a clear supernatant, which was again neutralized via 30 % NaOH and again centrifuged to remove any deposit. Further, water samples and milk samples were spiked with different concentrations of TET and DOX, separately, and the sensing of the same was performed.

4.2.8. M-CDs@BC Sensing TET and DOX

FL detection tests of various antibiotics by M-CDs@BC were carried out with a similar procedure adopted for M-CDs. The M-CD@BC hydrogel (3×3×0.5 cm³ hydrogel) was immersed in different antibiotics such as TET, DOX, NOR, AMP, VAN, CIP, ERY, and STR, prepared in 50 mL (200 μM) and further incubated for 5 min before FL analysis. The FL sensitivity of M-CD@BC towards TET and DOX was also examined by analyzing different concentrations of analyte (ranging from 0-200 μM).

4.2.9. Photocatalytic Experiments

The photocatalytic studies of as-synthesized M-CDs were performed towards the degradation of TET and DOX aqueous solutions under sunlight irradiation. Two 50 mL experimental solution mixtures were prepared, each containing M-CDs (11.2 mg/mL) spiked with TET and DOX (20 mg/L) separately. The mixtures were allowed to achieve adsorption and desorption equilibrium in the dark under continuous stirring for approximately 15 min. Afterward, all the photocatalysis experiments were performed under natural sunlight (from 11:30 am to 1:30 pm on March 2023 at IIT Indore campus, Simrol, India, with an average sunlight intensity of 1 kW/m²). At an interval of 15 min, 3 mL of solution was collected, and the changes in concentrations of TET and DOX were measured by noting λ_{\max} in a UV-vis spectrophotometer. The photodegradation of TET and DOX antibiotics was calculated using equation 4.4:

$$\% \text{ Degradation} = \frac{(C_0 - C_t)}{C_0} \times 100 \quad (4.4)$$

Where C_0 and C_t are the initial and remaining concentrations at time t , respectively, for TET and DOX.

Additionally, the values for photocatalytic degradation of TET and DOX were fitted to a pseudo-first-order equation (equation 4.5), and the rate constant (k) was calculated from the corresponding slope of a fitting line.

$$-\ln(C_t/C_0) = kt \quad (4.5)$$

The further photocatalytic performance of M-CDs@BC hydrogel (3×3×0.5 cm³) towards the degradation of TET and DOX under sunlight was investigated. Briefly, the hydrogel containing TET and DOX solutions was separately stirred in the dark for 15 min to ensure the achievement of adsorption-desorption equilibrium. After that, the above mixture was exposed to solar light to initiate photodegradation, and an aliquot solution of 3 mL was taken every 15 min degradation of TET and DOX was determined using UV-visible spectroscopy. The % degradation and the rate of reaction were determined by using

equations 4.4-4.5, respectively. After each cycle, the M-CDs@BC were washed thoroughly with dilute acid and multiple times with DI and resuspended in fresh TET and DOX for 5 cycles. All the experiments for TET and DOX were conducted separately.

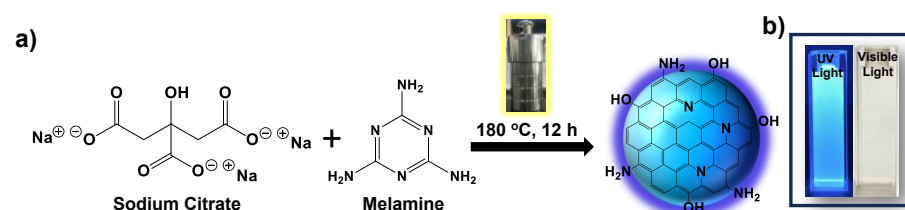
4.2.10. Electrochemical Photocurrent Measurement

The photocurrent using the amperometry *i-t* curve mode and electrochemical impedance spectra (EIS) over a frequency range of 1 to 105 Hz with an AC voltage amplitude of 10 mV was recorded in an AUTOLAB PGSTAT 204N electrochemical workstation, and all the electrochemical measurements were carried out using a three-electrode cell with 0.5 M Na₂SO₄ as an electrolyte. The M-CDs sample as a working electrode, Ag/AgCl as a reference, and a platinum (Pt) wire as a counter electrode were utilized. All the photo-electrochemical measurements were conducted using a blue light source with 100 mW cm⁻² power density.

4.3. Results and Discussion

4.3.1. Preparation and Characterization of M-CDs

The M-CDs were synthesized via the hydrothermal method from melamine precursors as shown in **Scheme 4.1a**. Melamine (triamino-s-triazine) is a nitrogen-rich compound of considerable economic, industrial, and scientific importance [39, 40]. Therefore, we selected melamine as a major precursor for synthesizing highly fluorescent CDs. **Scheme 4.1b** indicates the aqueous dispersion of M-CDs under UV with excitation wavelength (λ_{ex}) of 365 nm and visible light, which exhibited the light-yellow colour and strong blue FL, respectively.



Scheme 4.1. (a) Schematic illustration of the synthesized M-CDs, (b) photograph of the aqueous dispersion under UV ($\lambda_{\text{ex}} = 365 \text{ nm}$) and visible light illumination.

The M-CDs were characterized through XPS, TEM, FTIR, PXRD, UV-vis, and PL spectroscopy. A distinct absorption peak at 346 nm arises from the $n\text{-}\pi^*$ transition of multi-conjugate C=O and C-O on the M-CDs surface, along with the former peak at 245 nm, which arises due to $\pi\text{-}\pi^*$ transition of aromatic sp^2 carbon within CDs' core (**Figure 4.1a**). Upon excitation at 350 nm, the PL band of M-CDs is observed at 440 nm, with no shift in the emission wavelength (**Figure 4.1b**). The excitation-independent PL may result from the same emissive traps on the surface of M-CDs. The PL QY at an excitation wavelength of 350 nm is 16.7 %, which was calculated from **Equation 4.1**. From the decay curve, which was fitted biexponentially in **Figure 4.1c**, the average FL lifetime of M-CDs was observed to be 7.13 ns. The TEM image reveals a structural detail of M-CDs, which indicates the existence of evenly dispersed spherical M-CDs with a size ranging from 2.4-4.4 nm (**Figure 4.1d** and histogram; inset). The HR-TEM image displays distinct lattice fringes with a characteristic d-spacing of 0.26 nm, which is the in-plane (100) spacing of graphene (**Figure 4.1e**). Further, a broad PXRD peak at $2\theta = 23.6^\circ$ suggests the amorphous nature of these M-CDs (**Figure 4.1f**), which is for (002) graphitic carbon structures [41]. **Figure 4.1g** shows the FTIR spectrum of M-CDs demonstrates a wide peak at 3354 cm^{-1} is ascribed to the hydroxyl (-OH) or amine (-NH₂) groups. The stretching vibration peak of C=O/C=N is located at 1668 cm^{-1} , the bending vibration of N-H appears at 1566 cm^{-1} , and the peaks centered at 1405 and 1048 cm^{-1} could be ascribed to C-H bending and C-O-C stretching vibrations, suggesting the existence of O-H, N-H/NH₂, and C=O functional moieties on the surface of CDs.

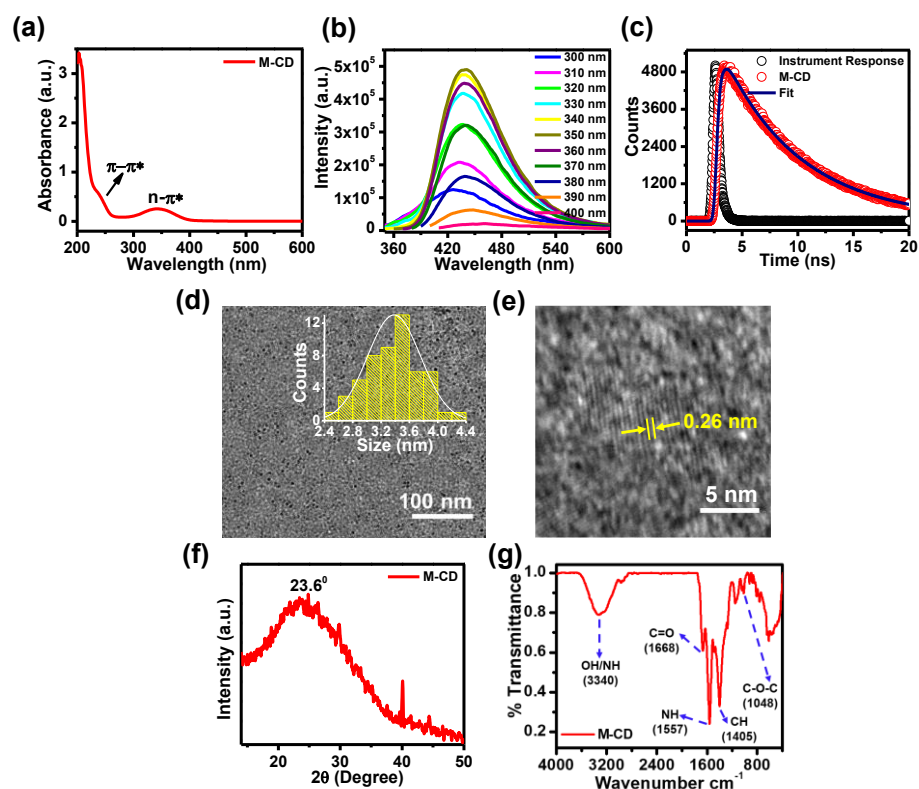


Figure 4.1. (a) Absorption, (b) FL spectra, and (c) lifetime data. (d) TEM image (inset; histogram), and (e) HR-TEM showing lattice fringes. (f) XRD spectra. (g) FTIR spectrum of the synthesized M-CDs.

The XPS survey scan reveals the surface functionality in the case of M-CDs, indicating the presence of carbon, oxygen, and nitrogen (**Figure 4.2a**). The deconvoluting C1s, N1s, and O1s spectra (**Figure 4.2b-d**) facilitated the determination of C-C/C=C, C-O, C=O, C-OH/COO- groups, pyrrolic-N, pyridinic-N, and graphitic-N. Several hydrophilic functional groups present on the surface of the CD enabled them to disperse well in the experimental solution.

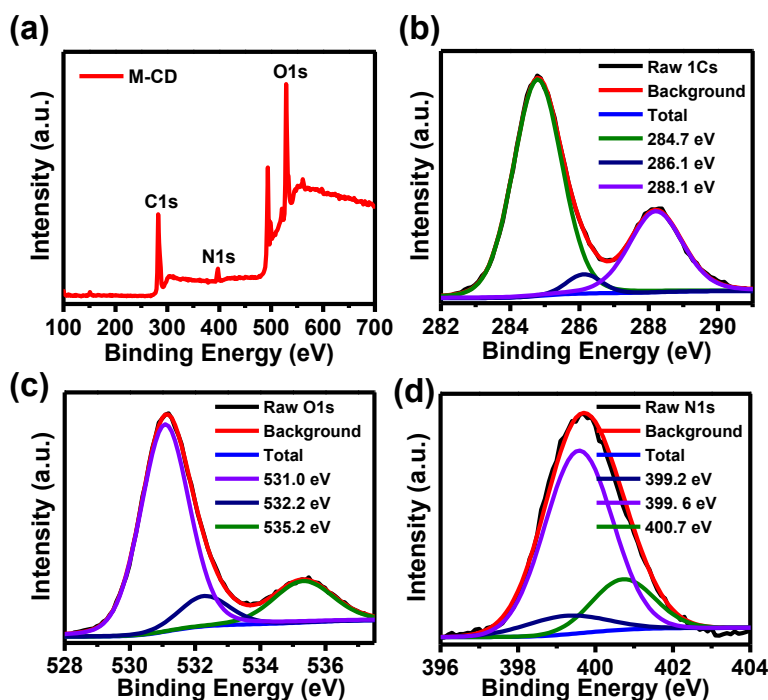


Figure 4.2. (a) XPS survey spectrum. High-resolution XPS spectra of: (b) C1s, (c) O1s, (d) N1s of M-CDs.

In addition, the M-CDS exhibited essential FL stability against different NaOH concentrations, pH values, and temperatures (**Figure 4.3a-c**). Overall, these results demonstrate the formation of evenly distributed, colloiddally stable, and luminescent spherical M-CDs, and these features are crucial for sensing TET and DOX in actual metrics.

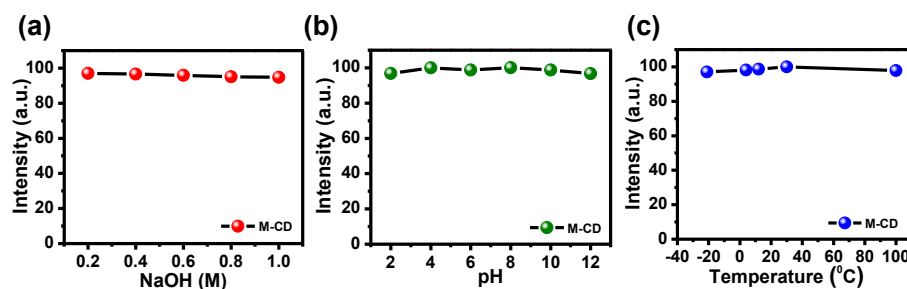


Figure 4.3. Stability plot of M-CDs in the presence of (a) NaOH, (b) pH, and (c) temperature.

4.3.2. Fabrication of M-CD@BC

The M-CD@BC were fabricated by reacting melamine dissolved in sodium citrate with BC under a one-step hydrothermal synthesis method (**Figure 4.4a**). All non-bounded M-CDs were washed off with

fresh water, and the leaching study was repeated until no more FL was observed in the washings. The lyophilized M-CD@BC was utilized further for various morphological and spectroscopical studies to substantiate the above argument and establish the approach. The morphological characterization reveals maximum fibers are within the size range of 60 nm. Also, for a better understanding of the incorporation of M-CDs onto BC, the TEM analysis has been performed, which confirms the adsorption or internalization of M-CDs within BC as indicated in **Figure 4.4b**. Further, the micromorphology of BC (**Figure 4.4c**) and composite M-CD@BC (**Figure 4.4di**) was confirmed by SEM. Importantly, SEM analysis indicates the incorporation of M-CDs on the polymeric network of BC, and they are well bound as indicated in the magnified SEM image of M-CD@BC shown in **Figure 4.4dii**. Also, the porosity of BC remains unaltered, which confirms the deposition of M-CDs on the membrane. Through SEM images, the thicknesses of fibers were analyzed and a histogram was drawn (**Figure 4.4c and 4.4di; inset**), showing the width of BC fibers falls in the 20-100 nm range.

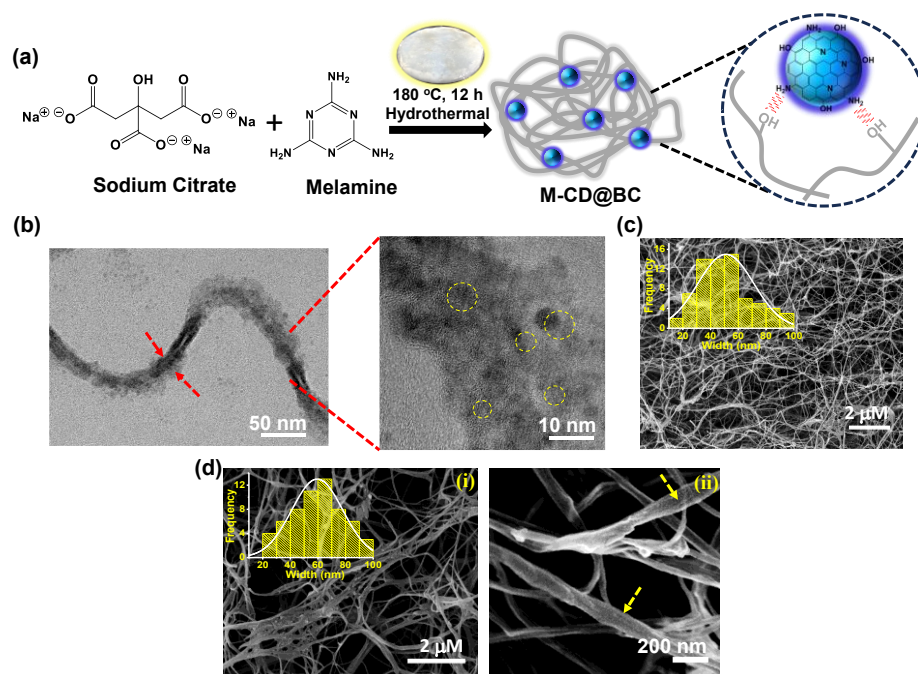


Figure 4.4. (a) Schematic illustration of the synthesis of M-CD@BC by the incorporation of M-CDs onto BC. b) TEM image of M-

CD@BC (red dotted arrows point to the attached M-CD on BC fibers). SEM images of M-CD@BC (c) BC showing nanofibrous porous network structure (inset: histogram from a width of cellulose fibers), (d) (i) Nanofibrous porous network of BC incorporating M-CDs (inset: histogram from a width of cellulose fibers), and (ii) magnified image.

The BET analysis was performed to know about the specific surface area and pore distribution (**Figure 4.5a-d**), which gives a high specific surface area before and after the incorporation of M-CDs on BC. Though the porosity of the composite was maintained upon incorporation of M-CDs, a small reduction in pore volume from 24.6 nm to 23.5 nm is evident, probably due to the incorporation of M-CDs.

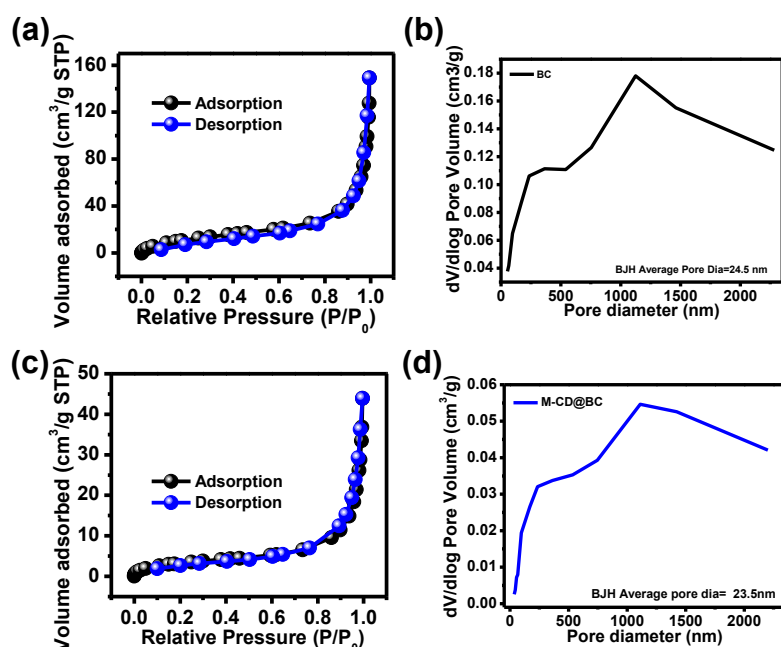


Figure 4.5. Nitrogen adsorption and desorption analysis conducted for control pristine BC and M-CD@BC aerogels: a) BET adsorption isotherms, and b) corresponding BJH pore volume plots for BC. c) BET adsorption isotherms, and d) corresponding BJH pore volume plots for M-CD@BC.

The surface chemistry of BC samples before and after modification can be discussed via ATR-FTIR. A comparison of the FTIR data observed for M-CD@BC with that of the BC and M-CDs is presented in **Figure 4.6a**. The stretching vibrational peaks corresponding to O-H/N-H

bonds appeared as a considerable broadband between 3111–3478 cm^{-1} in M-CDs. However, it is worth mentioning that the intensity of the -OH/N-H stretch vibrations (broad peak at 3354 cm^{-1} in M-CDs) is greatly reduced and shifted to 3340 cm^{-1} in M-CD@BC, which can be attributed to the interactions of a large proportion of -NH moieties of M-CDs with the functional groups of BC. Interestingly, a shift in the bending vibrations of N-H moieties was observed from 1563 to 1551 cm^{-1} in M-CDs and M-CD@BC, respectively. A shift in the -OH stretching of BC was observed from 1427 to 1434 cm^{-1} upon the formation of M-CD@BC. Altogether, these changes in the FTIR spectrum of M-CDs and BC upon the formation of M-CD@BC point towards the electrostatic interactions between the -NH and -OH groups of M-CDs and BC. These results, along with XPS data, further substantiate that M-CDs have been successfully integrated with BC. The XPS survey scan recorded for M-CD@BC, BC, and M-CDs are compared in **Figure 4.6b**. The XPS of M-CDs reveals the presence of carbon (C), oxygen (O), and nitrogen (N) (Red line) and survey scan spectra of BC exhibited two peaks at 284.0 and 530.4 eV, indicative of presence of C and O, respectively (**Figure 4.6b**; grey line). Further, the survey spectrum of M-CD@BC proves the coexistence of C, N, and O elements (**Figure 4.6b**; blue line), which confirms the anchoring of M-CDs on BC due to the reoccurrence of the N peak in M-CD@BC. These observations signify the successful incorporation of M-CDs onto BC.

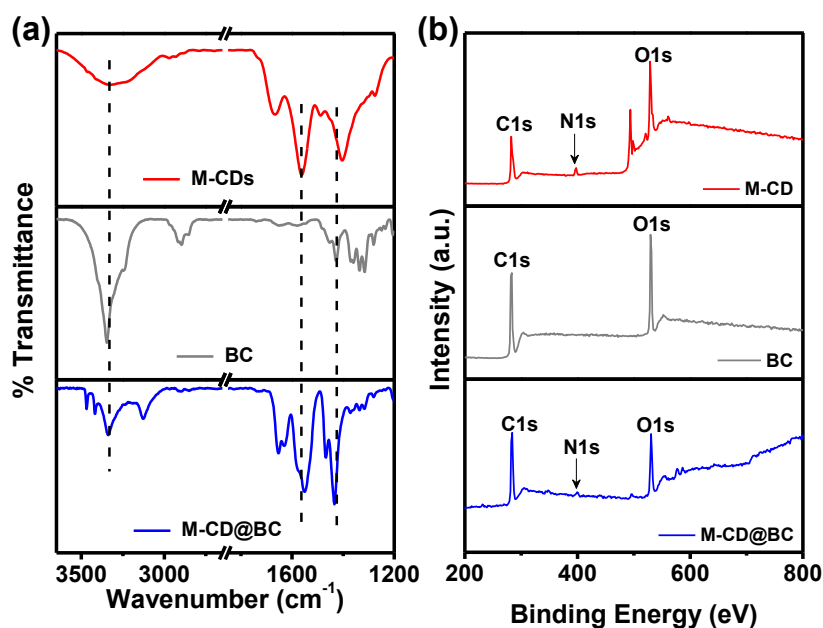


Figure 4.6. (a) ATR-FTIR spectrum, and (b) comparative XPS survey spectra of M-CD, BC, and M-CD@BC.

As displayed in **Figure 4.7a** (grey line), the spectral absorption values of pure BC are in the range of 200-800 nm, and there is only a small absorption peak in the wavelength range of 220 to 250 nm. The addition of M-CDs in BC increased the absorption in the range of 200-800 nm. An absorption spectrum for M-CD@BC is shown in **Figure 4.7a** (blue line) features 2 peaks at 229 nm and 455 nm. The later peak in M-CD@BC is one of the indications of interaction between neat M-CDs and BC and forms a hydrogel composite M-CD@BC. However, the optical band gap was measured at room temperature by extrapolating the linear portion of the plot of the square root of the absorption coefficient versus photon energy (**Figure 4.7b**). Further, the FL properties of both the hydrogel, i.e., BC and M-CD@BC, were studied. Equitable cuboid hydrogel (3×3×0.5 cm³) was utilized to check the FL property of the hydrogel. The results obtained in **Figure 4.7c** indicate that only the hydrogel-incorporated M-CDs are fluorescent, and their emission intensity is unaltered after purification. **Figure 4.7d** is the horizontal photograph view of the freshly prepared M-CD@BC hydrogel under visible and UV light. Thus, the composite incorporates the PL properties of the M-CDs in a macroscopic

network. The nanoscopic property is now expressed at the macroscopic scale.

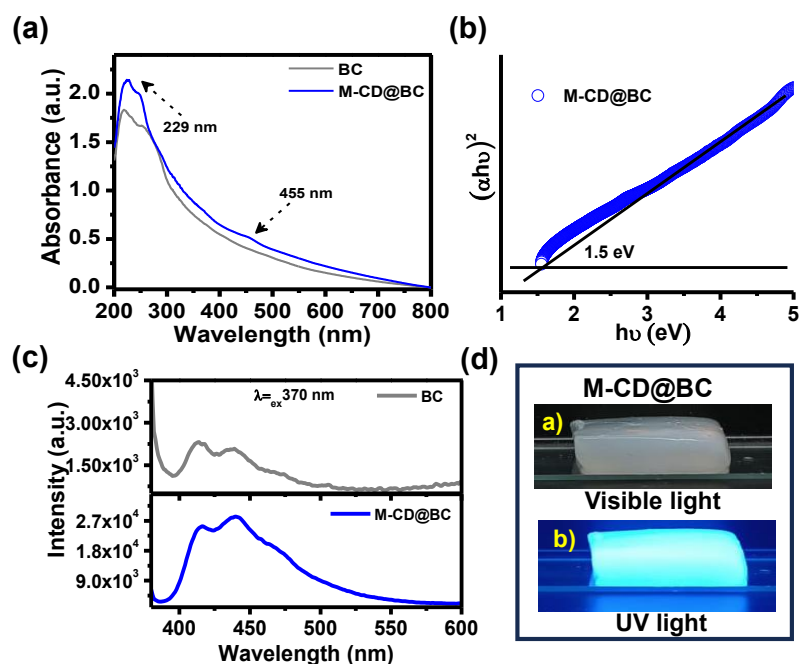


Figure 4.7. (a) Absorbance spectra of BC (grey line) and M-CD@BC (blue line), (b) band gap estimation of M-CD@BC. (c) FL spectra of BC (grey line) and M-CD@BC (blue line), and (d) digital photographs of M-CD@BC observed under visible and UV light ($\lambda_{\text{ex}} = 365 \text{ nm}$).

4.3.3. Selective Sensing of TET and DOX

After establishing the physiochemical properties, the M-CDs and composite M-CD@BC can be utilized as efficient TET and DOX sensors. Initially, their optical activities were investigated in the presence of various antibiotics. The FL quenching performance of various antibiotics (concentration of $200 \mu\text{M}$) was evaluated to evaluate the selective FL response of M-CDs to various antibiotics. **Figure 4.8a** shows the selective FL response of M-CDs (11.2 mg/mL) with various antibiotics such as TET, DOX, NOR, AMP, VAN, CIP, ERY, and STR. The F/F_0 values for both TET and DOX were significantly lower (FL off) compared to other antibiotics, indicating that M-CDs exhibited a high selectivity towards TET and DOX. The circumstances can be attributed to the presence of nitrogen and oxygen-containing functional groups in M-CDs. These functional

groups exhibit a greater affinity towards TET and DOX in comparison to other antibiotics [42]. **Figure 4.8b-c** demonstrates the effects of antibiotic concentration on the FL property. Specifically, the FL intensity of M-CDs gradually decreased as the concentration of TET and DOX (ranging from 0 to 200 μM) increased, respectively, illustrating that M-CDs can act as a sensor for detecting the turn-off behavior of TET and DOX. The plot of intensity variation vs different concentrations of both the antibiotics follows a linear trend as a function of TET (**Figure 4.8d**) and DOX (**Figure 4.8e**) in a concentration range of 0-100 μM and 0-80 μM , respectively. Furthermore, the fluorescent digital images (under UV lamp) of M-CDs were captured after mixing the M-CDs with different antibiotics and are shown in **Figure 4.8f**. The LOD was estimated by **Equation 4.2** and found to be 133 nM for TET and 138 nM for DOX.

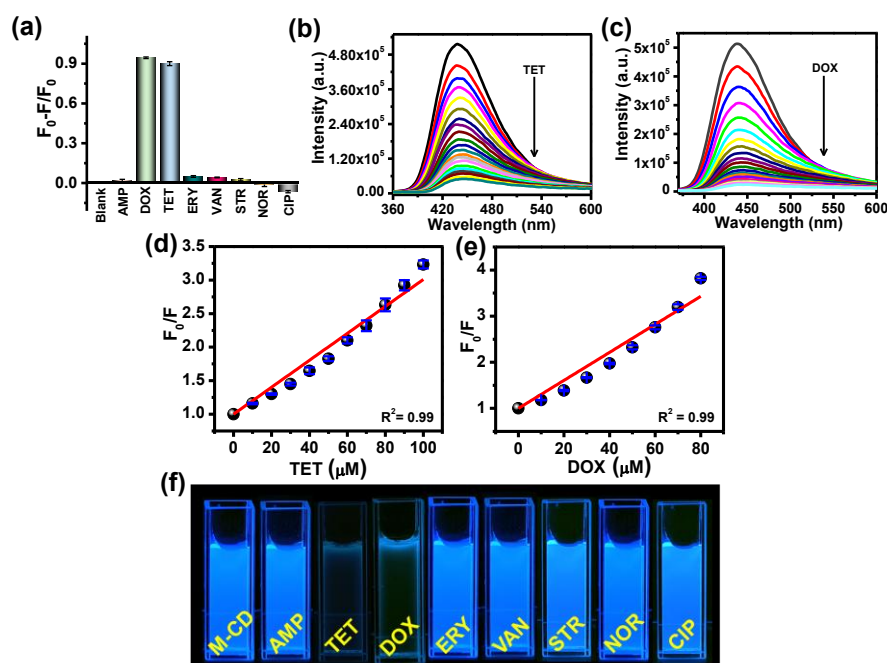


Figure 4.8. (a) FL intensity of the M-CDs recorded after incubation with the indicated different antibiotics for selective detection. M-CD emission spectra with different concentrations of (b) TET, and (c) DOX, ranging from 0-200 mM. The linearity plot of F/F_0 vs different concentrations of (d) TET and (e) DOX. (f) photographs of M-CDs in the presence of various antibiotics under UV light.

It was found that the findings were superior to most of the prior reported literature (**Table 4.1**). The K_{sv} was calculated from **Equation 4.3** and was found to be $2.0 \times 10^{-2} \text{ M}^{-1}$ in the presence of TET and $3.0 \times 10^{-2} \text{ M}^{-1}$ for DOX, indicating a strong interaction between functional groups and targeted antibiotics. As the value of K_{sv} is high, the quenching efficiency of M-CDs for antibiotic detection will be improved [43].

Table 4.1: The comparative performance of the sensing platform of antibiotics.

Sr. No.	Sensing Element	Analyte	Detection Range (μM)	LOD (nM)	Portable Platform	References
1.	Alginate-CDs nanocomposites	TC	1-20	2000	Hydrogel	9
2.	CDs	TC	10-400	6000	-	44
3.	Ag@SiO ₂	TC	0.2-400	16.2	-	45
4.	Cu-CQDs	TC	2-32	170	-	46
5.	N-CQDs	DC	-	250	-	5
6.	CDs/PVA composite	TC	0-350	170	Film	47
7.	Mn-PBA _{NaOH} @MIP	TC	0.2-200	70	-	48
8.	MoS ₂ QDs and Ca ²⁺	DC	0.2 to 100	23.2	-	7
9.	Eu ₂ -Al ₂ -MOG	DOX	2-200	770	Metal-Organic Gel	49
10.	M-CD	TET and DOX	0-100 and 0-80	133 and 138	-	Present Work
11.	M-CD@BC	TET and DOX	0-200	140 and 156	Hydrogel	Present Work

Furthermore, the interfering ability in detecting TET and DOX in the presence of other antibiotics was also assessed. The presence of interfering antibiotics did not have a substantial effect on the quenched FL signals, as demonstrated in **Figure 4.9**. Overall, the M-CDs exhibited excellent sensitivity and specificity towards TET and DOX compared to other antibiotics and were employed as a fluorescent probe for detecting TET and DOX in solution.

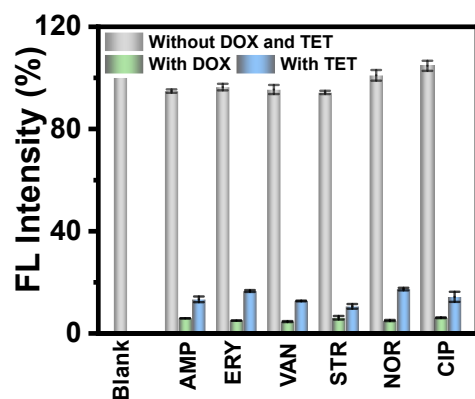


Figure 4.9. Competitive selectivity in the sensing response of M-CDs in the presence of various antibiotic compounds ($c = 1.0 \times 10^{-2}$ M).

4.3.4. Mechanism of FL Sensing

The quenching mechanism can be elucidated through various mechanisms, such as the inner filter effect (IFE), static or dynamic quenching, and so on. **Figures 4.10a-b** indicate the FL decay analysis of M-CDs with and without TET and DOX, where no remarkable change in average lifetime was observed, indicating the absence of dynamic quenching. To further confirm the quenching mechanism, the absorption spectra of TET and DOX, which extensively overlapped with the excitation spectra of M-CDs (**Figure 4.10c**), indicate that TET and DOX can induce suppression in FL of M-CDs attributed to IFE. Additionally, a shift in the UV-vis peak of M-CDs from 340 nm to 370 nm was observed when TET and DOX were added to M-CDs separately, and absorption intensity increased with TET and DOX concentration indicated in **Figure 4.10d-e**, respectively. The fact further confirms the IFE mechanism [5, 25]. **Figure 4.10f** is a schematic representation of M-CDs FL quenching in the presence of TET and DOX. From the above observations, we can summarize that M-CDs prefer static quenching and IFE as a mode of sensing mechanism.

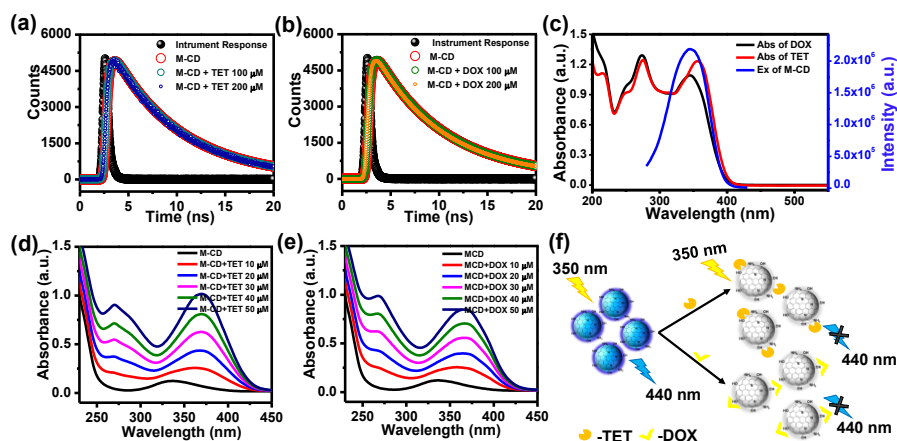


Figure 4.10. Lifetime decay curve with and without the presence of antibiotics: (a) TET, and (b) DOX. (c) UV-vis absorption spectra of TET and DOX showing spectral overlap with with FL excitation of M-CDs. UV-vis spectra of M-CD for different concentrations of d) TET and e) DOX. (f) Illustration of fluorometric detection of TET and DOX based on M-CDs.

4.3.5. TET and DOX Detection in Real Samples

Further, to imply the applicability of sensor M-CDs in the real world, the sensing of spiked samples was performed. The obtained results were summarized in **Tables 4.2-4.3**, which indicate that the M-CD has little or no effect on sensor response towards antibiotics other than TET and DOX when spiked in real water samples and milk. However, in the presence of M-CDs, the recovery of antibiotics TET and DOX is in the range of 98-104 % with a standard deviation of less than three. Excellent results with very low LOD, high precision, and the requirement of minimal pretreatment of the actual sample broaden the application of M-CDs for reliable and facile detection of TET and DOX.

Table 4.2. TET detection in real samples.

Sample	Spiked (μM)	Detected (μM)	Recovery (%)	SD (n=3)
Milk	0	ND ^a		
	20	19.9	98.3	2.2
	40	39.9	104.8	1.0
	60	59.9	99.9	0.7
Tap water	0	ND ^a		
	20	20.0	104.7	1.2
	40	39.8	99.7	0.5
	60	59.9	98.2	0.4
Sea water	0	ND ^a		
	20	19.9	100.5	0.8
	40	39.9	100.9	0.2
	60	59.9	99.9	0.1
Ground water	0	ND ^a		
	20	19.7	100.7	0.01
	40	40.0	104.5	0.6
	60	59.83	103.8	0.3

Table 4.3. DOX detection in real samples.

Sample	Spiked (μM)	Detected (μM)	Recovery (%)	SD (n=3)
Milk	0			
	20	19.9	99.5	1.8
	40	39.9	100.0	1.1
	60	59.8	99.7	0.4
Tap water	0			
	20	20.0	99.5	0.7
	40	39.8	104.2	0.2
	60	59.7	99.5	0.3
Sea water	0			
	20	19.9	99.1	0.4
	40	40.0	99.1	0.1
	60	59.7	100.7	0.1
Ground Water	0			
	20	19.9	104.9	0.1
	40	39.7	100.0	0.4
	60	60.0	99.7	0.2

4.3.6. Detection of TET and DOX with M-CD@BC Hydrogel

To enhance the reusability of M-CDs, we designed a hydrogel sensor by embedding M-CDs into BC, which not only builds a robust framework but also enables the detection of TET and DOX antibiotics. Because of the multiple advantages of these M-CDs, such as their luminescent properties when incorporated into a hydrogel substrate and static quenching process with TET and DOX, efforts were made to utilize these M-CDs as a luminescent hydrogel in the on-site field. The

porous, hydrophilic nature and high surface area make BC an appropriate substrate for composite formation [35]. The composite hydrogel with high porosity, hydrophilicity, and excellent FL properties is further utilized in the remediation of pollutants.

To illustrate the sensitivity and selectivity of M-CD@BC, we perform the changes in FL intensity of M-CD@BC hydrogel ($3 \times 3 \times 0.5 \text{ cm}^3$) as immersed in various antibiotics solutions including TET, DOX, NOR, AMP, VAN, CIP, ERY, and STR. As shown in **Figure 4.11a**, the M-CD@BC also exhibited excellent selectivity to both TET and DOX as compared to other antibiotics. **Figure 4.11b** indicates the visual representation of quenching in the FL of M-CD@BC upon the addition of TET and DOX among various antibiotics. We next studied the FL quenching properties of M-CD@BC as treated with different concentrations of TET and DOX. Encouraged by the remarkable FL characteristics of M-CD@BC, we utilized it as a solid-phase platform for the first time to examine the concentrations of TET and DOX sequentially. **Figure 4.11c** demonstrates a significant decrease in the FL of M-CD@BC upon the addition of TET. In addition, when the TET concentration reached 200 mM, the FL reduced greatly. **Figure 4.11d** shows a linear relationship between relative FL intensity (F_0/F) vs increased concentration of TET. The coefficient of determination ($R^2 = 0.99$) demonstrated a good linear relationship of (F_0/F) vs TET in a working dynamic range of 0-200 mM, with a LOD was determined to be 103 nM (formula in **Equation 4.2**). Therefore, the results suggested that the M-CD@BC hydrogel was a highly effective and sensitive probe for detecting TET. In addition, as M-CD@BC also exhibited a response to DOX, the detection of DOX was also conducted. **Figure 4.11e** demonstrates that the FL intensity of M-CD@BC consistently decreased as the concentration of DOX increased. A relative intensity ratio of (F_0/F) vs DOX concentration shows linearity (**Figure 4.11f**) with a coefficient of determination ($R^2 = 0.98$).

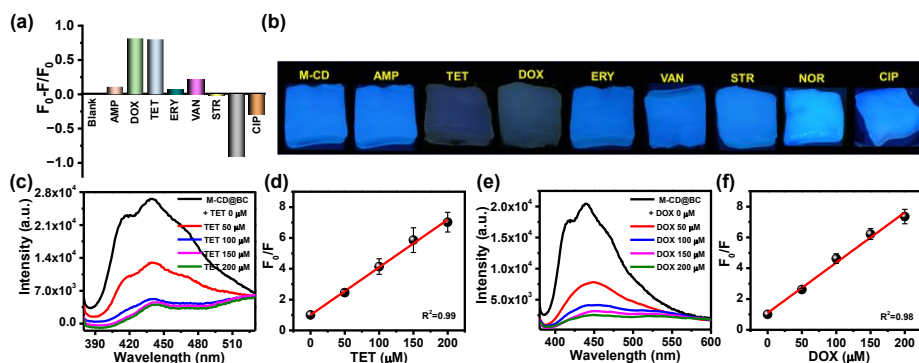


Figure 4.11. (a) Graph showing the relative FL intensity in the presence of different antibiotics, (b) fluorescent images of M-CD@BC after incubation with different antibiotics under UV irradiation ($\lambda_{\text{ex}}=365$ nm). FL response of M-CD@BC in the presence of (c) TET (0-200 mM), and corresponding Stern-Volmer plot depicting the linear relationship of (d) TET. (e) FL response of M-CD@BC in the presence of DOX (0-200 mM), and corresponding Stern-Volmer plot depicting the linear relationship of (f) DOX.

A working dynamic range of 0-200 mM with LOD of 156 nM, which outperforms any other FL sensing platform for TET and DOX sensing that has been reported (**Table 4.1**). Based on the above work, M-CD@BC can be utilized as a fluorescent probe for detecting TET and DOX. In addition, the fluorescent hydrogel-based system offers an excellent approach to be utilized as a selective probe because of its affordability, simplicity, stability, and on-site detection ability. The recyclability study of as-prepared M-CD@BC has also been performed.

Additionally, the ability to interfere with detecting TET and DOX in the presence of other antibiotics was also assessed. The presence of other interfering antibiotics did not have a substantial effect on the quenched FL signals, as demonstrated in **Figure 4.12a**. **Figure 4.12b-c** indicates the reusability of M-CD@BC for at least 5 cycles. After every cycle, the M-CDs@BC were washed several times with dilute acid and DI water for further reuse.

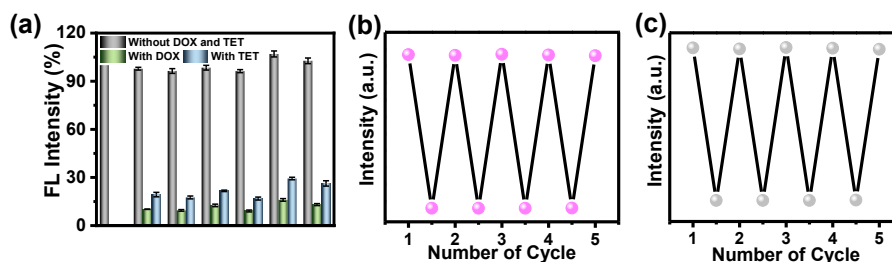


Figure 4.12. (a) Interfering studies for sensing response of M-CD@BC in the presence of various antibiotics ($c = 1.0 \times 10^{-2}$ M). Recyclability study for M-CD@BC (b) TET, and (c) DOX (200 mM).

4.3.7. Photocatalytic Degradation of TET and DOX

Beyond the scope of an on-site reusable FL sensor, the potential of this sorbent for complete remediation of TET and DOX is being act as a photocatalytic degradation platform, which is anticipated to be further explored. In general, CDs are viable photocatalysts for the photocatalytic remediation of various pollutants due to their excellent optoelectronic properties, reactive oxygen species (ROS) generation capacity, and biocompatibility [44].

Thus, the photocatalytic activity of M-CDs as a catalyst was evaluated using TET and DOX (20 mg L⁻¹, 50 mL) as model pollutants under sunlight. Initially, the concentration optimization of M-CDs was carried out to gain insight into the effect of PC amount in degradation studies in **Figure 4.13a** which indicates maximum degradation efficiency of ~79 % was obtained for TET (20 mg/L) and ~70 % was obtained for DOX (20 mg/L) with M-CDs (10 uL, 11.2 mg/mL) under sunlight and was calculated from **Equation 4.4**. A catalyst concentration above a limit in the analyte solution lowers degradation efficiency. This is due to multiple reasons, and some of them are as follows: i) due to lesser light penetration into the solution because of high CD concentration, ii) high catalyst concentration may lead to agglomeration and cause shielding of active sites. Furthermore, all the studies were performed with M-CDs catalyst with a concentration of 11.2 mg/mL. Other control sets of experiments were carried out in parallel with antibiotic solution (such as antibiotics without catalyst)

and in the dark, and exposed to sunlight. In the absence of a catalyst, no appreciable degradation was observed for TET and DOX under the irradiation of sunlight for 120 min. However, in the presence of M-CDs under dark conditions, a degradation efficiency of ~10 % for both TET and DOX was observed, and a comparative % degradation for all conditions was given in **Figure 4.13b**.

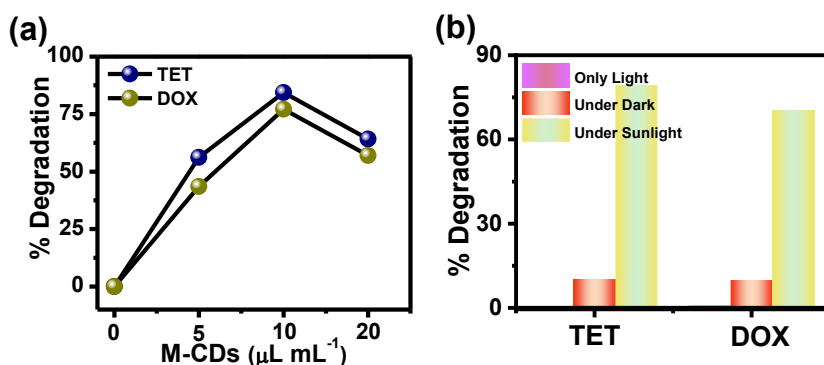


Figure 4.13. (a) Photocatalytic degradation studies of TET and DOX under various concentrations of M-CDs. (b) Degradation percentage of TET and DOX under sunlight without M-CDs, in the dark, and under sunlight with catalyst M-CDs.

Correspondingly, **Figures 4.14a-b** are comparative C/C_0 graphs of optimization studies with TET and DOX that clearly show that M-CDs possess better photocatalytic ability under sunlight irradiation for both antibiotics. An obvious increase in reaction rate while irradiated with sunlight can be seen for TET ($1.3 \times 10^{-2} \text{ min}^{-1}$) and DOX ($1.1 \times 10^{-2} \text{ min}^{-1}$) compared to the rates under dark (TET $6.1 \times 10^{-4} \text{ min}^{-1}$ and DOX $6.7 \times 10^{-4} \text{ min}^{-1}$) (**Figure 4.14c-d**) and calculated through **Equation 4.5**. The pseudo-first-order kinetic model followed the Langmuir-Hinshelwood approach in this photodegradation study.

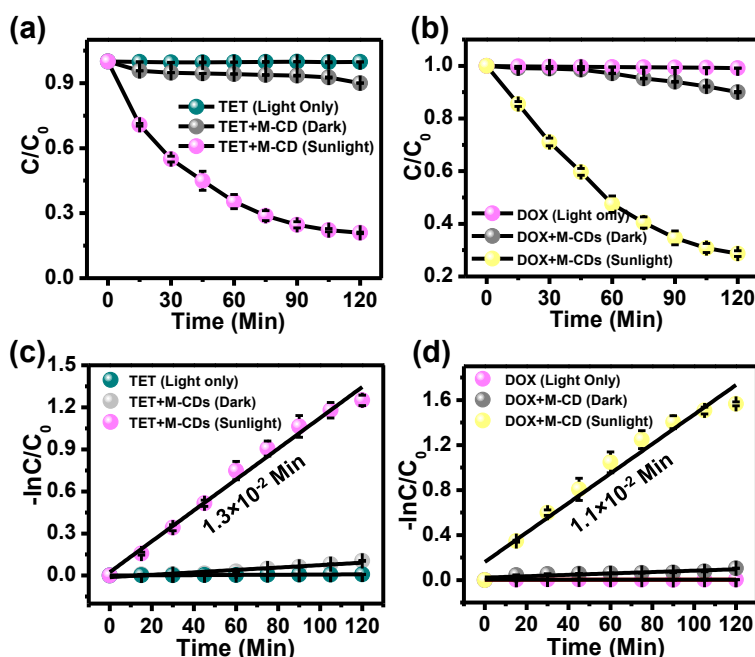


Figure 4.14. Degradation of (a) TET and (b) DOX under various conditions. Calculated rate constant of (c) TET and (d) DOX.

The superior performance of M-CDs over various photocatalysts reported for TET and DOX is listed in **Table 4.4**, which indicates the excellence of M-CDs compared to various reported catalysts.

Table 4.4. Comparison of the photocatalytic degradation of antibiotics TET and DOX by various photocatalysts.

Sr. No.	Catalysts	Pollutant	Antibiotics Conc. (ppm)	Time (Mins)	Degradation efficiency (%)	Light Intensity	References
1.	N-CQDs/BiPO ₄	TC	20	150	70	UV light source	50
2.	GQDs/mpg C ₃ N ₄	TC	20	120	67	300 W Xe arc lamp ($\lambda > 400$ nm)	51
3.	BiVO ₄ /N CQDs/Ag ₃ PO ₄	TC	10	90	59.8	A 300 W Xe lamp (320 nm< λ <780 nm, light intensity: 160mW/cm ²)	52
4.	GQDs/g-C ₃ N ₄	TC	15	120	80	300 W xenon lamp (420 nm cutoff filter)	53
5.	CQDs/ PbBiO ₂ Cl	TC	20	120	74.3	300 W Xe-lamp (400 nm light cut filter)	54
6.	LaFeO ₃ /SnS ₂	TC	20	120	28.8	300 W, Xe lamp	55
7.	CuBi ₂ O ₄ /BiOBr	TC	20	150	64.7	300 W, Xe lamp	56
8.	Vis/CDs-ZIS/PS	TC	20	120	83	Visible Light	57
9.	M-CDs	TET and DOX	20	120	79.4 and 70.3	Sunlight	Present Work
10.	M-CD@BC	TET and DOX	20	120	74.2 and 64.0	Sunlight	Present Work

In addition, electrochemical studies were performed to get deeper insight into the formation of charge carriers in the M-CD photocatalyst and the mechanism of degradation. The transient photocurrent response of M-CDs and the bare electrode was obtained for several on-

off cycles under visible light exposure and depicted in **Figure 4.15a**. The response of M CDs to the visible light on-off cycle is significantly stronger compared to the bare sample. This is due to the excellent separation of photogenerated electrons and holes in M-CDs, which reduces the recombination of photogenerated carriers. The enhanced photogeneration of charge carriers could result in increased photocatalytic activity of M-CDs. The EIS was conducted to further evaluate the charge transfer and recombination mechanism. **Figure 4.15b** demonstrates that the arc radius on the EIS Nyquist plot of M-CDs appears smaller than that of the bare sample when examined under visible light illumination. This suggests that there is an efficient separation of photogenerated electron-hole pairs and a more rapid charge transfer. This would enhance the photocatalytic activity.

Further, to gain insights into the mechanism of photocatalytic degradation, a further ROS generation test was carried out. The photocatalytic activity of M-CDs was investigated in the presence of scavengers such as t-BuOH ($\cdot\text{OH}$ scavenger), EDTA- Na_2 (h^+ scavenger), and BZQ ($\text{O}_2^{\cdot-}$ scavenger). **Figure 4.15c-d** displays comparative results of the effects of different scavengers on the % degradation of both antibiotics. The addition of t-BuOH, EDTA- Na_2 , and BZQ in TET showed a change in degradation efficiency of 79.4 %, 44.5 %, and 21.1 %, respectively. But in the case of DOX, the degradation % in the presence of t-BuOH, EDTA- Na_2 , and BZQ were found to be 70.3 %, 42.6 %, and 20.4 %, respectively. Notably, no appreciable changes were observed in the degradation of both TET and DOX in the presence of t-BuOH. However, upon addition of EDTA- Na_2 , approximately 45 % decrease in the degradation efficiency for both TET and DOX (44.5 and 42.6 %, respectively) was observed, highlighting the role of photogenerated holes. A similar decrease of approximately 71 % was observed in the degradation of TET and DOX (21.1 and 20.4 %, respectively) in the presence of BZQ, highlighting the role of superoxide radical in the photocatalytic degradation of TET and DOX. Therefore, the order of contribution of ROS in the photocatalytic reaction of both antibiotics by M-CDs is $\text{O}_2^{\cdot-} > \text{h}^+ > \cdot\text{OH}$.

The BZQ and EDTA- Na_2 affect the degradation efficiency greatly. This observation suggests that $\text{O}_2^{\cdot-}$ and h^+ play a major role in TET and DOX degradation. **Figure 4.15e** is a schematic that illustrates the plausible mechanism for the degradation of antibiotics through photocatalysis using M-CDs under sunlight irradiation. At first, the presence of M-CDs in TET and DOX solution facilitates the generation of excited state electrons (e^-) and holes (h^+) under the irradiation of sunlight. The h^+ ions effectively oxidized TET and DOX, converting them into CO_2 and H_2O . In addition, e^- activate dissolved oxygen (O_2) resulting in the formation of superoxide ions ($\text{O}_2^{\cdot-}$). This process enables the breakdown of TET and DOX into smaller hydrocarbon molecules.

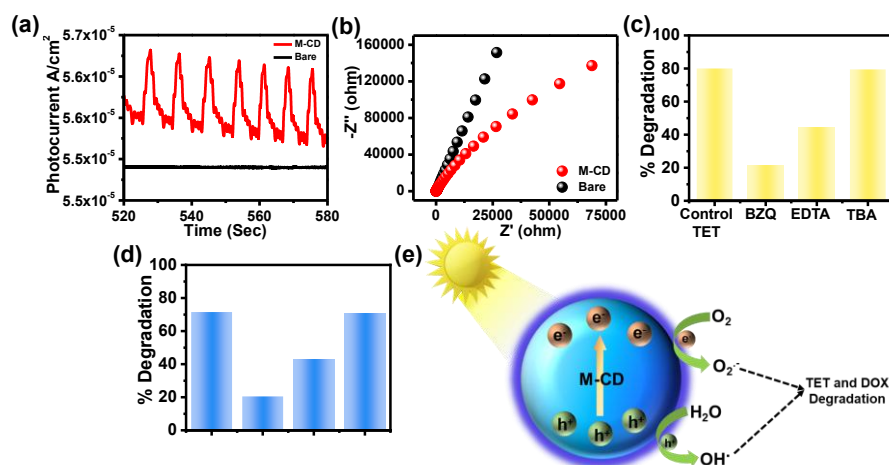


Figure 4.15. (a) Transient photocurrent density versus time plotted, and (b) EIS Nyquist plots of M-CDs under visible light in 0.5 M Na_2SO_4 electrolyte. Effect of scavengers on degradation of (c) TET and (d) DOX. (e) Schematic illustration of charge transfer in M-CDs for TET and DOX degradation.

4.3.8. Photodegradation with M-CD@BC

The immobilization of CDs on support would facilitate the handling of the catalytic system and avoid leaching issues, thereby permitting multiple working cycles. Thus, moving one step further toward large-scale adoption of technology, the embedding of CDs in a polymeric matrix was considered [59, 60]. In this respect, previous studies showed that CD-loaded composites enhanced the mechanical

properties of hydrogels as well as altered the optical properties of CDs [33, 61]. These CDs integrated polymer matrices have been employed for sensing and degradation of pollutants [9, 62, 63].

More importantly, the use of M-CD@BC serves as a dual role. Firstly, it helps to detect the antibiotics present widely in the water system, and secondly, it helps to degrade them effectively. The efficacy of M-CD@BC in photocatalysis was investigated by a set of preliminary experiments to identify the maximum removal of TET and DOX. For this, M-CD@BC was stirred separately with TET and DOX in the dark for 120 min before being irradiated. In the absence of light, the extent of adsorption of TET and DOX onto M-CD@BC is invariably low despite continuous stirring (**Figure 4.16a-b**). This, in turn, reflects the fact that surface adsorption is unlikely to play a pivotal role in photocatalysis.

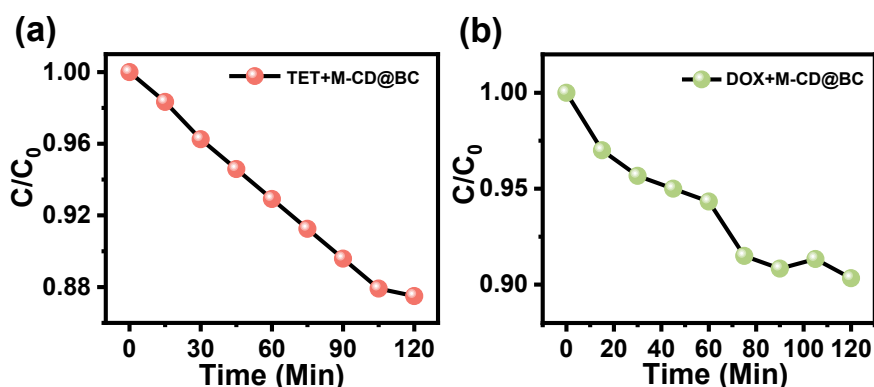


Figure 4.16. Removal of (a) TET, and (b) by M-CD@BC without sunlight illumination (experimental conditions: $C_0 = 20$ mg/L).

Furthermore, the TET and DOX containing solutions were irradiated in the presence of M-CD@BC hydrogel under sunlight, and the degradation of antibiotics was evaluated using UV-vis spectra. The photocatalytic activity of M-CD@BC indicates a decrease in absorbance intensity after photodegradation for 120 min, and % degradation was found to be 74.2 % for TET and 64.0 % for DOX. **Figure 4.17a** shows a C/C_0 graph of kinetic experiments for TET with M-CDs@BC, indicating a better photocatalytic efficiency under sunlight with a reaction rate of $1.2 \times 10^{-2} \text{ min}^{-1}$ (**Figure 4.17b**). **Figure**

4.17c is the C/C_0 graph for DOX, and **Figure 4.17d** indicates its photodegradation rate, which is $8.7 \times 10^{-3} \text{ min}^{-1}$. This photodegradation study employed the pseudo-first-order kinetic model, which is based on the Langmuir-Hinshelwood approach. Notably, the porous polymeric network of M-CD@BC with a large surface area, along with more pore volume, the lowest band gap, and multiple active sites, can lead to good photocatalytic activity. The superior photocatalytic performance of M-CD@BC may be attributed to the strong interaction between M-CD and BC. Particularly, the M-CDs on BC absorb the light to generate the electron-hole pairs to degrade TET and DOX, which could result in increased photocatalytic activity of M-CDs on BC. Furthermore, M-CDs embedded porous network allows effective diffusion of pollutants near the optically active M-CDs, which leads to excellent degradation efficiency. The reusability of the M-CD@BC matrix was further evaluated by performing five cycles of photodegradation of TET and DOX (**Figure 4.17e-f**, respectively). After the fifth cycle, the photocatalytic activity was almost retained with minimal effect on repeated degradation, which excludes significant leaching probability of active M-CD components from the BC matrix. The retention of photocatalytic activity suggests that the M-CDs are strongly anchored onto the BC matrix. A BC is known for its high mechanical strength and high surface area, which may create a stable environment for the carbon dots, preventing their leaching. The strong interactions between the CDs and BC could contribute to this stability. This demonstrates the efficacy of our M-CD@BC hydrogel composite for repeated photodegradation of antibiotic pollutants.

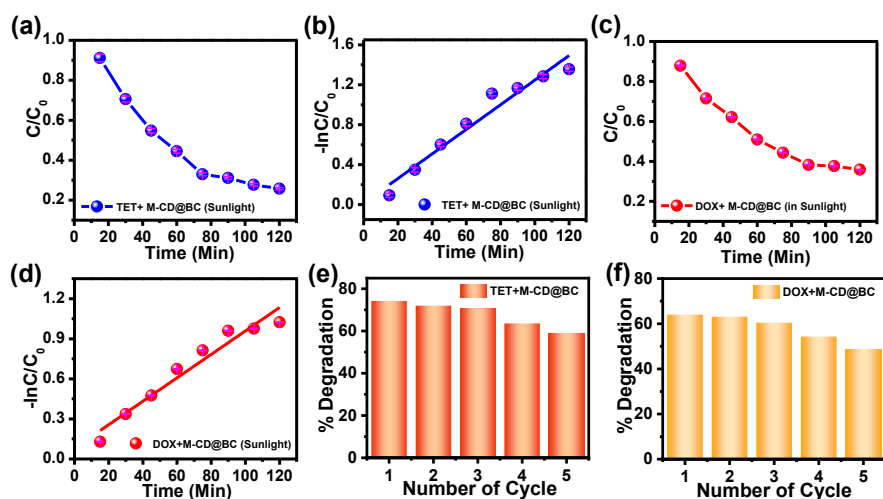


Figure 4.17. (a, b) Photodegradation of TET under sunlight and their rate, respectively; (c, d) photodegradation of DOX under sunlight and their rate, respectively. Recyclability study of composite hydrogel M-CD@BC towards (e) TET and (f) DOX.

4.3.9. Plausible Degradation Pathway for TET and DOX

Furthermore, the mass/charge (m/z) of degraded intermediates and possible degradation pathways of TET were analyzed using LC-MS analysis. The degradation intermediates of TET (**Scheme 4.2**) and LC-MS analysis are shown in **Figure 4.18a-b**. The TET degradation process proceeds by a contribution of reactive species such as $O_2^{\cdot-}$, h^+ , $\cdot OH$, and degradation follows in three main pathways, such as deamination, ring opening, and dihydroxylation (**Scheme 4.2**) [64]. For the first pathway, TET ($m/z = 445$) is degraded into P2 ($m/z = 427$) by dihydroxylation of TET and then undergoes removal of two N-methyl groups to yield P3 ($m/z = 413$) and P4 ($m/z = 399$), respectively. After deamination reaction, P5 ($m/z = 386$) and P6 ($m/z = 258$) were formed. For the second pathway, the formation of P7 ($m/z = 431$) and P8 ($m/z = 417$) was attributed to the elimination of the N-methyl substitute on TET ($m/z = 445$). Then, P8 was disintegrated into P9 ($m/z = 399$) via the detachment of water molecules. Then, P10 ($m/z = 315$) was formed by deamination, deamidation, and ring-opening reaction. Again, P10 was degraded into P11 ($m/z = 271$) and P12 ($m/z = 258$) through oxidation reaction. In the third pathway, the unstable

C=C double bond P13 ($m/z = 461$) is formed via a hydroxylation reaction. Next, P14 ($m/z = 372$) is formed because of the deamination and removal of N-methyl groups, and the detachment of the amino group and ring-splitting reaction from P14 leads to the formation of P15 ($m/z = 320$) which is then converted into P11 ($m/z = 271$) and P17 ($m/z = 253$). After 120 min of degradation, the molecular peak of TET at m/z 445 was decreased, and eventually, TET could be gradually decomposed by time into CO_2 , H_2O , and other molecules during photodegradation [65-67].

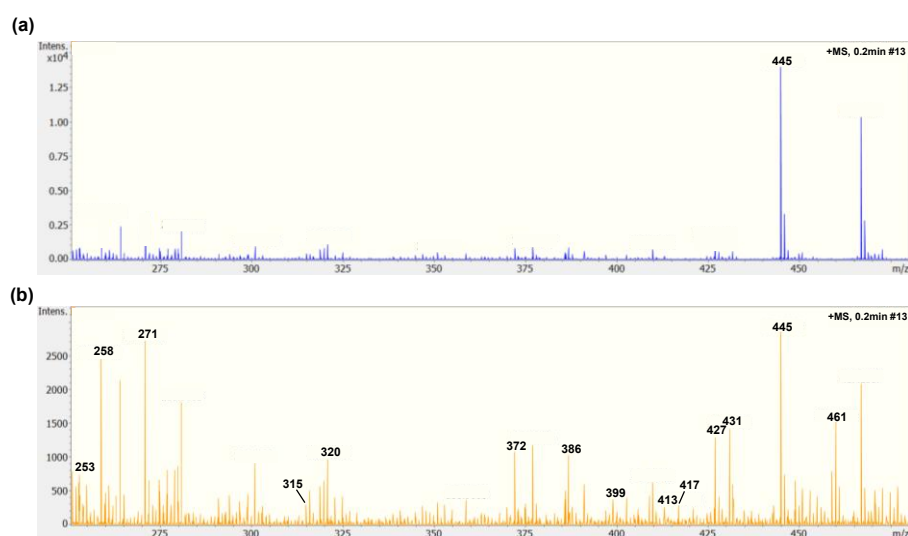
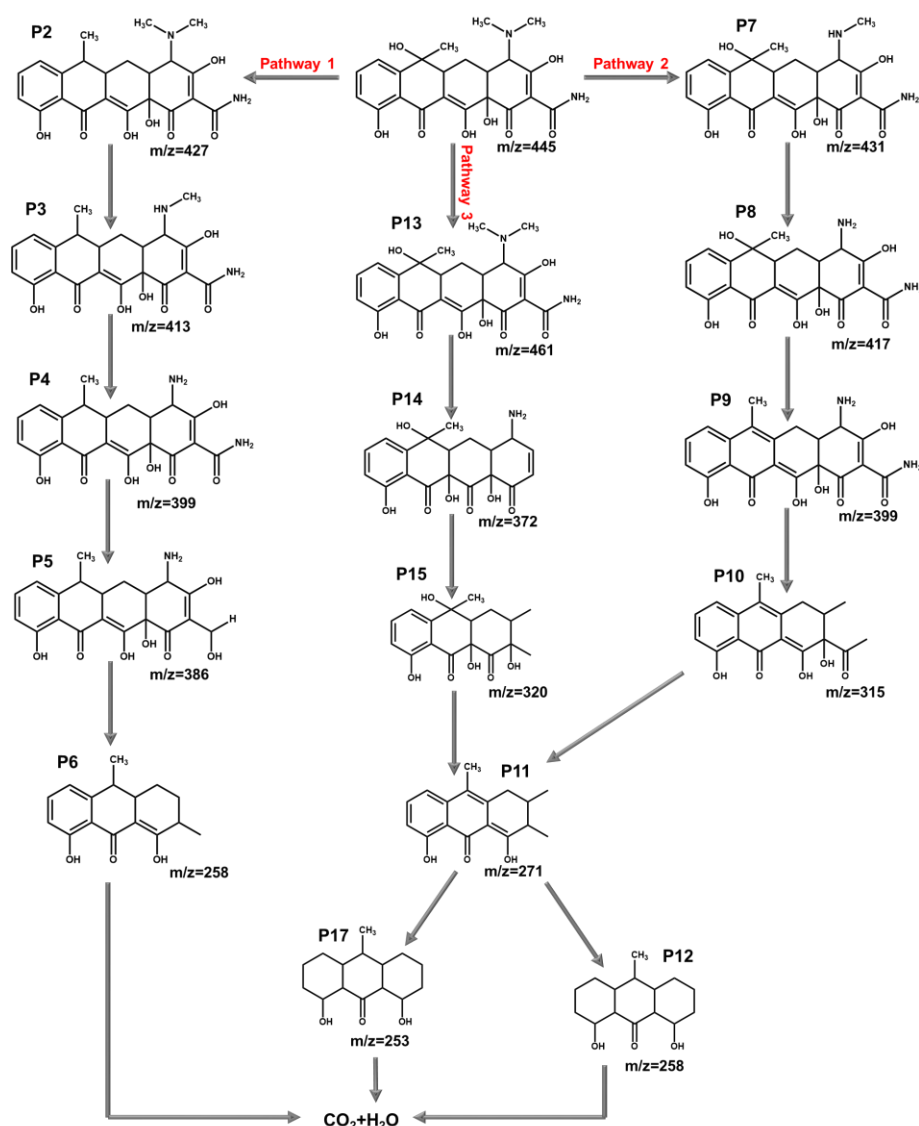


Figure 4.18. Mass spectra of (a) initial TET solution at 0 min, (b) degradation of TET in 120 min, and intermediate detected.



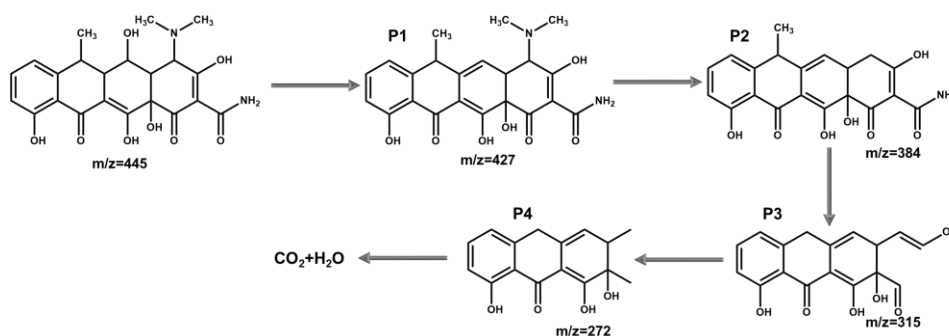
Scheme 4.2. Schematic suggested pathway for the photocatalytic degradation of TET and their intermediates.

DOX, on the other hand, undergoes a slightly different intermediate formation. According to the mass spectra shown in **Figure 4.19a-b**, the possible degradation pathway of DOX is also proposed (**Scheme 4.3**). The water molecule was lost from the DOX ($m/z = 445$) to obtain P1 ($m/z = 427$). P1 was converted into P2 ($m/z = 384$) through loss of amino groups. The P2 continued to lose amino and aldehyde groups, the benzene ring was attacked and opened, then a hydroxyl substitution reaction occurred, and P3 ($m/z = 315$) was formed. Further, one aldehyde and hydroxyl group has been removed, and P4 ($m/z = 272$) is generated. The degradation of DOX was completed by a detachment of

hydroxyl and methyl substituents, and the opening of a benzene ring [68]. The results show that DOX was oxidized into small molecular products and decomposed into CO_2 and H_2O .



Figure 4.19. Mass spectra of (a) initial DOX solution at 0 min, (b) degradation of DOX in 120 min, and intermediate detected.



Scheme 4.3. Schematic suggested pathway for photocatalytic degradation of DOX and its intermediates.

4.4. Conclusions

We have synthesized the melamine-derived carbon dots (M-CDs) and their composite hydrogel (M-CD@BC) for both photocatalytic degradation and simultaneous detection of pharmaceutical contaminants. The M-CDs not only serve as an effective and efficient sensor for the detection of TET and DOX with good sensitivity and selectivity, but also remove them from contaminated water. Notably, M-CDs exhibited the LOD of 133 nM and 138 nM for TET and DOX.

Additionally, optically active M-CDs were utilized for the photodegradation of TET and DOX. The mechanistic study indicates the generation of superoxide radicals along with photoinduced holes for the degradation of both pharmaceuticals. The M-CD@BC also shows excellent sensing ability towards TET and DOX. The photocatalytic degradations of TET and DOX in the presence of M-CD@BC slightly decrease due to the binding of the active surface of M-CDs with BC. Moreover, M-CD@BC is found to be recyclable for multiple catalytic cycles. Our present work paves the way for the generation of multifunctional CDs and embedded hydrogels for a wide range of applications.

Note: This is copyrighted material with permission from the Royal Society of Chemistry.

4.5. References

1. Fan G., Ning R., Li X., Lin X., Du B., Luo J., Zhang X. (2021), Mussel-Inspired Immobilization of Photocatalysts with Synergistic Photocatalytic–Photothermal Performance for Water Remediation, *ACS Appl. Mater. Interfaces*, *13*, 31066–31076. (DOI: 10.1021/acsami.1c02973)
2. Yang T., Zhu E., Guo H., Du J., Wu Y., Liu C., Che G. (2021), Visible Light-Driven D–A Conjugated Linear Polymer and Its Coating for Dual Highly Efficient Photocatalytic Degradation and Disinfection, *ACS Appl. Mater. Interfaces*, *13*, 51447–51458. (DOI: 10.1021/acsami.1c14240)
3. Hu Z., Luo Y., Wang L., Wang Y., Wang Q., Jiang G., Zhang Q., Cui F. (2023), Synthesis of Pyrene-Based Covalent Organic Frameworks for Photocatalytic Tetracycline Degradation, *ACS Appl. Polym. Mater.*, *5*, 9263–9273. (DOI: 10.1021/acsapm.3c01765)
4. Liu Y., Guo H., Wu, N., Peng L., Wang M., Tian J., Xu J., Yang W. (2023), Eu³⁺-Functionalized Nanoporous Covalent Organic Frameworks for Fluorescence Detection and Removal of Tetracycline, *ACS Appl. Nano Mater.*, *6*, 6627–6636. (DOI: 10.1021/acsanm.3c00323)
5. Raut J., Islam M. M., Saha S., Mandal S. M., Mandal S., Sahoo P. (2022), N-Doped Carbon Quantum Dots for Differential Detection of Doxycycline in Pharmaceutical Sewage and in Bacterial Cell, *ACS Sustainable Chem. Eng.*, *10*, 9811–9819. (DOI: 10.1021/acssuschemeng.2c01604)
6. Xie B., Peng H., Zhang R., Wang C., He Y. (2021), Label-Free Electrochemical Aptasensor Based on Stone-like Gold Nanoparticles for Ultrasensitive Detection of Tetracycline, *J. Phys. Chem. C*, *125*, 5678–5683. (DOI: 10.1021/acs.jpcc.0c10809)
7. Zhong Y., Guo L., Zou Y., Ge J., Chen Y., Lu Z., Wang D. (2023), Cys-Functionalized MoS₂ Quantum Dots and Calcium Ion for

- Ratiometric Fluorescence Probes for Doxycycline, *ACS Appl. Nano Mater.*, **6**, 22355–22362. (DOI: 10.1021/acsanm.3c04589)
8. Zhang T., Liu J., Zhou F., Zhou S., Wu J., Chen D., Xu Q., Lu J. (2020), Polymer-Coated Fe₂O₃ Nanoparticles for Photocatalytic Degradation of Organic Materials and Antibiotics in Water, *ACS Appl. Nano Mater.*, **3**, 9200–9208. (DOI: 10.1021/acsanm.0c01829)
 9. Ehtesabi H., Roshani S., Bagheri Z., Yaghoubi-Avini M. (2019), Carbon Dots-Sodium Alginate Hydrogel: A Novel Tetracycline Fluorescent Sensor and Adsorber, *J. Environ. Chem. Eng.*, **7**, 103419. (DOI: 10.1016/j.jece.2019.103419)
 10. Gowers S. A. N., Freeman D. M. E., Rawson T. M., Rogers M. L., Wilson R. C., Holmes A. H., Cass A. E., O'Hare D. (2019), Development of a Minimally Invasive Microneedle-Based Sensor for Continuous Monitoring of β -Lactam Antibiotic Concentrations in Vivo, *ACS Sens.*, **4**, 1072–1080. (DOI: 10.1021/acssensors.9b00288)
 11. Cao Y., Lu K., Chen Y., Zheng Q., Huang C., Jia N. (2023), In₂O₃/Bi₂S₃ S-Scheme Heterojunction-Driven Molecularly Imprinted Photoelectrochemical Sensor for Ultrasensitive Detection of Florfenicol, *ACS Appl. Mater. Interfaces*, **15**, 58397–58405. (DOI: 10.1021/acсами.3c13406)
 12. Dang V. D., Ganganboina A. B., Doong R.-A. (2020), Bipyridine- and Copper-Functionalized N-Doped Carbon Dots for Fluorescence Turn Off-On Detection of Ciprofloxacin, *ACS Appl. Mater. Interfaces*, **12**, 32247–32258. (DOI: 10.1021/acсами.0c04645)
 13. Kanzariya D. B., Goswami R., Muthukumar D., Pillai R. S., Pal T. K. (2022), Highly Luminescent MOF and Its In Situ Fabricated Sustainable Corn Starch Gel Composite as a Fluoro-Switchable Reversible Sensor Triggered by Antibiotics and Oxo-Anions, *ACS Appl. Mater. Interfaces*, **14**, 48658–48674. (DOI: 10.1021/acсами.2c13571)
 14. Tong X., Lin X., Duan N., Wang Z., Wu S. (2022), Laser-Printed Paper-Based Microfluidic Chip Based on a Multicolor

- Fluorescence Carbon Dot Biosensor for Visual Determination of Multiantibiotics in Aquatic Products, *ACS Sens.*, 7, 3947–3955. (DOI: 10.1021/acssensors.2c02008)
15. Zakharenkova S. A., Dobrovolskii A. A., Garshev A. V., Statkus M. A., Beklemishev M. K. (2021), Chlorophyll-Based Self-Assembled Nanostructures for Fluorescent Sensing of Aminoglycoside Antibiotics, *ACS Sustainable Chem. Eng.*, 9, 3408–3415. (DOI: 10.1021/acssuschemeng.0c08223)
 16. Bunnasit S., Thamsirianunt K., Rakthabut R., Jeamjumnunja K., Prasittichai C., Siriwatcharapiboon W. (2024), Sensitive Portable Electrochemical Sensors for Antibiotic Chloramphenicol by Tin/Reduced Graphene Oxide-Modified Screen-Printed Carbon Electrodes, *ACS Appl. Nano Mater.*, 7, 267–278. (DOI: 10.1021/acsanm.3c04388)
 17. Wang M., Cetó X., Valle D. M. (2022), A Sensor Array Based on Molecularly Imprinted Polymers and Machine Learning for the Analysis of Fluoroquinolone Antibiotics, *ACS Sens.*, 7, 3318–3325. (DOI: 10.1021/acssensors.2c01260)
 18. Kundu A., Maity B., Basu S. (2022), Rice Husk-Derived Carbon Quantum Dots-Based Dual-Mode Nanoprobe for Selective and Sensitive Detection of Fe^{3+} and Fluoroquinolones, *ACS Biomater. Sci. Eng.*, 8, 4764–4776. (DOI: 10.1021/acsbiomaterials.2c00798)
 19. Cai W., Li H., Li M., Wang M., Wang H., Chen J., Zang Z. (2021), Opportunities and Challenges of Inorganic Perovskites in High-Performance Photodetectors, *J. Phys. D: Appl. Phys.*, 54, 293002. (DOI: 10.1088/1361-6463/abf709)
 20. Xu Z., Zhuang Q., Zhou Y., Lu S., Wang X., Cai W., Zang Z. (2023), Functional Layers of Inverted Flexible Perovskite Solar Cells and Effective Technologies for Device Commercialization, *Small Struct.*, 4, 2200338. (DOI: 10.1002/sstr.202200338)
 21. Singh S., Vaishnav J. K., Mukherjee T. K. (2020), Quantum Dot-Based Hybrid Coacervate Nanodroplets for Ultrasensitive Detection of Hg^{2+} , *ACS Appl. Nano Mater.*, 3, 3604–3612. (DOI: 10.1021/acsanm.0c00317)

22. Wang D., Pillai S. C., Ho S.-H., Zeng J., Li Y., Dionysiou D. D. (2018), Plasmonic-Based Nanomaterials for Environmental Remediation, *Appl. Catal., B*, 237, 721–741. (DOI: 10.1016/j.apcatb.2018.05.094)
23. Wang L., Li M., Li W., Han Y., Liu Y., Li Z., Zhang B., Pan D. (2018), Rationally Designed Efficient Dual-Mode Colorimetric/Fluorescence Sensor Based on Carbon Dots for Detection of pH and Cu²⁺ Ions, *ACS Sustainable Chem. Eng.*, 6, 12668–12674. (DOI: 10.1021/acssuschemeng.8b01625)
24. Aggarwal R., Garg A. K., Kumar V., Jonwal H., Sethi S., Gadiyaram S., Sonkar S. K., Sonker A. K., Westman G. (2023), Cellulose-Derived Carbon Dots for Inner Filter Effect-Based Selective Sensing of Ofloxacin Antibiotics, *ACS Appl. Nano Mater.*, 6, 6518–6527. (DOI: 10.1021/acsanm.2c05526)
25. Cui J., Zhu X., Liu Y., Liang L., Peng Y., Wu S., Zhao Y. (2022), N-Doped Carbon Dots as Fluorescent “Turn-Off” Nanosensors for Ascorbic Acid and Fe³⁺ Detection, *ACS Appl. Nano Mater.*, 5, 7268–7277 (DOI: 10.1021/acsanm.2c01170)
26. Mate N., Khandelwal D., Nabeela K., Shaikh M. S. (2023), Portable and Non-Invasive Fluorescent Thin Films from Photocatalytically Active Carbon Dots for Selective and Trace-Level Detection of Picric Acid, *J. Mater. Chem. C*, 11, 16201–16213. (DOI: 10.1039/D3TC03625A)
27. Sui B., Zhu Y., Jiang X., Wang Y., Zhang N., Lu Z., Yang B., Li Y. (2023), Recastable Assemblies of Carbon Dots into Mechanically Robust Macroscopic Materials, *Nat. Commun.*, 14, 6782. (DOI: 10.1038/s41467-023-42516-8)
28. Kaur N., Tiwari P., Mate N., Sharma V., Shaikh M. S. (2022), Photoactivatable Carbon Dots as a Label-Free Fluorescent Probe for Picric Acid Detection and Light-Induced Bacterial Inactivation, *J. Photochem. Photobiol.*, B, 229, 112412. (DOI: 10.1016/j.jphotobiol.2022.112412)
29. Chen S., Zhang S.-Z., Jiang H. (2024), Modification of Crystal-Optimized TiO₂ with Biomass-Derived Carbon Quantum Dots for

- Highly Efficient Degradation of Favipiravir in Water, *ACS EST Water*, 4, 531–542. (DOI: 10.1021/acsestwater.3c00595)
30. Bhunia S., Ghorai N., Burai S., Purkayastha P., Ghosh H. N., Mondal S. (2021), Unraveling the Carrier Dynamics and Photocatalytic Pathway in Carbon Dots and Pollutants of Wastewater System, *J. Phys. Chem. C*, 125, 27252–27259. (DOI: 10.1021/acs.jpcc.1c06135)
 31. Cao H.-L., Cai F.-Y., Yu K., Zhang Y.-Q., Lü J., Cao R. (2019), Photocatalytic Degradation of Tetracycline Antibiotics over CdS/Nitrogen-Doped Carbon Composites Derived from in Situ Carbonization of Metal–Organic Frameworks, *ACS Sustainable Chem. Eng.*, 7, 10847–10854. (DOI: 10.1021/acssuschemeng.9b01685)
 32. Rajendran S., Ramanaiah D. V., Kundu S., Bhunia S. K. (2021), Yellow Fluorescent Carbon Dots for Selective Recognition of As³⁺ and Fe³⁺ Ions, *ACS Appl. Nano Mater.*, 4, 10931–10942. (DOI: 10.1021/acsanm.1c02391)
 33. Huang J., Liu X., Li L., Chen S., Yang J., Yan J., Xu F., Zhang X. (2021), Nitrogen-Doped Carbon Quantum Dot-Anchored Hydrogels for Visual Recognition of Dual Metal Ions through Reversible Fluorescence Response, *ACS Sustainable Chem. Eng.*, 9, 15190–15201. (DOI: 10.1021/acssuschemeng.1c04521)
 34. Mate N., Nabeela K., Preethikumar G., Pillai S., Shaikh M. S. (2024), A Lignin-Derived Carbon Dot-Upgraded Bacterial Cellulose Membrane as an All-in-One Interfacial Evaporator for Solar-Driven Water Purification, *Mater. Horiz.*, 11, 5114–5122 (DOI: 10.1039/D4MH00591K)
 35. Nabeela K., Thorat M. N., Backer S. N., Ramachandran A. M., Thomas R. T., Preethikumar G., Mohamed A. P., Asok A., Dastager S. G., Pillai S. (2021), Hydrophilic 3D Interconnected Network of Bacterial Nanocellulose/Black Titania Photothermal Foams as an Efficient Interfacial Solar Evaporator, *ACS Appl. Bio Mater.*, 4, 4373–4383. (DOI: 10.1021/acsabm.1c00143)

36. Jiang C., Zhou C., Tang W., Chen G., Yin S.-N., Xie W., Wu D. (2023), Crosslinking of Bacterial Cellulose toward Fabricating Ultrastretchable Hydrogels for Multiple Sensing with High Sensitivity, *ACS Sustainable Chem. Eng.*, *11*, 11548–11558. (DOI: 10.1021/acssuschemeng.3c01937)
37. Su T., Liu N., Lei D., Wang L., Ren Z., Zhang Q., Su J., Zhang Z., Gao Y. (2022), Flexible MXene/Bacterial Cellulose Film Sound Detector Based on Piezoresistive Sensing Mechanism, *ACS Nano*, *16*, 8461–8471. (DOI: 10.1021/acsnano.2c03155)
38. Kaur N., Tiwari P., Abbas Z., Shaikh M. S. (2022), Doxycycline Detection and Degradation in Aqueous Media via Simultaneous Synthesis of Fe-N@carbon Dots and Fe₃O₄-Carbon Dot Hybrid Nanoparticles: A One Arrow Two Hawk Approach, *J. Mater. Chem. B*, *10*, 5251–5262. (DOI: 10.1039/D2TB00475E)
39. Sattler A., Pagano S., Zeuner M., Zurawski A., Gunzelmann D., Senker J., Müller-Buschbaum K., Schnick W. (2009), Melamine–Melem Adduct Phases: Investigating the Thermal Condensation of Melamine, *Chem.–Eur. J.*, *15*, 13161–13170. (DOI: 10.1002/chem.200901518)
40. Rovina K., Siddiquee S. (2015), A Review of Recent Advances in Melamine Detection Techniques, *J. Food Compos. Anal.*, *43*, 25–38. (DOI: 10.1016/j.jfca.2015.04.008)
41. Ghosh P., Bairagi D., Hazra N., Jana S., Banerjee A. (2023), Carbon-Dot-Decorated Silver and Gold Nanocomposites for Antibacterial Activity and Degradation of Organic Dyes, *ACS Appl. Nano Mater.*, *6*, 18100–18112. (DOI: 10.1021/acsanm.3c03380)
42. Li L., Shi L., Jia J., Eltayeb O., Lu W., Tang Y., Dong C., Shuang S. (2021), Red Fluorescent Carbon Dots for Tetracycline Antibiotics and pH Discrimination from Aggregation-Induced Emission Mechanism, *Sens. Actuators, B*, *332*, 129513. (DOI: 10.1016/j.snb.2021.129513)
43. Mate N., Pranav, Nabeela K., Kaur N., Shaikh M. S. (2022), Insight into the Modulation of Carbon-Dot Optical Sensing

- Attributes through a Reduction Pathway, *ACS Omega*, 7, 43759–43769. (DOI: 10.1021/acsomega.2c04766)
44. Yan Y., Liu J. H., Li R. S., Li Y. F., Huang C. Z., Zhen S. J. (2019), Carbon Dots Synthesized at Room Temperature for Detection of Tetracycline Hydrochloride, *Anal. Chim. Acta*, 1063, 144–151. (DOI: 10.1016/j.aca.2019.02.047)
 45. Wang X., Zhang L., Hao A., Shi Z., Dai C., Yang Y., Huang H. (2020), Silica-Coated Silver Nanoparticles Decorated with Fluorescent CdTe Quantum Dots and DNA Aptamers for Detection of Tetracycline, *ACS Appl. Nano Mater.*, 3, 9796–9803. (DOI: 10.1021/acsanm.0c01890)
 46. Guo J., Lu W., Zhang H., Meng Y., Du F., Shuang S., Dong C. (2021), Copper Doped Carbon Dots as the Multi-Functional Fluorescent Sensing Platform for Tetracyclines and pH, *Sens. Actuators, B*, 330, 129360. (DOI: 10.1016/j.snb.2020.129360)
 47. Hu Y., Guan R., Zhang S., Fan X., Liu W., Zhang K., Shao X., Li X., Yue Q. (2022), A Convenient Fluorescence Sensor of Tetracycline Based on B, N Codoped Carbon Dots/Polymer Composite Film, *Food Chem.*, 372, 131287. (DOI: 10.1016/j.foodchem.2021.131287)
 48. Liu B., Zhu H., Liu J., Wang M., Pan J., Feng R., Hu P., Niu X. (2023), Alkali-Etched Imprinted Mn-Based Prussian Blue Analogues with Superior Oxidase-Mimetic Activity and Precise Recognition for Tetracycline Colorimetric Sensing, *ACS Appl. Mater. Interfaces*, 15, 24736–24746. (DOI: 10.1021/acsam.3c02207)
 49. Pang L., Zhou H., Qian Z., Munir H. A., Li J., Liu H. (2023), Water-Stable Luminescent Eu–Al-Nanoscale Metal–Organic Gels for the Detection of Doxycycline, *ACS Appl. Nano Mater.*, 6, 20220–20230. (DOI: 10.1021/acsanm.3c04035)
 50. Mate N., Khandelwal D., Nabeela K., Shaikh M. S. (2023), Portable and Non-Invasive Fluorescent Thin Films from Photocatalytically Active Carbon Dots for Selective and Trace-

- Level Detection of Picric Acid, *J. Mater. Chem. C*, *11*, 16201–16213. (DOI: 10.1039/D3TC03625A)
51. Di J., Xia J., Chen X., Ji M., Yin S., Zhang Q., Li H. (2017), Tunable Oxygen Activation Induced by Oxygen Defects in Nitrogen Doped Carbon Quantum Dots for Sustainable Boosting Photocatalysis, *Carbon*, *114*, 601–607. (DOI: 10.1016/j.carbon.2016.12.030)
 52. Liu J., Xu H., Xu Y., Song Y., Lian J., Zhao Y., Wang L., Huang L., Ji H., Li H. (2017), Graphene Quantum Dots Modified Mesoporous Graphite Carbon Nitride with Significant Enhancement of Photocatalytic Activity, *Appl. Catal., B*, *207*, 429–437. (DOI: 10.1016/j.apcatb.2017.01.071)
 53. Zhang J., Yan M., Yuan X., Si M., Jiang L., Wu Z., Wang H., Zeng G. (2018), Nitrogen Doped Carbon Quantum Dots Mediated Silver Phosphate/Bismuth Vanadate Z-Scheme Photocatalyst for Enhanced Antibiotic Degradation, *J. Colloid Interface Sci.*, *529*, 11–22. (DOI: 10.1016/j.jcis.2018.05.109)
 54. Yuan A., Lei H., Xi F., Liu J., Qin L., Chen Z., Dong X. (2019), Graphene Quantum Dots Decorated Graphitic Carbon Nitride Nanorods for Photocatalytic Removal of Antibiotics, *J. Colloid Interface Sci.*, *548*, 56–65. (DOI: 10.1016/j.jcis.2019.04.027)
 55. Sheng Y., Yi D., Qingsong H., Ting W., Ming L., Yong C., Yifan S., Jun D., Bin W., Xia J., Huaming L. (2019), CQDs Modified PbBiO₂Cl Nanosheets with Improved Molecular Oxygen Activation Ability for Photodegradation of Organic Contaminants, *J. Photochem. Photobiol., A*, *382*, 111921 (DOI: 10.1016/j.jphotochem.2019.111921)
 56. Luo J., Li R., Chen Y., Zhou X., Ning X., Zhan L., Ma L., Xu X., Xu L., Zhang L. (2019), Rational Design of Z-Scheme LaFeO₃/SnS₂ Hybrid with Boosted Visible Light Photocatalytic Activity towards Tetracycline Degradation, *Sep. Purif. Technol.*, *210*, 417–430. (DOI: 10.1016/j.seppur.2018.08.028)
 57. Huang S., Wang G., Liu J., Du C., Su Y. (2020), A Novel CuBi₂O₄/BiOBr Direct Z-Scheme Photocatalyst For Efficient

- Antibiotics Removal: Synergy of Adsorption and Photocatalysis on Degradation Kinetics and Mechanism Insight, *ChemCatChem*, 12, 4431–4445. (DOI: 10.1002/cctc.202000634)
58. Shi W., Hao C., Fu Y., Guo F., Tang Y., Yan X. (2022), Enhancement of Synergistic Effect Photocatalytic/Persulfate Activation for Degradation of Antibiotics by the Combination of Photo-Induced Electrons and Carbon Dots, *Chem. Eng. J.*, 433, 133741. (DOI: 10.1016/j.cej.2021.133741)
 59. Zhao L., Zhang M., Mujumdar A. S., Adhikari B., Wang H. (2022), Preparation of a Novel Carbon Dot/Polyvinyl Alcohol Composite Film and Its Application in Food Preservation, *ACS Appl. Mater. Interfaces*, 14, 37528–37539. (DOI: 10.1021/acsami.2c10869)
 60. Bhattacharyya S. K., Dule M., Paul R., Dash J., Anas M., Mandal T. K., Das P., Das N. C., Banerjee S. (2020), Carbon Dot Cross-Linked Gelatin Nanocomposite Hydrogel for pH-Sensing and pH-Responsive Drug Delivery, *ACS Biomater. Sci. Eng.*, 6, 5662–5674. (DOI: 10.1021/acsbiomaterials.0c00982)
 61. Singh S., Shauloff N., Jelinek R. (2019), Solar-Enabled Water Remediation via Recyclable Carbon Dot/Hydrogel Composites, *ACS Sustainable Chem. Eng.*, 7, 13186–13194. (DOI: 10.1021/acssuschemeng.9b02342)
 62. Xing B.-B., Liu B., Luo G.-X., Ge T., Jiao H., Xu L. (2023), A Europium Metal–Organic Framework and Its Polymer Composite Membrane as Switch-Off Fluorescence Sensors for Antibiotic Detection in Lake Water, *Inorg. Chem.*, 62, 21277–21289. (DOI: 10.1021/acs.inorgchem.3c03389)
 63. Khan S. A., Abbasi N., Hussain D., Khan T. A. (2022), Sustainable Mitigation of Paracetamol with a Novel Dual-Functionalized Pullulan/Kaolin Hydrogel Nanocomposite from Simulated Wastewater, *Langmuir*, 38, 8280–8295. (DOI: 10.1021/acs.langmuir.2c00702)
 64. Bisht K., Kumar G., Dutta R. K. (2022), Amine-Functionalized Crystalline Carbon Nanodots Decorated on Bi₂WO₆ Nanoplates as Solar Photocatalysts for Efficient Degradation of Tetracycline and

- Ciprofloxacin, *Ind. Eng. Chem. Res.*, *61*, 16946–16961. (DOI: 10.1021/acs.iecr.2c02635)
65. Sarkar A. N., Padhi S., Kumari S. Jagadevan S., Pal S. (2023), Facile Synthesis of Carbon Dot Deposited γ -FeOOH Nanosheet/Polypyrrole Composite: A Robust Photocatalyst for Degradation of Antibiotics under Sunlight Irradiation with Enhanced Antibacterial Activity, *Ind. Eng. Chem. Res.*, *62*, 1227–1244. (DOI: 10.1021/acs.iecr.2c03172)
66. Zhang X., Zha X., Luo Y., Liu T., Chen G., He X. (2023), In₂O₃ Nanoparticle/Bi₄O₅Br₂ Nanosheet S-Scheme Heterojunctions with Interfacial Oxygen Vacancies for Photocatalytic Degradation of Tetracycline, *ACS Appl. Nano Mater.*, *6*, 11877–11887. (DOI: 10.1021/acsanm.3c01720)
67. Luo T., Sun X., Ma D., Wang G., Yang F., Zhang Y., Huang J., Zhang H., Wang J., Peng F. (2023), Fabrication of TiO₂/CdS Heterostructure by Soluble Solid-State Titanium-Oxo-Clusters for Fast Photocatalytic Degradation of Tetracycline, *J. Phys. Chem. C*, *127*, 1372–1380. (DOI: 10.1021/acs.jpcc.2c06101)
68. Liu W., Kang Q., Wang L., Wen L., Li Z. (2022), Facile Synthesis of Z-Scheme g-C₃N₄@MIL-100 (Fe) and the Efficient Photocatalytic Degradation on Doxycycline and Disinfection by-Products by Coupling with Persulfate: Mechanism and Pathway, *Colloids Surf., A*, *635*, 128057. (DOI: 10.1016/j.colsurfa.2021.128057)



Chapter 5

**A Lignin-Derived Carbon Dot-
Upgraded Bacterial Cellulose
Membrane as an All-in-One Interfacial
Evaporator for Solar-Driven Water
Purification**

5.1. Introduction

Freshwater scarcity has been one of the greatest global problems due to water pollution, over-exploitation of water resources, and natural calamities in some underdeveloped and developing countries [1, 2]. Currently, the water purification, desalination, and remediation systems are not economically viable since they involve inefficient energy utilization and sophisticated infrastructure [3, 4]. Many efforts have been made to develop more economical, environmentally friendly, and convenient technologies for solar clean water production [5, 6]. One such technique involves the utilization of solar energy. Solar energy is the most abundant green alternative to fossil fuels one can exploit for freshwater production [7, 8]. Currently, solar desalination through interfacial evaporation is the most energy-efficient strategy for the production of fresh water [9].

In this respect, water technology has been reinforced by a variety of interfacial solar evaporator designs, which have attracted attention in recent years. A solar evaporator absorbs the solar energy through a photothermally active material, generates heat at the water-air interface, and converts water into steam to obtain clean water [10-12]. Highly efficient, wide-range absorption and excellent light-to-heat converting material are prerequisites for solar steam generation [13, 14]. Previously, many photothermal materials have been exploited for photothermal conversion, such as carbonaceous material [15], graphene [16, 17], CNT [18, 19], plasmonic structures [20], polymers [21], semiconductors [22, 23], Metal-organic frameworks [24], etc. Most such material has limited applicability due to its high fabrication cost, tedious synthesis, non-environmentally friendly nature, as well as insufficient scalability.

Interestingly, carbon-based quantum dots CDs are one of the emerging classes of nanomaterials with excellent broadband absorption in the near-infrared (NIR) range with interesting

optical properties, and distinct applicability [25, 26]. Most importantly, carbon dots (CDs) are environmentally friendly and can be easily synthesized from simple or complex organic materials. Recently, plant-derived organic compounds have been utilized as a green source [27] to attribute improved photophysical properties and biocompatibility to CDs [28]. Being the second-largest naturally occurring organic material on earth, lignin has also been explored as a green precursor for synthesizing CDs. Unlike cellulose, lignin has three-dimensional and cross-linked phenolic networks, possessing high carbon content by virtue of a large proportion of sp^2 -hybridized benzene rings. These features, together with abundant phenolic-OH groups, promote the formation of CDs [29]. Furthermore, lignin can be derived from renewable sources, which primarily exist as a waste by-product from the paper-pulp industry [30].

Moreover, the photophysical properties of CDs have also been explored for the degradation of organic pollutants by utilizing the entire solar spectrum through electron-hole recombination and enhancing photocatalytic degradation [31]. Furthermore, tunable photophysical properties of CDs can also be constructively exploited for solar thermal evaporation. The high solar light absorption, stability, and scalability of CDs are beneficial for such applications. CDs have a graphite-like sp^2 carbon cluster [32], which enables it to show lattice vibration when irradiated with solar light and convert it into thermal energy. During the electron transition of CDs after absorbing the energy, they undergo the energy level transition as well as nonradiative transitions, such transitions allow the CDs to release some energy in the form of heat. This thermal energy can further be utilized for photothermal water evaporation [33].

However, the only hurdle in the case of CDs is their tiny size (>10 nm), rendering the slow leaching in water media. Therefore, achieving better recyclability demands appending this material onto a polymeric porous matrix. Previously, CDs have been

incorporated into porous matrices to form composite materials that can be used for drug delivery [34], light-emitting devices [35], sensing [36], energy applications [37], photodynamic therapy [38], etc. As for steam generation applications, polymeric hydrogels enable the integration of nanostructured CDs into macroscopic materials [39-41]. The assembled composite hydrogels of novel properties are utilized in practical applications such as wastewater treatment [42], catalysis [43], etc. In this regard, bacterial cellulose (BC), having a highly porous nanofibrous network structure, was explored due to its strong mechanical properties, flexibility, biocompatibility, and thermal stability. BC, on the other hand, is a green alternative to artificial polymers [44] that are currently being explored for such applications. The porosity and hydrophilicity of BC, which promote water transport and the lower thermal conductivity, cause less heat loss to bulk water during solar evaporation.^[45] Several groups have explored the potential of BC as a solar evaporating platform hybridized with photothermally active material for the solar evaporation process [45-47].

In recent times, researchers have integrated multiple methods and exploited different properties of the photothermal evaporator material. For instance, Song et. al. developed a polyamide thin film membrane for forward osmosis and polypyrrole modified nano-sponge for photothermal evaporation. This coupling system comprehensively utilizes the advantages of both techniques, which improves the separation efficiency for wastewater treatment [48]. Similarly, various carbon-based photothermal materials and devices were employed for interfacial photothermal evaporation [1, 49-52].

In the present study, we have developed a facile cross-linking methodology for the fabrication of carbon dots-based multifunctional photothermal evaporators suitable for solar steam generation, desalination, as well as water decontamination by incorporating it into the bacterial cellulose. Lignin-derived CDs

(N-LCDs) showing excellent broad-spectrum absorption have been utilized to form *c*-BC@N-LCD, by a simple one-pot hydrothermal method. Here, the reusability issue with CDs has also been overcome by cross-linking them with bacterial cellulose. The *c*-BC@N-LCD shows phenomenal light absorption in the NIR range. This solar evaporator has shown an evaporation rate of $2.2 \text{ kg m}^{-2} \text{ h}^{-1}$ under 1 sun illumination with good reusability and robustness even after multiple purification cycles. Additionally, we demonstrate high-performance solar purification from various sources and desalination, as well as water remediation through the removal of heavy metal ions, pharmaceuticals, and dyes. To the best of our knowledge, this material has been the very first report on the fabrication of a potent all-in-one photothermal membrane out of sustainable precursors like lignin and BC. Thus, the multifunctional *c*-BC@N-LCD can have a wide range of applications, ranging from a large-scale industrial platform to a portable water-purifying appliance.

5.2. Experimental Section

5.2.1. Materials and Reagents

Lignin was purchased from TCI, sodium chloride (NaCl), ethylenediamine (EDA), and methylene blue (MB), methyl orange (MO), congo red (CR), and rhodamine B (RhB) were procured from Sigma-Aldrich. Kombucha and tea powder were purchased from the local market. Cobalt(II) sulphate monohydrate ($\text{CoSO}_4 \cdot \text{H}_2\text{O}$), Iron(II) chloride (FeCl_2), Silver nitrate (AgNO_3), and Cadmium chloride (CdCl_2) were purchased from Loba. Dextrose, epichlorohydrin (ECH), sodium hydroxide (NaOH), tetracycline (TET), and doxycycline (DOX) are obtained from SRL. All the chemicals were of analytical grade and used without further purification. Deionized water (DI) was used throughout the experiment.

5.2.2. Synthesis of N-LCDs

N-doped lignin-derived CDs (N-LCDs) were synthesized from 0.6 g lignin powder, which was dissolved in 25 mL of DI water, and 5 mL of EDA as a doping agent. Treat the above reaction mixture at 180 °C for 12 h hydrothermally. The obtained solution in the reaction mixture was centrifuged at 10000 rpm for 30 min to remove the settled debris and then dialyzed against the DI water for 24 h. The purified CD solution thus obtained was used for further studies.

5.2.3. Preparation of Bacterial Cellulose (BC)

The kombucha strains were acquired online, and tea powder was purchased from a regional market. Black tea powder was mixed with 1000 mL of water and boiled for 5 min. After obtaining the tea solution, it was cooled and the tea leaves via filtration. Then add 60 g of dextrose to form the culture media for Kombucha. A piece of kombucha (10 cm diameter) was added to the above freshly prepared growth medium and kept for culturing for 7 days in static conditions, maintaining the 30 °C. After the completion of BC growth, a brown-colored BC pellicle was harvested from the air-liquid interface. The impure BC pellicle was washed first with water and then allowed to be thoroughly washed with 2 % NaOH to eliminate the attached bacterial cells and other impurities. Following washing, the BC membranes were stored in water at 4 °C prior to use.

5.2.4. In-situ Synthesis of BC@N-LCDs (Without Cross-Linking)

The 2.4 g of lignin powder was dissolved in 70 mL of DI water, and 20 mL of EDA was further added to this solution. After ensuring complete dissolution of both reagents, the above-obtained BC pellicle (~5.1 cm diameter, ~0.8 cm thickness) was added and treated hydrothermally at 180 °C for 12 h. After the

reaction, BC@N-LCD was washed out with distilled water under continuous stirring for 24 h.

5.2.5. Cross-Linking of BC@N-LCDs with ECH

To overcome the problem of leaching, the BC@N-LCD was cross-linked with ECH. For the same, take 2.4 g lignin dissolved in 70 mL of DI, and add BC (5.1 cm diameter, 0.8 cm thickness) followed by stirring at 1000 RPM for 30 mins while heating gently. This is to ensure complete imbibition of the lignin solution. To this mixture, add 6 mL of 12 wt % NaOH and 1.2 mL of ECH. Then transfer the obtained solution into a Teflon-lined stainless steel hydrothermally and add 20 mL of EDA into it as a doping agent and treat them hydrothermally for 12 h at 180 °C. The obtained black-colored *c*-BC@N-LCD hydrogel was washed with distilled water several times under continuous stirring.

5.2.6. Characterization Techniques

The morphological analysis of *c*-BC@N-LCD was carried out using a scanning electron microscope (SEM), Carl Zeiss, Germany, with an accelerating voltage of 10 kV. Aerogel samples (obtained after lyophilization of hydrogels) for SEM were prepared by cutting using a sharp razor and sticking them on carbon tape. Samples were gold-sputtered prior to the imaging to avoid charging. Long BC fibers and the distribution of aggregate N-LCD in the BC matrix were visualized on an FEI Tecnai 30 G2S-TWIN transmission electron microscope (TEM) operated at an accelerating voltage of 300 kV. TEM sample preparations were done on a carbon-coated copper grid by drop-casting two to three drops of the well-dispersed dilute sample solution. The crystallinity of BC was determined from the wide-angle X-ray scattering (WAXS) measurements carried out on a Xeuss SAXS/WAXS system using a Genisxmicro source from Xenocs

operated at 50 kV and 0.6 mA. The powder X-ray diffraction (XRD) pattern of the N-LCD sample was taken on a PANalytical Empyrean instrument equipped with reference radiation of Cu K α ($\lambda = 1.54 \text{ \AA}$) at an operating voltage of 45 kV. X-ray photoelectron spectroscopy (XPS) was done to know about the chemical functionality and composition of NLCDs, BC, BC@N-LCD, and *c*-BC@N-LCD using PHI 5000 VersaProbe II (ULVAC-PHI Inc., USA), equipped with a micro-focused (100 μm , 15 kV) monochromatic Al-K α X-Ray source ($h\nu = 1486.6 \text{ eV}$). XPS spectra were processed using PHI's Multipak software. The binding energy was referenced to the C1s peak at 284.8 eV. The Attenuated Total Reflectance Fourier Transform Infrared (ATR-FTIR) spectra were recorded with a Bruker Alpha II system over the wavenumber range of 4000-400 cm^{-1} . Absorption, total reflectance, and diffuse reflectance spectra (DRS) of N-LCD and BC@N-LCD, and *c*-BC@N-LCD were recorded in the 200-2500 nm range, using a UV-VIS-NIR spectrometer (UV-2600). The measurements were corrected by the baseline/blank correction. The NIR solar reflectance (R^*) was measured using the solar spectral irradiance in the range of 700-2000 nm. The solar absorptions “A” of samples in the 700-2000 nm region were measured using equation 5.1.

$$A = \frac{\int (1-T) \cdot S \cdot d\lambda}{\int S \cdot d\lambda} \quad (5.1)$$

Where T is the reflectance of the sample, S is the solar spectral irradiance ($\text{Wm}^{-2} \text{ nm}^{-1}$), and λ is the wavelength. The wettability of samples was checked using a contact angle goniometer (KYOWA, DMe-201) by sessile-dropping water (2.0 μL) droplets on the porous BC@N-LCD. The specific surface areas of the aerogels were measured by the Brunauer-Emmett-Teller (BET) method using Autosorb-1C (AX1C-MP-LP) at 298 K. The pore size distribution was obtained by the Barrett-Joyner-Halenda (BJH) method. Differential Scanning Calorimeter (DSC)

measurements for finding the latent heat of vaporization were acquired on a PerkinElmer DSC 8000 instrument using an aluminum hermetic sample pan at a scan rate of 5 °C/min. The concentration of metal ions in the purified water sample was determined by Inductively Coupled Plasma Mass Spectrometry (ICP-MS) analysis performed in a Thermo Scientific iCAP RQ spectrometer.

5.2.7. Estimation of Photothermal Energy Conversion

The evaporation experiments were performed at room temperature under a xenon lamp (250 W) solar simulator coupled with a Newport monochromator (Newport Instruments). For water evaporation studies, *c*-BC@N-LCD and the control BC with ~0.8 cm thickness and ~5.1 cm diameter were used. *c*-BC@N-LCD were kept on a pure BC pellicle and allowed to append on normal tap water in a petri dish. The size of the petri dish was selected to fit the fabricated *c*-BC@N-LCD inside it. The approximate power density at the evaporating surface was kept at 1 kW m⁻². The mass loss corresponding to the evaporated water was calculated using an electronic weighing balance (iScale i-400c, India). The temperature profiles before and after illumination were captured on an IR thermal imaging camera (FLIR TG 267). The photothermal energy conversion from solar light into heat for vapor generation was calculated from the amount of evaporated water with and without *c*-BC@N-LCD and control BC. Equation 5.2 was used to calculate the power necessary for the evaporation of water (Q_e).

$$Q_e = \frac{m \times h_{LV}}{t} \times 100 \quad (5.2)$$

Where m is the mass of evaporated water per unit area, t is the time, and h_{LV} is the enthalpy of vaporization of water for a

particular evaporating system. h_{LV} of water when evaporating by a hydrogel system was obtained directly from a DSC thermogram of the corresponding hydrogel sample at a heating rate of 5 °C min⁻¹ under a nitrogen flow. The h_{LV} of free water was also calculated for comparison from the thermogram of pure water. If Q_s is the power of incident solar radiation monitored in a solar power meter (Newport Instruments, 91159A), the solar evaporation efficiency (η) is obtained as the ratio of Q_e and Q_s (equation 5.3)

$$\eta = Q_e / Q_s$$

The final equation for η in percentage is given in equation 5.4.

$$\eta = \frac{m \times h_{LV}}{I \times t}$$

Where $Q_s = I$, which is the incident solar power density.

5.2.8. Real-Time Solar Evaporation Experiments

The practicality of the solar evaporator was tested by performing evaporation experiments outdoors in real time with a lab-made setup on a sunny day with no clouds. To find out the solar intensity rate was continuously monitored every 10 min on a power meter, and the average value was considered for calculations. The rate of evaporation was examined by taking the water from different sources, such as lake water, RO water, tap water, pond water, and river water. In order to check the per-day performance of the prepared evaporator, generated steam was condensed and collected at the end of the day, while the solar power intensity, temperature, and humidity were noted each hour.

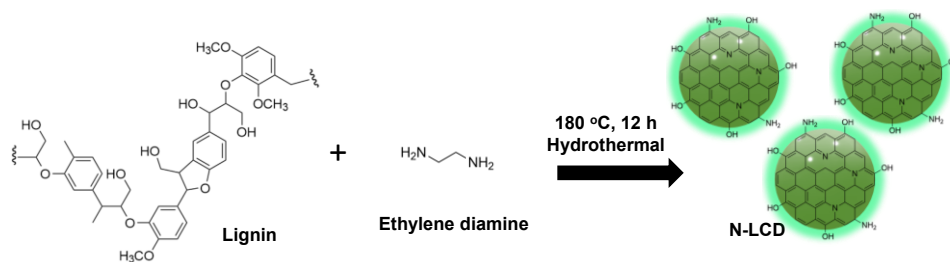
5.2.9. Evaporation Rate at Different Water Sources, Desalination and Removal of Pollutants by *c*-BC@N-LCDs

The rate of evaporation was examined by taking the water from different sources, such as lake water, RO water, tap water, pond water, and river water. The solar evaporation, as mentioned above, was performed. For seawater desalination, the 3.5 % NaCl was used as a feed solution and irradiated the *c*-BC@N-LCD with 1 kW m^{-2} sun illumination. The loss in weight is measured by a weighing balance (iScale i-400c, India) and used to calculate the evaporation rate and evaporation efficiency. To evaluate the removal of heavy metal ions from water, a certain amount of wet *c*-BC@N-LCD was added to 50 mL of aqueous solutions containing 2 ppm of $\text{CoSO}_4 \cdot \text{H}_2\text{O}$, FeCl_2 , AgNO_3 , and CdCl_2 , respectively. Each sample of simulated water was treated with *c*-BC@N-LCD, and the final water samples were collected, followed by measurement of metal ion concentrations through ICP-MS. Similarly, *c*-BC@N-LCD hydrogels were placed separately in aqueous solutions containing dyes like MO, MB, RB, and CR, etc. (2 ppm each), and pharmaceutical drugs such as TET and DOX (both 10 ppm). Efficacy in water purification in these cases was checked after irradiating the *c*-BC@N-LCD-containing evaporating system with sunlight in real time (illumination intensity of $\sim 1 \text{ kW/m}^2$). The decrement in the concentration of dyes and pharmaceutical drugs before and after treatment was monitored with a UV-visible spectrophotometer.

5.3. Results and Discussion

5.3.1. Preparation and Characterizations of N-LCDs

N-LCDs were prepared by one-pot hydrothermal synthesis using lignin as a precursor for carbon and EDA as an N dopant (Scheme 5.1).



Scheme 5.1. Illustration of the synthesis of N-LCDs

Notably, a deep black-brown color dispersion was obtained after the hydrothermal synthesis of N-LCDs with an intense green color fluorescence (FL) (**Figure 5.1a**). The morphology of N-LCDs was studied using TEM. **Figure 5.1bi-ii** shows the presence of a homogenous distribution of spherical-shaped CDs throughout the solution. Notably, the HR-TEM image of N-LCDs shows a well-defined lattice fringe with a d-spacing of 0.24 nm that corresponds to the (112) plane of the graphitic structure (**Figure 5.1b iii**). **Figure 5.1c** reveals that the histogram of the size distribution of CDs falls in the 2.4-4.2 nm range. A broad absorption spectrum of N-LCDs in **Figure 5.1d** with peaks positioned at 290 nm belongs to the π - π^* transition occurring from core states of carbon, and peaks at 350 nm and 415 nm are obtained from n - π^* transition from surface states [53]. The N-LCDs in solution yielded the FL at 390 nm emissions with an excitation wavelength of 410 nm due to the up-conversion FL phenomenon as indicated in **Figure 5.1e**. The yield of N-LCDs was found to be 619 mg/mL. This result demonstrates the potential of as-prepared N-LCDs for sensing and photocatalytic applications. A broad diffraction peak in **Figure 5.1f** is observed at 23.0° , corresponding to the (002) plane of graphite [54]. The suitability of N-LCDs was checked by acquiring diffused reflectance spectra (DRS) of dried N-LCD samples at the NIR range (700-2500 nm). As anticipated in **Figure 5.1g**, N-LCDs show very little reflectance loss, i.e., 10.53 %, making it an attractive photothermal substance for designing a robust interfacial solar evaporation platform.

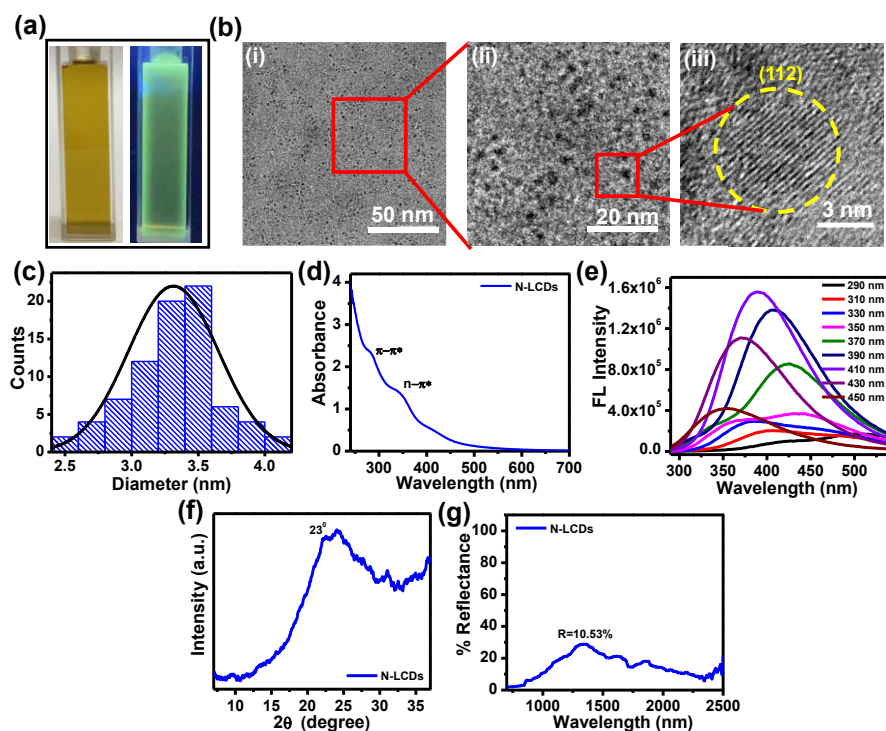


Figure 5.1. Characterizations of N-LCD: (a) digital photographs of N-LCD dispersion captured under bright light (right) and UV light (left), (b) TEM images of N-LCD captured at different magnification levels, (c) histogram representing size distribution, (d) UV-visible absorption spectrum, (e) FL spectra taken under varied excitation wavelengths. (f) XRD pattern. (g) DRS spectrum of N-LCD in the NIR range.

The functionalities of N-LCD were examined by FTIR spectrum (**Figure 5.2a**). A broad peak from 3350-2851 cm^{-1} is assigned to the combinations of stretching vibrations of O-H/N-H and C-H bonds. Other prominent peaks at 1664, 1558, 1398, and 1327 cm^{-1} are assigned to C=O stretching, N-H bending, and C-N stretching, and aromatic ring vibrations, respectively. The peak at 1185 cm^{-1} is from C-O functionality. Further, the functionalities and chemical composition of N-LCDs were inspected by XPS. The XPS survey spectrum of N-LCDs (**Figure 5.2b**) confirms doping with N elements and chemical composition. The deconvoluted high-resolution (HR) spectra for C1s, O1s, and N1s are provided in **Figure 5.2c-e**. In high-resolution C1s XPS spectra (**Figure 5.2c**), the peaks at 284.7, 286.0, and 287.7 eV are attributed to C-C/C=C, C-N/C-O, and C=O,

respectively. In the HR O1s XPS spectra (**Figure 5.2d**), the peaks at 531.5 and 532.8 eV are assigned to C=O and C-O-C/C-OH, respectively. **Figure 5.2e** indicates the high-resolution spectra of N1s, the peaks at 399.5 and 400.8 eV are for pyridinic-N and pyrrolic-N. The surface functionalization of CDs plays an integral part in their dispersibility in aqueous and organic solvents, as the surface groups of CDs make them either hydrophilic or hydrophobic. Notably, functional groups such as hydroxyl, carboxyl, amines, amide, thiols, etc, give CDs hydrophilicity, making them highly dispersible in water. The as-synthesized N-LCDs possess OH/NH, C-H, C=O, and C-O groups on their surface, which makes them dispersible in water [55].

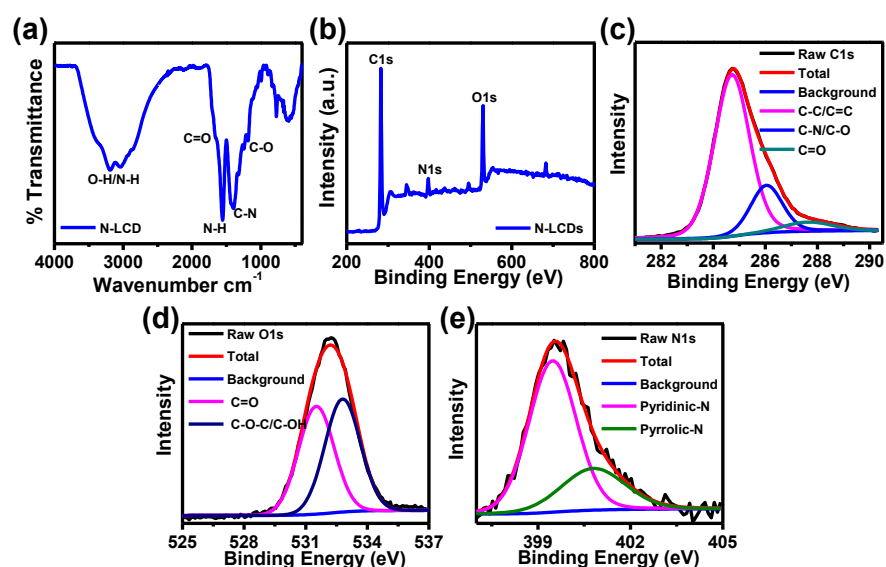


Figure 5.2. Chemical functional characterization of N-LCDs: (a) FTIR, (b) XPS survey scan. Details of XPS deconvoluted spectra of N-LCDs (c) C1s, (d) O1s, and (e) N1s.

5.3.2. Preparation Strategies of NIR-Active Composite Membrane

Despite promising broadband absorption of N-LCDs, its photothermal activity can be exploited for the solar evaporation application only if it is stabilized against leaching to the feed water media. This is because the size of photothermally active N-LCDs is in the 2.4 - 4.2 nm range. Here, we chose BC as a convenient porous and biocompatible substrate to accommodate

N-LCDs without losing its photothermal activity. BC also serves as a superior thermal insulating platform, which would facilitate effective thermal management in the anticipated solar evaporating membrane during the interfacial evaporation process [44].

By culturing the Kombucha strain, BC was produced at the liquid-air interface as a thick pellicle. **Figure 5.3a** shows a digital image of a BC pellicle that was procured after multiple steps of purification. **Figure 5.3b** represents the robust network structure of a lyophilized BC pellicle as observed in the SEM (a lower magnification image is given in the inset). The thicknesses of fibrils are analyzed and a histogram is drawn (**Figure 5.3c**), showing that the width of BC fibrils falls in the 20-100 nm range. Furthermore, the ATR-FTIR spectrum of BC is shown in **Figure 5.3d**, featuring all the characteristic peaks of cellulose. The peak at 3352 cm^{-1} arises due to the hydroxyl groups (-OH) stretching vibration of BC. The 2895 cm^{-1} is attributed to C-H stretching vibrations. The peak observed at $1035\text{-}1059\text{ cm}^{-1}$ belongs to C-O-C and C-O-H stretching vibrations of the pyranose ring [56]. The XPS survey spectrum of BC exhibited two peaks at 284.0 and 530.4 eV, indicative of the presence of C and O, respectively (**Figure 5.3e**). The HR C1s peak of cellulose (**Figure 5.3f**) shows three resolved peaks at 284.7 eV, 286.6 eV, and 288.0 eV, assigned to C-C/C-H sp^3 type carbon, C-O-, and O-C-O, respectively. The HR O1s peak (**Figure 5.3g**) confirms the existence of C-O-C (531.2 eV) and C-OH (532.6 eV) functionalities in BC [57].

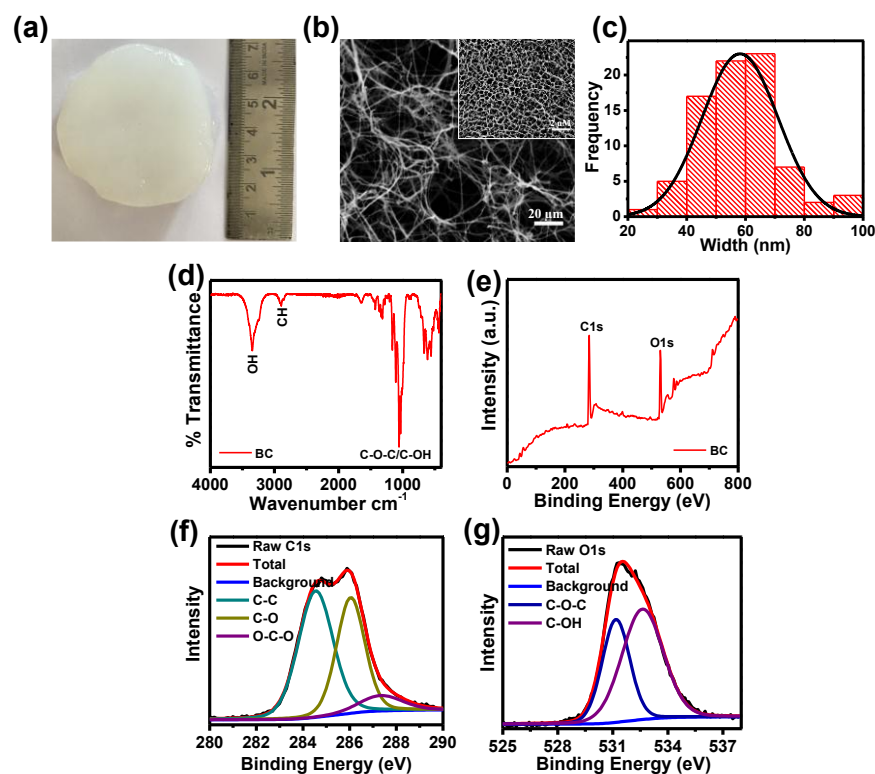
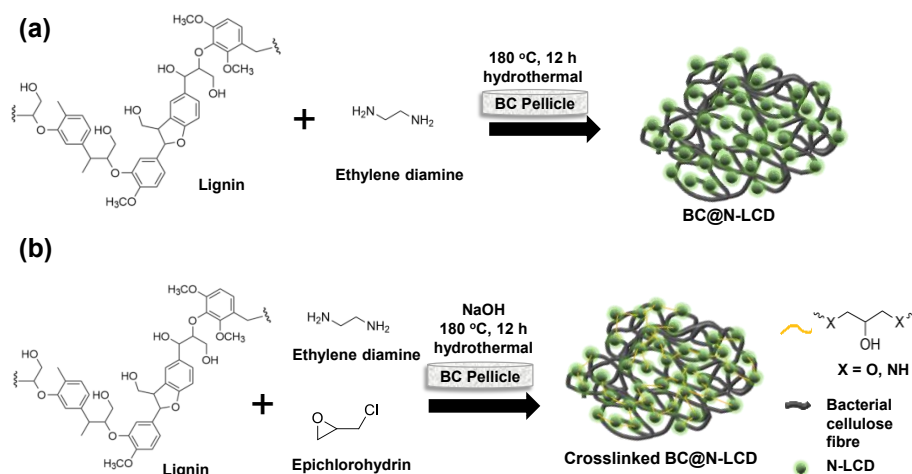


Figure 5.3. Characterizations of BC: (a) digital photograph, (b) SEM image showing nanofibrous porous network structure, (c) histogram drawn for width of cellulose fibers, (d) ATR-FTIR spectrum, (e) XPS survey scan. HR deconvoluted peak for (f) C1s and (g) O1s.

As a first trial, N-LCDs were incorporated into the BC matrix by the in situ hydrothermal method. The BC@N-LCD obtained was black and showed good NIR activity. However, we observed a decline in solar evaporation efficiency upon repeated cycles. Therefore, we rationally designed a cross-linking strategy to covalently attach N-LCDs onto BC fibers. The incorporation of photothermally active N-LCDs in the BC matrix was carried out by preparing a homogenous solution of lignin and cross-linker ECH, afterward treating them hydrothermally. **Scheme 5.2a** illustrates the fabrication of a photothermally active evaporation membrane by direct incorporation of N-LCDs onto BC, while **Scheme 5.2b** illustrates a synthesis of *c*-BC@N-LCD by cross-linking N-LCDs onto BC.



Scheme 5.2. Schematic illustration of: a) synthesis of BC@N-LCD by direct incorporation of N-LCD onto BC, b) synthesis scheme of *c*-BC@N-LCD by *in situ* cross-linking of N-LCD and BC.

Further, keep both solar evaporation membranes in water for 24 h under sunlight (**Figure 5.4**). In the former case, (**Figure 5.4a**) feed water evidently showed brown coloration to feed water due to the slow leaching of N-LCDs from BC@N-LCD, showing the ineffectuality of appending N-LCDs to the BC matrix, whereas after cross-linking with ECH, *c*-BC@N-LCD (**Figure 5.4b**) impart no visible coloration to feed water, showing the effective covalent anchoring of N-LCDs onto BC fibrils.

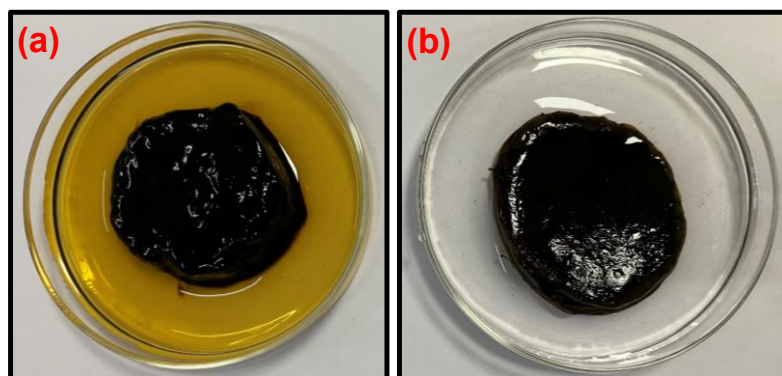


Figure 5.4. Demonstration of leaching of N-L@CD from the hydrogel composites (a) before (BC@N-LCD), (b) after cross-linking with ECH (*c*-BC@N-LCD).

5.3.3. Characterizations of *c*-BC@N-LCD Hydrogel Composite

The physical appearance of the as-synthesized *c*-BC@N-LCD hydrogel membrane is shown in **Figure 5.5a**. The micromorphological characteristics of the *c*-BC@N-LCD composite were examined using TEM (**Figure 5.5b**) and SEM (**Figure 5.5c**), confirming that the N-LCDs are well bound to BC nanofibrils (see red arrows marked in **Figure 5.5b**). A comparison of FTIR curves obtained for *c*-BC@N-LCD with those of non-crosslinked composite and N-LCDs is presented in **Figure 5.5d**. A group of strong vibrations emerged at 1005, 1028, and 1150 cm^{-1} , which are not much evident in the non-crosslinked BC@N-LCD composite, and are attributed to C-O-C bonds formed via cross-linking with ECH. Peaks at 1640 and 1430 cm^{-1} were attributed to C=O (carbonyl) stretching and C=C stretching (from aromatic rings) from the lignin moiety. Stretching vibrational peaks corresponding to C-H and O-H/N-H bonds are merged and appear as a considerably broad band between 2700-3600 cm^{-1} in both N-LCDs and non-cross-linked BC@N-LCD. However, it is worth mentioning that the intensity of O-H/N-H stretch vibrations (broad peak $>3000 \text{ cm}^{-1}$) is greatly reduced in *c*-BC@N-LCD because a large proportion of -OH and -NH moieties from N-LCDs were engaged in cross-linking by ECH.

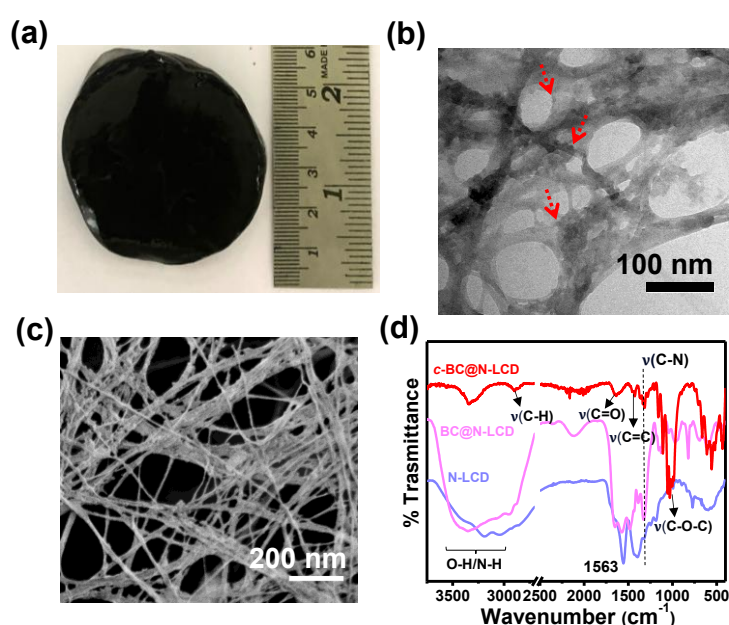


Figure 5.5. (a) Digital photograph of the fabricated *c*-BC@N-LCD hydrogel. Morphological characterizations of *c*-BC@N-LCD by: (b) TEM (red dotted arrows point to the attached N-LCDs on BC fibres), and (c) SEM. Comparison study of *c*-BC@N-LCD, BC@N-LCD, and N-LCDs by (d) FTIR.

Furthermore, the XPS survey scan recorded for *c*-BC@N-LCD, non-cross-linked BC@N-LCD, and N-LCD is compared in **Figure 5.6a**. All three samples contain peaks corresponding to C1s, N1s, and O1s at the peak intensities of 281.6, 398.4, and 531.6 eV, respectively. A comparison of HR C1s peaks of the same samples is also provided in **Figure 5.6b**.

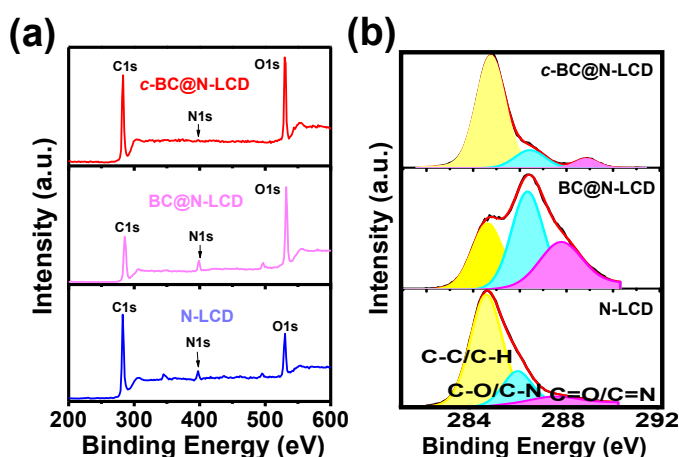


Figure 5.6. (a) XPS survey scan, and (b) HR scan of C1s.

Based on the above discussion a plausible cross-linking mechanism is proposed and illustrated in Fig. 1e. In the presence of OH⁻ in the reaction medium, alkoxide (-RO-) groups from BC and/or -NH₂ groups from N-LCDs can react with ECH in two ways: One way, to form oxirane moieties in close vicinity by eliminating Cl⁻ (**Figure 5.7i and iii**), whereas a second possibility to initiate oxirane ring opening as shown in **Figure 5.7ii** [58]. It is worth mentioning that cross-linking might be possible with two N-LCDs and two cellulose nanofibers, as well as between N-LCDs and BC. A representative cross-linked product is hence

presented in **Figure 5.7iv** as a possible chemical structure of *c*-BC@N-LCD.

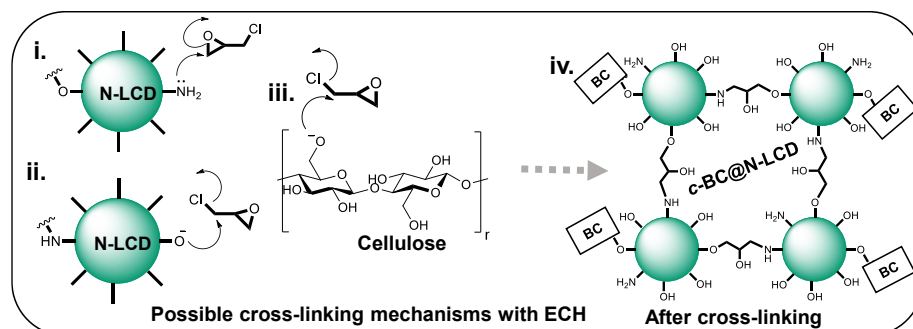


Figure 5.7. Possible mechanisms of cross-linking by ECH: (i) and (ii) linking with the oxirane moiety by eliminating Cl^- of ECH by RO^- from N-LCDs and BC, respectively, and (iii) opening of the oxirane ring by -NH_2 of N-LCDs. (iv) Representative structure of *c*-BC@N-LCD formed after cross-linking.

Moreover, BET surface area analysis was performed to reveal the surface area and nature of porosity of *c*-BC@N-LCD aerogel compared to native BC material. BET surface area plots and BJH pore volume plots of both samples are provided in **Figure 5.8a-d**. Though the mesoporosity of the photothermal composite was maintained upon incorporation of N-LCDs, a reduction in pore volume from 237 Å to 183 Å is evident.

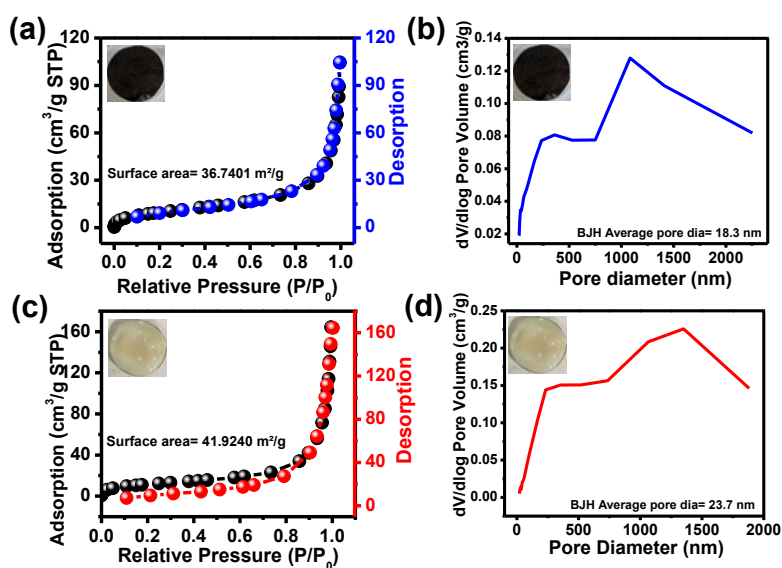


Figure 5.8. Nitrogen adsorption and desorption analysis conducted for *c*-BC@N-LCD and control pristine BC aerogels: (a) BET adsorption isotherms, and (b) corresponding BJH pore volume plots for *c*-BC@N-LCD. (c) BET adsorption isotherms, and (d) corresponding BJH pore volume plots for BC. The digital photographs of the samples analyzed are given as insets.

Besides, experiment details to prove the hydrophilicity and sorption capacity of *c*-BC@N-LCD, the sessile drop contact angle tests are performed. To illustrate the hydrophilic nature of the material, wettability studies were carried out as sessile drop water contact angle experiments on BC (**Figure 5.9a**) and *c*-BC@N-LCD (**Figure 5.9b**). The good hydrophilic nature of BC and *c*-BC@N-LCD renders quick absorption of water when a small drop of water comes into contact with the hydrogel composite. This supports easy wicking of water through the fabricated evaporator. Both the mesoporous and microporous nature of the photothermal composite with good hydrophilic nature would therefore be expected to enhance the rate of evaporation by facilitating faster water transport to the points of evaporation.

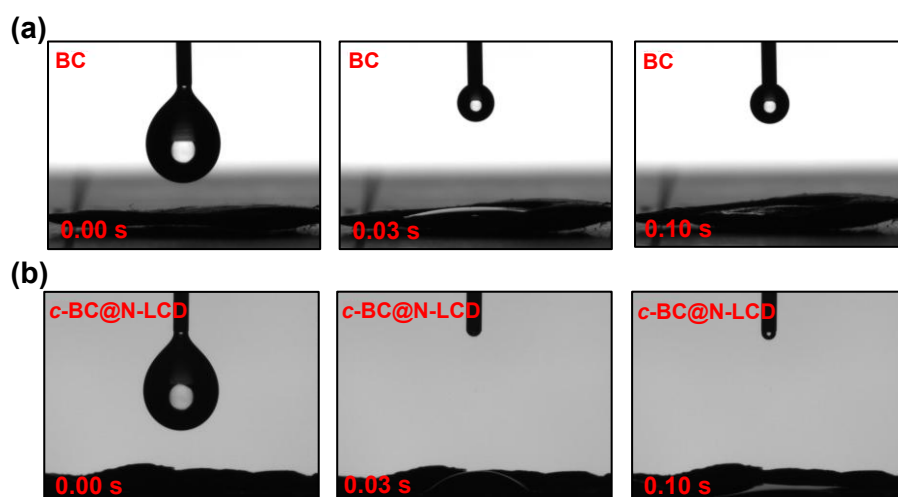


Figure 5.9. Wettability studies performed by contact angle measurements: (a) BC, (b) *c*-BC@N-LCD.

5.3.4. *c*-BC@N-LCD as a Photothermal Platform

The above design thus can greatly facilitate the interfacial heating since a better light-to-heat conversion for steam generation can be anticipated by using the 3D interconnected porous network of BC for hosting wide-spectrum active N-LCDs [59]. Further, to evaluate the light-harvesting capability of the *c*-BC@N-LCD hydrogel, we acquired its DRS spectrum in wet conditions (**Figure 5.10a**). The percentage NIR reflectance spectrum derived from DRS data is presented in **Figure 5.10b**. NIR absorption of *c*-BC@N-LCD is calculated to be 88.1 %. Further, to verify the effective photothermal conversion by the composite, the temperature rise of *c*-BC@N-LCD was recorded while illuminating with 1 kW m⁻² solar light. A temperature vs time plot is drawn for the photothermal platform fabricated (**Figure 5.10c**). A control BC and water are also kept for reference. In reconciliation with the above findings, the *c*-BC@N-LCD hydrogel is endowed with a captivating photothermal property and shows a sharp increase in surface temperature within the first 30 sec and reaches a highest temperature of 53.2 °C within 152 sec upon illumination of 1 kW m⁻² sunlight. Thermal profiles of the same composite captured by an infrared (IR) thermal imaging camera before and after illumination under 1 kW m⁻² sunlight for 60 min are presented in **Figure 5.10d**. The surface temperature of BC increased only to some extent from 25.4 to 33.3 °C, whereas a visible surface temperature rise to 53.2 °C was noticed in *c*-BC@N-LCD. The effect of *c*-BC@N-LCD-water interaction on the overall evaporation performance of *c*-BC@N-LCD is a decisive factor in determining the total evaporation performance. The h_{LV} of water alone and with *c*-BC@N-LCD were measured using a DSC experiment; thermograms are shown in **Figure 5.10e**. A significant broadness in the evaporation peak of *c*-BC@N-LCD hydrogel can be seen in contrast to the sharp peak for pure water. Knowingly, the liquid-to-gas transition happened sharply at the boiling temperature in the case of free-state water

and decreased immediately. However, evaporation started with less required energy in the hydrogel system and decreased gradually after reaching a maximum. It is remarkable that the completion of evaporation still happens at a higher temperature due to the considerably high energy needed for the evaporation of bound water. Additionally, the broadness of the evaporation curve indicates the existence of multiple possible water states due to the interaction between cellulose polymer and water [44]. On the other hand, the overall h_{LV} of water from c -BC@N-LCD hydrogel was calculated to be 1971 kJ kg^{-1} , which is lower than free water evaporation enthalpy, i.e., 2267 kJ kg^{-1} (i.e., close to the theoretical value = 2260 kJ kg^{-1}).

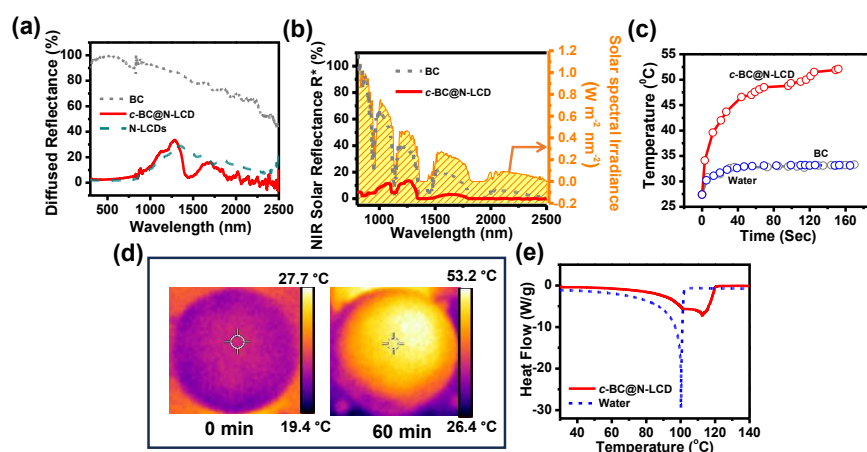


Figure 5.10. (a) DRS of N-LCD, BC, and c -BC@N-LCD acquired in the full spectrum range, (b) corresponding % NIR reflectance. (c) The comparative temperature rise in water (blue), BC (grey), and c -BC@N-LCD (red) after illuminating the evaporator for approximately 2 min. (d) IR thermal image of BC and c -BC@N-LCD captured after illumination of 1 kW m^{-2} simulated solar light for 60 min (top view). (e) DSC curves show a difference in evaporation of c -BC@N-LCD and pure water.

5.3.5. Solar Evaporation Performance Studies

To demonstrate the substantiated effective localization of heat generated at c -BC@N-LCD–water interface (composite kept on the top of the water, which is taken in a cuvette) while irradiating

with simulated sunlight (1 kW m^{-2}) as shown in photographs of **Figure 5.11a** (digital) and **Figure 5.11b** (thermal). Once the practicality of *c*-BC@N-LCD as a photothermal platform for freshwater production was established, interfacial solar-driven evaporation experiments were accomplished using a lab-made setup in schematic **Figure 5.11c**. Next step, the evaporation performance of *c*-BC@N-LCD was correlated with two control experiments, i.e., a pristine BC and the same volume of blank water. The cumulative water evaporated observed in each case is plotted in **Figure 5.11d**. *c*-BC@N-LCD hydrogel achieved an elevated ER, $2.2 \text{ kg m}^{-2} \text{ h}^{-1}$, and photothermal evaporation efficiency of 120.4 % at solar irradiation of 1 kW m^{-2} , verifying its excellent light-to-vapor conversion efficiency. The efficiency of above 100 % can come from the underestimation of the harvested solar energy, which ultimately reflects in the final efficiency value. Also, several factors can lead to this speculation, such as 1) additional energy can be gained from the environment, 2) many factors, such as uneven interfacial temperature across the membranes, and changes in humidity, can also lead to underestimation of the light energy that falls on the evaporator surface, etc [60-62]. **Figure 5.11e** represents the comparative rate of water evaporated in BC, water, and *c*-BC@N-LCD. In addition, the durability and stability of *c*-BC@N-LCD hydrogel were tested for practical applications. After 10 cycles, ER remains at $2.2 \text{ kg m}^{-2} \text{ h}^{-1}$ (**Figure 5.11f**), indicating the longevity of the *c*-BC@N-LCD evaporator.

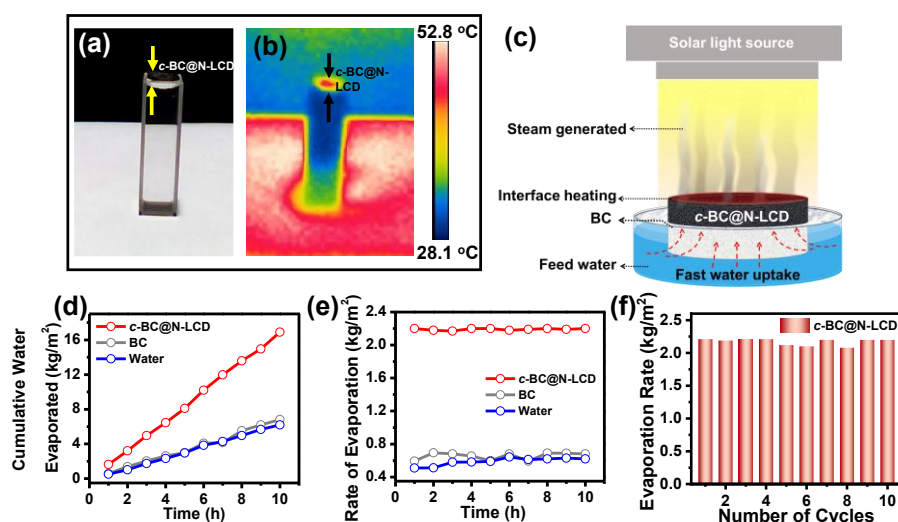


Figure 5.11. (a) Digital, and (b) IR thermal profile captured for demonstrating heat localization at the *c*-BC@N-LCD-water interface upon exposure to 1 kW m^{-2} solar light. (c) Schematic representation of a lab-made setup used for solar evaporation experiments (red arrow marks signify effective up-side bulk water transportation). Comparative studies of water mass loss for BC, water, and *c*-BC@N-LCD; (d) cumulative mass of water evaporated vs time plot, (e) rate performance plot, and (f) cyclic performance carried out for 10 cycles.

As indicated in **Table 5.1**, which tabulates ERs obtained by mass loss of water for *c*-BC@N-LCD, BC, and blank water.

Table 5.1. Represents the ER of the composite, BC, and water.

Sr. No.	Material	Evaporation Rate ($\text{kg m}^{-2} \text{ h}^{-1}$)
1.	<i>c</i> -BC@N-LCD	2.2
2.	BC	0.65
3.	Water	0.58

Moreover, the effect of loading (**Figure 5.12a-b**) on photothermal efficiency was checked and studied further. The composition of a photothermal *c*-BC@N-LCD platform consists of 1) N-LCD, responsible for the photothermal activity, 2) a cross-linking part connecting each N-LCD and BC, and 3) BC as a matrix. To calculate the active component loading, a *c*-BC@N-LCD composite of $2 \text{ cm} \times 2 \text{ cm} \times 0.4 \text{ cm}$ ($l \times b \times h$) was taken and compared with the weight of a

pure BC pellicle of the same dimension (mass from crosslinking units was neglected). Thus, % loading with 86 %, 80 %, 79 %, and 73 % were obtained by varying the amount of lignin precursor as 600 mg, 400 mg, 200 mg, and 100 mg, respectively, during the preparation of *c*-BC@N-LCD. The loading of 86 % was the maximum active component loading possible, above which the cross-linking could not hold N-LCD to the BC matrix. This maximum composition has therefore been selected for further studies. While checking the evaporation performance on the composition, an obvious increase in the rate of evaporation was observed (**Figure 5.12a**) because of the greater availability of NIR active components on the exposed *c*-BC@N-LCD surface. Furthermore, variation in the intensity of irradiation has been studied and shown in **Figure 5.12b**, which indicates that as we increase the solar power intensity, there is an increase in the rate of evaporation observed.

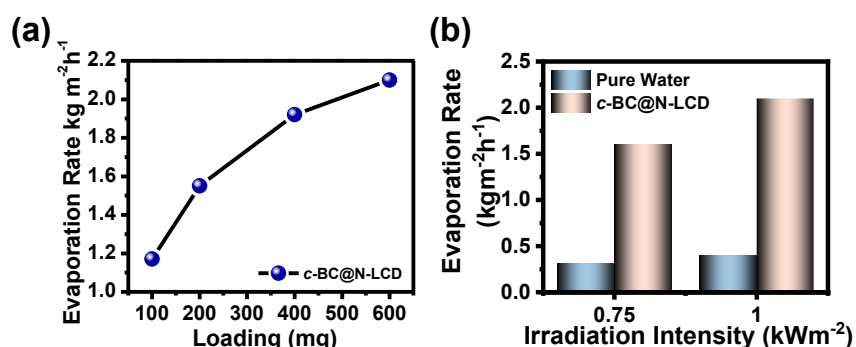


Figure 5.12. (a) Evaporation rate of *c*-BC@N-LCDs under different loading. (b) Effect of irradiation intensity on photothermal evaporation performance.

The evaporation performance of as-fabricated *c*-BC@N-LCD with several reported solar evaporators is compared and given in **Table 5.2**, indicating an excellent evaporation performance of our system achieved by following a simple fabrication strategy.

Table 5.2. Indicative of a different solar evaporator for comparing the composition and evaporation rate.

Sr. No.	Sample	Composition	Evaporation rate ($\text{kg m}^{-2} \text{h}^{-1}$)	Solar irradiation (1 kW m^{-2})	Reference
1.	3D wooden cone evaporator	Tannic acid and iron sulfate hydrate, Poplar veneer	1.79	1	63
2.	Integrated carbon-based aerogel	GO/SWCNTs/SA	1.6	1	64
3.	Biochar-based interfacial systems	Carbonized corn straw	1.4	1	65
4.	Mesoporous interfacial system	Graphite and wood	1.2	1	66
5.	Semiconductor decorated wood membrane	CuFeSe ₂ N/ wood	1.3	5	67
6.	Water Delivery Channel in solar evaporator	Polyethylene foam and Air-laid paper	1.46	1	68
7.	Hierarchical structures	Suedette sponge, filter paper, and polydopamine	1.8	1	69
8.	Bifunctional MoS ₂ -based evaporator	MoS ₂ nanoflowers, Air-laid paper, Expandable polyethylene	1.27	1	70
9.	Carbon Dot/ Hydrogel	Carboxymethyl cellulose/Chitosan/C-Dots	1.4	1	58
10.	Au@Bi ₂ MoO ₆ -carbon dots solar steamer	Nanopyramids/Nanoparticle/Carbon-dots	1.69	1	71
11.	c-BC@N-LCDs	Lignin derived CDs and bacterial cellulose	2.2	1	Present work

5.3.6. Practical All-Around Water Purification by c-BC@N-LCD

Moreover, for converting light energy into steam energy, ideal solar-driven water purifiers should be able to handle complex water sources, which often include pollutants like metal salts, organic compounds, pharmaceuticals, etc. At first, the ER of water from different water sources, consisting of lake water, pond water, reverse osmosis water, tap water, river water, etc., with c-BC@N-LCD were compared under real-time conditions (**Figure 5.13a**, 21st November 2023, at 28 °C temperature, Humidity = 56 %). The ER using water from various sources as feed water under 1 kW m^{-2} sun irradiation in real-time conditions was ~ 2.1 - $2.6 \text{ kg m}^{-2} \text{ h}^{-1}$, which is higher than the rate obtained for ideal laboratory conditions. This might be due to wind (average 6 m/s) present in the outside atmosphere.

Furthermore, a conventional solar evaporator used for desalination accumulates the salt on the evaporator surface, obstructing the ability of the evaporator to absorb sunlight and provide a passage for vapors to leave, which limits vapor generation efficiency. Thus, a reliable solar desalination

technique requires addressing the problems related to water fouling or salt accumulation. To quantitatively measure the water evaporation performance of *c*-BC@N-LCD in saline water, the mass change is measured by a weighing balance via irradiating the *c*-BC@N-LCDs under 1 kW m^{-2} solar power density. **Figure 5.13b** indicates that the rate of evaporation under 1 sun illumination (1 kW m^{-2}) for saline water was measured to be $2.1 \text{ kg m}^{-2} \text{ h}^{-1}$ with evaporation efficiency up to 120 % for five cycles (**Figure 5.13c**). On the contrary, the evaporation rates of saline water with BC and with water were found to be 0.60 and $0.46 \text{ kg m}^{-2} \text{ h}^{-1}$, respectively. *c*-BC@N-LCD membrane retains its performance even after five cycles with saline solution, making it a suitable candidate for desalination.

Next, to prove the resilience of *c*-BC@N-LCD for the evaporation of polluted water, different simulated water feed was investigated. A major share of water pollution is caused by an indiscriminate release of pollutants like dyes, pharmaceuticals, metal salts, etc., from various industries. These toxic effluents contain unreacted chemicals and their by-products, which endanger aquatic as well as terrestrial life. As a concept model, the removal of various water-polluting metal ions, dyes, and a few pharmaceutical drugs using *c*-BC@N-LCD ($3 \times 3 \text{ cm}^2$) was tested with corresponding simulated water samples, and results are presented in **Figure 5.13d-f**. Efficient removal of metal ions like Cd^{2+} , Fe^{2+} , Ag^+ , and Co^{2+} from feed water by *c*-BC@N-LCD hydrogel within 2 h was observed (**Figure 5.13d**). Removal of these metal ions was noticed both in light and dark conditions. Among the various available techniques, the adsorption process has evolved as a prominent method for removing pollutants from the water system. The removal efficiency of metal ions depends on the phenomenon of adsorption, which is affected by many factors such as pH, ionic strength, hard-soft acid-base theory, electronegativity, etc. The removal efficiency also depends upon hydrogel morphology and

functional groups present on the surface of the *c*-BC@N-LCD hydrogel. The hydrogel contains polar functional groups such as hydroxyl, amines, and carbonyl, which can bind ions through van der Waal forces, electrostatic interaction, etc. and this could be the most possible reason behind this removal of metal ions from seed water [14, 15] which suggests that the metal ions probably get trapped by the surface amino and hydroxyl groups of N-LCDs, which are present even after cross-linking. Similarly, the degradation of dyes like MO, MB, RB, and CR was analyzed by means of UV-visible spectroscopy. Among them, MB shows a reduction in concentration after performing the degradation with *c*-BC@N-LCD hydrogel (irradiating under sunlight) shown in **Figure 5.13e**. Finally, the potential of this photothermal platform for remediating the pharmaceutical pollutants present in feed water was also tested with DOX and TET as model drugs. Initially, the characteristic peaks for DOX and TET were observed at 372 nm and 360 nm, respectively. After exposure to sunlight for 60 min, the peak intensity decreased, indicating a decrease in the concentration of pharmaceuticals in the feed water. A bar diagram for % degradation before and after treatment with *c*-BC@N-LCD is provided in **Figure 5.13f**, indicating the excellent efficiency of this photothermal membrane towards environmental remediation.

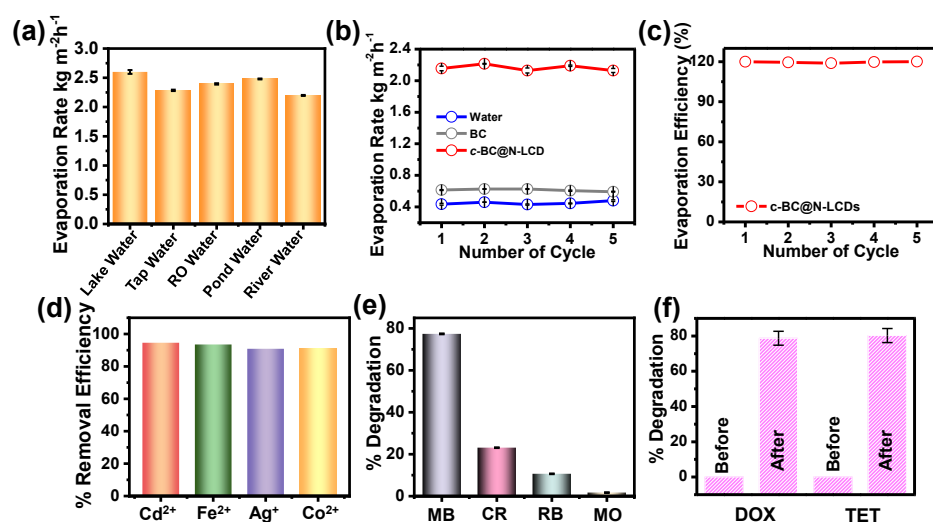


Figure 5.13. Remediation of water by *c*-BC@N-LCD photothermal hydrogel membrane. Bar plots for: (a) evaporation rates calculated for various water sources, and (b) the rate of evaporation in saline water. (c) Evaporation efficiency in saline water, (d) heavy metal ion removal from water bodies, (e) percentage degradation of various dyes from water bodies, (f) percentage degradation of pharmaceutical drugs present in water. Samples were irradiated for 60 min with 1 kW m^{-2} solar light.

Besides, the real-time outdoor experiment for freshwater collection has also been performed. To further demonstrate the practicality of *c*-BC@N-LCD hydrogel under a real-time atmosphere, an outdoor experiment was conducted in a prototype evaporation device under natural sunlight on a sunny day from 10:00 to 17:00 on 14th October 2023. The outdoor solar evaporation device, composed of an evaporation chamber with a *c*-BC@N-LCD solar evaporator (one piece with a diameter of 5.1 cm), was kept inside (**Figure 5.14a**). This device was laid on the roof of an experimental building exposed to sunlight. Within 10 min only it starts forming the vapours (**Figure 5.14b**). During the evaporation, the vapors are formed and condensed as water droplets (**Figure 5.14c**) and collected at the bottom of the vessel **Figure 5.14d**. The variation of outdoor solar intensity, temperature, and humidity for each hour is plotted in **Figure 5.14e**. The evaporation device shows the highest water production rate of $2.5 \text{ kg m}^{-2} \text{ h}^{-1}$ at peak h. An improved evaporation rate was observed here might be due to the lower humidity and the effect of wind, which is not otherwise present under laboratory experimental conditions.

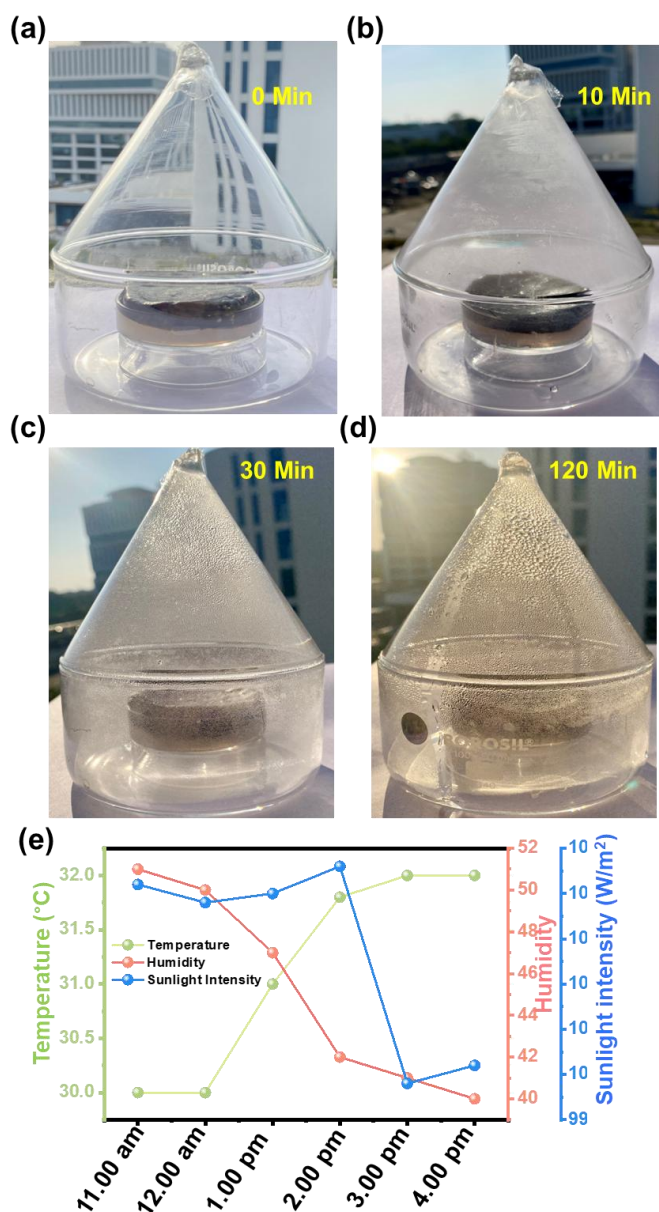


Figure 5.14. Demonstration of fresh water production with the aid of *c*-BC@N-LCD performed outdoors. Digital photographs were taken (a) initially ($t=0$ min) and (b) after steam was produced ($t=10$ min). The formation of water droplets conical roof ensures the formation and condensation of fresh water produced. (c) Formation, condensation ($t=30$ mins), and (d) collection of water droplets ($t=120$ mins). (e) Temperature, humidity, and intensity plots are drawn from the values recorded in real-time.

5.4. Conclusions

A multifunctional *c*-BC@N-LCD hydrogel was fabricated from lignin-derived CDs cross-linked with BC. N-LCDs, being the NIR active material, helped to harvest solar light and transform into heat. The highly porous nature of BC, by virtue of its nanofibrous network structure, has high water uptake and serves as a support matrix for N-LCDs. The cross-linking between N-LCDs and BC by ECH has an important role in stabilizing the membrane against the leaching of photothermal-active N-LCDs. As-fabricated solar water evaporator was demonstrated for generating clean water vapors and for decontaminating polluted water. The evaporator acquires a high ER of $2.2 \text{ kg m}^{-2} \text{ h}^{-1}$. Additionally, the versatility of the as-developed evaporator was also checked with different water sources, including saline water. The rate of evaporation during desalination was found to be $\sim 2.1 \text{ kg m}^{-2} \text{ h}^{-1}$. Besides, decontamination of water simulated with different classes of water pollutants (metal ions, dye, pharmaceutical drugs, etc.) was also successfully demonstrated. As-designed *c*-BC@N-LCD, made from affordable, biocompatible, and eco-friendly building blocks, can therefore fit for purifying broad classes of water feeds.

Note: This is copyrighted material with permission from the Royal Society of Chemistry.

5.5. References

1. Xu N., Li J., Wang Y., Fang C., Li X., Wang Y., Zhou L., Zhu B., Wu Z., Zhu S., Zhu J. (2019), A Water Lily-Inspired Hierarchical Design for Stable and Efficient Solar Evaporation of High-Salinity Brine, *Sci. Adv.*, *5*, eaaw7013. (DOI: 10.1126/sciadv.aaw7013)
2. Liang H., Mu Y., Yin M., He P.-P., Guo W. (2023), Solar-Powered Simultaneous Highly Efficient Seawater Desalination and Highly Specific Target Extraction with Smart DNA Hydrogels, *Sci. Adv.*, *9*, eadj1677. (DOI: 10.1126/sciadv.adj1677)
3. Meng F., Ding Z., Chen Z., Wang K., Liu X., Li J., Lu T., Xu X., Pan, L. (2022), N-Doped Carbon@Cu Core-Shell Nanostructure with Nearly Full Solar Spectrum Absorption and Enhanced Solar Evaporation Efficiency, *J. Mater. Chem. A*, *10*, 9575–9581. (DOI: 10.1039/D1TA10591D)
4. Xu Z., Yu J., Shan H., Wang J., Gao J., Ye Z., Wang R. (2023), Solar Evaporation with Solute Replacement towards Real-World Applications, *Energy Environ. Sci.*, *16*, 5325–5338. (DOI: 10.1039/D3EE02592F)
5. Zhu R., Liu M., Hou Y., Zhang L., Li M., Wang D., Wang D., Fu S. (2020), Biomimetic Fabrication of Janus Fabric with Asymmetric Wettability for Water Purification and Hydrophobic/Hydrophilic Patterned Surfaces for Fog Harvesting, *ACS Appl. Mater. Interfaces*, *12*, 50113–50125. (DOI: 10.1021/acsami.0c12646)
6. Sharma P. R., Sharma S. K., Lindström T., Hsiao B. S. (2020), Nanocellulose-Enabled Membranes for Water Purification: Perspectives, *Adv. Sustainable Syst.*, *4*, 1900114. (DOI: 10.1002/adsu.201900114)
7. Cheng P., Wang D. (2023), Easily Repairable and High-Performance Carbon Nanostructure Absorber for Solar Photothermoelectric Conversion and Photothermal Water Evaporation, *ACS Appl. Mater. Interfaces*, *15*, 8761–8769. (DOI: 10.1021/acsami.2c22077)

8. Guo Y., Zhao X., Zhao F., Jiao Z., Zhou X., Yu G. (2020), Tailoring Surface Wetting States for Ultrafast Solar-Driven Water Evaporation, *Energy Environ. Sci.*, *13*, 2087–2095. (DOI: 10.1039/D0EE00399A)
9. Kuang Y., Chen C., He S., Hitz E. M., Wang Y., Gan W., Mi R., Hu L. (2019), A High-Performance Self-Regenerating Solar Evaporator for Continuous Water Desalination. *Adv. Mater.*, *31*, 1900498. (DOI: 10.1002/adma.201900498)
10. Bu Y., Zhou Y., Lei W., Ren L., Xiao J., Yang H., Xu W., Li J. (2022), A Bioinspired 3D Solar Evaporator with Balanced Water Supply and Evaporation for Highly Efficient Photothermal Steam Generation, *J. Mater. Chem. A*, *10*, 2856–2866. (DOI: 10.1039/D1TA09288J)
11. Niu R., Ding Y., Hao L., Ren J., Gong J., Qu J. (2022), Plant-Mimetic Vertical-Channel Hydrogels for Synergistic Water Purification and Interfacial Water Evaporation, *ACS Appl. Mater. Interfaces*, *14*, 45533–45544. (DOI: 10.1021/acsami.2c14773)
12. Fan Y., Tian Z., Wang F., He J., Ye X., Zhu Z., Sun H., Liang W., Li A. (2021), Enhanced Solar-to-Heat Efficiency of Photothermal Materials Containing an Additional Light-Reflection Layer for Solar-Driven Interfacial Water Evaporation, *ACS Appl. Energy Mater.*, *4*, 2932–2943. (DOI: 10.1021/acsaem.1c00391)
13. Gong L., Sun J., Zheng P., Lin F., Yang G., Liu Y. (2021), Two Birds One Stone: Facile and Controllable Synthesis of the Ag Quantum Dots/Reduced Graphene Oxide Composite with Significantly Improved Solar Evaporation Efficiency and Bactericidal Performance, *ACS Appl. Mater. Interfaces*, *13*, 17649–17657. (DOI: 10.1021/acsami.1c02480)
14. Zhang D., Cai Y., Liang Q., Wu Z., Sheng N., Zhang M., Wang B., Chen S. (2020), Scalable, Flexible, Durable, and Salt-Tolerant CuS/Bacterial Cellulose Gel Membranes for Efficient Interfacial Solar Evaporation, *ACS Sustainable Chem. Eng.*, *8*, 9017–9026. (DOI: 10.1021/acssuschemeng.0c01707)

15. Xiong Z.-C., Zhu Y.-J., Qin D.-D., Yang R.-L. (2020), Flexible Salt-Rejecting Photothermal Paper Based on Reduced Graphene Oxide and Hydroxyapatite Nanowires for High-Efficiency Solar Energy-Driven Vapor Generation and Stable Desalination, *ACS Appl. Mater. Interfaces*, *12*, 32556–32565. (DOI: 10.1021/acsami.0c05986)
16. Storer D. P., Phelps J. L., Wu X., Owens G., Khan N. I., Xu H. (2020), Graphene and Rice-Straw-Fiber-Based 3D Photothermal Aerogels for Highly Efficient Solar Evaporation, *ACS Appl. Mater. Interfaces*, *12*, 15279–15287. (DOI: 10.1021/acsami.0c01707)
17. Huang T.-H., Tian X.-Y., Chen Y.-Y., Widakdo J., Austria H. F. M., Setiawan O., Subrahmanya T. M., Hung W.-S., Wang D.-M., Chang C.-Y., Wang C.-F., Hu C.-C., Lin C.-H., Lai Y.-L., Lee K.-R., Lai J.-Y. (2024), Multifunctional Phra Phrom-like Graphene-Based Membrane for Environmental Remediation and Resources Regeneration. *Adv. Funct. Mater.*, *34*, 2308321. (DOI: 10.1002/adfm.202308321)
18. Jin Y., Gong X., He Y., Wang H., Li S., Liu J. (2023), Free-Standing and Highly Tough 3D Network of Carbon Nanotubes and MXene Constructed by Facile “Egg-Box” Coordination Mechanism for High-Efficiency Solar Evaporator, *Solar RRL*, *7*, 2300548. (DOI: 10.1002/solr.202300548)
19. Xiong Z.-C., Zhu Y.-J., Qin D.-D., Chen F.-F., Yang R.-L. (2018), Flexible Fire-Resistant Photothermal Paper Comprising Ultralong Hydroxyapatite Nanowires and Carbon Nanotubes for Solar Energy-Driven Water Purification, *Small*, *14*, 1803387. (DOI: 10.1002/smll.201803387)
20. Farid M. U., Kharraz J. A., An A. K. (2021), Plasmonic Titanium Nitride Nano-Enabled Membranes with High Structural Stability for Efficient Photothermal Desalination, *ACS Appl. Mater. Interfaces*, *13*, 3805–3815. (DOI: 10.1021/acsami.0c17154)
21. Li S.-Q., Deng Y., Huang J., Wang P., Liu G., Xie H.-L. (2023), Light-Absorbing Copolymers of Polyimides as Efficient

- Photothermal Materials for Solar Water Evaporation, *Aggregate*, 4, e371. (DOI: 10.1002/agt2.371)
22. Chhetri S., Nguyen A. T., Song S., Park D. H., Ma T., Gaillard N., Yoon S.-H., Lee W. (2023), Enhanced Photothermal Effect Assisted by Resonance Energy Transfer in Carbon/Covellite Core–Shell Nanoparticles toward a High-Performance Interfacial Water Evaporation Process, *ACS Appl. Mater. Interfaces*, 15, 54773–54785. (DOI: 10.1021/acsami.3c10778)
 23. Liu H., Wu F., Liu X.-Y., Yu J., Liu Y.-T., Ding B. (2023), Multiscale Synergetic Bandgap/Structure Engineering in Semiconductor Nanofibrous Aerogels for Enhanced Solar Evaporation, *Nano Lett.*, 23, 11907–11915. (DOI: 10.1021/acs.nanolett.3c04059)
 24. Qian Y., Xue G., Chen L., Xu G., Wang G.-E. (2024), Conductive Metal–Organic Framework Nanosheets Constructed Hierarchical Water Transport Biological Channel for High-Performance Interfacial Seawater Evaporation, *Adv. Mater.*, 36, 2310795. (DOI: 10.1002/adma.202310795)
 25. Wang L., Li W., Yin L., Liu Y., Guo H., Lai J., Han Y., Li G., Li M., Zhang J., Vajtai R., Ajayan P. M., Wu M. (2020), Full-Color Fluorescent Carbon Quantum Dots. *Sci. Adv.*, 6, eabb6772. (DOI: 10.1126/sciadv.abb6772)
 26. Rahmawati I., Indriyati, Permatasari F. A., Irham M. A., Nugraha M. I., Anthopoulos T. D., Iskandar F. (2023), Modulating Photothermal Properties of Carbon Dots through Nitrogen Incorporation Enables Efficient Solar Water Evaporation, *ACS Appl. Nano Mater.*, 6, 2517–2526. (DOI: 10.1021/acsanm.2c04893)
 27. Mate N., Khandelwal D., Nabeela K., Shaikh M. M. (2023), Portable and Non-Invasive Fluorescent Thin Films from Photocatalytically Active Carbon Dots for Selective and Trace-Level Detection of Picric Acid, *J. Mater. Chem. C*, 11, 16201–16213. (DOI: 10.1039/D3TC03625A)

28. Wareing T. C., Gentile P., Phan A. N. (2021), Biomass-Based Carbon Dots: Current Development and Future Perspectives, *ACS Nano*, *15*, 15471–15501. (DOI: 10.1021/acsnano.1c03886)
29. Gan J., Chen L., Chen Z., Zhang J., Yu W., Huang C., Wu Y., Zhang K. (2023), Lignocellulosic Biomass-Based Carbon Dots: Synthesis Processes, Properties, and Applications, *Small*, *19*, 2304066. (DOI: 10.1002/sml.202304066)
30. Lawoko M., Berglund L., Johansson M. (2021), Lignin as a Renewable Substrate for Polymers: From Molecular Understanding and Isolation to Targeted Applications, *ACS Sustainable Chem. Eng.*, *9*, 5481–5485. (DOI: 10.1021/acssuschemeng.1c01741)
31. Dar A. A., Usman M., Zhang W., Zhu Q., Pan B., Sial A., Wang C. (2022), Synergistic Degradation of 2,4,4'-Trihydroxybenzophenone Using Carbon Quantum Dots, Ferrate, and Visible Light Irradiation: Insights into Electron Generation/Consumption Mechanism, *ACS EST Eng.*, *2*, 1942–1952. (DOI: 10.1021/acsestengg.2c00118)
32. Mate N., Pranav, Nabeela K., Kaur N., Shaikh M. M. (2022), Insight into the Modulation of Carbon-Dot Optical Sensing Attributes through a Reduction Pathway, *ACS Omega*, *7*, 43759–43769. (DOI: 10.1021/acsomega.2c04766)
33. Chao W., Li Y., Sun X., Cao G., Wang C., Ho S.-H. (2021), Enhanced Wood-Derived Photothermal Evaporation System by in-Situ Incorporated Lignin Carbon Quantum Dots, *Chem. Eng. J.*, *405*, 126703. (DOI: 10.1016/j.cej.2020.126703)
34. Bhattacharyya S. K., Dule M., Paul R., Dash J., Anas M., Mandal T. K., Das P., Das N. C., Banerjee S. (2020), Carbon Dot Cross-Linked Gelatin Nanocomposite Hydrogel for pH-Sensing and pH-Responsive Drug Delivery, *ACS Biomater. Sci. Eng.*, *6*, 5662–5674. (DOI: 10.1021/acsbiomaterials.0c00982)
35. Zhang M., Xue J., Zhu Y., Yao C., Yang D. (2020), Multiresponsive White-Light Emitting Aerogel Prepared with Codoped Lanthanide/Thymidine/Carbon Dots, *ACS Appl. Mater. Interfaces*, *12*, 22191–22199. (DOI: 10.1021/acsami.0c04253)

36. Huang J., Liu X., Li L., Chen S., Yang J., Yan J., Xu F., Zhang X. (2021), Nitrogen-Doped Carbon Quantum Dot-Anchored Hydrogels for Visual Recognition of Dual Metal Ions through Reversible Fluorescence Response, *ACS Sustainable Chem. Eng.*, *9*, 15190–15201. (DOI: 10.1021/acssuschemeng.1c04521)
37. Wei J.-S., Song T.-B., Zhang P., Zhu Z.-Y., Dong X.-Y., Niu X.-Q., Xiong H.-M. (2020), Integrating Carbon Dots with Porous Hydrogels to Produce Full Carbon Electrodes for Electric Double-Layer Capacitors, *ACS Appl. Energy Mater.*, *3*, 6907–6914. (DOI: 10.1021/acsaem.0c00990)
38. Dong A., Xiao W., Yuan W., Zuo K. (2023), Self-Healable and Injectable Nanocomposite Hydrogel Loading Iron-Doped Carbon Dots for Synergistic Antibacterial Peptide-Photothermal-Photodynamic Antibacterial Therapy, *ACS Appl. Polym. Mater.*, *5*, 9564–9573. (DOI: 10.1021/acsapm.3c02024)
39. Li Z., Zhang Y., Huang Q., Chen Z., Wang W., Li W. (2023), Tailorable Lignocellulose-Based Aerogel to Achieve the Balance between Evaporation Enthalpy and Water Transport Rate for Efficient Solar Evaporation, *ACS Appl. Mater. Interfaces*, *15*, 11827–11836. (DOI: 10.1021/acsami.2c22615)
40. Wilson H. M., Lim H. W., Lee S. J. (2022), Highly Efficient and Salt-Rejecting Poly(Vinyl Alcohol) Hydrogels with Excellent Mechanical Strength for Solar Desalination, *ACS Appl. Mater. Interfaces*, *14*, 47800–47809. (DOI: 10.1021/acsami.2c14885)
41. Lu Y., Fan D., Wang Y., Xu H., Lu C., Yang X. (2021), Surface Patterning of Two-Dimensional Nanostructure-Embedded Photothermal Hydrogels for High-Yield Solar Steam Generation, *ACS Nano*, *15*, 10366–10376. (DOI: 10.1021/acsnano.1c02578)
42. Devre P. V., Gore A. H. (2024), Agro-Waste Valorization into Carbonaceous Eco-Hydrogel: A Circular Economy and Zero Waste Tactic for Doxorubicin Removal in Water/Wastewater, *Langmuir*, *40*, 141–158. (DOI: 10.1021/acs.langmuir.3c02256)
43. Jiao L., Xu W., Yan H., Wu Y., Gu W., Li H., Du D., Lin Y., Zhu C. (2019), A Dopamine-Induced Au Hydrogel Nanozyme for

- Enhanced Biomimetic Catalysis, *Chem. Commun.*, **55**, 9865–9868. (DOI: 10.1039/C9CC04436A)
44. Nabeela K., Thorat M. N., Backer S. N., Ramachandran A. M., Thomas R. T., Preethikumar G., Mohamed A. P., Asok A., Dastager S. G., Pillai S. (2021), Hydrophilic 3D Interconnected Network of Bacterial Nanocellulose/Black Titania Photothermal Foams as an Efficient Interfacial Solar Evaporator, *ACS Appl. Bio Mater.*, **4**, 4373–4383. (DOI: 10.1021/acsabm.1c00143)
 45. Jin M., Wu Z., Guan F., Zhang D., Wang B., Sheng N., Qu X., Deng L., Chen S., Chen Y., Wang H. (2022), Hierarchically Designed Three-Dimensional Composite Structure on a Cellulose-Based Solar Steam Generator, *ACS Appl. Mater. Interfaces*, **14**, 12284–12294. (DOI: 10.1021/acsami.1c24847)
 46. Jiang Q., Derami H. G., Ghim D., Cao S., Jun Y.-S., Singamaneni, S. (2017), Polydopamine-Filled Bacterial Nanocellulose as a Biodegradable Interfacial Photothermal Evaporator for Highly Efficient Solar Steam Generation, *J. Mater. Chem. A*, **5**, 18397–18402. (DOI: 10.1039/C7TA04834C)
 47. Li N., Qiao L., He J., Wang S., Yu L., Murto P., Li X., Xu X. (2021), Solar-Driven Interfacial Evaporation and Self-Powered Water Wave Detection Based on an All-Cellulose Monolithic Design, *Adv. Funct. Mater.*, **31**, 2008681. (DOI: 10.1002/adfm.202008681)
 48. Song X., Dong W., Zhang Y., Abdel-Ghafar H. M., Toghan A., Jiang H. (2022), Coupling Solar-Driven Interfacial Evaporation with Forward Osmosis for Continuous Water Treatment, *Exploration*, **2**, 20220054. (DOI: 10.1002/EXP.20220054)
 49. in D.-D., Zhu Y.-J., Chen F.-F., Yang R.-L., Xiong Z.-C. (2019), Self-Floating Aerogel Composed of Carbon Nanotubes and Ultralong Hydroxyapatite Nanowires for Highly Efficient Solar Energy-Assisted Water Purification, *Carbon*, **150**, 233–243. (DOI: 10.1016/j.carbon.2019.05.010)
 50. Wang G., Fu Y., Guo A., Mei T., Wang J., Li J., Wang X. (2017), Reduced Graphene Oxide–Polyurethane Nanocomposite Foam as a

- Reusable Photoreceiver for Efficient Solar Steam Generation, *Chem. Mater.*, **29**, 5629–5635. (DOI: 10.1021/acs.chemmater.7b01280)
51. Wang, H.; Du, A.; Ji, X.; Zhang, C.; Zhou, B.; Zhang, Z.; Shen, J. Enhanced Photothermal Conversion by Hot-Electron Effect in Ultrablack Carbon Aerogel for Solar Steam Generation. *ACS Appl. Mater. Interfaces* **2019**, *11* (45), 42057–42065. (DOI: 10.1021/acsami.9b12918)
 52. Li Y., Shi Y., Wang H., Liu T., Zheng X., Gao S., Lu J. (2023), Recent Advances in Carbon-Based Materials for Solar-Driven Interfacial Photothermal Conversion Water Evaporation: Assemblies, Structures, Applications, and Prospective, *Carbon Energy*, *5*, e331. (DOI: 10.1002/cey2.331)
 53. Soni N., Singh S., Sharma S., Batra G., Kaushik K., Rao C., Verma N. C., Mondal B., Yadav A., Nandi C. K. (2021), Absorption and Emission of Light in Red Emissive Carbon Nanodots, *Chem. Sci.*, *12*, 3615–3626. (DOI: 10.1039/D0SC05879C)
 54. Burai S., Ghorai N., Ghosh H. N., Mondal S. (2022), Discerning the Ultrafast Charge Dynamics in Photostable Perovskite-Carbon Dot Composite Systems: Role of Doped Carbon Dots, *J. Phys. Chem. C*, *126*, 20092–20100. (DOI: 10.1021/acs.jpcc.2c06672)
 55. Zhao P., Zhu L. (2018), Dispersibility of Carbon Dots in Aqueous and/or Organic Solvents, *Chem. Commun.*, *54*, 5401–5406. (DOI: 10.1039/C8CC02279H)
 56. Ma Y., Xie X., Lv R., Na B., Ouyang J., Liu H. (2018), Nanostructured Polyaniline–Cellulose Papers for Solid-State Flexible Aqueous Zn-Ion Battery, *ACS Sustainable Chem. Eng.*, *6*, 8697–8703. (DOI: 10.1021/acssuschemeng.8b01014)
 57. Pan X., Wang Q., He P., Liu K., Ni Y., Ouyang X., Chen L., Huang L., Wang H., Tan Y. (2019), Mussel-Inspired Nanocomposite Hydrogel-Based Electrodes with Reusable and Injectable Properties for Human Electrophysiological Signals Detection, *ACS Sustainable Chem. Eng.*, *7*, 7918–7925. (DOI: 10.1021/acssuschemeng.9b00579)

58. Singh S., Shauloff N., Jelinek R. (2019), Solar-Enabled Water Remediation via Recyclable Carbon Dot/Hydrogel Composites, *ACS Sustainable Chem. Eng.*, 7, 13186–13194. (DOI: 10.1021/acssuschemeng.9b02342)
59. Tao P., Ni G., Song C., Shang W., Wu J., Zhu J., Chen G., Deng T. (2018), Solar-Driven Interfacial Evaporation, *Nat Energy*, 3, 1031–1041. (DOI: 10.1038/s41560-018-0260-7)
60. Yuan P., Men C., Zhao L., Cao P., Yang Z., Niu Y., Zhang Y., Yu Y., Li Q. (2022), Spontaneous Salt-Preventing Solar–Thermal Water Evaporator with a High Evaporation Efficiency through Dual-Mode Water Transfer, *ACS Appl. Mater. Interfaces*, 14, 15549–15557. (DOI: 10.1021/acsami.2c01757)
61. Wang Y., Wu X., Yang X., Owens G., Xu H. (2020), Reversing Heat Conduction Loss: Extracting Energy from Bulk Water to Enhance Solar Steam Generation, *Nano Energy*, 78, 105269. (DOI: 10.1016/j.nanoen.2020.105269)
62. Hong S., Shi Y., Li R., Zhang C., Jin Y., Wang P. (2018), Nature-Inspired, 3D Origami Solar Steam Generator toward Near Full Utilization of Solar Energy, *ACS Appl. Mater. Interfaces*, 10, 28517–28524. (DOI: 10.1021/acsami.8b07150)
63. Xie M., Zhang P., Cao Y., Yan Y., Wang Z., Jin C. (2023), A Three-Dimensional Antifungal Wooden Cone Evaporator for Highly Efficient Solar Steam Generation, *npj Clean Water*, 6, 1-9. (DOI: 10.1038/s41545-023-00231-3)
64. Hu X., Xu W., Zhou L., Tan Y., Wang Y., Zhu S., Zhu J. (2017), Tailoring Graphene Oxide-Based Aerogels for Efficient Solar Steam Generation under One Sun, *Adv. Mater.*, 29, 1604031. (DOI: 10.1002/adma.201604031)
65. Zhang Q., Li L., Jiang B., Zhang H., He N., Yang S., Tang D., Song Y. (2020), Flexible and Mildew-Resistant Wood-Derived Aerogel for Stable and Efficient Solar Desalination, *ACS Appl. Mater. Interfaces*, 12, 28179–28187. (DOI: 10.1021/acsami.0c05806)
66. Li T., Liu H., Zhao X., Chen G., Dai J., Pastel G., Jia C., Chen C., Hitz E., Siddhartha D., Yang R., Hu L. (2018), Scalable and Highly

- Efficient Mesoporous Wood-Based Solar Steam Generation Device: Localized Heat, Rapid Water Transport, *Adv. Funct. Mater.* 28, 1707134. (DOI: 10.1002/adfm.201707134)
67. Liu H., Chen C., Wen H., Guo R., Williams A. N., Wang B., Chen F., Hu L. (2018), Narrow Bandgap Semiconductor Decorated Wood Membrane for High-Efficiency Solar-Assisted Water Purification, *J. Mater. Chem. A*, 6, 18839–18846. (DOI: 10.1039/C8TA05924A)
 68. Wang X., Gan Q., Chen R., Peng H., Zhang T., Ye M. (2020), Water Delivery Channel Design in Solar Evaporator for Efficient and Durable Water Evaporation with Salt Rejection, *ACS Sustainable Chem. Eng.*, 8, 7753–7761. (DOI: 10.1021/acssuschemeng.9b06844)
 69. Sun Y., Zong X., Qu D., Chen G., An L., Wang X., Sun Z. (2021), Water Management by Hierarchical Structures for Highly Efficient Solar Water Evaporation, *J. Mater. Chem. A*, 9, 7122–7128. (DOI: 10.1039/D1TA00113B)
 70. Chen R., Wang X., Gan Q., Zhang T., Zhu K., Ye M. (2019), A Bifunctional MoS₂-Based Solar Evaporator for Both Efficient Water Evaporation and Clean Freshwater Collection, *J. Mater. Chem. A*, 7, 11177–11185. (DOI: 10.1039/C9TA02002K)
 71. Zheng Z., Li H., Zhang X., Jiang H., Geng X., Li S., Tu H., Cheng X., Yang P., Wan Y. (2020), High-Absorption Solar Steam Device Comprising Au@Bi₂MoO₆-CDs: Extraordinary Desalination and Electricity Generation, *Nano Energy*, 68, 104298. (DOI: 10.1016/j.nanoen.2019.104298)



Chapter 6

**Organic Network Comprising
Sustainable Carbon Dot-Upgraded
Bacterial Cellulose Evaporator for
Interfacial Solar-Driven Water
Evaporation**

6.1. Introduction

The depletion of freshwater resources is a critical challenge faced by the world today [1]. Despite the Earth's surface being predominantly covered with water, around 97 % of the planet's water is saline or brackish, rendering it unsuitable for direct human consumption [2]. Developing innovative water treatment technologies with a smaller carbon footprint is a crucial method for mitigating water scarcity and the consequent ecological crisis. Recently, sunlight-driven interfacial evaporation has evolved to be a sustainable and economically viable technique for freshwater generation [3, 4]. It enables solar energy to facilitate the generation of vapor at the air/water interface [5]. A solar-driven interface evaporation system mainly comprises a solar absorber that converts solar energy into thermal energy [6-8]. Various materials with a wider absorption range, as well as excellent light-to-heat converting ability, are essential for solar steam generation [9, 10].

Traditionally, numerous photothermal materials have been widely adopted for research. For example, Wang et al. synthesized pyrrole using the polymerization method to acquire polypyrrole decorated wood for solar water evaporation which also shows potential for seawater desalination and purification [11]. Similarly, Yang and co-workers proposed a polydopamine functionalized hybrid material for solar evaporation and contaminant adsorption for clean water production, which is fabricated by polymerization of dopamine onto a commercial sponge [12]. Li and co-workers fabricated solar-steam generators based on hyper-cross-linked polymers via in situ doping with carbon black, which are randomly distributed on the polymer skeleton [13]. Although these reports show the excellent light absorption capability, evaporation efficiency, and water purification ability, structural imperfections, leaching, fabrication complexity, salt scaling, and long-term stability are still the major concerns [14, 15]. Moreover, carbon dots (CDs) represent a novel category of nanomaterials with unique optical characteristics and diverse applicability, which can be utilized as photothermal material. CDs also

show catalytic properties, which can be utilized for the remediation of organic pollutants and various metal ions [16, 17]. CDs are predominantly eco-friendly and synthesized from a wide range of both complex and simple organic substances [18, 19]. Recent findings indicate that efforts have been made to broaden the absorbance and improve the electron/hole separation efficiency in CDs by incorporating them with a substantial conjugated structure, resulting in a CD-based network with covalent organic frameworks [20, 21]. These CD-based networks are possibly significant for photocatalysis [22], photodynamic applications [20], and the fabrication of light-emitting devices [23]. However, minimal research has been devoted to these materials for photothermal water evaporation.

Alongside this, the primary research objective in developing an efficient solar vapor generator is to optimize thermal management, which involves minimizing radiation and convection losses to the atmosphere and reducing conductive losses to the underlying bulk water, thereby maximizing the use of solar energy [24]. As a result, various designs were introduced to prevent the loss of energy through radiation and convection [25, 26]. Typically, numerous photothermal materials necessitate a lightweight substrate such as polymers to render them porous, flexible, buoyant, and/or readily moldable [27-29]. Moreover, lowering the energy required for water evaporation, through interactions between the water and polymer-rich hydrogels bearing hydrophilic functional groups, presents a groundbreaking and transformative strategy to enhance the evaporation rate [30]. Consequently, hydrophilic polymers such as poly(vinyl alcohol) [31], chitosan [32], etc have been utilized widely. Also, sustainable materials like cellulose [27], wood, jute [33], loofahs [34], etc., have recently been extensively explored by various research groups as promising green alternatives to synthetic polymers for designing solar-driven pure water evaporators. Recently, nanocellulose fibers with many surface-OH functionalities for developing high-performance photothermal systems have been widely explored [35]. In this context, bacterial

cellulose (BC) is mechanically robust, flexible, and thermally stable [36, 37], and could be an environmentally friendly alternative to current polymeric materials. Numerous studies have demonstrated that BC serves as a potential porous scaffold, capable of hosting various photo-thermal entities, and also enables rapid water transport and minimizes heat loss, resulting in significant improvements in total solar evaporation performance [37, 38]. This material exhibits exceptional purity and biocompatibility regardless of culture media, providing a significant benefit for clean water production applications.

So herein, we report a superior photothermal membrane (F-CD-p@BC) composed of a novel wide light-absorbing CD-based organic network of porphyrin (F-CD-POR) integrated with BC hydrogel, offering clean water production, excellent stability, and multifunctional performance for desalination, organic pollutants, and heavy metal ions removal. The F-CD-p@BC, which is synthesized through a straightforward mixing method, is composed of an ultra-porous solar light-collecting layer that facilitates effective interfacial vapor formation with minimized energy consumption. The F-CD-p@BC membrane shows great hydrophilicity and phenomenal NIR region absorption with an excellent evaporation rate of $2.3 \text{ kg m}^{-2} \text{ h}^{-1}$ under 1 sun intensity. Due to the robustness of the photothermal membrane, it possesses reusability even after repeated cycles. Furthermore, F-CD-p@BC exhibits extremely effective solar water purification from diverse water sources alongside desalination and water remediation via the removal of organic pollutants and heavy metal ions. Consequently, versatile F-CD-p@BC possesses a diverse array of applications, extending from extensive industrial platforms to small water purification devices.

6.2. Experimental Section

6.2.1. Materials and Reagents

Furfural aldehyde, pyrrole, sodium hydroxide (NaOH), and cadmium chloride (CdCl_2) were received from SRL. Dichloromethane (DCM),

Dichloromethane (DMF), and 2,3-Dichloro-5,6-dicyano-p-benzoquinone (DDQ) were procured from Spectrochem. Tetra-trifluoroacetic acid (TFA) was purchased from Loba Chemie. Ethanol was procured from an Analytical CSS reagent. Sulfuric acid (H_2SO_4) and methanol were obtained from Merck. The cobalt(II) sulfate (CoSO_4) was received from NR CHEM, and Lead(II) chloride (PbCl_2) was from Acros Organics. The potassium dichromate ($\text{K}_2\text{Cr}_2\text{O}_7$) was procured from SD Fine Chemicals Limited. All the reagents were utilized without further purification unless otherwise mentioned. The distilled water (DI) used was obtained from a central facility of IIT Indore, India.

6.2.2. Synthesis of F-CDs

The furfural aldehyde-derived CDs (F-CDs) were synthesized from 5 mL of furfural mixed with 20 mL of ethanol, following the procedure given in the literature with some modifications [39]. Hydrothermally heat the reaction mixture at 180 °C for a duration of 8 h. The resulting solution from the reaction mixture was subjected to centrifugation at 10000 RPM for 15 min, followed by dialysis against deionized water for 24 h. The dialysis product was obtained and used further.

6.2.3. Preparation of BC

A symbiotic culture of bacteria and yeast grown in Kombucha was obtained from Peepal Farm, Himachal Pradesh, India. Further, it was co-cultured in a mixture of nutrient sources to obtain BC pellicle. The above mixture was cultured in static conditions. The obtained membranes were rinsed with deionized water and then thoroughly washed with NaOH to remove the impurities and adhered cells. After rinsing to remove residuals, the BC membranes were preserved in water at 4 °C until use.

6.2.4. Fabrication of F-CD-p@BC Photothermal Membrane

Take 120 mL dry DCM in a round-bottom flask, add 24 mL (mg/mL) F-CDs, and 1 piece of BC ($5 \times 5 \times 0.8 \text{ cm}^3$). Stir the reaction mixture in

an inert N₂ atmosphere for 15 min. While maintaining the condition, add 4 mL of pyrrole and 9.6 mL of TFA and stir the reaction under a N₂ atmosphere for another 3 h. After the completion of this reaction, add 12 g of DDQ slowly. After the reaction is completed, the obtained composite of BC is washed thoroughly with first DCM, then with methanol multiple times, and then finally with DI water until there is no evidence of leaching in water from the composite. Follow the same procedure for F-CD-POR synthesis, except for adding the BC at an initial stage.

6.2.5. Characterization Techniques

The morphological analysis of F-CD-p@BC was carried out using a scanning electron microscope (SEM), Carl Zeiss, Germany, with an accelerating voltage of 10 kV. SEM samples were prepared by cutting dry samples using a sharp razor and sticking them on carbon tape. Samples were gold-sputtered before the imaging to avoid charging. Long BC fibers and the distribution of aggregate F-CD-POR in the BC matrix were visualized on an FEI Tecnai 30 G2S-TWIN transmission electron microscope (TEM) operated at an accelerating voltage of 300 kV. TEM sample preparations were done on a carbon-coated copper grid by drop-casting two to three drops of the sample solution. The powder X-ray diffraction (XRD) pattern of the F-CDs sample was taken on a PANalytical Empyrean instrument equipped with reference radiation of Cu K α ($\lambda = 1.54 \text{ \AA}$) at an operating voltage of 45 kV. The attenuated total reflectance-Fourier transform infrared (ATR-FTIR) spectra were recorded with a Bruker Alpha II system over the wavenumber range of 4000-400 cm⁻¹. Absorption, total reflectance, and diffuse reflectance spectra (DRS) of BC and F-CD-p@BC were recorded in the range of 200-2500 nm using a UV-VIS-NIR spectrometer (UV-2600). The measurements were corrected by the baseline/blank correction. The NIR solar reflectance (R^*) was measured using solar spectral irradiance in the range 700-2500 nm. The solar absorptions “A” of samples in the 700-2500 nm region were measured using equation 6.1.

$$A = \frac{\int (1 - T) \cdot S \cdot d\lambda}{\int S \cdot d\lambda} \quad (6.1)$$

Where T is the reflectance of the sample, S is the solar spectral irradiance ($\text{Wm}^{-2} \text{ nm}^{-1}$), and λ is the wavelength. The UV-vis spectroscopic studies of F-CDs and dye removal were recorded using a Shimadzu UV-1900 spectrophotometer. The wettability of samples was checked using a contact angle goniometer (KYOWA, DMe-201) by sessile-dropping water (2.0 μL) droplets on the porous BC and F-CD-p@BC. The specific surface areas of the aerogels were measured by the Brunauer-Emmett-Teller (BET) method using Autosorb-1C (AX1C-MP-LP) at 298 K. The pore size distribution was obtained by the Barrett-Joyner-Halenda (BJH) method. A Differential Scanning Calorimeter (DSC) was acquired on a PerkinElmer DSC 8000 instrument. An Inductively Coupled Plasma Mass Spectrometry (ICP-MS) analysis was performed in a Thermo Scientific iCAP RQ spectrometer for heavy metal ions detection. A Laser Raman Imaging System measured Raman spectra with a 532 nm excitation source (Invia Reflex) to obtain the states of water in a hydrogel. Inductively Coupled Plasma Atomic Emission Spectrometry (ICP-AES) analysis was performed in ARCOS, a Simultaneous ICP Spectrometer for metal ions removal from saline water.

6.2.6. Solar Evaporation Experiments

The evaporation experiments were conducted at ambient temperature using a 250 W xenon lamp solar simulator coupled with a Newport monochromator (Newport Instruments). For water evaporation studies, F-CD-p@BC and control BC samples, each with an approximate thickness of 0.8 cm and a diameter of 5 cm, were utilized. In a petri dish, F-CD-p@BC was allowed to append on regular DI water for observation. The size of the petri dish was chosen to accommodate the fabricated F-CD-p@BC, ensuring no bare water surface was exposed to irradiation. The pristine BC was placed below it to facilitate the easy transport of water from the feed water. The evaporating surface was

maintained at an approximate power density of 1 kW m^{-2} . The iScale i-400c electronic weighing balance was used to determine the mass loss associated with the evaporated water. Further, the rate of evaporation (R) is determined as follows:

$$R = \frac{\Delta m}{A \cdot \Delta t} \quad (6.2)$$

Where,

R: Rate of Evaporation

Δm : Mass of water evaporated (kg)

A: Surface area of the evaporator (m^2)

Δt : Time intervals (s)

Moreover, the estimation of Photothermal Energy Conversion (η) was calculated by the following formula:

$$\eta = \frac{m \times h_{LV}}{C_{opt} \times q_i} \quad (6.3)$$

Where,

η : solar-to-vapor energy conversion efficiency (%)

m: Rate of evaporation ($\text{kg m}^{-2} \text{ h}^{-1}$)

h_{LV} : Total enthalpy of vapour-liquid phase change of water (kJ kg^{-1})

C_{opt} : Optical density

q_i : Solar radiation power (1 kW m^{-2})

Further, the temperature profiles were documented before and during illumination using an infrared thermal imaging camera, specifically the FLIR TG 267 model.

6.2.7. Dark Evaporation Experiments

The dark evaporation experiments were utilized to measure the evaporation enthalpy. For each experiment, the evaporator and pure

water were simultaneously placed in a closed, dark environment for evaporation, and the temperature was maintained at 25 °C. The equivalent evaporation enthalpy of the water in the F-CD-p@BC evaporator was calculated using the following equation:

$$\frac{h_{\text{vap}} T_s m_{\text{water}}}{S_{\text{water}}} = \frac{h_{\text{equ}} m_{\text{sample}}}{S_{\text{sample}}} \quad (6.4)$$

Where, S_{sample} and S_{water} are the evaporated areas of the F-CD-p@BC and pure water; m_{sample} and m_{water} are the mass change (kg) of the water in the F-CD-p@BC membrane and pure water in a closed constant temperature and constant-humidity environment over a period of 10 h; h_{vap} , T_s are the evaporation enthalpy of the pure water, h_{equ} denotes the equivalent evaporation enthalpy of the water in the F-CD-p@BC.

6.2.8. F-CD-p@BC for Water Purification Experiments

For evaluating the practical applicability of F-CD-p@BC, the solar water evaporation test was conducted, and the rate of evaporation was determined for water from various sources under 1 sun irradiation. The water evaporation test using methylene blue (MB) and methyl orange (MO) dye-polluted water was assessed, and condensed water was collected to measure the dye removal efficacy of F-CDp@BC through UV-vis spectroscopy. Also, to assess the efficacy of heavy metal ion removal from water, a specific amount of wet F-CD-p@BC was introduced into 50 mL of aqueous solutions, each containing 2 ppm of PbCl_2 , CoSO_4 , $\text{K}_2\text{Cr}_2\text{O}_7$, and CdCl_2 , respectively. The swollen F-CD-p@BC was agitated, and water was collected. Subsequently, the concentration of metal ions was determined using ICP-MS in the collected water. Further, the F-CD-p@BC feasibility towards simulated seawater for outdoor evaporation tests was performed. The tests were conducted in the homemade solar evaporation device. The metal ions removal ratio of the evaporator was calculated according to the following equation.

$$\varphi = \frac{C_0 - C_t}{C_0} \times 100 \quad (6.5)$$

Where,

φ : Salt removal efficiency

C_0 : Ion concentration of water before purification

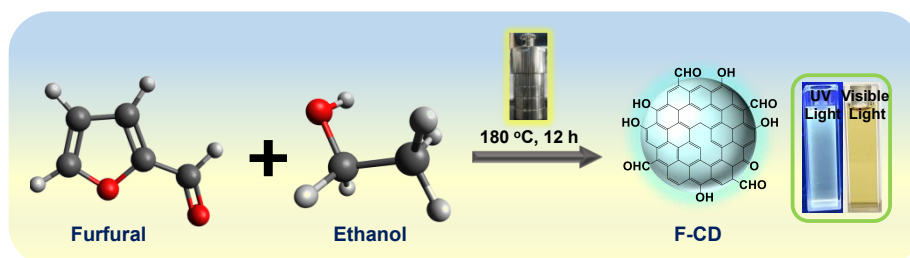
C_t : Ion concentration of water after purification

The potential of F-CD-p@BC was also checked under strong acid (1M H_2SO_4) and strong alkali (1M NaOH) conditions. The evaporation test was performed for both conditions, and pH was checked before and after evaporation. Furthermore, the sample was subjected to real-time analysis in an outdoor environment, exposed to direct sunlight on a clear day, with an ambient temperature of 31 °C and humidity of 43 %. The intensity of solar power was systematically recorded at 60 min intervals using a power meter, and the mean value obtained was utilized for subsequent calculations to find out the evaporation rate outdoors. Throughout the experiment, evaporated water was collected under real-time conditions.

6.3. Results and Discussion

6.3.1. Characterization of F-CDs

The furfural-derived CDs have been synthesized through a hydrothermal method by treating the reaction mixture, maintained at 180 °C for a duration of 8 h. The obtained solution shows a light brown color under visible light, which gives a cyan color FL under UV light, as shown in **Scheme 6.1**.



Scheme 6.1. Schematic of F-CDs synthesis through the hydrothermal method.

The as-synthesized F-CDs show a broad absorption peak at 272 nm (**Figure 6.1a**). **Figure 6.1b** indicates FL spectra, which show the excitation-independent behavior with emission wavelength at 386 nm when excited at 400 nm due to the up-conversion phenomenon. The morphology of F-CDs is shown in **Figure 6.1c**, which depicts evenly distributed F-CDs throughout the solution with the particle size in the range of 3.5-8 nm. The XPS survey spectrum in **Figure 6.1d** provided a deeper understanding of the elemental composition of CDs. As anticipated, the CD surface contains several aldehyde functionalities, as evidenced by the FT-IR spectra in **Figure 6.1e**. The FTIR spectrum featured peaks corresponding to O-H stretching, C-H stretching from furfural, C=O (aldehyde) functionality on F-CDs, and C=C stretching within the aromatic CDs structure. The XRD pattern indicates the amorphous nature of F-CDs with a broad peak at a 2θ angle of 21.31° , which is associated with a disordered graphitic structure (**Figure 6.1f**).

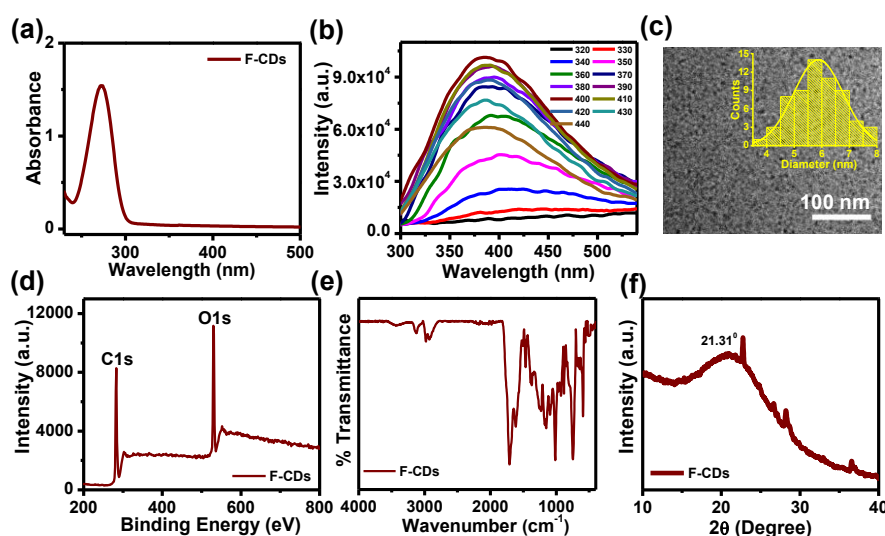
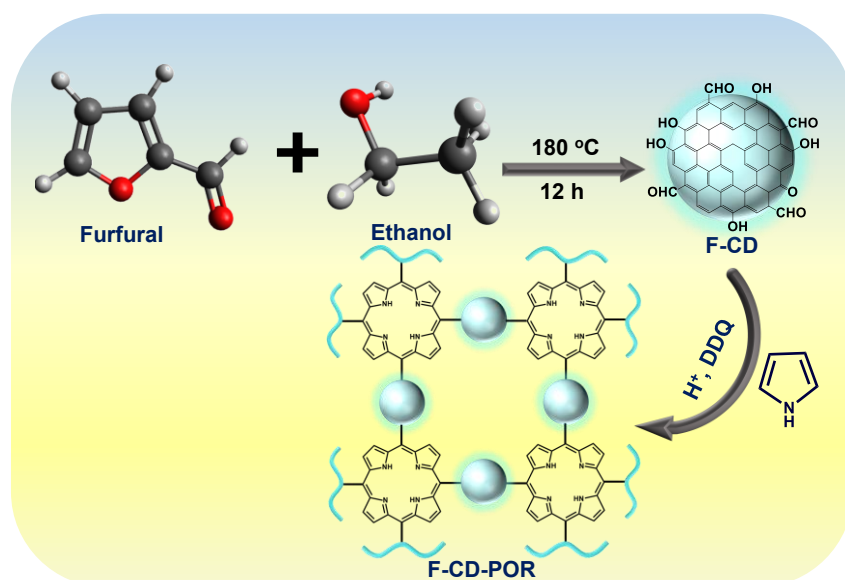


Figure 6.1. Characterization of F-CDs: (a) UV-vis absorption spectrum, (b) FL spectra taken under varied excitation wavelengths, (c) TEM Image with inset representing size distribution histogram, (d) XPS survey scan, (e) FTIR, and (f) XRD spectra.

6.3.2. Characterization of F-CD-POR and F-CD-p@BC

The efficiency of absorption and electron/hole separation in CDs was enhanced by incorporating them with an extensive conjugated

framework, culminating in a CD-based network with a framework structure. This enhancement widened their absorbance and boosted their activity. Further, the polymerization of F-CDs was accomplished in the presence of pyrrole via the Alder-Longo reaction, and utilized TFA as a catalyst. Subsequently, the formation of F-CD-POR was achieved by adding the oxidant DDQ, and the resulting product was then characterized [40, 41]. Notably, the F-CDs exhibited a reactive surface with exposed aldehyde groups. Hence, the formation of porphyrin moieties can be efficiently achieved by reacting the CD's aldehydic groups with pyrrole, under the specified conditions as illustrated in **Scheme 6.2** to yield F-CD-POR moieties.



Scheme 6.2. A schematic illustration shows the synthesis of F-CD-POR.

Following the reaction, a reduction in the number of aldehydic moieties on the surface of the CDs was observed, as evidenced by the FTIR spectra shown in **Figure 6.2a**. This shows the involvement of aldehyde groups attached to CDs in the formation of porphyrin units. Additionally, the minute O-H peak at 3349 cm^{-1} indicates hydroxyl groups on F-CDs, which are not fully consumed even after F-CD-POR formation; the signal of C=O at 1709 cm^{-1} in FTIR spectra almost disappeared in the F-CD-POR composite as compared to F-CD derived from furfuraldehyde. The stretching vibration at 1614 cm^{-1} for C=N

arises due to aromatic conjugation from porphyrin. This finding further validated that pyrrole successfully reacted with aldehyde on the CD's surface to form porphyrin moieties. Further confirmation of F-CD-POR formation is explored via optical spectroscopy. The absorption spectra of F-CD-POR dispersed in DMF are illustrated in **Figure 6.2b**. As compared to F-CDs, the F-CD-POR spans the entire UV-vis spectrum with minor bands on the spectrum, probably attributed to the porphyrin pattern. The absorption characteristic observed around 421 nm can be specifically attributed to porphyrin [20, 42]. This conclusion is derived by comparing it with the absorption characteristics of the corresponding F-CD that lacks porphyrin. The excitation spectrum corroborates these results by displaying a band around 435 nm. Here, the material synthesized from CD and pyrrole exhibits properties that are partially comparable to those of materials comprising porphyrin moieties [43]. In **Figure 6.2c**, there is an overlap of the excitation spectra of FCD-POR with the bands found in their absorption spectra. Also, the presence of dual bands in the F-CD-POR excitation spectrum implies that the excited state emission arises from two distinct states; both these features can be attributed to the porphyrin. The emission band in **Figure 6.2d** exhibits dual emission, with a prior peak originating from CDs and a secondary peak observed at 650 nm, along with a shoulder at 715 nm is attributable to porphyrin [43, 44], indicating the formation of F-CD-POR. The F-CD-POR exhibited a broader and extended visible absorbance compared to F-CDs, indicating an enhanced potential for use as a photothermal material.

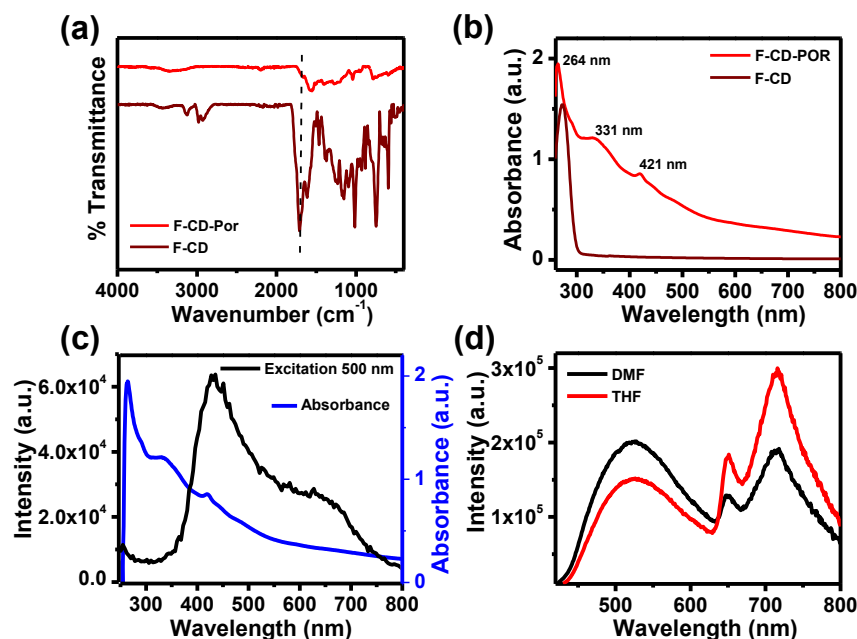
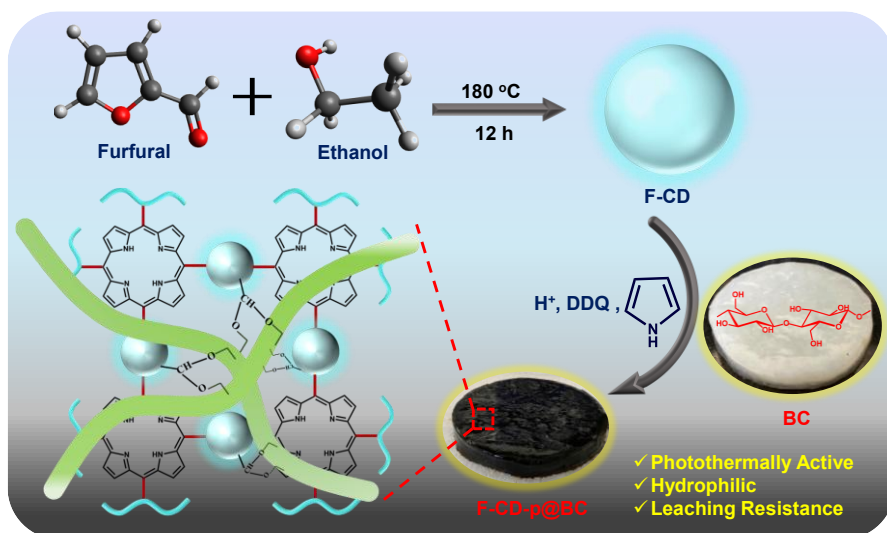


Figure 6.2. Representing the comparison between F-CD and F-CD-POR: (a) FTIR Spectra, (b) UV-vis spectra, (c) UV-vis spectra of F-CD-POR in comparison with fluorescence excitation spectra obtained by excitation at 500 nm, and (d) fluorescence spectra of F-CD-POR obtained in different solvents excited at 420 nm.

Further, we rationally designed a post-chemical modification strategy to attach the F-CD-POR onto BC for the fabrication of a photothermal membrane. The F-CD derived from furfuraldehyde was cross-linked with BC by means of pyrrole units, resulting in F-CD-p@BC via the “Alder-Longo” reaction, as illustrated in **Scheme 6.3**. F-CD-POR retains reactive functional aldehydic groups, which could form covalent bonds with OH groups on BC through acetal or hemiacetal linkages under acidic conditions. Moreover, F-CD-POR also possesses free C=O and -OH groups that can form hydrogen bonds with the hydroxyl-rich BC surface. The obtained F-CD-p@BC was black and exhibited good NIR activity. So, after multiple washings, the fabricated F-CD-p@BC was further characterized.



Scheme 6.3. Schematic of the Synthesis of F-CD-p@BC Hydrogel by Incorporation of F-CD-POR onto BC.

The digital image of the as-fabricated F-CD-p@BC hydrogel membrane is displayed in **Figure 6.3a**, which indicates a black color membrane with a diameter of 5×5 cm². The micromorphological characteristics of F-CD-p@BC were examined by TEM and SEM imaging. The TEM image in **Figure 6.3bi** indicates the successful binding of F-CD-POR on BC fibers, and **Figure 6.3bii** reveals the evenly dispersed F-CD within the F-CD-p@BC membrane. SEM of BC in comparison to F-CD-p@BC was examined as shown in **Figure 6.3ci-ii**, which indicates the attachment and formation of some agglomerates of F-CD-POR on BC fibers. The FTIR curves obtained for the F-CD-p@BC hydrogel membrane with that of BC are presented in **Figure 6.3d**, which indicates the O-H stretching shifted slightly from cellulose (3349 → 3347 cm⁻¹), indicating hydrogen bonding or interaction of BC with F-CD-POR. The C-H stretching peaks at 2917 cm⁻¹ in BC shifted to 2847 cm⁻¹, suggesting modification in F-CD-POR to form F-CD-p@BC. The peak at 1109 cm⁻¹ in F-CD-p@BC is indicative of C-O-C bond formation due to acetal or hemiacetal linkages between F-CD-POR and BC, the slight shift in the peak of C-O from 1054 cm⁻¹ (BC) to 1058 cm⁻¹ (F-CD-p@BC) confirming modified cellulose. FTIR results confirm that F-CD-p@BC is formed through both physical and chemical interactions. Furthermore, the XPS

survey scan recorded for F-CD-p@BC and BC is compared as illustrated in **Figure 6.3e**. All the samples exhibit peaks corresponding to C1s and O1s, with peaks at 281 and 529 eV, respectively. However, the emergence of the N1s peak in F-CD-p@BC supports the formation of porphyrin and its embedment into BC.

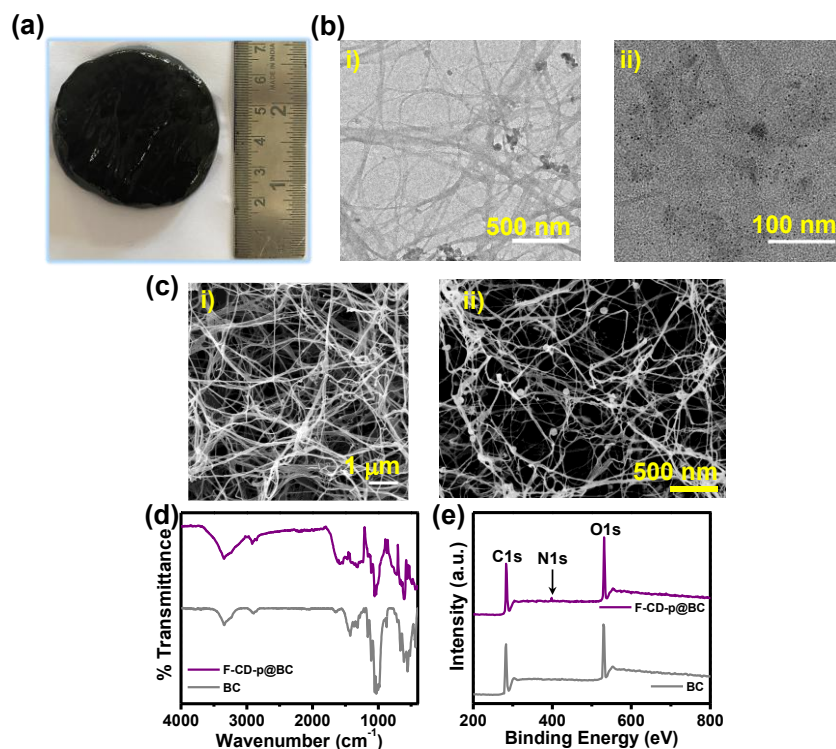


Figure 6.3. Characterization of fabricated F-CD-p@BC hydrogel: (a) Digital photograph, (b) TEM image at: (i) lower magnification, (ii) higher magnification (indicates the attached F-CD-POR on BC fibers), and (c) SEM image of (i) BC, (ii) F-CD-p@BC (indicates the incorporation of F-CD-POR on BC fibers). Comparison of (d) FTIR and (e) XPS spectra of F-CD-p@BC and BC.

Further deconvoluted spectra of F-CD-p@BC are studied. **Figure 6.4ai-ii** shows the comparative C1s spectra of BC and F-CD-p@BC, which indicate the peaks that are assigned to different functional groups, such as C=C (283.8 eV), C-H (284.8 eV), C-OH (286.4 eV), and C=O (288.9 eV) in BC. After composite formation, these peaks are shifted, or there has been a decrease in intensity. In F-CD-p@BC, a slight shift in the peak of C=C to 283.2 eV and a reduction in intensity of the sp^2 carbon peak at 284.8 eV suggest a reduction in aromaticity

due to interaction with BC. Also, the peak of F-CD-p@BC at 288.8 eV arises from C=O and C=N groups of F-CD-POR, whose intensity is decreased, suggesting that some free aldehydes from F-CD-POR have reacted with the hydroxyl of BC to form an acetal or hemiacetal. The deconvoluted O1s spectra of BC depict the peak at 532.4 (C-O) and 533.6 eV (oxygen atom in adsorbed water) in **Figure 6.4bii**. In **Figure 6.4bi**, F-CD-p@BC indicates a new peak at 531.6 eV, which supports the formation of C-O-C bonds likely from covalent bonding between free aldehyde groups on F-CD-POR and hydroxyl groups on BC. The minute shift in 533.6 eV of BC to 533.3 eV reflects the altered hydrogen bonding due to the interaction between BC and F-CD-POR. Also, the presence of nitrogen-specific peaks confirms the successful integration of F-CD-POR into BC and the formation of F-CD-p@BC composite. As shown in **Figure 6.4c**, which indicates the N1s spectra of F-CD-p@BC with peaks at 398.0 and 399.4 eV, this is indicative of the formation of C=N bonds in the porphyrin ring and interaction of F-CD-POR with hydroxyl groups on BC. These observations reinforce the successful functionalization of BC and the formation of F-CD-p@BC.

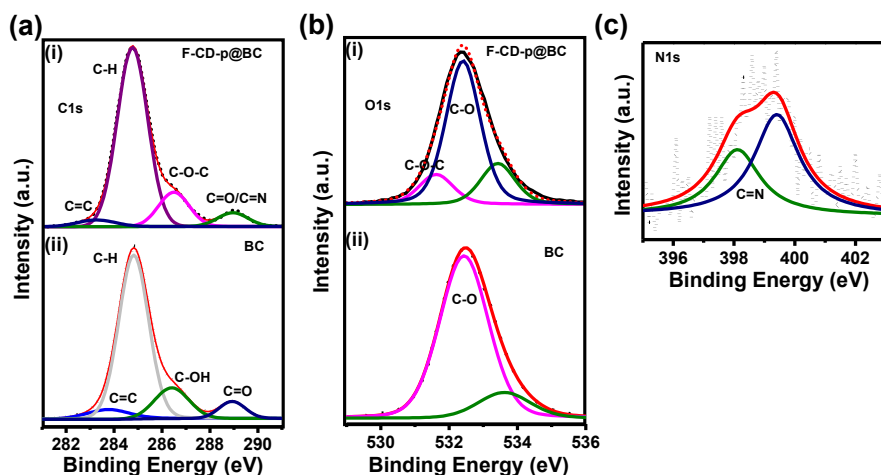


Figure 6.4. Details of XPS deconvoluted spectra of BC and F-CD-p@BC for (a) C1s, (b) O1s, and (c) N1s.

6.3.3. Light Absorption and Photothermal Performance

The optical absorption performance of the F-CD-p@BC membrane compared to that of the control BC was evaluated using a UV-vis-NIR spectrophotometer. The F-CD-p@BC membrane with a thickness of 0.8 cm exhibits very little optical reflectance (8.29 %) across the entire solar spectrum range (300-2500 nm) in **Figure 6.5a** (purple line), and BC shows the diffused reflectance of 89.45 % in **Figure 6.5a** (grey line). This signifies superior solar absorption by the F-CD-p@BC composite, related to the optical absorption properties of F-CD-POR and light scattering within the interconnected fibrous network, which extends the optical transfer path length. **Figure 6.5b** presents the data for the percentage of the NIR reflectance spectrum. A high light absorbance of 91.7 % is achieved by F-CD-p@BC, which makes it a potential evaporator for solar steam generation, along with excellent photothermal efficiency, as investigated further. The corresponding digital photograph of the F-CD-p@BC membrane is shown in **Figure 6.5c** with a dimension of $5 \times 5 \times 0.8 \text{ cm}^3$ and was utilized further for photothermal conversion studies. **Figure 6.5d** demonstrates a slight increase in the surface temperature of pristine BC, rising from 26.4 to 31.3 °C, and water, from 26.5 to 31.1 °C, when exposed to 1 kW m^{-2} sun intensity. In contrast, the surface temperature of the F-CD-p@BC hydrogel rapidly increases from 27.1 to 50.2 °C within approximately 2 min (with inset illustrating thermal images of F-CD-p@BC compared to BC and water after 1 sun irradiation) and eventually stabilizes at 50.8 °C in 60 min, as shown in digital and thermal images of **Figure 6.5e**.

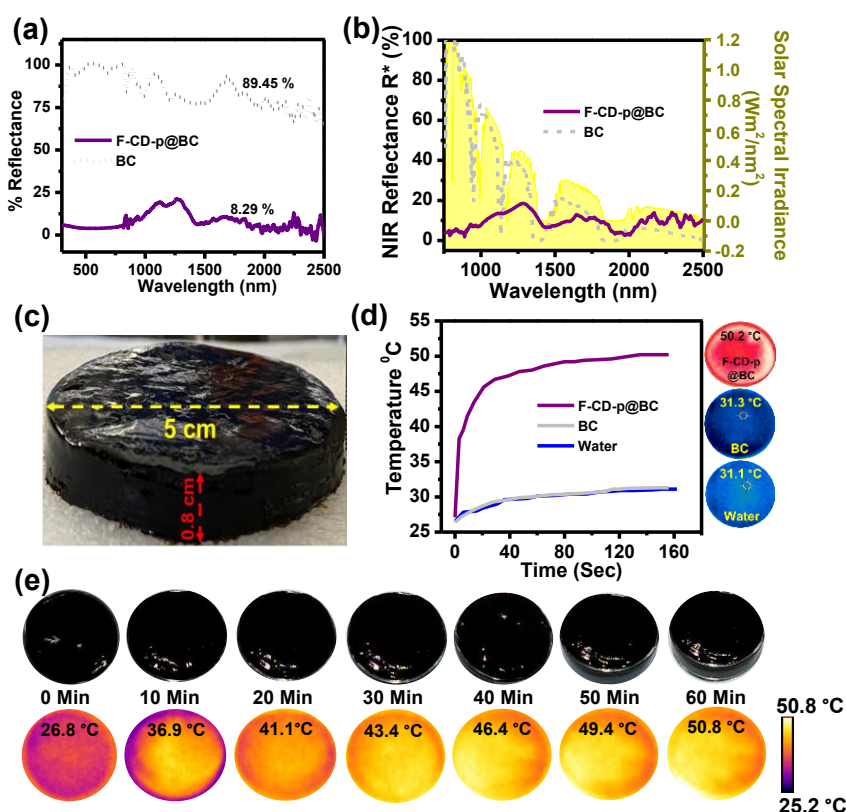


Figure 6.5. Solar harvesting property of BC and F-CD-p@BC: (a) UV-vis-NIR diffuse reflection spectra of the aerogels, (b) corresponding % NIR reflectance, (c) Digital photograph of membrane utilized for photothermal conversion studies, (d) comparative temperature change curves of evaporation systems F-CD-p@BC (purple), BC (gray), and water (blue) vs time under one solar irradiation (inset: respective thermal images), (e) Infrared thermal images of F-CD-p@BC surface captured at 0, 10, 20, 30, 40, 50, and 60 min intervals under 1 sun irradiation.

Moreover, BET surface area analysis was performed to reveal the surface area and porosity of the F-CD-p@BC aerogel compared to the native BC material. The specific surface area and pore volume of the F-CD-p@BC membrane compared to native BC were measured by BET and BJH, respectively. As shown in **Figure 6.6a-b**, the surface area of F-CD-p@BC was greater than compared of pristine BC. The F-CD-p@BC maintains the mesoporosity in the photothermal composite, and a pore volume of 18.1 nm is also increased in F-CD-p@BC, compared to 14.3 nm in native BC, as shown in **Figure 6.6c**.

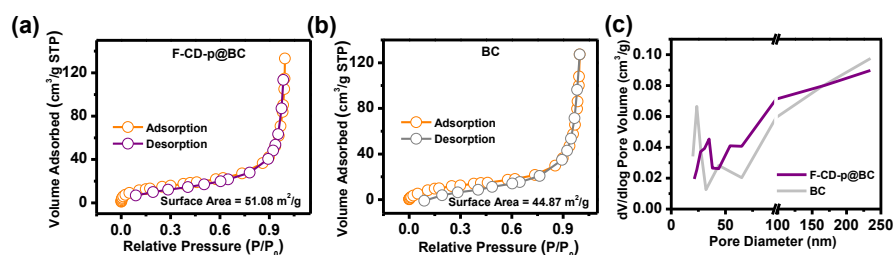


Figure 6.6. Adsorption-desorption curves of nitrogen for (a) F-CD-p@BC, (b) BC, and (c) comparative pore size distribution curve of F-CD-p@BC and BC.

The porous nature of F-CD-p@BC greatly improves the hydrophilic nature, as demonstrated by contact angle measurements. **Figure 6.7** proves the excellent wettability of BC and F-CD-p@BC. When a single drop of water comes into contact with BC and F-CD-p@BC, it is instantly sorbed by both the aerogel surface (within ca. 0.8 and 0.9 s, respectively), leaving a 0° contact angle. The high hydrophilicity of platforms is due to a fibrous network of material, and a high porosity manifests a fast absorption of water, facilitating improved photothermal water absorption and evaporation. Moreover, the fibrous network and high wettability of F-CD-p@BC make it easier for water wicking and subsequent steam escape from its surface.

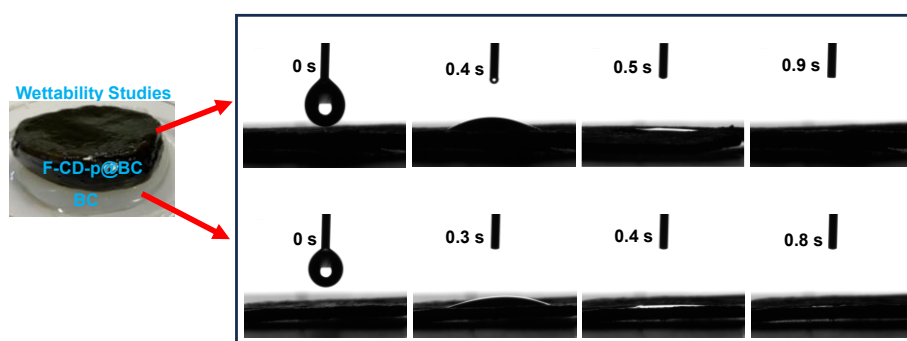


Figure 6.7. Digital photographs of F-CD-p@BC and BC showing water contact angle measurements on each layer.

To analyze the capillary action in F-CD-p@BC, we performed capillary wicking of methyl orange aqueous solution using a white tissue placed at the top of F-CD-p@BC. Notably, the white tissue was stained orange upon keeping it over F-CD-p@BC dipped in methyl

orange solution, highlighting effective water transportation through F-CD-p@BC (**Figure 6.8ai-ii**). In addition, water molecules can exist in three states within a hydrogel, i.e., free water (FW), bound water (BW), and intermediate water (IW) [45]. Raman spectra further indicated the different states of water in the hydrogel. As presented in **Figure 6.8b**, a spectrum of F-CD-p@BC was fitted into four peaks through Gaussian functions. The peaks at 3222 and 3417 cm^{-1} correspond to the asymmetric and symmetric -OH stretch of FW, and peaks at 3550 and 3630 cm^{-1} were assigned to the -OH stretch of IW [46]. Moreover, as compared to pure water (**Figure 6.8c**), the F-CD-p@BC spectra show a higher proportion of IW, which also favors water evaporation. To further assess the influence of IW on the vaporization enthalpy of water in F-CD-p@BC, the DSC spectra of bulk water and F-CD-p@BC were analyzed. As illustrated in **Figure 6.8d**, the evaporation enthalpy of water in F-CD-p@BC, determined from the peak of the heat flow signal, which was 1807 J g^{-1} , was significantly lower than that of pure water (2111 J g^{-1}), which closely aligns with the theoretical value [47]. This indicates a decrease in the energy required for water evaporation and demonstrates the existence of IW in the F-CD-p@BC membrane, which leads to an improvement in the evaporation rate of the solar evaporator.

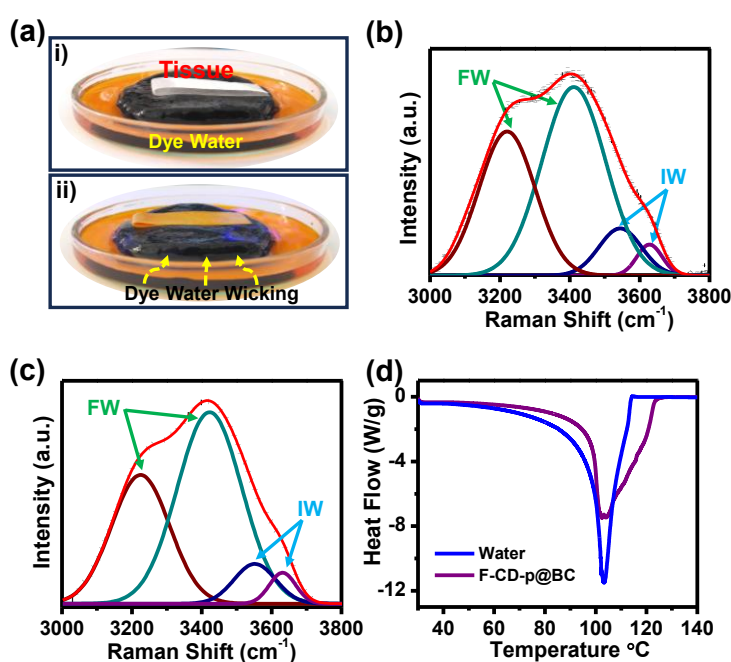


Figure 6.8. (a) Photographs of tissue paper placed on the top of F-CD-p@BC surface before and after wicking methyl orange solution, (b) deconvoluted Raman spectra with FW and IW peaks in F-CD-p@BC, and (c) pure water. (d) DSC measurement curves for pure water and water in F-CD-p@BC.

6.3.4. Water Evaporation Performance of F-CD-p@BC

Notably, the evaporation enthalpy estimated under dark conditions showed similar results, further validating the above conclusion. The evaporation enthalpy of water in F-CD-p@BC under dark conditions was calculated by using **Equation 6.4** and was found to be 1529 J g^{-1} , significantly less than the evaporation enthalpy of pure water, indicating that the energy required for the evaporation of water in F-CD-p@BC was decreased. It is worth noting that the enthalpy values measured by the DSC method are higher compared to the test results in the dark evaporation experiments. This may be due to the DSC results showing the complete dehydration of the samples, and therefore, the results may deviate from the actual evaporation enthalpies [48]. In contrast, the dark evaporation experiments showed a very little dehydration process, and therefore, the measured enthalpies were slightly lower than those from DSC results [49]. A favorable light absorption, excellent hydrophilicity, and good photothermal conversion endow F-CD-p@BC hydrogels with promising photothermal evaporation performance.

Also, the significantly effective localization of heat produced at the F-CD-p@BC-water interface (composite positioned at the top of the water in a cuvette) under irradiation with simulated sunlight (1 kW m^{-2}) is illustrated in **Figure 6.9a** (digital) and **Figure 6.9b** (thermal). A lab-made setup was used for an interfacial solar-driven evaporation experiment (**Figure 6.9c**).

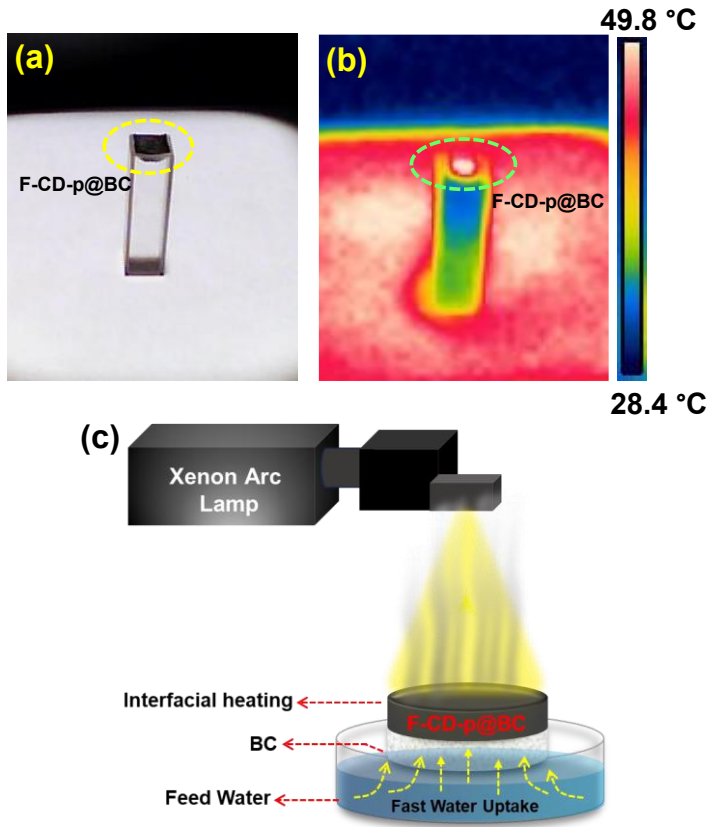


Figure 6.9. Illustrate heat localization at the F-CD-p@BC-water interface after exposure to 1 kW m^{-2} solar radiation, (a) a digital and (b) an infrared thermal profile. (c) Schematic representation of lab-made solar evaporation test setup (yellow arrows indicate efficient bulk water transportation in an upward direction).

Subsequently, the evaporation performance of F-CD-p@BC was correlated to two control experiments, namely, pristine BC and an equivalent volume of pure water. The cumulative water evaporation for each case was measured and depicted in **Figure 6.10a**, which indicates an increase in the evaporation rate with respect to time. The hourly evaporation rate of the F-CD-p@BC membrane accomplished an elevated evaporation rate of $2.3 \text{ kg m}^{-2} \text{ h}^{-1}$ calculated by **Equation 6.2**, in comparison to BC and water alone (**Figure 6.10b and Table 6.1**) under a 1 kW m^{-2} sun power intensity.

Table 6.1. Represents the ER of Composite, BC, and Water.

Sr. No.	Material	Evaporation Rate ($\text{kg m}^{-2} \text{h}^{-1}$)
1.	F-CD-p@BC	2.3
2.	BC	0.55
3.	Water	0.46

Equation 6.3 was utilized to calculate evaporation efficiency, which was found to be 97.7 % for F-CD-p@BC. So, the system demonstrated excellent light-to-vapor conversion efficiency. For practical applications, we also estimated the durability of F-CD-p@BC and observed no visible decline in the water evaporation rate after ten cycles (Figure 6.10c). To assess the findings, recent related works are summarized and presented in Figure 6.10d, demonstrating that the F-CD-p@BC evaporator possesses the most excellent photothermal ability compared to studies reported in terms of the evaporation rate and surface temperature.

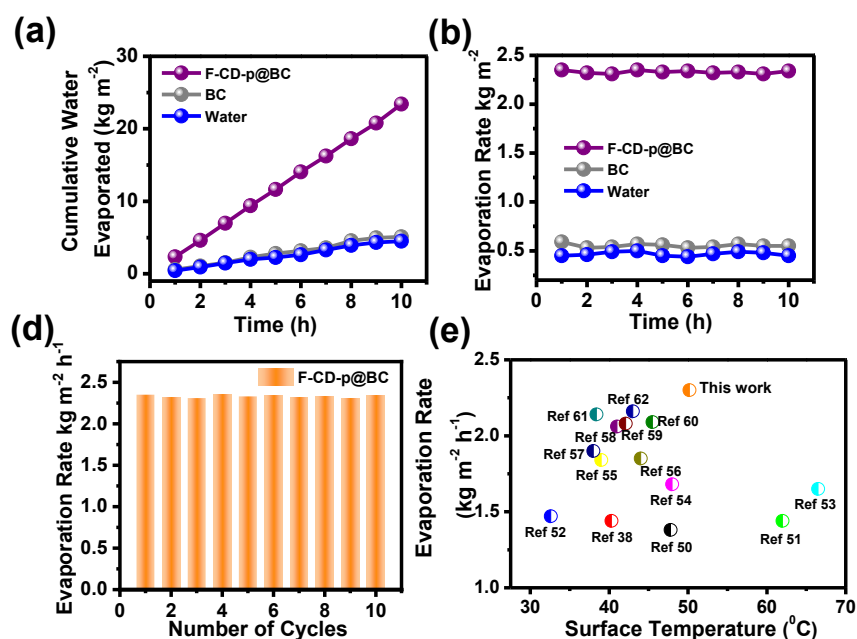


Figure 6.10. Water mass loss comparison between BC, bare water, and F-CD-p@BC: (a) the cumulative mass of evaporated water is plotted against time, (b) evaporation rate performance, (c) cyclic performance conducted across 10 cycles, (d) comparison of F-CD-p@BC with other photothermal materials reported in previous literature.

Furthermore, the effect of variation in the intensity of the irradiation light has been studied. The instrument that we are using for performing photothermal studies, “a xenon lamp (250 W) solar simulator coupled with a Newport monochromator (Newport Instruments)”, provides a maximum irradiation intensity of 1 kW m^{-2} . Therefore, we have checked the evaporation rate under 0.5, 0.75, and 1 kW m^{-2} during the experiment. The obtained evaporation rate with FCD-p@BC and pure water is measured under the intensity mentioned above and plotted as shown in **Figure 6.11**, which indicates that as the intensity of solar irradiation increases from 0.5 to 1 kW m^{-2} , the water evaporation rate also increases from 1.1 to $2.3 \text{ kg m}^{-2} \text{ h}^{-1}$. The results confer strict requirements on the water supply capacity of the material.

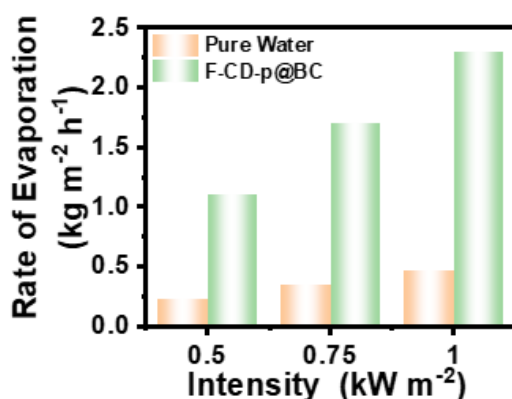


Figure 6.11. Influence of radiation intensity on the rate of photothermal evaporation.

6.3.5. Practical All-Around Water Purification

An ideal solar-driven water purification system should proficiently convert solar energy to steam energy while simultaneously managing diverse water sources and removing organic pollutants and heavy metal ions. The evaporation performance of F-CD-p@BC was investigated by utilizing various water sources under real-time conditions (11th November 2023, at 29°C , humidity = 52 %), including waters sourced from rivers, lakes, ponds, a reverse osmosis system, and taps. Under 1 sun irradiation, the evaporation rate of F-CD-p@BC membrane using multiple water sources as feedwater consistently

ranges between 2.2 and 2.3 kg m⁻² h⁻¹ (**Figure 6.12a**), highlighting the applicability of F-CD-p@BC in a practical environment. Moreover, the removal efficiency of dyes such as MB and MO from dye-polluted water is evaluated through UV-vis absorption spectra. As shown in **Figure 6.12b-c**, over 99 % of the dye is removed after purification, and the inset images show that the dye solution turns into a colorless liquid after purification. Further, the wastewater purification capacity of F-CD-p@BC at 1 kW m⁻² was evaluated for heavy metal ion-contaminated water. The ICP-MS results indicate that F-CD-p@BC hydrogel effectively removes metal ions such as Cr²⁺, Cd²⁺, Pb²⁺, and Co²⁺ from feedwater within 2 h (**Figure 6.12d**). The removal efficiency of these metal ions was calculated by **Equation 6.5**, and it was observed under both light and dark conditions, demonstrating the exceptional performance of the hydrogel in purifying heavy metal ion-contaminated wastewater [63]. **Figure 6.12e** demonstrates that the evaporator F-CD-p@BC could maintain excellent evaporation performance in a strong acid (1 M H₂SO₄) and alkali (1 M NaOH) environment. After purification, the pH values of purified water were found to be close to those of deionized water.

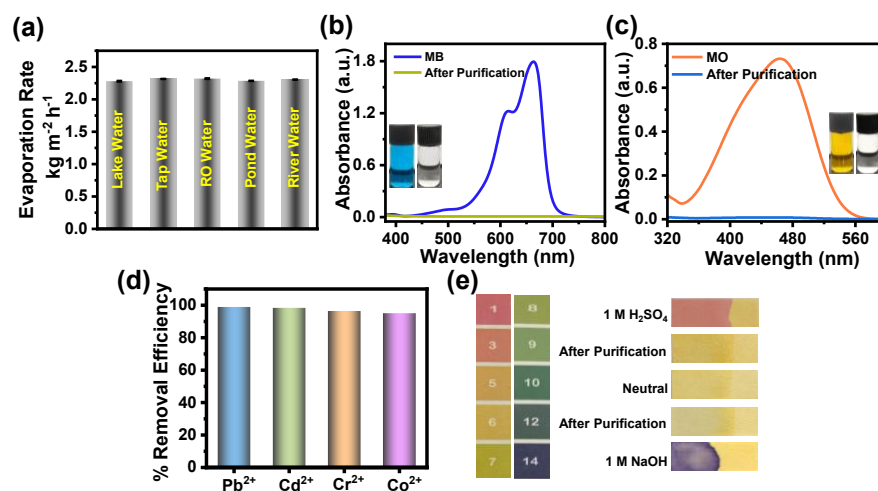


Figure 6.12. Illustrates the purification of water by utilizing the F-CD-p@BC photothermal membrane: (a) Depicting evaporation rates obtained for different water sources, (b, c) UV-vis spectra of MB and MO before and after purification, respectively, (d) removal of heavy

metal ions from aquatic environments, (e) comparison showing pH of solution before and after purification.

Additionally, the salt tolerance of the evaporator is vital for long-term stability in salty water. The salt resistance experiment was executed. Here, 1 g of NaCl was placed on the surface of F-CD-p@BC. Most of the salt crystals present on a surface of F-CD-p@BC start dissolving in 1 h and completely dissolve after 4 h in a dark environment, suggesting a good self-cleaning capability (**Figure 6.13a**), attributed to the porous network and hydrophilicity of BC, which helps in rapid water exchange and advection of salt into feedwater overcoming the ability of traditional solar evaporators employed for desalination. Also, as shown in **Figure 6.13b**, no salt deposition happens on the surface of F-CD-p@BC under 12 h of continuous solar irradiation in simulated seawater. Due to excellent salt resistance ability, the water evaporation performance of F-CD-p@BC, as compared to BC and water in saline water, is persistent for 5 cycles with an evaporation rate of $2.1 \text{ kg m}^{-2} \text{ h}^{-1}$ under 1 kW m^{-2} solar irradiation (**Figure 6.13c**), which is approximately similar to the evaporation rate of F-CD-p@BC in normal water. The ion concentration of simulated seawater after purification in condensed freshwater was determined by ICP-AES. It was found that the concentrations of all four primary ions of Na^+ , Mg^{2+} , Ca^{2+} , and K^+ present in simulated seawater were significantly reduced and far below the limits of drinking water set by the World Health Organization (WHO) [64]. Further, we calculated the ion removal ratio of F-CD-p@BC according to **Equation 6.5**. The estimated salt removal ratios of Na^+ , Mg^{2+} , Ca^{2+} , and K^+ were 99.33, 99.94, 98.31, and 99.84, respectively, as indicated in **Figure 6.13d**, which demonstrates that the F-CD-p@BC membrane is potentially reliable for long-term solar water desalination. In addition, the atmospheric acidification and heavy industrial pollution lead to the earth's water sources being acidic or alkaline beyond the pH requirement of drinkable water (range of 6.5-8.5), according to the Environmental Protection Agency [65].

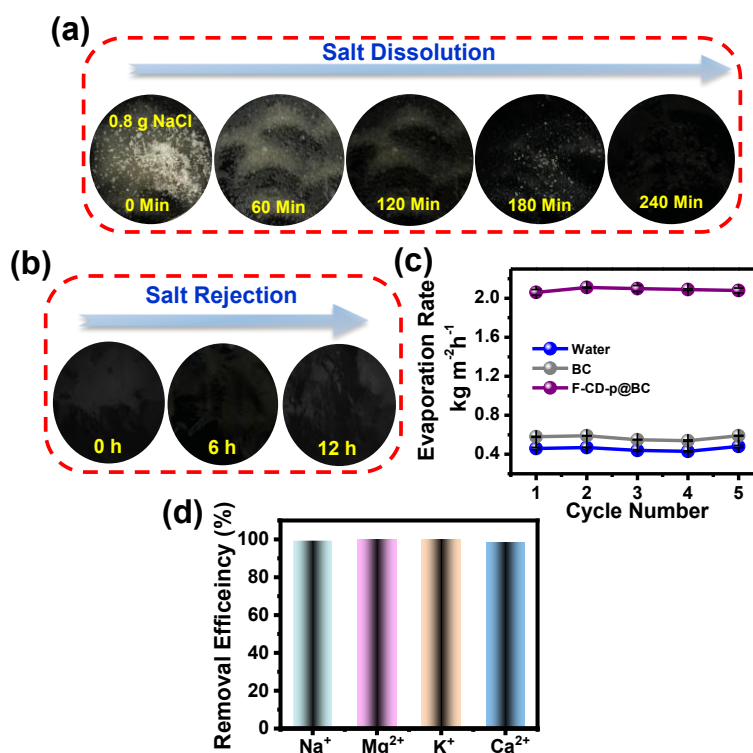


Figure 6.13. (a) Image showing salt ablation experiment on the surface of F-CD-p@BC in the dark, (b) Photographs showing no deposition of salt on the upper surface of F-CD-p@BC during solar desalination until 12 h, (c) recyclability and evaporation rate for saline water under 1 sun, (d) ions removal of simulated seawater after desalination.

6.3.6. Real-Time Application

Moreover, to validate the practical application of the F-CD-p@BC hydrogel in real-time conditions, an outdoor experiment was carried out using a prototype evaporation device. The experiment was carried out from 11:05 to 16:05 on October 29, 2024, in natural sunlight. The outdoor solar evaporation device, consisting of an evaporation chamber containing a single F-CD-p@BC solar evaporator with a diameter of 5 cm, was placed inside the chamber, as shown in **Figure 16.4a**. This device was placed on the roof of a sunlit experimental building. During evaporation, the vapors are generated and subsequently condensed into water droplets within 60 min, which are then collected at the bottom of the vessel. The evaporation rate can be determined by recording the mass of water at various time intervals with a balance. Throughout the process, data on evaporation rate, solar

intensity, temperature, and humidity were recorded and presented in **Figure 16.4b**. The exceptional evaporation rate of $2.7 \text{ kg m}^{-2} \text{ h}^{-1}$ for the evaporation device is observed during peak hours. The observed enhancement in evaporation rate may be attributed to lower humidity and the influence of wind, which is otherwise not present under laboratory experimental conditions, highlighting the excellent capability of the device for freshwater production.

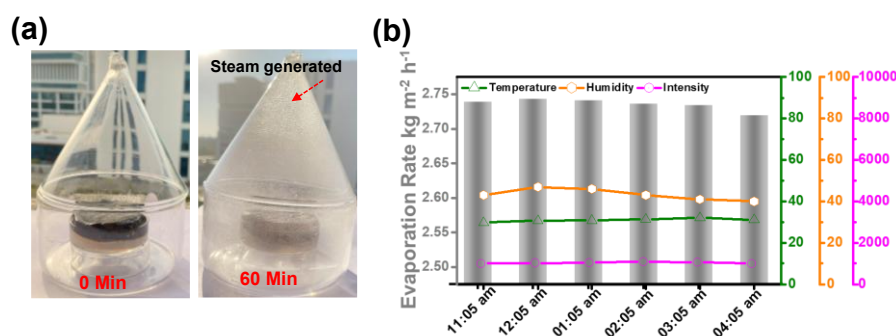


Figure 6.14. (a) photographs of a lab-made outdoor evaporation device containing the evaporator at 0 and 60 min (indicates the generation of steam), and (b) outdoor freshwater evaporation rate along with temperature, humidity, and intensity plots drawn from the values recorded in real-time.

6.4. Conclusions

In summary, we successfully fabricated a highly efficient, portable solar evaporator (F-CD-p@BC) by incorporating a novel carbon-dot-based organic network (F-CD-POR) into a BC hydrogel via the Alder-Longo reaction. The synthesized F-CD-p@BC exhibits broad-spectrum light absorption and achieves a high evaporation rate of $2.3 \text{ kg m}^{-2} \text{ h}^{-1}$ (1 kW m^{-2}). The interconnected porous structure facilitated the water transport ability of a solar absorber, minimizing heat loss and making the F-CD-p@BC membrane ideal for solar desalination and wastewater treatment. The membrane exhibited long-term stability, maintaining salt-resistance ability with a $2.1 \text{ kg m}^{-2} \text{ h}^{-1}$ evaporation rate for seawater and also effectively removing organic pollutants and heavy metal ions, showcasing its potential for real-world applications. Additionally, outdoor testing confirmed its robustness, with an

evaporation rate of $2.7 \text{ kg m}^{-2} \text{ h}^{-1}$, surpassing many advanced solar evaporators. The study highlights a scalable and eco-friendly approach for clean water production, offering a viable solution for water purification in remote areas. The innovative design of covalently linked carbon-dot networks opens emerging avenues for next-generation photothermal materials, with applications beyond desalination, including photocatalysis and solar energy harvesting.

Note: This is copyrighted material with permission from the American Chemical Society.

6.5. References

1. Liu Z., Zhou Z., Wu N., Zhang R., Zhu B., Jin H., Zhang Y., Zhu M., Chen Z. (2021), Hierarchical Photothermal Fabrics with Low Evaporation Enthalpy as Heliotropic Evaporators for Efficient, Continuous, Salt-Free Desalination, *ACS Nano*, *15*, 13007–13018. (DOI: 10.1021/acsnano.1c01900)
2. Gu Y., Wang D., Gao Y., Yue Y., Yang W., Mei C., Xu X., Xu Y., Xiao H., Han J. (2023), Solar-Powered High-Performance Lignin-Wood Evaporator for Solar Steam Generation, *Adv. Funct. Mater.*, *33*, 2306947. (DOI: 10.1002/adfm.202306947)
3. Ko Y., Lee S., Jang J., Kwon G., Lee K., Jeon Y., Lee A., Park T., Kim J., You J. (2025), Nanocellulose-Based Interfacial Solar Evaporator: Integrating Sustainable Materials and Micro-/Nano-Architectures for Solar Desalination, *Adv. Funct. Mater.*, *35*, 2414576. (DOI: 10.1002/adfm.202414576)
4. Chen J., Li B., Hu G., Aleisa R., Lei S., Yang F., Liu D., Lyu F., Wang M., Ge X., Qian F., Zhang Q., Yin Y. (2020), Integrated Evaporator for Efficient Solar-Driven Interfacial Steam Generation, *Nano Lett.*, *20*, 6051–6058. (DOI: 10.1021/acs.nanolett.0c01999)
5. Zhou X., Zhao F., Zhang P., Yu G. (2021), Solar Water Evaporation Toward Water Purification and Beyond, *ACS Materials Lett.*, *3*, 1112–1129. (DOI: 10.1021/acsmaterialslett.1c00304)
6. Tao P., Ni G., Song C., Shang W., Wu J., Zhu J., Chen G., Deng T. (2018), Solar-Driven Interfacial Evaporation, *Nat Energy*, *3*, 1031–1041. (DOI: 10.1038/s41560-018-02607)
7. Wang S., Almenabawy S. M., Kherani N. P., Leung S. N., O'Brien P. G. (2020), Solar-Driven Interfacial Water Evaporation Using Open-Porous PDMS Embedded with Carbon Nanoparticles, *ACS Appl. Energy Mater.*, *3*, 3378–3386. (DOI: 10.1021/acsaem.9b02399)

8. Vaghasiya J. V., Sonigara K. K., Mayorga-Martinez C. C., Pumera M. (2024), 3D Printed $\text{Ti}_3\text{C}_2\text{@Polymer}$ Based Artificial Forest for Autonomous Water Harvesting System, *npj Clean Water*, 7, 1–12. (DOI: 10.1038/s41545-024-00384-9)
9. Ding T., Zhou Y., Ong W. L., Ho G. W. (2021), Hybrid Solar-Driven Interfacial Evaporation Systems: Beyond Water Production towards High Solar Energy Utilization, *Mater. Today*, 42, 178–191. (DOI: 10.1016/j.mattod.2020.10.022)
10. Guo Y., Zhao X., Zhao F., Jiao Z., Zhou X., Yu G. (2020), Tailoring Surface Wetting States for Ultrafast Solar-Driven Water Evaporation, *Energy Environ. Sci.*, 13, 2087–2095. (DOI: 10.1039/D0EE00399A)
11. Wang Z., Yan Y., Shen X., Jin C., Sun Q., Li H. (2019), A Wood–Polypyrrole Composite as a Photothermal Conversion Device for Solar Evaporation Enhancement, *J. Mater. Chem. A*, 7, 20706–20712. (DOI: 10.1039/C9TA04914B)
12. Zhang Y., Yin X., Yu B., Wang X., Guo Q., Yang J. (2019), Recyclable Polydopamine-Functionalized Sponge for High-Efficiency Clean Water Generation with Dual-Purpose Solar Evaporation and Contaminant Adsorption, *ACS Appl. Mater. Interfaces*, 11, 32559–32568. (DOI: 10.1021/acsami.9b10076)
13. Xiao C., Liang W., Hasi Q.-M., Wang F., Chen L., He J., Liu F., Sun H., Zhu Z., Li A. (2020), Efficient Solar Steam Generation of Carbon Black Incorporated Hyper-Cross-Linked Polymer Composites, *ACS Appl. Energy Mater.*, 3, 11350–11358. (DOI: 10.1021/acsam.0c02290)
14. Li G., Xu J., Xu C., Xie X., Chen W., Liu Y. (2024), Equilibrium and Optimization of Water-Heat Transfer in Natural Cellulose-Based Hybrid Hydrogel for Efficient Solar Desalination, *Chem. Eng. J.*, 486, 150398. (DOI: 10.1016/j.cej.2024.150398)
15. Jin B., Cui T., He Y., Zhang M., Qi Y., Ye C. (2024), 3D Cellulose-Based Solar Evaporator with Tunable Porous Structures for High Steam Generation, *Adv. Sustain. Syst.*, 8, 2300670. (DOI: 10.1002/adisu.202300670)

16. Mate N., Pranav, Nabeela, K., Kaur N., Shaikh M. M. (2022), Insight into the Modulation of Carbon-Dot Optical Sensing Attributes through a Reduction Pathway, *ACS Omega*, 7, 43759–43769. (DOI: 10.1021/acsomega.2c04766)
17. Mate N., Khandelwal D., Nabeela K., Shaikh M. M. (2023), Portable and Non-Invasive Fluorescent Thin Films from Photocatalytically Active Carbon Dots for Selective and Trace-Level Detection of Picric Acid, *J. Mater. Chem. C*, 11, 16201–16213. (DOI: 10.1039/D3TC03625A)
18. Wareing T. C., Gentile P., Phan A. N. (2021), Biomass-Based Carbon Dots: Current Development and Future Perspectives, *ACS Nano*, 15, 15471–15501. (DOI: 10.1021/acsnano.1c03886)
19. Mate N., Satwani V., Pranav, Shaikh M. M. (2025), Blazing Carbon Dots: Unfolding Its Luminescence Mechanism to Photoinduced Biomedical Applications, *Chem. Asian J.*, 20, e202401098. (DOI: 10.1002/asia.202401098)
20. Chen S., Sun T., Zheng M., Xie Z. (2020), Carbon Dots Based Nanoscale Covalent Organic Frameworks for Photodynamic Therapy, *Adv. Funct. Mater.*, 30, 2004680. (DOI: 10.1002/adfm.202004680)
21. Shi Y., Wang Z., Meng T., Yuan T., Ni R., Li Y., Li X., Zhang Y., Tan Z., Lei S., Fan L. (2021), Red Phosphorescent Carbon Quantum Dot Organic Framework-Based Electroluminescent Light-Emitting Diodes Exceeding 5% External Quantum Efficiency, *J. Am. Chem. Soc.*, 143, 18941–18951. (DOI: 10.1021/jacs.1c07054)
22. Mate N., Nabeela K., Shaikh M. M. (2025), A Carbon Dot Anchored Bacterial Cellulose Hybrid Platform as a Fluorescent Sensor and Photocatalytic Remover of Pharmaceuticals, *J. Mater. Chem. C*, 13, 4691–4701. (DOI: 10.1039/D4TC04536J)
23. Shi Y., Su W., Yuan F., Yuan T., Song X., Han Y., Wei S., Zhang Y., Li Y., Li X., Fan L. (2023), Carbon Dots for Electroluminescent Light-Emitting Diodes: Recent Progress and Future Prospects, *Adv. Mater.*, 35, 2210699. (DOI: 10.1002/adma.202210699)

24. Liu S., Li S., Lin M. (2023), Understanding Interfacial Properties for Enhanced Solar Evaporation Devices: From Geometrical to Physical Interfaces, *ACS Energy Lett.*, *8*, 1680–1687. (DOI: 10.1021/acsenergylett.3c00054)
25. Yao H., Zhang P., Yang C., Liao Q., Hao X., Huang Y., Zhang M., Wang X., Lin T., Cheng H., Yuan J., Qu L. (2021), Janus-Interface Engineering Boosting Solar Steam towards High-Efficiency Water Collection, *Energy Environ. Sci.*, *14*, 5330–5338. (DOI: 10.1039/D1EE01381E)
26. Zhang L., Li X., Zhong Y., Leroy A., Xu Z., Zhao L., Wang E. N. (2022), Highly Efficient and Salt Rejecting Solar Evaporation via a Wick-Free Confined Water Layer, *Nat. Commun.*, *13*, 849. (DOI: 10.1038/s41467-022-28457-8)
27. Li N., Qiao L., He J., Wang S., Yu L., Murto P., Li X., Xu X. (2021), Solar-Driven Interfacial Evaporation and Self-Powered Water Wave Detection Based on an All-Cellulose Monolithic Design, *Adv. Funct. Mater.*, *31*, 2008681. (DOI: 10.1002/adfm.202008681)
28. Xie M., Zhang P., Cao Y., Yan Y., Wang Z., Jin C. (2023), A Three-Dimensional Antifungal Wooden Cone Evaporator for Highly Efficient Solar Steam Generation, *npj Clean Water*, *6*, 1–9. (DOI: 10.1038/s41545-023-00231-3)
29. Sah A., Mandal A. K., Tiwari S., Mukherji S., Subramaniam C. (2023), Scalable and High Throughput Photothermal Water Disinfection with Negligible CO₂ Footprint Utilizing Nanostructured Carbon Coatings, *npj Clean Water*, *6*, 1–10. (DOI: 10.1038/s41545-023-00284-4)
30. Guo Y., de Vasconcelos L. S., Manohar N., Geng J., Johnston K. P., Yu G. (2022), Highly Elastic Interconnected Porous Hydrogels through Self-Assembled Templating for Solar Water Purification, *Angew. Chem., Int. Ed.*, *61*, e202114074. (DOI: 10.1002/anie.202114074)
31. Wilson H. M., Lim H. W., Lee S. J. (2022), Highly Efficient and Salt-Rejecting Poly(Vinyl Alcohol) Hydrogels with Excellent

- Mechanical Strength for Solar Desalination, *ACS Appl. Mater. Interfaces*, *14*, 47800–47809. (DOI: 10.1021/acsami.2c14885)
32. Arunkumar T., Suh Y., Lim H. W., Christopher S., Lee S. J. (2024), Sustainable Solar Desalination through Interfacial Evaporation: Integration of Chitosan Aerogel-Impregnated Graphene Nanoplatelets Solar Evaporator and Phase Change Material, *Desalination*, *572*, 117102. (DOI: 10.1016/j.desal.2023.117102)
 33. Subri Ivan M. N. A., Mortuza Saleque A., Ahmed S., Liang Guo Z., Zu D., Xu L., Ibne Alam T., Umme Hani S., Hong Tsang Y. (2023), Jute Stick Derived Self-Regenerating Sustainable Solar Evaporators with Different Salt Mitigation Mechanisms for Highly Efficient Solar Desalination, *J. Mater. Chem. A*, *11*, 3961–3974. (DOI: 10.1039/D2TA08237C)
 34. Yue Y., Wang Y., Bai Y., Han J., Cheng W., Han G., Wu Q., Jiang J. (2023), A Loofah-Based All-Day-Round Solar Evaporator with Phenolic Lignin as the Light-Absorbing Material for a Highly Efficient Photothermal Conversion, *Chem. Eng. J.*, *477*, 147298. (DOI: 10.1016/j.cej.2023.147298)
 35. Cao S., Rathi P., Wu X., Ghim D., Jun Y.-S., Singamaneni S. (2021), Cellulose Nanomaterials in Interfacial Evaporators for Desalination: A “Natural” Choice, *Adv. Mater.*, *33*, 2000922. (DOI: 10.1002/adma.202000922)
 36. Nabeela K., Thorat M. N., Backer S. N., Ramachandran A. M., Thomas R. T., Preethikumar G., Mohamed A. P., Asok A., Dastager S. G., Pillai S. (2021), Hydrophilic 3D Interconnected Network of Bacterial Nanocellulose/Black Titania Photothermal Foams as an Efficient Interfacial Solar Evaporator, *ACS Appl. Bio Mater.*, *4*, 4373–4383. (DOI: 10.1021/acsabm.1c00143)
 37. Mate N., Nabeela K., Preethikumar G., Pillai S., Shaikh M. M. (2024), A Lignin-Derived Carbon Dot-Upgraded Bacterial Cellulose Membrane as an All-in-One Interfacial Evaporator for Solar-Driven Water Purification, *Mater. Horiz.*, *11*, 5114. (DOI: 10.1039/D4MH00591K)

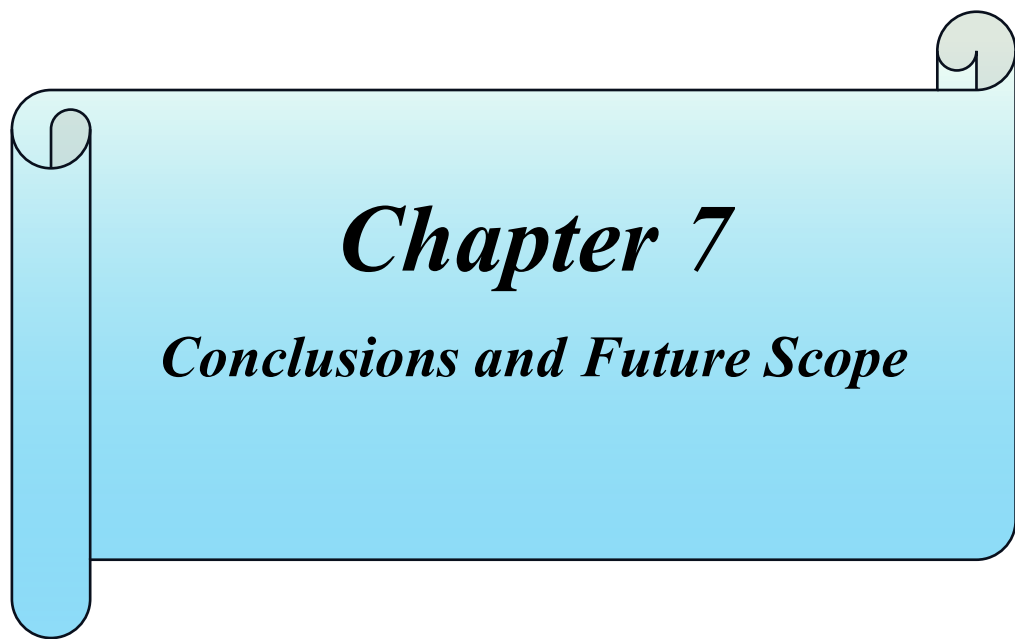
38. Zhang D., Zhang M., Chen S., Liang Q., Sheng N., Han Z., Cai Y., Wang H. (2021), Scalable, Self-Cleaning and Self-Floating Bi-Layered Bacterial Cellulose Biofoam for Efficient Solar Evaporator with Photocatalytic Purification, *Desalination*, 500, 114899. (DOI: 10.1016/j.desal.2020.114899)
39. Luo X., Wan J., Meckbach N., Strehmel V., Li S., Chen Z., Strehmel B. (2022), A Porphyrin-Based Organic Network Comprising Sustainable Carbon Dots for Photopolymerization, *Angew. Chem., Int. Ed.*, 61, e202208180. (DOI: 10.1002/anie.202208180)
40. Lindsey J. S., Schreiman I. C., Hsu H. C., Kearney P. C., Marguerettaz A. M. (1987) Rothmund and Adler-Longo Reactions Revisited: Synthesis of Tetraphenylporphyrins Under Equilibrium Conditions. *J. Org. Chem.*, 52, 827–836. (DOI: 10.1021/jo00381a022)
41. Lindsey J. S., Hsu H. C., Schreiman I. C. (1986), Synthesis of Tetraphenyl porphyrins under Very Mild Conditions, *Tetrahedron Lett.*, 27, 4969–4970. (DOI: 10.1016/S0040-4039(00)85109-6)
42. Santos C. I. M., Rodríguez-Pérez L., Gonçalves G., Dias C. J., Monteiro F., Faustino M. do A. F., Vieira S. I., Helguero L. A., Herranz M. Á., Martín N., Neves M. G. P. M. S., Martinho J. M. G., Maçôas E. M. S. (2021), Enhanced Photodynamic Therapy Effects of Graphene Quantum Dots Conjugated with Aminoporphyrins, *ACS Appl. Nano Mater.*, 4, 13079–13089. (DOI: 10.1021/acsanm.1c02600)
43. Ram Kumar P., Johnee Britto N., Kathiravan A., Neels A., Jaccob M., Mothi M. E. (2019), Synthesis and Electronic Properties of A 3 B-Thienyl Porphyrins: Experimental and Computational Investigations, *New J. Chem.*, 43, 1569–1580. (DOI: 10.1039/C8NJ04289F)
44. Wu F., Su H., Cai Y., Wong W.-K., Jiang W., Zhu X. (2018), Porphyrin-Implanted Carbon Nanodots for Photoacoustic Imaging and in Vivo Breast Cancer Ablation, *ACS Appl. Bio Mater.*, 1, 110–117. (DOI: 10.1021/acsbm.8b00029)

45. Liu Y., Tian Y., Liu N., Zhao S., Zhai H., Ji J., Cao W., Tao L., Wei Y., Feng L. (2024), A Self-Adaptive and Regenerable Hydrogel Interfacial Evaporator with Adjustable Evaporation Area for Solar Water Purification, *Small*, 20, 2305903. (DOI: 10.1002/smll.202305903)
46. Zhou X., Zhao F., Guo Y., Rosenberger B., Yu G. (2019), Architecting Highly Hydratable Polymer Networks to Tune the Water State for Solar Water Purification, *Sci. Adv.*, 5, eaaw5484. (DOI: 10.1126/sciadv.aaw5484)
47. Xu Y., Wang Z., Wang X., Guo Z., Sultan Irshad M., Arshad N., Gong J., Liu H., Li G. (2024), Harvesting Solar Energy with a Ni-MOF-Based Evaporator for Efficient Solar Thermal Storage and Steam Generation, *J. Mater. Chem. A*, 12, 12064–12076. (DOI: 10.1039/D4TA00203B)
48. Zhang W., Chang Q., Xue C., Yang J., Hu S. (2021), A Gelation-Stabilized Strategy toward Photothermal Architecture Design for Highly Efficient Solar Water Evaporation, *Solar RRL*, 5, 2100133. (DOI: 10.1002/solr.202100133)
49. Sun Y., Xiang Y., Tan X., Yuan X., Li J. (2024), Construction of Bilayer Cellulose-Based Aerogel with Salt-Resistant Design for Efficient Solar Desalination and Wastewater Purification, *Chem. Eng. J.*, 498, 155384. (DOI: 10.1016/j.cej.2024.155384)
50. Lv B., Yang S. (2025), Turning Corn Stalk Trashes into a Photothermal Agent for Interfacial Solar Water Evaporation for Sustainable Water Purification, *Energy Technol.*, 13, 2401534. (DOI: 10.1002/ente.202401534)
51. Huang J., Pereira V., Wang C., Li H., Lee H. K., Han J. (2023), A Dual-Functional Device Based on CB/PVDF@BFP for Solar-Driven Water Purification and Water-Induced Electricity Generation, *J. Mater. Chem. A*, 11, 8110–8118. (DOI: 10.1039/D3TA00032J)
52. Fattahimoghaddam H., Kim I. H., Dhandapani K., Jeong Y. J., An T. K. (2024), Copper-Nanoparticle-Decorated Hydrothermal Carbonaceous Carbon–Polydimethylsiloxane Nanocomposites:

Unveiling Potential in Simultaneous Light-Driven Interfacial Water Evaporation and Power Generation, *Small*, 20, 2403565. (DOI: [10.1002/sml.202403565](https://doi.org/10.1002/sml.202403565))

53. Cao S., Jiang J., Tian Q., Guo C., Wang X., Dai K., Xu Q. (2022) Building of Multifunctional and Hierarchical HxMoO₃/PNIPAM Hydrogel for High-Efficiency Solar Vapor Generation. *Green Energy & Environ.*, 7, 1006–1013. (DOI: [10.1016/j.gee.2020.12.012](https://doi.org/10.1016/j.gee.2020.12.012))
54. Wen B., Zhang X., Yan Y., Huang Y., Lin S., Zhu Y., Wang Z., Zhou B., Yang S., Liu J. (2021), Tailoring Polypyrrole-Based Janus Aerogel for Efficient and Stable Solar Steam Generation, *Desalination*, 516, 115228. (DOI: [10.1016/j.desal.2021.115228](https://doi.org/10.1016/j.desal.2021.115228))
55. Lin X., Wang P., Hong R., Zhu X., Liu Y., Pan X., Qiu X., Qin Y. (2022), Fully Lignocellulosic Biomass-Based Double-Layered Porous Hydrogel for Efficient Solar Steam Generation, *Adv. Funct. Mater.* 32, 2209262. (DOI: [10.1002/adfm.202209262](https://doi.org/10.1002/adfm.202209262))
56. Jin M., Wu Z., Guan F., Zhang D., Wang B., Sheng N., Qu X., Deng L., Chen S., Chen Y., Wang H. (2022), Hierarchically Designed Three-Dimensional Composite Structure on a Cellulose-Based Solar Steam Generator, *ACS Appl. Mater. Interfaces*, 14, 12284–12294. (DOI: [10.1021/acsami.1c24847](https://doi.org/10.1021/acsami.1c24847))
57. Hou X., Dong F., Fan H., Wang H., Yu W., Bian Z. (2024), Novel Sponge-Based Carbonaceous Hydrogel for a Highly Efficient Interfacial Photothermal-Driven Atmospheric Water Generator, *ACS Appl. Mater. Interfaces*, 16, 69492. (DOI: [10.1021/acsami.4c18191](https://doi.org/10.1021/acsami.4c18191))
58. Hu G., Cao Y., Huang M., Wu Q., Zhang K., Lai X., Tu J., Tian C., Liu J., Huang W., Ding L. (2020), Salt-Resistant Carbon Nanotubes/Polyvinyl Alcohol Hybrid Gels with Tunable Water Transport for High-Efficiency and Long-Term Solar Steam Generation, *Energy Technol.*, 8, 1900721. (DOI: [10.1002/ente.201900721](https://doi.org/10.1002/ente.201900721))
59. Chen Y., Yang J., Zhu L., Jia X., Wang S., Li Y., Song H. (2021), An Integrated Highly Hydrated Cellulose Network with a

- Synergistic Photothermal Effect for Efficient Solar-Driven Water Evaporation and Salt Resistance, *J. Mater. Chem. A*, *9*, 15482–15492. (DOI: 10.1039/D1TA04325K)
60. Gui J., Chen Y., Yu D., Wang W. (2024), Novel Nanocellulose-Based Self-Floating and Salt-Collectible Evaporator Prepared by a 3D Template Method Applied for Multiscenario Water Evaporation, *ACS Sustainable Chem. Eng.*, *12*, 13687. (DOI: 10.1021/acssuschemeng.4c06043)
 61. Wei D., Wang C., Shi G., Zhang J., Wang F., Tan P., Zhao Z., Xie Y. (2024), Enabling Self-Adaptive Water-Energy-Balance of Photothermal Water Diode Evaporator: Dynamically Maximizing Energy Utilization Under the Ever-Changing Sunlight, *Adv. Mater.*, *36*, 2309507. (DOI: 10.1002/adma.202309507)
 62. Yu Z., Gu R., Tian Y., Xie P., Jin B., Cheng S. (2022), Enhanced Interfacial Solar Evaporation through Formation of Micro-Menisci and Microdroplets to Reduce Evaporation Enthalpy, *Adv. Funct. Mater.*, *32*, 2108586. (DOI: 10.1002/adfm.202108586)
 63. Huang Z., Wei J., Wan Y., Li P., Yu J., Dong J., Wang S., Li S., Lee C.-S. (2021), Aligned Millineedle Arrays for Solar Power Seawater Desalination with Site-Specific Salt Formation, *Small*, *17*, 2101487. (DOI: 10.1002/sml.202101487)
 64. Gao C., Li Y., Lan L., Wang Q., Zhou B., Chen Y., Li J., Guo J., Mao J. (2024), Bioinspired Asymmetric Polypyrrole Membranes with Enhanced Photothermal Conversion for Highly Efficient Solar Evaporation, *Adv. Sci.*, *11*, 2306833. (DOI: 10.1002/advs.202306833)
 65. Tomasetti S. J., Gobler C. J. (2020), Dissolved Oxygen and pH Criteria Leave Fisheries at Risk, *Science*, *368*, 372–373. (DOI: 10.1126/science.aba4896)



Chapter 7

Conclusions and Future Scope

7.1. Conclusions

The rapid industrialization and urbanization of modern society have resulted in the increased contamination of water resources by pollutants, such as heavy metal ions, pharmaceuticals, dyes, and explosives. To address the dual challenge of water scarcity and pollution, the development of efficient, sustainable, environmentally friendly technologies for environmental remediation and water purification is a pressing global priority. To address these challenges, carbon dots, a novel class of zero-dimensional carbon-based nanomaterials, have emerged as highly promising candidates owing to their unique photophysical and chemical properties.

This thesis focuses on developing carbon dot-based optical sensors and photothermally active membranes for water remediation. As compared to semiconductor quantum dots and other organic fluorophores, carbon dots exhibit outstanding characteristics such as tunable photoluminescence, excellent aqueous dispersibility, remarkable biocompatibility, resistance to photobleaching, simple and cost-effective synthesis, and superior NIR light-harvesting ability. These unique features make them particularly suitable for applications in sensing, photocatalytic degradation, and solar-driven water evaporation. This thesis underscores the benefits of using carbon-rich natural resources as well as chemical precursors for the synthesis of carbon dots via bottom-up approaches, especially the hydrothermal method. The use of biomass-derived precursors converts low-value waste into high-performance nanomaterials. A key highlight of this research is the functionalization of CDs through strategies like doping and chemical reduction to tune their optical properties. These modifications significantly enhance the photoluminescence quantum yield and broaden the emission range, thereby expanding the scope of CDs in various environmental applications.

In this regard, green carbon dots were derived from banana peel, which was further reduced to tune their optical properties. Further, sensing

attributes of both these carbon dots were explored towards metal ion sensing. The non-reduced carbon dots show selective sensitivity towards cobalt, whereas the reduced carbon dots are highly sensitive towards cobalt and mercury. To ensure recyclability and portability, the carbon dots were incorporated into polymeric or biopolymeric matrices, such as bacterial cellulose and polyvinylidene fluoride, which further enhanced their applicability by improving mechanical stability, reusability, and operational feasibility. Such carbon dot-based nanocomposites (CNCs) have demonstrated exceptional performance in key environmental applications.

So far, very little work has been done towards the fabrication of-film for picric acid detection. Picric acid is a key member of nitroaromatic compounds and is considered a significant groundwater contaminant as it discharges into water bodies. Therefore, effective monitoring and trace-level detection are of critical importance. Thus, utilizing *C. thevetia*-derived carbon dots, picric acid was detected at a trace level. Further, the reusability of these carbon dots has been increased by incorporating them in PVDF to form a flexible, portable thin film for highly selective sensing of picric acid. The fabricated thin film works well in various real-time conditions and can be utilized for real-sample analysis as well, highlighting its practicality.

The excessive and widespread use of antibiotic drugs such as tetracycline and doxycycline for treating bacterial infections has a detrimental effect on human health and water sources. Therefore, their removal, i.e., detection and degradation, is vital to ensure human and environmental safety. The melamine-derived photocatalytically active carbon dots have been synthesized and further incorporated into three-dimensional bacterial cellulose to fabricate the portable fluorescence sensor. The as-synthesized carbon dot and its composite hydrogel are utilized for sensing as well as degradation of tetracycline and doxycycline.

Owing to broad-spectrum light absorption and high photothermal conversion efficiency, the carbon dots were further utilized for fabricating photothermally active membranes by embedding them in porous matrices. Toward this end, a multifunctional hydrogel was fabricated from lignin-derived carbon dots incorporated into bacterial cellulose hydrogel via cross-linking. The fabricated hydrogel shows excellent NIR absorption, which was demonstrated for the generation of clean water and also for decontaminating polluted water.

In another related work, an efficient solar evaporator was fabricated by incorporating a novel carbon dot-based organic network into bacterial cellulose via the Alder-Longo reaction. The synthesized solar evaporator is ideal for freshwater generation and desalination. The membrane exhibited long-term stability and works well with the water from various sources, and also at different environmental conditions for a sustainable solution. Overall, this study underscores the versatility and potential of CDs as multifunctional nanomaterials for addressing global environmental challenges. The findings validate the strategic importance of CDs in the development of next-generation materials for water purification, pollutant sensing, and renewable energy harvesting.

7.2. Scope for Future Work

Despite the progress made, several challenges and avenues for future research remain.

- ❖ Deeper insights are required to know about the exact photoluminescence mechanism of carbon dots; computational modelling and advancing spectroscopic techniques will be key in this field.
- ❖ As carbon dots are derived from various sources and methods, standardizing the synthesis protocol could greatly improve their consistency in performance during bulk synthesis.

- ❖ Developing a hybrid nanocomposite that combines carbon dots with other functional materials such as MOF, 2D materials, etc, to enhance multifunctionality.
- ❖ Incorporating a carbon dot-based system into smart sensors, wearable devices, and environmental monitoring platforms for real-time detection and remediation processes.
- ❖ Carbon dots show a promising role in solar-driven water evaporation, so extending work for real-time application and also expanding their use in electricity generation during water evaporation is a high-impact area for sustainable energy research.

Annexure 1
Table A1

Table A1. Permission to reproduce the materials.

Figure 1.1.	Representation of freshwater usage worldwide	Data taken from the 2024 United Nations World Water Development Report
Figure 1.3	Schematic illustration highlighting the distinct types of carbon dots	Reproduced from Ref. [64]: Chapter 1, with permission from wiley.
Figure 1.5a	Carbon dots derived from (a) Orange peels	Reproduced from Ref. [71]: Chapter 1, with permission from ACS.
Figure 1.5b	Carbon dots derived from (b) banana peel,	Reproduced from Ref. [72]: Chapter 1, with permission from RSC.
Figure 1.5c	Carbon dots derived from (c) <i>Rosa Roxburghii</i>	Reproduced from Ref. [73]: Chapter 1, with permission from ACS.
Figure 1.5d	Carbon dots derived from (d) chicken eggshell	Reproduced from Ref. [74]: Chapter 1, with permission from RSC.
Figure 1.5e	Carbon dots derived from (e) fish scalp	Reproduced from Ref. [75]: Chapter 1, with permission from RSC.
Figure 1.5f	Carbon dots derived from (f) elephant manure	Reproduced from Ref. [76]: Chapter

		1, with permission from Elsevier.
Figure 1.6a	(a) Initial steps for the reaction of citric acid and phenylalanine to synthesize CDs	Reproduced from Ref. [85]: Chapter 1, with permission from ACS.
Figure 1.6b	(b) Synthesis route of CQDs by radical-assisted synthetic strategy using perylene precursors	Reproduced from Ref. [86]: Chapter 1, with permission from Wiley.
Figure 1.6c	(c) Synthesis process of multicolor emissive CDs with ionic liquid as solvent and citric acid, pyrocatechol, and o-phenylenediamine as precursors	Reproduced from Ref. [87]: Chapter 1, with permission from Wiley.
Figure 1.10a	Schematic Illustration of: (a) aggregation-induced FL enhancement mechanism of the SCD solution in the presence of mercury	Reproduced from Ref. [154]: Chapter 1, with permission from ACS.
Figure 1.10b	Schematic Illustration of: (b) NCDs show a turn-off strategy for the detection of ascorbic acid and Fe^{3+}	Reproduced from Ref. [155] Chapter 1, with permission from ACS.
Figure 1.10c	Schematic Illustration of: (c) Dual quenching mechanism for picric acid detection using NCD	Reproduced from Ref. [156]: Chapter 1, with permission from ACS.
Figure 1.10d	Schematic Illustration of: (d) TP-CQDs for CTC detection	Reproduced from Ref. [157]: Chapter 1, with permission from ACS.
Figure 1.11a	Schematic showing: (a) CDs	Reproduced from

	generate reactive radical species for pollutant degradation	Ref. [158]: Chapter 1, with permission from ACS.
Figure 1.11b	Schematic showing: (b) BCQD@TiO ₂ for degradation of Favipiravir	Reproduced from Ref. [18]: Chapter 1, with permission from ACS.
Figure 1.11c	Schematic showing: (c) synthesis of PVP-CD hybrid hydrogel for adsorption and photodegradation of dye	Reproduced from Ref. [167]: Chapter 1, with permission from Elsevier.
Figure 1.12a	Schematic illustration of: (a) C-LCDCA material exhibiting high efficiency evaporation, salt tolerance, and self-cleaning ability. ¹⁷⁴	Reproduced from Ref. [174]: Chapter 1 with permission from Elsevier.
Figure 1.12b	Schematic illustration of: (b) Fabrication of the CD-Wood evaporator and the setup of the solar steam generation device	Reproduced from Ref. [175]: Chapter 1 with permission from Elsevier.
Figure 1.12c	Schematic illustration of: (c) Schematic representation of the synthesis pathways for F-CDs, PA-CDs, and HA-CDs, along with the hierarchical assembly mechanism of HA-CDs in the solar evaporator	Reproduced from Ref. [176]: Chapter 1 with permission from Wiley.



INDIAN INSTITUTE OF TECHNOLOGY INDORE

I hereby certify that the work which is being presented in the thesis entitled **Multifunctional Carbon Dots-Based Nanocomposites for Sustainable Environmental Management and Solar-Driven Water Evaporation** in the partial fulfillment of the requirements for the award of the degree of **DOCTOR OF PHILOSOPHY** and submitted in the **DEPARTMENT OF CHEMISTRY, Indian Institute of Technology Indore**, is an authentic record of my own work carried out during the time period from **AUGUST 2020** to **JUNE 2025** under the supervision of **Dr. Shaikh M. Mobin**, Professor, Department of Chemistry, IIT Indore.

The matter presented in this thesis has not been submitted by me for the award of any other degree of this or any other institute.

Nirmite

Signature of the student with date
(NIRMITI MATE)

This is to certify that the above statement made by the candidate is correct to the best of my knowledge.

M. Shaikh

Signature of Thesis Supervisor with date
(PROF. SHAIKH M. MOBIN)

NIRMITI MATE has successfully given his/her Ph.D. Oral Examination held on *Dec. 9, 2025*

M. Shaikh

Signature of Thesis Supervisor with date
(PROF. SHAIKH M. MOBIN)
